Quasiparticle dynamics in aluminium superconducting microwave resonators

Pieter de Visser

Quasiparticle dynamics in aluminium superconducting microwave resonators

Quasiparticle dynamics in aluminium superconducting microwave resonators

Proefschrift

ter verkrijging van de graad van doctor
aan de Technische Universiteit Delft,
op gezag van de Rector Magnificus prof. ir. K. Ch. A. M. Luyben,
voorzitter van het College voor Promoties,
in het openbaar te verdedigen op dinsdag 11 maart 2014 om 15:00 uur

door

Pieter Jan DE VISSER

natuurkundig ingenieur
geboren te Vlissingen.

Dit proefschrift is goedgekeurd door de promotor:
Prof. dr. ir. T. M. Klapwijk

Copromotor:
Dr. ir. J. J. A. Baselmans

Samenstelling van de promotiecommissie:

Rector Magnificus,	voorzitter
Prof. dr. ir. T. M. Klapwijk	Technische Universiteit Delft, promotor
Dr. ir. J. J. A. Baselmans	SRON Netherlands Institute for Space Research, Utrecht, copromotor
Prof. dr. K. D. Irwin	Stanford University, Verenigde Staten
Prof. dr. R. J. A. Röttgering	Universiteit Leiden
Prof. dr. ir. J. E. Mooij	Technische Universiteit Delft
Prof. dr. Y. V. Nazarov	Technische Universiteit Delft
Dr. L. DiCarlo	Technische Universiteit Delft
Prof. dr. ir. L. M. K. Vandersypen	Technische Universiteit Delft, reservelid

Published by: P. J. de Visser

Printed by: GVO printers & designers | Ponsen & Looijen, Ede, The Netherlands

Cover design: The main photograph is taken while shining a green laser onto a boiling bath of nitrogen (courtesy Rik Hortensius and Cosmonano). It visualises the title of Chapter 7: ‘Fluctuations (the bubbles) in the electron system of a superconductor (the sea) exposed to a photon flux (the beam)’. In the background, an SEM image of the X-slot antenna is visible, which was used to couple terahertz radiation into our microwave resonator detectors. The noise trace is a measurement of the response of such a resonator as a function of time, showing a cosmic ray hit halfway. The image at the back is a sculpture by the author, which shows the typical posture of a PhD student during reading, writing, thinking, taking notes, taking data, soldering, and drinking.

Casimir PhD Series, Delft-Leiden, 2014-3

ISBN 978-90-8593-178-2

Contents

Chapter 1

Introduction

1.1 Night owls

The eye is the most fundamental light detector for a human being. It allows us to distinguish the intensity, colour, and spatial distribution of the light we receive remarkably well. Every photographer will recognise the problem of scenes that look promising by eye, but which are very difficult to capture with a camera. In astronomy the eye has long been the only available detector. One of the relics of these times is the system of magnitudes with which the brightness of stars is expressed, which dates back to the star catalogue by Hipparchos of ∼150 BC [1]. Over the centuries several instruments were developed to determine the position of objects more accurately. Later on lens systems and telescopes enhanced the dynamic range and resolution of the observations. The eye remained the detector element for a long time although, as we know now, it is a rather limited astronomical instrument. Even owl eyes, which are legendary for their night vision, have only a few times better sensitivity than the human eye [2]. Moreover, they cannot take away the drawbacks to using the eye, such as the inability to perform an exact measurement of the intensity and colour of an object and the limited capacity and speed to efficiently map large pieces of sky. The latter is not so much a problem of the eye itself, which contains about 100 million rod-receptors for night vision, but of the image analysis performance of the brain. These drawbacks are resolved by digital cameras with millions of pixels, which are nowadays commercially available. Such a camera is usually based on semiconductor technology in which each photon creates only a single (electron-hole) excitation, because of the high excitation energy in semiconductors. Therefore the energy of the photon can be only determined using colour filters in front of the detector. The high excitation energy causes the major disadvantage of eyes as well as of semiconductor detectors: the limitation to visible (and shorter) wavelengths.

Superconducting detectors

In a superconductor at low temperatures, the electrons form pairs with a binding energy of less than $1/1000^{\mathrm{th}}$ of the excitation energy in a semiconductor. Therefore, optical photons create more than 1000 excitations in a superconductor, enabling a measure of the photon energy. More importantly, superconductors open up the radiation window of frequencies far below the optical regime. For example aluminium has an excitation energy of 0.18 meV, corresponding to 90 GHz photons. An aluminium based superconducting detector can therefore access the whole terahertz regime. The terahertz regime is defined in almost as many ways as there are people defining it, with the widest window from 0.1 - 10 THz. It has overlap with definitions of the submillimetre- and far-infrared range. Remarkably, half of the luminosity of the universe is contained in this frequency regime. In addition, a lot of spectral lines of simple and complex molecules fall in this regime, which are important signatures for the composition of the interstellar medium [3].

The change in the properties of a superconductor upon absorption of radiation can be measured in several ways. First we distinguish three types of superconducting detectors. Pair-breaking detectors rely on the principle of breaking Cooper pairs in the superconductor directly. They are operated at temperatures far below the critical temperature of the superconductor to reduce thermal excitations. Bolometric detectors absorb the radiation in an absorbing structure in which the energy is converted to heat. The change in temperature is subsequently detected by a sensitive temperature sensor which is biased at the transition temperature of the superconductor (transition edge sensor [4]). A small change in temperature will therefore result in a large excursion of the resistance. These detectors operate at very low temperature ($\sim$100 mK), because the thermal noise is reduced linearly with decreasing temperature. Both pair-breaking and bolometric detectors can be used as direct detectors in multipixel cameras. The third type is the coherent detector, which performs a phase-preserving measurement by mixing the signal with a local oscillator. They are mainly used for few pixel, very high resolution spectroscopy, which has been proven highly valuable in the study of astrochemistry, for example in the HIFI instrument aboard the Herschel telescope and nowadays in the ALMA instrument. Coherent detectors cannot be used in large arrays, because of the local oscillator and the complex electronic backend that is required for each pixel.

To complement the well-developed high resolution spectroscopy, large format imaging arrays are needed to efficiently map large pieces of sky. Large, mega-pixel size arrays of photon-noise limited pixels are required. Photon-noise is the fundamental noise source due to the random arrival rate of photons from a thermal source. Since cryogenic detectors are needed, these large arrays present a real challenge in terms of readout electronics. An interesting new development is that of on-chip spectrometers with a large instantaneous bandwidth [5, 6], in which spectral bands are defined with superconducting resonators, each connected to a detector pixel. Spectrometry on chip therefore requires the same detector technology: large arrays of photon-noise limited detectors, although with higher sensitivity, because the radiation power is spread over narrow spectral bands. On-chip spectrometers can be more sensitive in space based instruments than heterodyne spectrometers and offer a very attractive way of miniaturizing spectroscopic systems, especially imaging spectrometers.

Over the whole submillimetre and terahertz range, the earth's atmosphere strongly limits astronomical observations. Especially the water in the atmosphere absorbs radiation in this spectral range. Even in the spectral windows that are open for observations, the atmosphere fully determines the background power. The best observation sites on earth are therefore inhospitable places such as Chili's Atacama desert at 5000 m altitude or the Antarctic. Space based telescopes resolve this problem. The recent Herschel Space Observatory mission [7], which covered the wavelength range of 55-672 μm, with a 3.5 m mirror, has been very successful in exploring the formation of galaxies and stars. The imaging spectrometer instruments discovered many new submillimetre galaxies and the high resolution spectrometer HIFI provided a wealth of molecular lines in star forming regions. A new generation of space telescopes is planned to follow up on Herschel's success, which requires even more sensitive detectors. SPICA is a proposed mission to observe in the wavelength range of 5-210 μm [8]. The key difference with other instruments is that the telescope mirror will be actively cooled to $\sim$6 K, which reduces the thermal radiation of the mirror and makes the instrument truly background limited. Most relevant for this thesis is the required sensitivity for a background limited imaging array. The detector NEP should be lower than $1\text{-}4\times10^{-19}$ W/Hz$^{1/2}$, dependent on the wavelength. For imaging spectrometry in space, detectors with a 20 times lower NEP are required. Although the SPICA instrument will have the most stringent detector requirements, other planned space observatories for this spectral range, such as Millimetron [9], require similarly sensitive detectors.

Quasiparticle excitations in a pair-breaking detector

The low excitation energy of the superconductor makes it an ideal element of a highly sensitive detector [10]. In a superconducting pair-breaking detector Cooper pairs are broken up into quasiparticle excitations by photons. To reach a high sensitivity with such a detector, excess quasiparticles that occur not due to the signal have to be reduced. The number of thermal quasiparticles decreases exponentially with decreasing temperature, which promises therefore high detector sensitivity by just lowering the operation temperature. A pair-breaking detector should be operated well below the critical temperature of the superconductor (T_c) to reduce the number of quasiparticles, typically $T_c/10$. However, any disturbance in the environment of the detector will also be detected and reduces the sensitivity to the real signal. These problems boil down to the more fundamental questions of why excess quasiparticles occur, how many excess quasiparticles are present in a superconductor, and whether or not their number can be reduced.

These questions are not only relevant to reaching the ultimate detector sensitivity, but also to other devices that rely on the absence of quasiparticle excitations at low

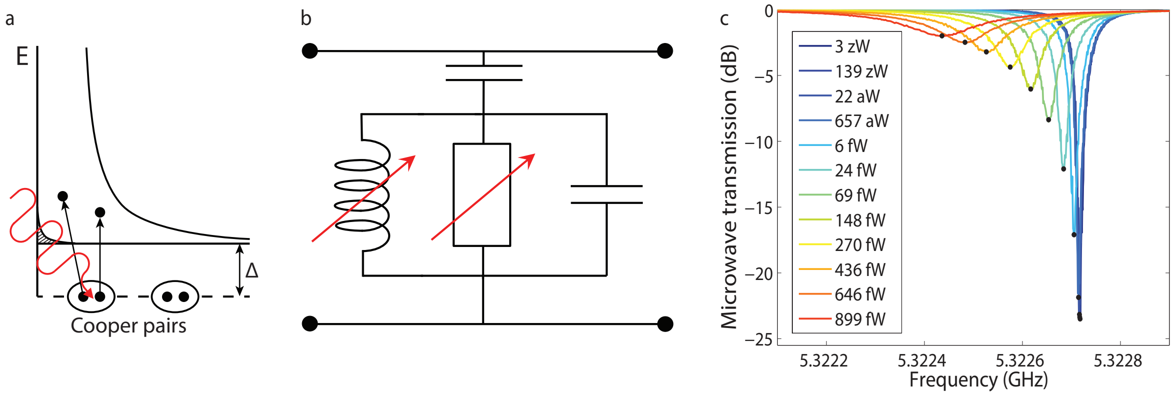

Figure 1.1: (a), Schematic of pair-breaking in a superconductor. A photon with an energy $hf > 2\Delta$ breaks a Cooper pair and excites two additional quasiparticles. (b), Simplified circuit diagram of a microwave resonator, which is capacitively coupled to a readout line. The change in the number of quasiparticles and Cooper pairs induces a change in the kinetic inductance and resistance of the resonator. (c), The microwave transmission as a function of frequency in an aluminium microwave resonator. Upon absorption of pair-breaking radiation, the resonant frequency shifts (inductance) and the depth of the resonance dip decreases (resistance). The legend gives the applied radiation power at 1.54 THz.

temperatures. In the field of circuit quantum electrodynamics, superconducting qubits are used as the building blocks of a quantum computer. Not only the building blocks, but also the embedding circuitry is superconductor based [11]. Quasiparticle excitations are detrimental to the coherence time of the qubit state and need to be eliminated to preserve the qubit state long enough to perform useful computations. Other devices based on low temperature superconductors suffer from excess quasiparticles as well, such as single-electron transistors [12]. For solid-state refrigeration based on superconducting junctions, excess quasiparticles could deteriorate the cooling power and limit the temperature to which a superconducting system can be cooled down [13].

1.2 Detection of radiation with superconducting resonators

The number of quasiparticle excitations can be measured in several ways. An established method is by measuring the current arising from photo-excited quasiparticles through a tunnel barrier (STJ) [14]. These detectors have to be tuned individually, which is an important drawback for use in large arrays. The number of quasiparticles can also be measured by monitoring the charge of a Cooper pair box, coupled to an absorber by tunnel-junctions, the quantum capacitance detector (QCD) [15]. QCDs can potentially be used in large arrays, because they can be embedded in microwave resonators and they have recently proven high sensitivity [16].

A change in the number of quasiparticles also changes the complex conductivity of the superconductor. In particular the kinetic inductance, which arises because of the inertia of the charge carriers, changes when the number of quasiparticles is changed. Since at low temperatures most electrons are bound into Cooper pairs, the resistance for an AC signal is low and the kinetic inductance of the Cooper pairs dominates the response to an electromagnetic field. It was realised by McDonald [17] that the temperature change in a bolometer could be detected by inductive coupling. But the absorption of pair-breaking radiation also changes the complex conductivity directly [18]. The connection of microwave resonators to the problem of detecting the change in the complex conductivity of the superconductor was made by Zmuidzinas and coworkers. The pair-breaking photons excite quasiparticles in the superconductor, which changes the kinetic inductance. The detector is therefore called Kinetic Inductance Detector (KID) [19]. The kinetic inductance affects the resonant frequency of a microwave resonator. Since superconducting microresonators can reach quality factors of 10^6, a small change in the kinetic inductance can be very sensitively detected. The resonant frequency of the resonator shifts downward when more radiation power is absorbed. On top of that, the quasiparticles increase the dissipation at microwave frequencies, which changes the quality factor of the resonator. Therefore one can use either the reactive or the dissipative response of the resonator to monitor the number of quasiparticles, depending on which gives the highest signal-to-noise. The detection principle is schematically depicted in Fig. 1.1.

The resonant frequency of a waveguide-based resonator is determined by its phase-velocity (capacitance and inductance) and its length. Therefore the resonant frequency of each resonator (pixel) can be designed to be slightly different by choosing a slightly different length. Thousands of resonators with different frequencies can therefore be coupled to the same readout line and can be read out simultaneously using frequency domain multiplexing. Since the fabrication of microresonators only requires one or two metal layers and lithography, this concept, with its intrinsic multiplexability, is very promising both for multipixel imaging and imaging spectroscopy on chip. In circuit quantum electrodynamics the same multiplexability of microwave resonators is exploited to address multiple qubits simultaneously. When millions of pixels are considered, profane aspects such as the cost per pixel start to be a design constraint, for which KIDs are favourable as well [20]. Several groups are therefore currently building instruments based on KIDs for large array, ground-based observations. Figure 1.2 shows part of the A-MKID chip for ground-based observations in the 850-950 GHz atmospheric window. Several reviews have summarised the progress in this field over the last decade [21–23]. Zmuidzinas [24] provides the most detailed review and discusses the historical development of the field extensively.

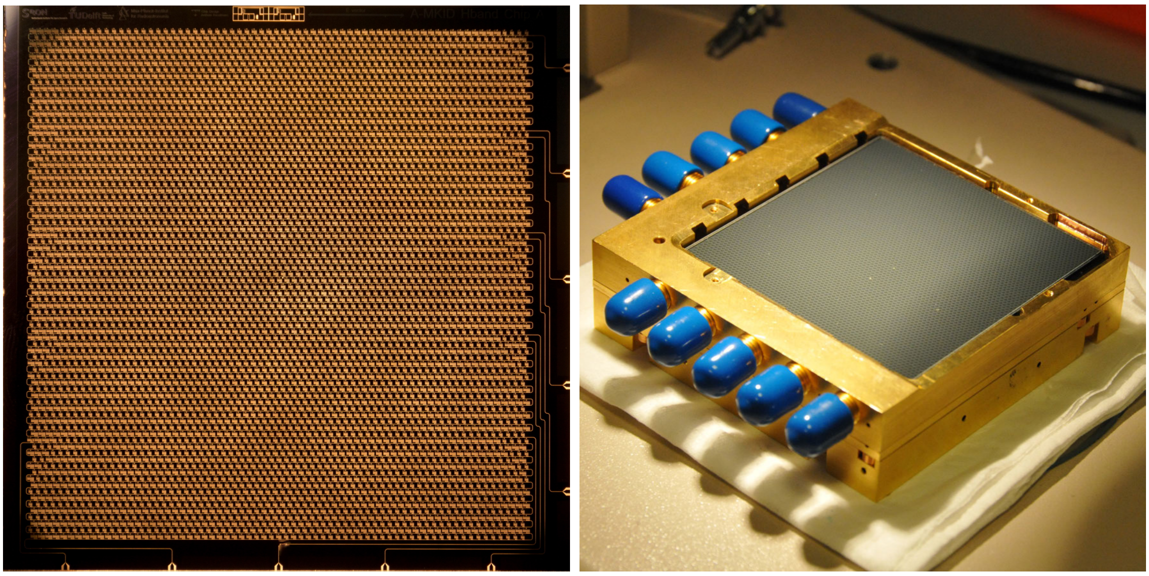

Figure 1.2: (left) The optical micrograph shows a chip with 5 transmission lines each connected to two bond pads at the edge of the chip. Each transmission line is connected to 1080 antenna-coupled Kinetic Inductance Detectors. The resonators are fabricated from a NbTiN film. The sensitive element of these detectors is a 1 mm long aluminium section close to the antenna in which pair-breaking radiation from the telescope is absorbed. When in operation, a Si microlens array with 5400 lenses is glued to the chip backside to allow efficient radiation coupling (right). In this configuration each of the antennas is in the focus of one single lenslet. The antennas are optimised for coupling to the 850-950 GHz atmospheric window. This chip is part of the A-MKID imaging array, which has four identical chips with 21600 pixels in total for the aforementioned atmospheric window. The instrument has another array of four similar chips, optimised for the 325-375 GHz atmospheric window. Courtesy of Jochem Baselmans.

Intrinsic noise: quasiparticle fluctuations

In essence, a pair-breaking detector counts the number of quasiparticle excitations. The random generation and recombination of these quasiparticle excitations gives rise to a noise mechanism intrinsic to the detection principle: generation-recombination noise. The detector noise is thus ideally limited by generation-recombination noise. A measurement of generation-recombination noise would mean that other noise sources are reduced sufficiently. Moreover as will be shown in this thesis, a measurement of these fluctuations is a reliable probe of the number of quasiparticles and their recombination lifetime, which provides valuable insight into the basic questions presented above. When the detector is illuminated continuously, the generation of quasiparticles fluctuates due to fluctuations in the photon stream (photon-noise), the fundamental limit to any power integrating detector. We distinguish photon-noise as fundamental fluctuations due to the source of radiation and generation-recombination noise as the fundamental fluctuations without applied radiation (i.e. the fundamental detector noise). The timescale with which the excited quasiparticles disappear is again the quasiparticle recombination time. The recombination time presents a design trade-off. It has to be long to enhance the sensitivity, but also short enough not to limit the speed of the detector. Understanding these properties of the superconductor is essential to understand the detection mechanism and enhance its sensitivity. In fact, the detailed measurement of quasiparticle fluctuations (Chapters 5 and 6) in an aluminium resonator provided the necessary insight to fabricate and characterise the most sensitive microresonator detector to date. We demonstrate in Chapter 7 an aluminium based detector at 1.54 THz, which shows photon-noise limited detection over more than four orders of magnitude in power, from 0.7 pW down to 0.1 fW. Below 0.1 fW the optical NEP saturates at 3.8×10^{-19} W/Hz$^{1/2}$, due to the generation-recombination noise caused by excess quasiparticles. Clearly these detectors start to fulfil their promise for space-based imaging as well.

1.3 Outline of this thesis

This thesis focuses on the intrinsic limits of pair-breaking radiation detection with aluminium superconducting microwave resonators. The main focus is on the fundamental noise processes in these devices, generation-recombination noise and photon noise. We show that generation-recombination noise is as well a powerful method to study basic properties of a superconductor, the number of quasiparticles and their recombination lifetime. The second important question is how the absorbed microwave readout power affects the response of the superconductor and therewith the response of microwave resonators.

Chapter 2 introduces the concepts of superconductivity, Cooper pairs and quasiparticles. The microwave response of a superconductor is discussed, which is mostly determined by the distribution of the quasiparticles over energy. We present expressions for the response of the complex conductivity to changes in the number of quasiparticles. Quasiparticle number fluctuations are introduced and we discuss their characteristic signatures. Two processes that affect the superconductor and the quasiparticle distribution are discussed: the absorption of pair-breaking photons (the detection mechanism) and the absorption of microwave photons from the readout signal. Finally the properties of some commonly used materials are reviewed.

Chapter 3 presents the experimental setup and which requirements it has to fulfil to enable the study of the fundamental noise processes. The main focus is on reducing the effects of the environment on the measurement and on how to introduce radiation in a controlled way to effectively mimic the conditions for a space-based detector. The basics of microwave resonators are reviewed and we discuss how the observables in a resonator experiment are connected with the concepts introduced in *Chapter 2*. We present the microwave readout circuitry and discuss how the measurements are performed. Finally we briefly review the fabrication of the devices.

In *Chapter 4* we present a model in which the absorption of microwave readout power in the resonator is treated as heating. We solve the heat balance between microwave heating due to the readout power and cooling through electron-phonon interaction. We show that the effective quasiparticle temperature is increased dramatically, which leads to a strong distortion of the resonance curves. For high power levels this even leads to hysteretic switching between different thermal states.

Chapter 5: we directly measure quasiparticle number fluctuations in an aluminium microwave resonator. These fluctuations cause fluctuations in the complex conductivity, which show up in the microwave response of the resonator. The roll-off in the spectrum of the fluctuations is a measure of the quasiparticle recombination time. We also derive the number of quasiparticles from the noise spectra. We observe a saturation in the recombination time at low temperatures, which is explained by a saturation in the measured number of quasiparticles.

In *Chapter 6* we continue to analyse measurements of quasiparticle number fluctuations. We investigate correlated fluctuations in the response of the quasiparticles and in the response of the condensate, which show up in the amplitude (dissipation) and phase (kinetic inductance) response of the resonator respectively. Because uncorrelated noise sources vanish, the quasiparticle fluctuations can be studied with a sensitivity close to the vacuum noise level. We reveal a microwave readout power dependent number of quasiparticles, which elucidates the origin of the saturation in the number of quasiparticles observed in *Chapter 5.* Based on these dark measurements the lowest generation-recombination limited (detector) NEP is 2×10^{-19} W/Hz$^{1/2}$.

Chapter 7 describes an experiment in which we illuminate an aluminium microwave resonator with pair-breaking radiation at 1.54 THz. Radiation is coupled to the resonator through a lens and an antenna. A large range in radiation power can be chosen by carefully filtering the radiation from a thermal blackbody source. Two regimes occur. At radiation powers of 0.1 fW and higher, we observe photon-noise limited detection, which is verified through a measurement of the spectra of quasiparticle fluctuations. Below 0.1 fW the fluctuations are dominated by excess quasiparticles. In this regime the sensitivity saturates to an optical NEP of 3.8×10^{-19} W/Hz$^{1/2}$, close to the predicted value based on the dark experiments in *Chapters 5 and 6.* The optical responsivity in the saturation regime is readout power dependent as expected from *Chapter 6.*

Chapter 8: we show that microwave absorption in the quasiparticle system of the superconductor leads to redistribution of quasiparticles. The non-equilibrium distribution functions lead to a nonlinear response of the complex conductivity, which is measured through the quality factor and resonant frequency of an aluminium microwave resonator. At low temperature, excess quasiparticles are being created (consistent with the observations in *Chapters 5 and 6*), which reduces the quality factor and resonator frequency, not unlike the heating model in *Chapter 4.* At higher temperatures the opposite behaviour is observed (higher quality factor and resonant frequency with increasing

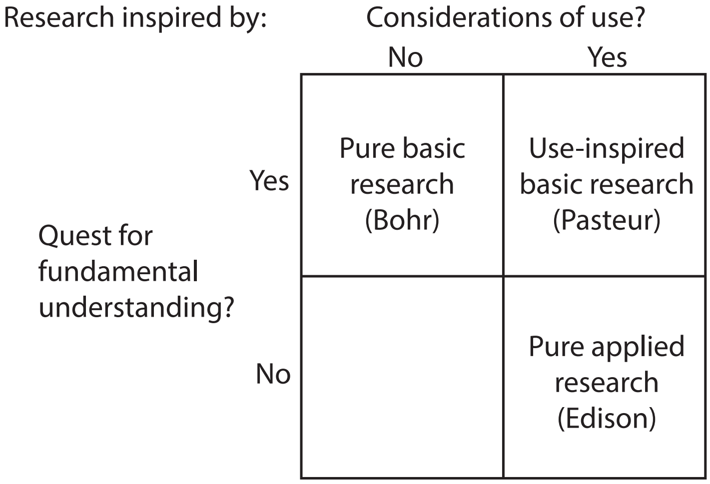

Figure 1.3: Quadrant model of scientific research according to Stokes [25].

power), which can only be explained by the shape of the non-equilibrium quasiparticle distribution functions. The redistribution of quasiparticles at low temperature is the origin of the excess quasiparticles, which currently limit the sensitivity of aluminium microwave resonator detectors.

Detector research as use-inspired basic science

The question could arise whether the research presented in this thesis is applied or more fundamental research. While the astronomer asks for the most sensitive instrument possible, the chief technology's goal is to develop and build that instrument, the instrument scientists task is to solve technical challenges and the device physicist's desire is to understand what actually happens when a particular photon is absorbed, or why it is absorbed at all. In this respect the organisation of detector development is exemplary of the question how to organise science and technology in a society and how to fund it. Unsatisfied with the classical one-dimensional contrast between basic and applied science, Stokes [25] put forward a two dimensional model to understand science and technology, which is shown in Fig. 1.3. Whereas Bohr and Edison serve as examples of researchers driven respectively by the quest for fundamental understanding or purely by consideration of use, he identifies Pasteur's research as an example of use-inspired basic research. In a one-dimensional picture, Pasteur's research would require two separated points: on the one hand, he had a strong drive toward understanding (basic) and on the other hand a drive toward control (applied). The example of Pasteur makes clear that a one-dimensional model of scientific research is too simple. The quadrant model takes account of the colourful palette of approaches to scientific. There is no inherent judgement in this model, all three examples caused a revolution in their own way. For the development of sensitive detectors different development routes can be imagined. One extreme would be to first resolve all basic questions about the physics of the device, before starting to build a detector. The opposite approach is to just build it based on the users need and see whether or not it works. In organisational form separate institutes for astronomy, instrument development and basic physics research exist. For many steps in the process of developing a large instrument, the separation of tasks is practical. However for detector research, it appears to be particularly fruitful to explicitly organise and finance interaction layers in which the user inspiration and the basic research strengthen each other. In such an environment an ideal mixture of the two development routes can be pursued.

References

[1] C. R. Kitchin, *Astrophysical Techniques*, Taylor & Francis Group, LLC, 4^{th} edition, 2003.

[2] G. R. Martin, *An owl's eye: Schematic optics and visual performance in Strix aluco L.*, J. Compar. Physiology **145**, 341 (1982).

[3] G. J. Stacey, *THz Low Resolution Spectroscopy for Astronomy*, IEEE Trans. Terahertz Sci. Tech. **1**, 241 (2011).

[4] K. D. Irwin, G. C. Hilton, D. A. Wollman, and J. M. Martinis, *X-ray detection using a superconducting transition-edge sensor microcalorimeter with electrothermal feedback*, Appl. Phys. Lett. **69**, 1945 (1996).

[5] A. Endo, P. van der Werf, R. M. J. Janssen, P. J. de Visser, T. M. Klapwijk, J. J. A. Baselmans, L. Ferrari, A. M. Baryshev, and S. J. C. Yates, *Design of an Integrated Filterbank for DESHIMA: On-Chip Submillimeter Imaging Spectrograph Based on Superconducting Resonators*, J. Low Temp. Phys. **167**, 341 (2012).

[6] A. Kovács, P. S. Barry, C. M. Bradford, G. Chattopadhyay, P. Day, S. Doyle, S. Hailey-Dunsheath, M. Hollister, C. McKenney, H. G. LeDuc, N. Llombart, D. P. Marrone, P. Mauskopf, R. C. O'Brient, S. Padin, L. J. Swenson, and J. Zmuidzinas, *SuperSpec: design concept and circuit simulations*, Proc. SPIE **8452**, 84522G (2012).

[7] The Herschel website http://herschel.esac.esa.int/ provides an overview of the mission, the instruments and the many astronomy publications based on Herschel observations.

[8] SPICA Study Team Collaboration, *SPICA Assessment Study Report for ESA Cosmic Vision 2015-2025 Plan*, ESA/SRE(2009)6 , available on http://arxiv.org/abs/1001.0709.

[9] W. Wild et al., *Millimetron - a large Russian-European submillimeter space observatory*, Exp. Astronomy **23**, 221 (2009).

[10] K. D. Irwin, *Seeing with Superconductors*, Scientific American **295**, 86 (2006).

[11] R. J. Schoelkopf and S. M. Girvin, *Wiring up quantum systems*, Nature **451**, 664 (2008).

[12] J. P. Pekola, O.-P. Saira, V. F. Maisi, A. Kemppinen, M. Möttönen, Y. A. Pashkin, and D. V. Averin, *Single-electron current sources: Toward a refined definition of the ampere*, Rev. Mod. Phys. **85**, 1421 (2013).

[13] J. T. Muhonen, M. Meschke, and J. P. Pekola, *Micrometre-scale refrigerators*, Rep. Prog. Phys. **75**, 046501 (2012).

[14] A. Peacock, P. Verhoeve, N. Rando, A. van Dordrecht, B. G. Taylor, C. Erd, M. A. C. Perryman, R. Venn, J. Howlett, D. J. Goldie, J. Lumley, and M. Wallis, *Single optical photon detection with a superconducting tunnel junction*, Nature **381**, 135 (1996).

[15] M. D. Shaw, J. Bueno, P. Day, C. M. Bradford, and P. M. Echternach, *Quantum capacitance detector: A pair-breaking radiation detector based on the single Cooper-pair box*, Phys. Rev. B **79**, 144511 (2009).

[16] P. M. Echternach, K. J. Stone, C. M. Bradford, P. K. Day, D. W. Wilson, K. G. Megerian, N. Llombart, and J. Bueno, *Photon shot noise limited detection of terahertz radiation using a quantum capacitance detector*, Appl. Phys. Lett. **103**, 053510 (2013).

[17] D. G. McDonald, *Novel superconducting thermometer for bolometric applications*, Appl. Phys. Lett. **50**, 775 (1987).

[18] N. Bluzer, *Analysis of quantum superconducting kinetic inductance photodetectors*, J. Appl. Phys. **78**, 7340 (1995).

[19] P. K. Day, H. G. LeDuc, B. A. Mazin, A. Vayonakis, and J. Zmuidzinas, *A broadband superconducting detector suitable for use in large arrays*, Nature **425**, 817 (2003).

[20] L. J. Swenson, P. K. Day, C. D. Dowell, B. H. Eom, M. I. Hollister, R. Jarnot, A. Kovcs, H. G. Leduc, C. M. McKenney, R. Monroe, T. Mroczkowski, H. T. Nguyen, and J. Zmuidzinas, *MAKO: a pathfinder instrument for on-sky demonstration of low-cost 350 micron imaging arrays*, Proc. SPIE **8452**, 84520P (2012).

[21] B. A. Mazin, *Microwave Kinetic Inductance Detectors: The First Decade*, AIP Conf. Proc. **1185**, 135 (2009).

[22] S. Doyle, P. Mauskopf, J. Zhang, A. Monfardini, L. Swenson, J. J. A. Baselmans, S. J. C. Yates, and M. Roesch, *A review of the lumped element kinetic inductance detector*, Proc. SPIE **7741**, 77410M (2010).

[23] J. Baselmans, *Kinetic Inductance Detectors*, J. Low Temp. Phys. **167**, 292 (2012).

[24] J. Zmuidzinas, *Superconducting Microresonators: Physics and Applications*, Ann. Rev. Condens. Matter Phys. **3**, 169 (2012).

[25] D. E. Stokes, *Pasteur's Quadrant*, Brookings Institution Press, Washington, 1997.

Chapter 2

A pair-breaking detector: superconductivity and photons

A microwave kinetic inductance detector is based on the principle of breaking Cooper pairs in a superconductor into quasiparticles by absorption of radiation. The change in the number of Cooper pairs is detected with a microwave resonator. As such, we need to understand the basic principles of superconductivity and what we mean by Cooper pairs and quasiparticles, which is described in Section 2.1. In Section 2.2 the response of the microwave readout signal to a change in the number of quasiparticles is discussed. The fundamental source of noise is due to fluctuations in the number of quasiparticles (Section 2.3). The quasiparticle system can be changed in different ways. In Section 2.4 we describe how microwave absorption, with a photon energy smaller than the superconducting energy gap, leads to a non-equilibrium quasiparticle distribution. How pair-breaking radiation affects the superconductor is discussed in Section 2.5. In Section 2.6 we discuss how material dependent parameters affect the detector sensitivity and review some of the most popular materials.

2.1 Superconductivity

Many solids conduct electricity, an indication that there are electrons that can move more or less freely through the material. Solid state materials consist of heavy positively charged ions in a lattice, which are surrounded by more mobile electrons. The arrangement of the lattice and the interaction between the electrons and the ions determines the available energy states for the electrons. The interaction with the lattice gives rise to energy bands: regions in energy with available states, separated by regions without available states, the band gaps. The electrons occupy the lowest energy levels available to minimise the total energy of the system. Because of the Pauli exclusion principle, which forbids that two electrons occupy the same state, electrons have to fill up higher energy states as well. When all electrons are distributed the electrons occupy states up to a certain energy, which is defined as the Fermi energy. When all states in a low lying band are occupied (i.e. the Fermi energy is at the top of the energy band) and there is a large band gap, the electrons cannot move to states with different energies, which is needed for charge transport, and the material is insulating. Only high energy excitations (photons for instance) can bring electrons into the conduction band. In the case that the bandgap is sufficiently small to allow some thermal excitations to unoccupied states across the bandgap, the material behaves as a semiconductor. If the Fermi energy is in the middle of an energy band, excitations with any small energy are possible. The electrons can move freely and metallic behaviour occurs [1].

In a normal metal, the transport of electrons can be well described with a free electron model, where interactions between the electrons are negligible. However, there is a strong repulsive interaction between the electrons, the Coulomb interaction, which acts over distances larger than the typical inter-electron distance. But, since each electron is surrounded by a cloud of electrons, the long range interaction is effectively screened. As the electron moves through the electron cloud, its screening cloud moves along as if it were an independent particle. The collectively moving entity is called a quasiparticle. The metal thus forms a gas of weakly interacting quasiparticles, which behave electron-like and can each be described with their own, independent wave function [2].

In superconductors, the quasiparticles form a bound state. The attractive interaction which is needed for such a bound state cannot be delivered by interaction of the electrons alone, which is always repulsive. It was already known in 1950 that the critical temperature of superconductors depends on the mass of the isotopes in the material [3, 4]. Therefore a role of the lattice in the emergence of superconductivity was expected, although the high energies associated with lattice vibrations seem to contradict with the low energy scales associated with superconductivity (the Debye temperature is of order 200-400 K whereas the critical temperature is typically 1-10 K). Cooper derived that for two electrons in the presence of non-interacting electrons (the Fermi sea), a bound state exists, even for the weakest attractive interaction [5]. For the lowest energy the two electrons have equal and opposite momenta and have opposite spin. The net attractive interaction can be understood by considering the attractive force between the electrons and the positively charged ions in the lattice. An electron that moves through the lattice leaves a wake of enhanced positive charge behind, because the ions move more slowly than the electrons. The positive region can attract another electron, which than effectively forms a pair with the first one. The only prerequisite is thus that the electron-phonon coupling is stronger than the effective Coulomb interaction, which is weakened by screening as discussed earlier.

The formation of these Cooper pairs is not restricted to just one pair of electrons, but one would expect all the electrons to pair as long as it is energetically favourable. The mathematical description of the superconducting ground state, in which all the conduction electrons are paired at zero temperature, was postulated by Bardeen, Cooper and Schrieffer (BCS) [6] and is given by

$$|\psi_G >= \Pi_{\mathbf{k}}(u_{\mathbf{k}} + v_{\mathbf{k}} c^*_{\mathbf{k}\uparrow} c^*_{-\mathbf{k}\downarrow})|\phi_0 >, \tag{2.1}$$

where $|\phi_0 >$ is the vacuum state. The operator $c^*_{\mathbf{k}\uparrow}$ creates an electron of momentum $\mathbf{k}$ and spin up. The probability of a pair $(\mathbf{k}\uparrow, -\mathbf{k}\downarrow)$ being occupied is $|v_{\mathbf{k}}|^2$. The probability that it is unpaired is $|u_{\mathbf{k}}|^2 = 1 - |v_{\mathbf{k}}|^2$. The sphere of influence or the size of the Cooper pair is called the coherence length and is given by $\xi_0 = \hbar v_F/\pi\Delta_0$, with v_F the Fermi velocity, $\hbar$ the reduced Planck constant, and Δ_0 the energy gap at zero temperature. The electrons thus condense into a collective state of Cooper pairs. As such, all the electrons can be described with just one wavefunction $|\Delta|\exp(i\phi)$. $|\Delta|^2 \propto n_s$, with n_s the Cooper pair density. This macroscopic quantum state has a well-defined phase ϕ, which gives rise to phase-dependent phenomena such as flux quantisation and the Josephson effects.

The excitations of the superconductor are the excitations above the collective groundstate of Eq. 2.1, and are called Bogoliubov quasiparticles or Bogoliubons. The excitations have a minimum energy $E \geq \Delta$, which reflects the energy gap of the superconductor. The quasiparticles can be both electron-like and hole-like or a mixture of the two, but can be treated as single fermionic particles, like in normal metals. Because of the collective nature of the superconducting state, excitations also affect the binding energy of the rest of the condensate. The value of Δ is determined by the distribution function of the quasiparticles over energy $f(E)$ and given by

$$\frac{1}{N_0 V_{sc}} = \int_{\Delta(T)}^{k_B T_D} \frac{1 - 2f(E)}{\sqrt{E^2 - \Delta^2(T)}} dE, \tag{2.2}$$

where N_0 is the single-spin density of states at the Fermi surface, V_{sc} the potential energy describing electron-phonon exchange, T_D the Debye temperature, T the temperature, E the energy relative to the Fermi level, and k_B Boltzmann's constant. Eq. 2.2 gives an implicit relation for $\Delta(T)$ and has to be solved iteratively in practice. Only for $T = 0$ and $T \to T_c$ an exact expression can be derived [7]. For fermions in thermal equilibrium $f(E)$ is the Fermi-Dirac distribution given by

$$f(E) = \frac{1}{1 + \exp(E/k_B T)}. \tag{2.3}$$

The temperature dependence of Δ from Eq. 2.2 is shown in Fig. 2.1a. At higher temperature, the energy gap disappears at the critical temperature T_c.

When the quasiparticle system absorbs energy, the system is driven out of the thermal-equilibrium state. In the case of pair-breaking radiation, an effective temperature can still be a reasonable assumption to the induced non-equilibrium $f(E)$, which we will discuss in Section 2.2.2. When the system is perturbed by a microwave field we will see in Section 2.4 that $f(E)$ is determined by the balance of absorbing microwave photons and energy relaxation by electron-phonon interaction.

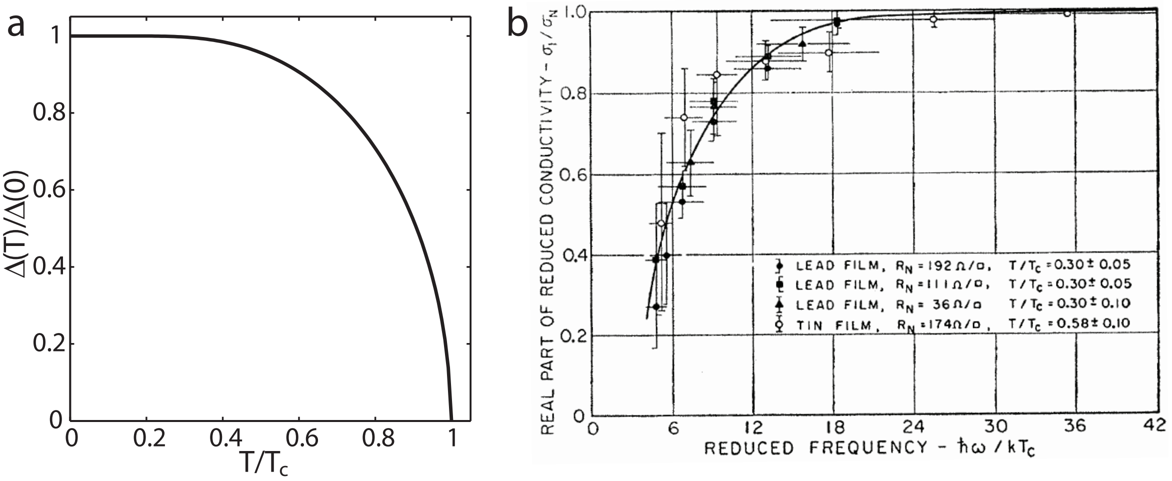

Figure 2.1: (a) The energy gap of the superconductor, normalised to the gap at zero temperature, as a function of normalised temperature. (b) The real part of the complex conductivity σ_1 (absorption) as a function of frequency for lead and tin films. The picture demonstrates that at $\hbar\omega \simeq 3k_BT_c \approx 2\Delta$ an absorption edge appears due to the onset of Cooper pair breaking. Figure from Ref. [8].

Photon absorption in the superconductor can happen due to two mechanisms, either due to the a transition of a quasiparticle from energy E to $E + \hbar\omega$ (ω is the angular frequency), or by directly breaking a Cooper pair. The strength of the first mechanism will decrease strongly towards lower temperatures, because of the lower number of available quasiparticles. When the absorption is measured as a function of frequency at low temperatures a sharp rise in absorption shows up at $\hbar\omega \approx 2\Delta$, because the pair-breaking mechanism starts to contribute. This so called absorption edge appeared from measurements of the transmission of far-infrared radiation by Glover and Tinkham [8] at temperatures well below T_c. The absorption derived from these measurements is shown as a function of frequency in Fig. 2.1b. A clear rise in absorption suggests that $2\Delta \approx 3k_BT_c$ (the BCS value is $2\Delta = 3.52k_BT_c$). Pair breaking can also be caused by phonons with sufficient energy. Therefore, the density of quasiparticles is temperature dependent and is given by

$$n_{qp} = 4N_0 \int_0^\infty N_s(E) f(E) dE \approx 2N_0 \sqrt{2\pi k_B T \Delta} \exp(-\Delta/k_B T), \tag{2.4}$$

where $N_s(E)$ is the normalised quasiparticle density of states $N_s = \mathrm{Re}\left(\frac{E}{\sqrt{E^2-\Delta^2}}\right)$. The first expression is valid for any distribution $f(E)$. The approximation is only valid for a thermal quasiparticle distribution and for $k_BT \ll \Delta$. The number of quasiparticles in a system is given by $N_{qp} = n_{qp}V$, with V the volume.

2.2 Response to a high frequency field

The discovery of superconductivity involved a measurement of the DC resistance, which was at that time expected to be finite down to the lowest temperatures. In normal metals the resistance at higher temperatures is dominated by collisions of the conduction electrons with thermally excited lattice vibrations. This electron-phonon scattering leads to a resistance that decreases with decreasing temperature. At low temperatures, the scattering of electrons on impurities starts to dominate, which causes a saturation in the resistance. In very pure metals, the resistance at low temperature may thus approach zero, but will still be finite due to a small number of impurities.

After confirming this hypothesis for several materials such as platinum and gold, it came thus as a surprise to Kamerlingh Onnes when the resistance of mercury suddenly dropped to zero below a temperature of 4.2 K [9]. The absence of resistance below a critical temperature is the most famous hallmark of superconductivity. The next important discovery on a superconductor is the Meissner effect. Importantly this effect includes both the fact that a magnetic field is excluded from entering the superconductor, but also that the field is expelled from the sample when it is cooled through T_c [10]. To expel the magnetic field, screening currents flow on the surface of the superconductor which generate a magnetic field opposite to the applied field. An expression for these screening currents was proposed by the London brothers [11] and is given by

$$\mathbf{j} = -\frac{n_s e^2}{m}\mathbf{A}, \tag{2.5}$$

where $\mathbf{j}$ is the current density, e the electron charge, m the electron mass and $\mathbf{A}$ the vector potential. n_s is the superfluid density which, at $T = 0$, can be taken equal to the electron density in the normal state. The solution to this equation yields a magnetic field that penetrates the superconductor and decays exponentially in the superconductor, with a characteristic length λ_L. In the interior of the superconductor the magnetic field is thus zero, i.e. the Meissner effect. The London penetration depth is given by (see e.g. [1, 10, 11])

$$\lambda_L(0) = \sqrt{\frac{m}{\mu_0 n_s e^2}}, \tag{2.6}$$

which is typically a few tens of nanometres. μ_0 is the permeability of vacuum.

In a normal metal, the current and the electric field are related through Ohm's law $\mathbf{j} = \sigma\mathbf{E}$, which reflects the finite resistance due to scattering. For a superconductor, the second London equation reads

$$\frac{d\mathbf{j}}{dt} = \frac{n_s e^2}{m}\mathbf{E}, \tag{2.7}$$

which shows that in the absence of resistance, the current keeps accelerating the electrons. In a finite frequency field, the solution to Eq. 2.7 yields for the conductivity

$$\sigma = -j\frac{n_s e^2}{\omega m}, \tag{2.8}$$

which shows that in a finite frequency field, there is an inductive response due to the inertia of the superconducting electrons (kinetic inductance). The London equations thus describe both the perfect diamagnetism and the absence of resistance of the superconductor, despite the phenomenological character of the expressions.

Length scales

The London relations only describe the response of the electrons that take part in superconductivity. However at finite temperature and finite frequency there are also normal electrons that carry part of the current and cause dissipation, because of the regular scattering mechanisms. A two fluid description was suggested in which part of the current is carried by the superconducting electrons and part by the normal electrons [12]. The real part of the conductivity due to the normal electrons is than given by the Drude model: $\sigma_1 = n_n e^2 \tau / m$, with n_n the density of normal electrons and τ the scattering time. The imaginary part of the conductivity is given by Eq. 2.8.

The first measurements of the magnetic penetration depth in superconductors resulted in larger values than predicted by the London expression, Eq. 2.6 [10]. Pippard realised that, analogous to Ohm's law, the London equations only cover a local response of the superfluid. He adopted Chambers' expression for a nonlocal response of a normal metal to describe the nonlocal response of a superconductor [13]. In a normal metal the current at a point **r** depends on the electric field throughout a volume given by the electron mean free path ℓ. For a superconductor Pippard proposed a similar length ξ_0, the coherence length which was introduced in Section 2.1. Since the electron mean free path is also supposed to play a limiting role to the sphere of influence of the field, ξ_0 is adopted in the following way to get an effective coherence length

$$\frac{1}{\xi} = \frac{1}{\xi_0} + \frac{1}{\ell}. \tag{2.9}$$

With the three length scales that characterise the superconductor: λ, ξ, and ℓ, we can distinguish several limiting cases for the electrodynamic response. First there is a clean limit $\ell >> \xi_0$, in which $\xi = \xi_0$. The opposite limit, in which the mean free path limits the coherence length, $\ell << \xi_0$, is called the dirty limit.

When the penetration depth λ of the magnetic field is long compared to the coherence length, $\lambda >> \xi$, the response is local. The effective penetration depth is than given by $\lambda = \lambda_L \sqrt{1 + \xi_0/\ell}$, which in the clean limit results in $\lambda \simeq \lambda_L$.

If $\lambda << \xi$, Cooper pairs extend over a longer distance than the penetration of the field. In terms of normal electron transport, they have passed through a spatially varying field since the last collision. Therefore, the response is non-local. The effective penetration depth in this regime is $\lambda = 0.65(\lambda_L \xi_0)^{1/3}$.

For thin superconducting films also the film thickness d plays a role in the electrodynamic response [10]. For a thin film in a magnetic field where $d < \ell$, the thickness is the limiting scattering lengthscale. For an applied perpendicular field, another effect plays a role. The screening distance is not given any more by the bulk λ, but by $\lambda_\perp \approx \lambda^2/d$, the Pearl length [14]. Therefore for a thin superconducting strip, the current penetrates much further towards the centre of the strip than just λ as will be shown for a representative strip in Section 2.4.5.

2.2.1 Complex conductivity

After the development of the BCS theory, which gave a microscopic foundation for the phenomenon of superconductivity, a microscopic treatment of the complex conductivity was derived by Mattis and Bardeen [15], which consistently takes into account both the Cooper pair condensate and the quasiparticle excitations. Their expression for the current density is

$$\mathbf{j}(\mathbf{r},\omega) = \frac{e^2 N_0 v_F}{2\pi^2 \hbar c} \int \frac{\mathbf{R}(\mathbf{R}\cdot\mathbf{A}(\mathbf{r}',\omega))}{R^4} I(\omega,R,T)\exp(-R/\ell)d\mathbf{r}', \tag{2.10}$$

with $\mathbf{R} = \mathbf{r} - \mathbf{r}'$, $R = |\mathbf{R}|$ and c the speed of light. In the clean, non-local limit (also called the extreme anomalous limit), the response kernel $I(\omega,R,T)$ varies slowly in space with respect to the other terms and can be taken constant. In the dirty limit, the characteristic length scale of $I(\omega,R,T)$ is ℓ and the integral can be simplified to a local response [16, 17]. In these limits a complex conductivity $\sigma = \sigma_1 - i\sigma_2$ can be formulated analogous to Ohm's law $\mathbf{j} = \sigma\mathbf{E}$.

The Mattis-Bardeen expression for the complex conductivity, valid in both the dirty limit and the extreme anomalous limit, is given by

$$\begin{aligned}\frac{\sigma_1}{\sigma_N} &= \frac{2}{\hbar\omega}\int_\Delta^\infty [f(E) - f(E+\hbar\omega)]g_1(E)dE \\ &+ \frac{1}{\hbar\omega}\int_{min(\Delta-\hbar\omega,-\Delta)}^{-\Delta} [1-2f(E+\hbar\omega)]g_1(E)dE, \qquad (2.11)\\ \frac{\sigma_2}{\sigma_N} &= \frac{1}{\hbar\omega}\int_{max(\Delta-\hbar\omega,-\Delta)}^{\Delta} [1-2f(E+\hbar\omega)]g_2(E)dE, \qquad (2.12)\end{aligned}$$

where

$$\begin{aligned}g_1(E) &= \frac{E^2+\Delta^2+\hbar\omega E}{(E^2-\Delta^2)^{1/2}[(E+\hbar\omega)^2-\Delta^2]^{1/2}}, \qquad (2.13)\\ &= \left(1+\frac{\Delta^2}{E(E+\hbar\omega)}\right)N_s(E)N_s(E+\hbar\omega),\\ g_2(E) &= \frac{E^2+\Delta^2+\hbar\omega E}{(\Delta^2-E^2)^{1/2}[(E+\hbar\omega)^2-\Delta^2]^{1/2}}, \qquad (2.14)\end{aligned}$$

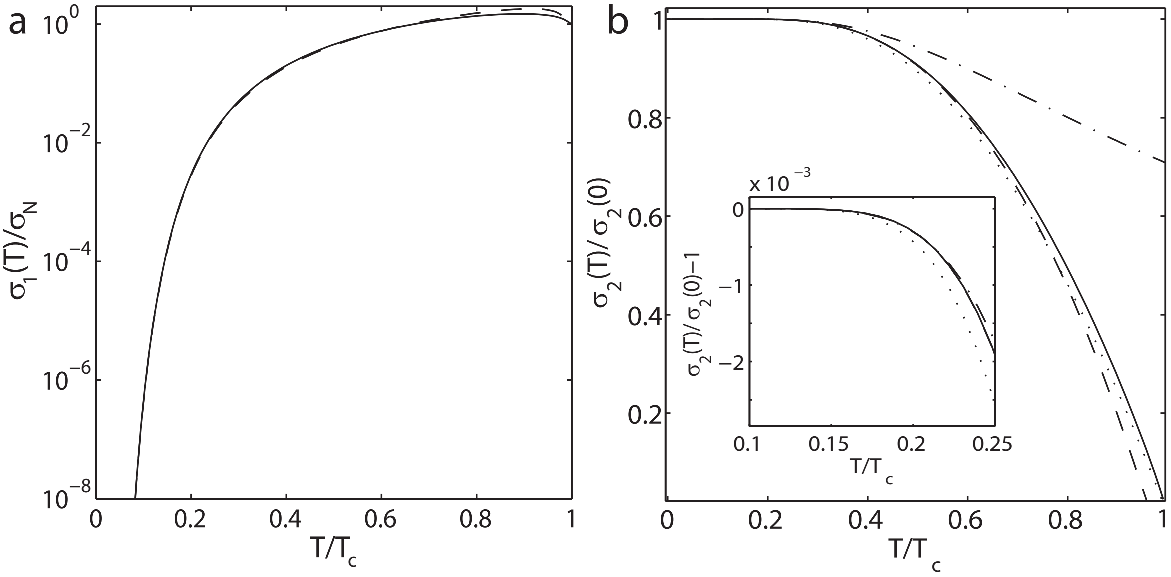

Figure 2.2: (a) The real part of the complex conductivity as a function of temperature. The solid line is the full Mattis-Bardeen equation, Eq. 2.11. The dashed line is the approximation of Eq. 2.16. (b) The imaginary part of the complex conductivity as a function temperature. The solid line is the Mattis-Bardeen expression Eq. 2.12. The dashed line is the approximation of Eq. 2.17. The dotted line is the relation Eq. 2.15, with the temperature dependent gap $\Delta(T)$. The dash-dotted line is the same expression with $\Delta = \Delta(0)$, which is clearly only a good approximation for the lowest temperatures (inset). In the inset the solid and dashed lines are on top of each other. For both graphs a microwave energy $\hbar\omega = \Delta/10$ is used.

and σ_N is the normal state conductivity. The second integral of Eq. 2.11 describes absorption of radiation involving Cooper pair breaking and is therefore only relevant for energies $\hbar\omega > 2\Delta$. The temperature dependence of σ_1 and σ_2 is shown in Fig. 2.2. The integral boundaries assume a density of states with no available states at $|E| < \Delta$ (a hard gap). When a broadened density of states or subgap states are introduced, these boundaries have to be reconsidered.

The first integral in σ_1 describes the process of radiation absorption by a quasiparticle at energy E, which is then integrated over all energies. The equation describes the net transition rate of a quasiparticle from a state at energy E to a state at energy $E + \hbar\omega$ upon absorption of a photon. The transition rate into the level at $E + \hbar\omega$ is proportional to the number of occupied states $f(E)N_s(E)$ and to the number of unoccupied states $f(E + \hbar\omega)(1 - f(E + \hbar\omega))N_s(E + \hbar\omega)$. When the rate from $E + \hbar\omega$ to E is subtracted, we see that the net transition rate is proportional to $(f(E) - f(E + \hbar\omega))N_s(E)N_s(E + \hbar\omega)$.

For a material in the dirty limit, it is instructive to see that the effective magnetic penetration depth as obtained from the BCS theory can be approximated by [10]

$$\frac{\lambda(T)}{\lambda(0)} = \left(\frac{\Delta(T)}{\Delta(0)} \tanh\left(\frac{\Delta(T)}{2k_BT}\right)\right)^{-1/2} \approx \left(\tanh\left(\frac{\Delta(0)}{2k_BT}\right)\right)^{-1/2}, \tag{2.15}$$

where the last approximation only holds for very low temperatures where $\Delta(T) \approx \Delta(0)$. Eq. 2.15 shows that the temperature dependence of the penetration depth is mainly determined by the energy gap. A measurement of the penetration depth is thus an accurate way to determine the energy gap. Eq. 2.15 is however only correct for a hard gap in the density of states and for a thermal quasiparticle distribution $f(E)$. For a non-equilibrium distribution, the relation is more complicated as is shown in Chapter 8. λ is related to σ_2 as $\sigma_2(T)/\sigma_2(0) = \lambda^2(0)/\lambda^2(T)$. The accuracy of the approximations in Eq. 2.15 is shown in Fig. 2.2b.

More details on the electrodynamics of superconductors and the historic development of its understanding can be found in Refs. [10, 16, 18].

2.2.2 Response to a change in the number of quasiparticles

For a thermal quasiparticle distribution, the expressions for σ_1 and σ_2 can be simplified for $kT, \hbar\omega < 2\Delta$ [19, 20].

$$\frac{\sigma_1}{\sigma_N} = \frac{4\Delta}{\hbar\omega}\exp(-\Delta/k_BT)\sinh\left(\frac{\hbar\omega}{2k_BT}\right)K_0\left(\frac{\hbar\omega}{2k_BT}\right), \tag{2.16}$$

$$\frac{\sigma_2}{\sigma_N} = \frac{\pi\Delta}{\hbar\omega}\left[1 - 2\exp(-\Delta/k_BT)\exp\left(\frac{-\hbar\omega}{2k_BT}\right)I_0\left(\frac{\hbar\omega}{2k_BT}\right)\right], \tag{2.17}$$

with I_0 and K_0 the modified Bessel functions of the first and second kind. These equations for the complex conductivity can be combined with Eq. 2.4 to obtain an expression for the change in σ_1 and σ_2 upon a change in the quasiparticle density, $d\sigma/dn_{qp}$, which is given by [20]

$$\frac{d\sigma_1}{dn_{qp}} \simeq \sigma_N\frac{1}{N_0\hbar\omega}\sqrt{\frac{2\Delta_0}{\pi k_BT}}\sinh\left(\frac{\hbar\omega}{2k_BT}\right)K_0\left(\frac{\hbar\omega}{2k_BT}\right), \tag{2.18}$$

$$\frac{d\sigma_2}{dn_{qp}} \simeq \sigma_N\frac{-\pi}{2N_0\hbar\omega}\left[1 + 2\sqrt{\frac{2\Delta_0}{\pi k_BT}}\exp\left(\frac{-\hbar\omega}{2k_BT}\right)I_0\left(\frac{\hbar\omega}{2k_BT}\right)\right]. \tag{2.19}$$

The temperature dependence of $d\sigma/dn_{qp}$ is shown in Fig. 2.3a for material parameters of aluminium: $\Delta = 177\ \mu\text{eV}$, $N_0 = 1.72 \times 10^{10}\ \text{eV}^{-1}\mu\text{m}^{-3}$ and a microwave energy $\hbar\omega = \Delta/10$. We observe a slow temperature dependence, which means that for not too large variations in n_{qp} and temperatures up to $T_c/3$, the complex conductivity changes approximately linearly with n_{qp}. It has been shown by Gao et al. [20] that Eqs. 2.18

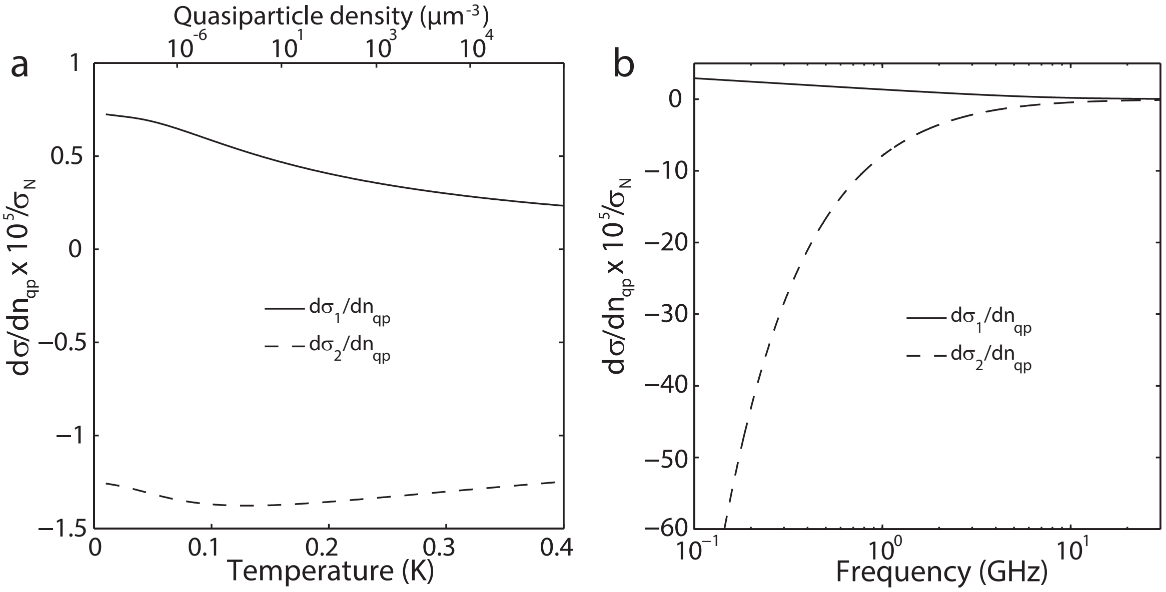

Figure 2.3: (a) The response of the complex conductivity to a change in the quasiparticle density, derived for a thermal quasiparticle distribution and for a frequency of $\hbar\omega = \Delta/10$. The top axis shows the corresponding quasiparticle density at several temperature points. (b) The response to a change in the quasiparticle density as a function of frequency for $T = T_c/8$.

and 2.19 can be derived through a thermal response, $d\sigma/dn_{qp} = \frac{\partial\sigma/\partial T}{\partial n_{qp}/\partial T}$, where we have here neglected an additional term of order unity. Eqs. 2.18 and 2.19 are obtained exactly (given Eqs. 2.16 and 2.17) when the excess quasiparticles due to pair breaking are described by an effective chemical potential μ^* [21]. The quasiparticle distribution then becomes $f(E) = 1/(1 + \exp(E - \mu^*)/k_BT)$ and the result for $d\sigma/dn_{qp}$ is given by Eqs. 2.18 and 2.19. This reasoning implies that a microwave resonator responds similarly to a temperature change and to pair breaking radiation, which was confirmed experimentally [20]. In other words, the quasiparticle distribution due to pair breaking radiation can be approximated by a thermal distribution at an effective temperature or an effective chemical potential, as far as the complex conductivity is concerned. We will revisit this assumption in sections 2.4 and 2.5.

In Fig. 2.3b, $d\sigma/dn_{qp}$ is shown as a function of frequency for a temperature $T_c/8$. We observe that the responsivity of the complex conductivity to a change in the quasiparticle density increases towards lower frequencies and that $d\sigma_2/d\sigma_1$ increases rapidly to lower frequencies. Thus to optimise the signal in σ_2 low frequency operation is beneficial [22].

2.2.3 Observables in a microwave resonator measurement

The surface impedance in the dirty limit for films with arbitrary thickness, relevant for the measurements reported in this thesis, is given by [23, 24]

$$Z_s = \sqrt{\frac{i\mu_0\omega}{\sigma_1 - i\sigma_2}}\coth(\sqrt{i\omega\mu_0\sigma}d) = R_s + i\omega L_s, \tag{2.20}$$

where Z_s can be split into its real part, the surface resistance R_s, and its imaginary part, the surface inductance L_s. The last factor in Eq. 2.20 accounts for the thickness of the film being comparable to or smaller than λ, which is easier to see if we rewrite it as $\sqrt{i\omega\mu_0\sigma}d = \frac{d}{\lambda}\sqrt{1 + i\frac{\sigma_1}{\sigma_2}}$.

For thick films, $Z_s = \sqrt{\frac{i\mu_0\omega}{\sigma_1 - i\sigma_2}}$. For low temperatures, $\sigma_2 >> \sigma_1$, and the surface resistance and reactance are given by $R_s = \sqrt{\frac{\mu_0\omega}{\sigma_2}}\frac{\sigma_1}{2\sigma_2}$ and $L_s = \sqrt{\frac{\mu_0}{\omega\sigma_2}} = \mu_0\lambda$. The latter relation follows from the London equation, assuming that $\sigma \approx -i\sigma_2$, and shows the relationship between the surface inductance, the penetration depth and the complex conductivity.

The measurement of the microwave losses and penetration depth in resonators (or cavities) has a long tradition due to its application in particle accelerators [25]. Due to the high quality factor of these resonators the Mattis-Bardeen theory has been accurately tested. The quality factor of a resonator is generally described as the ratio of the stored energy divided by the energy loss per cycle,

$$Q = \frac{\omega E_{stored}}{P_{loss}}, \tag{2.21}$$

with P_{loss} the power that is either lost by internal dissipation or through the coupler with which the resonator is coupled to the readout line. The relation of the total (loaded) quality factor of the resonator to the internal quality factor Q_i and the coupling quality factor Q_c is given by

$$\frac{1}{Q} = \frac{1}{Q_i} + \frac{1}{Q_c}. \tag{2.22}$$

The internal quality factor of a resonator, characterising the internal losses, is given by [19]

$$Q_i = \frac{\omega L}{R} = \frac{1}{\alpha_k}\frac{\omega L_s}{R_s} = \frac{2}{\alpha_k\beta}\frac{\sigma_2}{\sigma_1}, \tag{2.23}$$

with α_k the fraction of kinetic inductance over the total inductance (L) and $\beta = 1 + \frac{2d/\lambda}{\sinh(2d/\lambda)}$. The resonant frequency ω_0 of such a resonator is mainly determined by σ_2 through $\omega_0 \propto 1/\sqrt{LC}$, with C the capacitance. To relate the resonant frequency to theory, it is more convenient to consider a (small) frequency shift $\delta\omega_0 = \omega - \omega_0$, which is given by

$$\frac{\delta\omega_0}{\omega_0} = \frac{\alpha_k \beta}{4} \frac{\delta\sigma_2}{\sigma_2}. \tag{2.24}$$

A change in the quality factor can be described in a similar way:

$$\delta\left(\frac{1}{Q_i}\right) = \frac{\alpha_k \beta}{2} \frac{\delta\sigma_1}{\sigma_2}, \tag{2.25}$$

where we used the fact that $\delta\sigma_1 >> \delta\sigma_2$ at temperatures $T << T_c$ (see Fig. 2.2). Thus upon a change in the number of quasiparticles in a microwave resonator (Eqs. 2.18 and 2.19), the change in σ_1 is reflected in a change in Q_i and the change in σ_2 in a shift of the resonant frequency.

Q_i and ω_0 are useful observables to characterise resonators, but for the readout of a real detector it is more convenient to use the response of the amplitude A and the phase θ, relative to the resonance circle in the complex plane, upon a change in the number of quasiparticles. We will discuss the resonance circle in more depth in Chapters 3, 5 and 7. The response of the resonator amplitude and phase to a change in the number of quasiparticles is given by [26]

$$\frac{dA}{dN_{qp}} = -\frac{\alpha_k \beta Q}{|\sigma| V} \frac{d\sigma_1}{dn_{qp}}, \tag{2.26}$$

$$\frac{d\theta}{dN_{qp}} = -\frac{\alpha_k \beta Q}{|\sigma| V} \frac{d\sigma_2}{dn_{qp}}, \tag{2.27}$$

where $|\sigma| \approx \sigma_2$ for $T << T_c$. Here the quality factor is assumed to be constant, which means that it has to be either coupling limited or that Q_i is not limited by quasiparticle losses. For a high responsivity it is advantageous to have a high quality factor, a long penetration depth (high α_k) and a small volume.

2.3 Quasiparticle dynamics

The properties of the superconductor can be described with a distribution function $f(E)$ and a quasiparticle and Cooper pair density (Eqs. 2.3 and 2.4). These are static, average properties which do not reflect any temporal dynamics. But even in thermal equilibrium, lattice vibrations continuously break Cooper pairs or scatter on quasiparticles to change their energy. Therefore the quasiparticle density is time dependent as well as the observables discussed above.

2.3.1 The quasiparticle recombination time

When the superconductor is excited and a Cooper pair is broken, two quasiparticle-excitations are created. Because the system tends towards a state with low energy, it tries to restore the equilibrium (or steady state) by recombining the quasiparticles to a Cooper pair. The recombination of two quasiparticles at energies E and E' results in a Cooper pair and the emission of a phonon with energy $\Omega = E + E' - 2\Delta$. It therefore involves the energy distribution of the quasiparticles $f(E)$ and the energy distribution of the phonons $n(\Omega)$. The recombination time for a quasiparticle at energy E was derived by Kaplan et al. [27] and is given by

$$\frac{1}{\tau_{qp}(E)} = \int_{E+\Delta}^{\infty} \frac{\Omega^2 N_s(\Omega - E)}{\tau_0 (k_B T_c)^3 [1 - f(E)]} \left(1 + \frac{\Delta^2}{E(\Omega - E)}\right) [n(\Omega) + 1] f(\Omega - E) d\Omega, \quad (2.28)$$

where τ_0 is the characteristic electron-phonon interaction time, which is material dependent. In the original equation there are two additional functions, the phonon density of states $F(\Omega)$, and the matrix element for electron-phonon interaction $\alpha^2_{ph}(\Omega)$. Since the generation-recombination process involves only low energy phonons (compared to the Debye energy), it is a good approximation to take $\alpha^2_{ph}(\Omega)F(\Omega) = b\Omega^2$ [27]. This is the origin of the factor Ω^2 in Eq. 2.28. The constant b is absorbed in τ_0. From Ref. [27] we expect for aluminium that $\tau_0 = 438$ ns, which was based on an extrapolation of band structure calculations [28], which were itself based on neutron-scattering data. The τ_0 which we obtain experimentally (458 ns, see Chapter 5) is remarkably close. τ_{qp} is in general an energy dependent quantity. The recombination time is shorter for quasiparticles with higher energies, which becomes important for a strong non-equilibrium $f(E)$ [29]. For a thermal distribution and $T << T_c$ the recombination time for a quasiparticle at the gap edge ($E = \Delta$) can be approximated by

$$\tau_{qp} = \frac{\tau_0}{\sqrt{\pi}} \left(\frac{k_B T_c}{2\Delta}\right)^{5/2} \sqrt{\frac{T_c}{T}} \exp(\Delta / k_B T) = \frac{\tau_0}{n_{qp}} \frac{N_0 (k_B T_c)^3}{2\Delta^2}, \quad (2.29)$$

where the last equality shows that the quasiparticle recombination lifetime is inversely proportional to the quasiparticle density. $\tau_{qp} \propto 1/n_{qp}$ also holds for certain non-equilibrium distributions as will be shown in Chapter 8.

2.3.2 The role of the phonons

The energy of an excitation has to be carried away through the phonon system in the film towards the bath, usually a dielectric substrate. Therefore the phonon distribution in the film $n(\Omega)$ naturally arises in Eq. 2.28. In particular, when most of the energy is taken away through recombination, an excess population of 2Δ phonons arises. In Fig. 2.4a the quasiparticle and phonon systems involved are schematically depicted. The electron-phonon interaction can occur both due to scattering and recombination. If we only keep track of the phonons with energy $\Omega > 2\Delta$, such a phonon can either be reabsorbed by pair breaking or escape from the film and we can reduce the system to the number-representation in Fig. 2.4b. The phonon pair breaking time τ_{pb} is the average lifetime of a phonon before breaking a pair, which is material dependent [27]. The

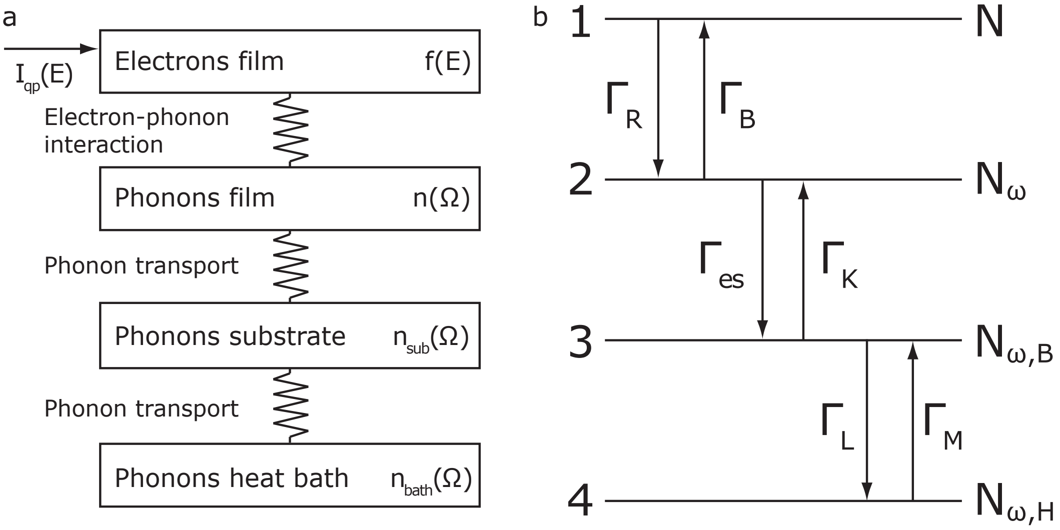

Figure 2.4: (a) Schematic representation of the quasiparticle and phonon systems in the superconductor, with their respective energy distributions and the interaction mechanisms. $I_{qp}(E)$ is a general transition rate of quasiparticles at energy E due to an external drive. (b) Quasiparticle and phonon number representation of the same system, with the transition rates Γ.

phonon escape time is determined by the thickness of the film d, the phonon velocity u and the film-substrate transparency η_{ph}. η_{ph} is determined by the acoustic mismatch between film and substrate. The escape time is given by $\tau_{esc} = 4d/u\eta_{ph}$ [30]. The effective quasiparticle recombination time in a measurement is modified by the phonon-trapping effect as $\tau_{qp}^{eff} = \tau_{qp}(1 + \tau_{esc}/\tau_{pb})$. For the 20-100 nm thick aluminium films on silicon or sapphire substrates we typically use, the correction factor is close to 1. Whereas τ_{qp} (or τ_{qp}^{eff}) has typical values of 5 μs - 5 ms, dependent on temperature, both τ_{pb} and τ_{esc} are less than 1 ns. Therefore these phonon times do not cause a measurable timescale in the presented experiments.

When the phonon escapes to the substrate, there is still the possibility that it returns to the film. In an experiment the substrate has to be mounted to a sample box, which creates another interface for phonon reflection. This causes an additional phonon bottleneck and thus an additional timescale. When we compare non-equilibrium (pulse) with equilibrium (noise) experiments in Chapter 5, the recombination time in equilibrium does follow Eq. 2.29, but the pulse decay-time does saturate to about 80 μs at higher temperatures. The pulse decay-time will be dominated by the slowest timescale that limits the equilibration of the system. This saturation (10-100 μs) is also reported in other experiments [31–33] and attributed to a phonon bottleneck due to the substrate. Although this is usually not a very well defined interface, one can estimate the typical timescale from heat capacity, C_{sub}, and conductance, G, considerations: $\tau = C_{sub}/G$. A phonon-bottleneck can also be introduced on purpose, to enhance the effective quasiparticle recombination time.

2.3.3 Quasiparticle number fluctuations

A superconductor in equilibrium at a finite temperature is subject to thermal fluctuations. Therefore the number of quasiparticles present in a system fluctuates in time around the average. In a system in which the number of quasiparticle excitations is the quantity to be measured, these fluctuations are a fundamental source of noise. In semiconductors generation-recombination noise is an extensively studied and well understood phenomenon [34]. The excitations involved in a semiconductor are electron-hole pairs. In a superconductor the only signature of generation-recombination noise was found so far in the tunnelling current in a small Al box [35]. In connection to these experiments Wilson and Prober formulated the theoretical framework for quasiparticle number fluctuations in a superconductor [36, 37], which is based upon a master equation approach developed for generation-recombination noise in semiconductors [38]. The starting point is the insight that one only needs to keep track of either quasiparticles or Cooper pairs, because their total number is conserved. The master equation for the number of quasiparticles becomes

$$\begin{aligned}\frac{\partial P(N_{qp},t|k,0)}{\partial t} &= - [g(N_{qp})+r(N_{qp})]P(N_{qp},t|k,0)\\ &+ g(N_{qp}-\delta N_{qp})P(N_{qp}-\delta N_{qp},t|k,0)\\ &+ r(N_{qp}+\delta N_{qp})P(N_{qp}+\delta N_{qp},t|k,0),\end{aligned} \tag{2.30}$$

where $P(N_{qp},t|k,0)$ is the probability of having a number of quasiparticles N_{qp} at time t, given that at time $t=0$ there were k quasiparticles. $g(N_{qp})$ and $r(N_{qp})$ are the probabilities of a generation or recombination event per unit time. $\delta N_{qp}=2$ is the number of quasiparticles added or removed by a generation or recombination event respectively. For not too large fluctuations the variance of the number of quasiparticles is given by

$$\left\langle \Delta N_{qp}^2 \right\rangle = \delta N_{qp} \frac{r(N_{qp}^0)}{\frac{dr}{dN(N_{qp}^0)} - \frac{dg}{dN(N_{qp}^0)}}, \tag{2.31}$$

with[1] $N_{qp}=N_{qp}^0+\Delta N_{qp}$. The autocorrelation function $R_N(u)$ of the fluctuations at lag u is given by

$$R_N(u) = \langle \Delta N_{qp}(0)\Delta N_{qp}(u)\rangle = \left\langle \Delta N_{qp}^2 \right\rangle \exp\left(-\frac{u}{\tau}\right), \tag{2.32}$$

with $\tau=\tau_{qp}^{eff}$ the effective relaxation time of a fluctuation.

In the simple case of two subsystems, the rate equation is of the form

$$\frac{dN_{qp}}{dt} = \delta N_{qp}[g(N_{qp})-r(N_{qp})]. \tag{2.33}$$

---

[1] Note that Δ is not the energy gap of the superconductor here, but the difference with respect to the equilibrium value.

Following Wilson and Prober [36] the generation rate of quasiparticles can be taken constant and the recombination rate as $r(N_{qp}) = RN_{qp}^2/2V$, with V the volume of the system and R the recombination constant. Using Eq. 2.31 we arrive at $< \Delta N_{qp}^2 >= N_{qp}^0$, the variance of a Poissonian process. The power spectral density of the quasiparticle fluctuations is obtained by Fourier transforming the autocorrelation function Eq. 2.32 and given by

$$S_N(\omega) = \frac{4\left\langle \Delta N_{qp}^2 \right\rangle \tau_{qp}}{1 + (\omega\tau_{qp})^2} = \frac{4N_{qp}\tau_{qp}}{1 + (\omega\tau_{qp})^2}, \tag{2.34}$$

which shows that the spectrum of the fluctuations is of a simple Lorentzian form, with a roll-off frequency due to the quasiparticle recombination time (Figure 2.5b).

In a more realistic system, not only the quasiparticle number fluctuates, but also the number of phonons, due to the electron-phonon nature of the recombination process. Since we are here concerned with generation and recombination of quasiparticles, the phonons to consider are only those with energies $\Omega > 2\Delta$. Figure 2.4a shows the system we consider, which is represented in panel b as different levels with a number population and a transition rate. N_{qp} is the number of quasiparticles, N_ω the number of phonons in the superconducting film and $N_{\omega,B}$ the number of phonons in the bath, which is here the substrate. $\Gamma_B = 1/\tau_{pb}$ is the pair breaking rate, $\Gamma_{es} = 1/\tau_{esc}$ the phonon escape rate from film to substrate and Γ_K the phonon escape rate from substrate to film. The temporal dynamics of this system can be described by three coupled differential equations:

$$\frac{dN_{qp}}{dt} = -\frac{RN_{qp}^2}{V} + 2\Gamma_B N_\omega, \tag{2.35}$$

$$\frac{dN_\omega}{dt} = \frac{RN_{qp}^2}{2V} - \Gamma_B N_\omega - \Gamma_{es} N_\omega + \Gamma_K N_{\omega,B}, \tag{2.36}$$

$$\frac{dN_{\omega,B}}{dt} = \Gamma_{es} N_\omega - \Gamma_K N_{\omega,B}, \tag{2.37}$$

where $\Gamma_R = 1/\tau_{qp} = RN_{qp}^2/2V$.

If the substrate is considered to be the phonon bath, the fluctuations will not significantly change $N_{\omega,B}$. If $N_{\omega,B}$ is constant, $\Gamma_{es} N_\omega^0 = \Gamma_K N_{\omega,B}^0$. The superscripts ‘0’ denote the steady state value. We are than left with two equations, Eq. 2.35 and a modified Eq. 2.36, which reads

$$\frac{dN_\omega}{dt} = \frac{RN_{qp}^2}{2V} - \Gamma_B N_\omega - \Gamma_{es}(N_\omega - N_\omega^0). \tag{2.38}$$

These two equations are the well-known Rothwarf-Taylor equations for quasiparticle dynamics [39]. How these rate equations lead to a spectrum of fluctuations is presented in detail in Ref. [36] and part of the analysis in Appendix B. There is one important step in the derivation to mention. Before calculating the spectrum, the equations are

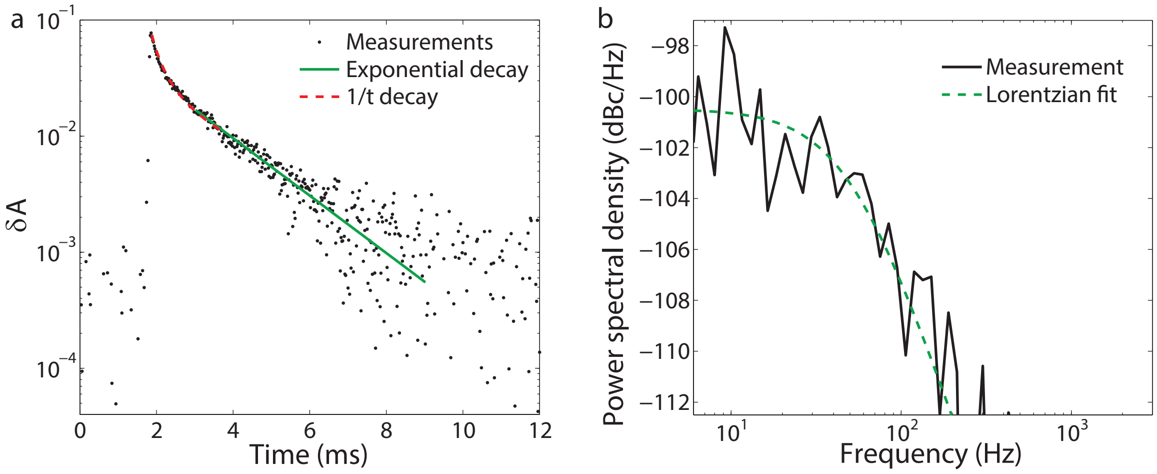

Figure 2.5: (a) The amplitude response of an aluminium microwave resonator at 100 mK upon a large energy hit as a function of time. (b) Spectrum of the amplitude response of a microwave resonator to quasiparticle number fluctuations. The lines are described in the text.

linearized by assuming small perturbations: $N_{qp} = N_{qp}^0 + \delta N_{qp}$, which mainly serves to remove the quadratic term in N_{qp}. This is a valid assumption provided that the number of quasiparticles N_{qp}^0 is large compared to the perturbation. An important restriction in the comparison of quasiparticle recombination times from pulse-excitations and fluctuation-spectra arises here. If a pulse excitation is too large, the excitation itself changes τ_{qp}, and the N_{qp}^2 term is needed to describe the pulse-decay. The best representation of the equilibrium τ_{qp} from a pulse excitation is therefore obtained by extracting the decay time in the tail of the excitation, close to equilibrium, where the decaying pulse can be described with an exponential decay [40]. To illustrate the regimes, a decay of the response of an Al microwave resonator to a large energy pulse (a cosmic ray) is shown in Fig. 2.5a. The tail of the decay is well described with an exponential decay (solid line) with a timescale of 1.8±0.2 ms, close to the timescale we get from a measurement of the spectrum of quasiparticle number fluctuations as shown in panel b (2.6±0.5 ms). The initial part of the decay can be described by considering only the N_{qp}^2 decay term in Eq. 2.35. The general solution to $\frac{dN_{qp}}{dt} = -aN_{qp}^2$ is $N_{qp}(t) = \frac{1}{at-b}$. Fig. 2.5a shows that this equation indeed describes the initial part of the pulse-decay, where the excitation is large compared to N_{qp}^0 (dashed line). For small energy pulses, the decay can usually be described with just a single exponential decay.

In general, the resulting power spectral density of quasiparticle number fluctuations has two timescales, one due to the the quasiparticle fluctuations and one due to the phonon fluctuations. However Γ_{esc} and Γ_B are so much larger than the quasiparticle fluctuation rate that they are not measurable. The power spectral density can thus be approximated by

$$S_N(\omega) = \frac{4N_{qp}\tau_{qp}^{eff}}{1 + (\omega\tau_{qp}^{eff})^2}, \tag{2.39}$$

where the phonon trapping effect is included in τ_{qp}^{eff} as discussed in the previous section. Thus if there is only one dominant timescale the spectrum of the fluctuations is just that of a two-level system as in Eq. 2.34, but with a modified relaxation time. An example of such a spectrum is shown in Fig. 2.5b. The amplitude response of an aluminium microwave resonator was measured as a function of time at a temperature of 100 mK. The power spectral density of the fluctuations in that amplitude response are shown in Fig. 2.5b. An extensive discussion of the experiment is presented in Chapter 5.

There are several mechanisms which can cause an additional timescale in the spectrum of quasiparticle fluctuations, which change Eq. 2.39. Generally two (or more) components can be distinguished and the spectrum is given by

$$S(\omega) = \frac{S_1}{1 + (\omega\tau_1)^2} + \frac{S_2}{1 + (\omega\tau_2)^2}, \tag{2.40}$$

where S_1 and S_2 are the levels and τ_1 and τ_2 the timescales of the two components. Such a second timescale already arises from the phonon-trapping effect, but in practice these timescales are too short to be measurable as discussed before. Wilson and Prober [36] also discuss quasiparticle trapping, which causes another subsystem in Fig. 2.4 and therefore another timescale associated with trapping and the release of quasiparticles.

A second timescale is also introduced by the C_{sub}/G time of the substrate as discussed in Section 2.3.2. In Fig. 2.4b this is accounted for by the addition of another phonon-system, that of the sample holder. In Appendix B experimental data with two timescales in the quasiparticle fluctuation spectrum will be shown. The second timescale is almost temperature-independent and similar to the saturation level of the measurement of τ_{qp} with a pulse-excitation. Both these observations are consistent with an additional phonon timescale as suggested in Refs. [31–33]. In a pulse-experiment such a phonon timescale can lead to a decay with two consecutive single-timescale exponential decays in the case that $\tau_{phonon} > \tau_{qp}$.

2.3.4 Quasiparticle fluctuations in steady state

The preceding treatment of fluctuations assumes thermal equilibrium in which case the generation and recombination rates and the transition rates between the phonon subsystems balance. In Chapter 5 we will see that at higher temperatures and without applied radiation, the quasiparticle number and the recombination time are well described by Eqs. 2.4 and 2.29 and thermal equilibrium is a good assumption. However at low temperatures the number of quasiparticles saturates due to microwave readout power dissipation. Microwave absorption gives rise to a cascade of absorption events which, through the creation of excess $\Omega > 2\Delta$ phonons, leads to excess quasiparticles (Section 2.4.1). Thus if only the number of quasiparticles and $\Omega > 2\Delta$ phonons are considered the net effect of microwave absorption is the injection of pair breaking phonons. In steady state, the transition rates between the top level and the second level in Fig. 2.4b are therefore still balanced [36, 41]. Since only the population of the top level (the number of quasiparticles) can be measured, the above presented framework still applies. In the experimental data in Chapters 5 and 6 there is no sign that a description in terms of the number of quasiparticles and their recombination lifetime is inappropriate. For very strong non-equilibrium it could be necessary to treat the fluctuations as fluctuations in the distribution function, $f(E,t)$ [42]. In that case one would need to compute the spectrum of the fluctuations from the kinetic equations that are discussed in Section 2.4.1.

When pair-breaking radiation is applied and the number of quasiparticles is dominated by the radiation, another driven steady state situation arises. In this case the main source of fluctuations is in the drive itself. Fluctuations in the arrival rate of the photons (Section 2.5) cause fluctuations in the number of generated quasiparticles. The recombination process is still random and the recombination rate is determined by N_{qp}. The variance arising from recombination is smaller than that due to the photon fluctuations. A more detailed discussion is presented in Chapter 7. The detector is ideally limited by this photon noise. In the photon noise limit, the treatment of noise is easier, because the photon fluctuations dominate the quasiparticle fluctuations.

The applied microwave field may also cause order parameter oscillations at the drive frequency. However the scattering in Al is so slow that such an effect can only change average properties, except for very close to T_c [43]. It does not cause a dynamical process at a measurable timescale > 1 μs. Propagating order-parameter fluctuations (collective modes) can exist as well [44, 45], but these modes have fluctuation timescales in the GHz range and have only been observed close to T_c.

2.3.5 Generation-recombination noise in a detector

Quasiparticle fluctuations are thus the fundamental source of noise in a pair-breaking detector, the incident power is detected through a change in the number of quasiparticles. As such, quasiparticle fluctuations limit the noise equivalent power (NEP) of a detector. The noise equivalent power is defined as the power which can be detected with a signal-to-noise ratio of one with a bandwidth of 1 Hz. The generation-recombination noise contribution to the NEP is given by [46]

$$NEP = \frac{2\Delta}{\eta_{pb}}\sqrt{\frac{N_{qp}}{\tau_{qp}}} \propto N_{qp}, \tag{2.41}$$

where the presence of η_{pb} reflects that we do not only consider quasiparticle fluctuations as described by Eq. 2.39, but also the fact that the absorbed power has to be converted to quasiparticles. The parameter η_{pb} is further discussed in Section 2.5. A derivation can be found in Barends [19]. Since $NEP \propto N_{qp}$ it is necessary to go to low temperatures (Eq. 2.4) and to reduce the number of excess quasiparticles to obtain the highest sensitivity.

2.4 Absorption of microwave photons, $\hbar\omega < 2\Delta$

In Section 2.2.1 we have discussed the response of the superconductor to a microwave signal. The complex conductivity in the Mattis-Bardeen picture is in essence a linear response function, which assumes that the quasiparticle distribution $f(E)$ does not change due to the applied field. However, the physical mechanism behind σ_1 is the absorption of microwave photons by the quasiparticle system, which inherently causes transitions of the quasiparticles from energies E to $E + \hbar\omega$. These transitions lead inevitably to a non-equilibrium $f(E)$. For a small microwave field, the equilibrium $f(E)$ is still a good approximation, but at higher field the distribution $f(E)$ changes dramatically due to microwave absorption, which was first shown by Eliashberg [47].

2.4.1 Redistribution of quasiparticles due to microwave absorption

Absorption of microwave photons does not immediately break Cooper pairs, but can lead to a non-equilibrium $f(E)$ for a sufficiently strong microwave field. The transition rate from or into energy level E under interaction with microwaves in a superconductor was derived by Eliashberg et al. [47, 48] and is given by[2]

$$\begin{aligned} I_{qp}(E) = \frac{2\alpha_\omega}{\hbar}\Bigg[& \left(1+\frac{\Delta^2}{E(E-\hbar\omega)}\right) N_s(E-\hbar\omega)(f(E-\hbar\omega)-f(E)) \\ & -\left(1+\frac{\Delta^2}{E(E+\hbar\omega)}\right) N_s(E+\hbar\omega)(f(E)-f(E+\hbar\omega)) \\ & -\left(1+\frac{\Delta^2}{E(E-\hbar\omega)}\right) N_s(E-\hbar\omega)(1-f(E)-f(\hbar\omega-E))\Bigg], \quad (2.42) \end{aligned}$$

where the first term has a limit $E \geq \Delta + \hbar\omega$ and the second term $E \geq \Delta$. The first two terms describe a transition by microwave absorption (note the similarity to σ_1). The last term describes absorption of radiation by breaking a Cooper pair, with $\hbar\omega \geq 2\Delta$ and $\Delta \leq E \leq \hbar\omega - \Delta$. In this section we focus on radiation that cannot break Cooper pairs directly, i.e. $\hbar\omega < 2\Delta$. In practice for the microwave experiments described in this thesis $\hbar\omega \approx 0.15\Delta$. For these frequencies, the last term in Eq. 2.42 is zero. α_ω relates the transition rates to the strength of the magnetic field and is given by $\alpha_\omega = \frac{e^2 D}{\hbar} A_\omega^2$,

---

[2] Note that I_{qp} is defined here and in Chapter 8 as given in Ref. [29], which is related to the original I_ω in Ref. [48] as $I_{qp}(E) = I_\omega(E)/N_s(E)$.

in which D is the diffusion constant and $A_\omega \exp(i\omega t)$ the vector potential of the applied field. In terms of the current density j, α_ω is given by [49]

$$\alpha_\omega = \frac{2e^2 D}{\hbar\omega^2 |\sigma^2|} j^2. \tag{2.43}$$

The transition rate of quasiparticles to higher energies due to I_{qp} leads to a higher quasiparticle population at higher energies. The transition rate up in energy is counteracted by electron-phonon scattering and recombination of quasiparticles. In the Eliashberg approach, a basic understanding of how microwave absorption acts on $f(E)$ is provided by the relation $I_{qp}(E) = \delta f(E)/\tau$, where $\delta f(E)$ is the non-equilibrium part of the distribution function $\delta f(E) = f(E, \alpha_\omega) - f(E, T)$. τ is here a generalised timescale which takes into account quasiparticle-phonon scattering and quasiparticle recombination [48]. The stationary non-equilibrium distribution $\delta f(E)$ is controlled by α_ω/τ and thus depends on the balance between the applied field (α_ω) and τ. The latter is strongly material dependent. The applied field needed to create the same non-equilibrium $\delta f(E)$ therefore varies between materials. For the redistribution framework to apply, the condition $\omega\tau >> 1$ has to be fulfilled. If $\omega\tau < 1$, $f(E)$ can follow the temporal dynamics of the field and the time dependence of $f(E, \omega t)$ has to be considered.

2.4.2 Enhancement effects close to T_c

The Eliashberg formalism successfully explains a number of spectacular effects observed in a superconductor under microwave irradiation: enhancement of the critical current, the energy gap and the critical temperature. The first experiments suggesting critical current enhancement were reported in microbridge experiments, the Dayem-Wyatt effect [50, 51]. Critical current enhancement was shown to be consistent with the Eliashberg framework in thin film aluminium strips, where measurements as a function of microwave frequency, microwave power and temperature were performed [52–54]. Fig. 2.6a shows the critical current as a function of temperature and microwave field strength in a one dimensional strip, which clearly demonstrates the critical current enhancement. In this experiment geometry effects were ruled out [53]. Critical temperature enhancement can be inferred from the same measurements [53] and was confirmed using various methods in Ref. [55]. Gap enhancement was experimentally demonstrated using tunnel junctions [56, 57]. A review of these various experiments can be found in Pals et al. [58].

All of these experiments are consistent with a non-equilibrium $f(E)$ due to microwave absorption as described by Eliashberg. The experimental connection between gap-enhancement and a microwave-induced non-equilibrium $f(E)$ was presented by Wolter and Horstman [57, 59]. They measured $f(E)$ in an aluminium thin film in the presence of microwave irradiation using tunnel junctions. The measured $f(E)$ is shown in Fig. 2.6b, from which we observe that quasiparticles are redistributed from the region below $\Delta + \hbar\omega$ to $E > \Delta + \hbar\omega$ compared to a thermal distribution. Peaks are

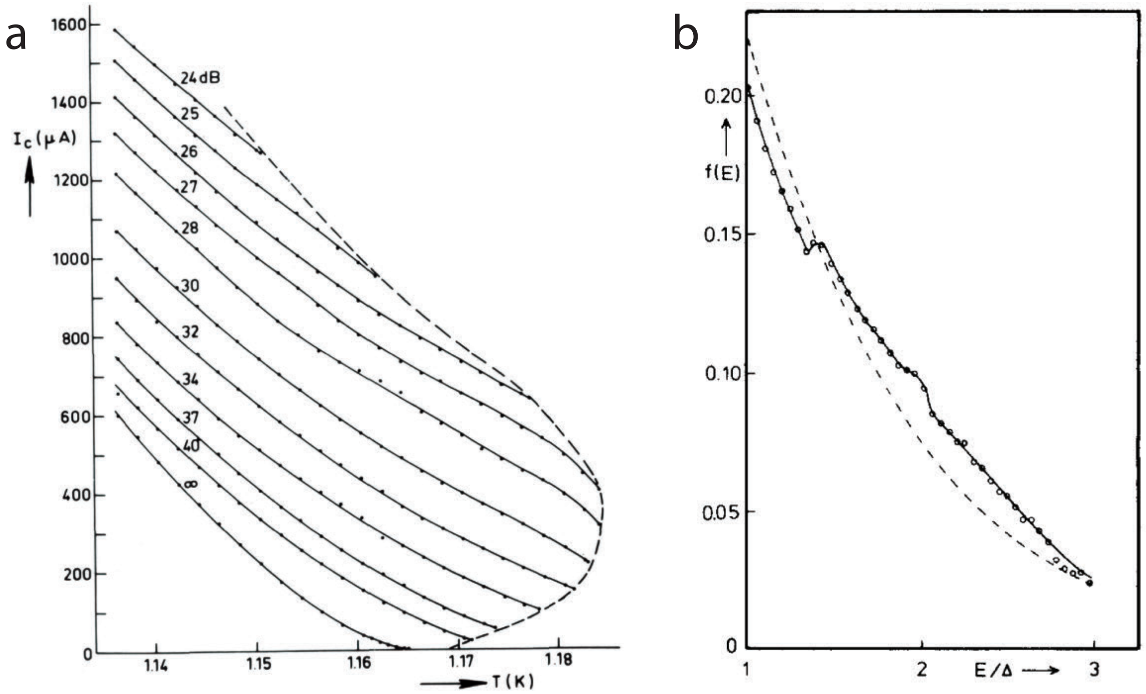

Figure 2.6: (a) Critical current of an aluminium strip as a function of temperature for various microwave powers (the numbers represent attenuation). Clearly the critical current is enhanced by microwave absorption. The dashed line indicates the region where the critical current could be observed. Figure from Ref. [53]. (b) The measured quasiparticle distribution as a function of energy for an aluminium thin film, subject to microwave absorption. The dashed line is the thermal, Fermi-Dirac distribution at a temperature of $T/T_c = 0.85$. Figure from Ref. [57].

visible at multiples of $\hbar\omega$. If we now compare such a non-equilibrium distribution with the equation for the energy gap, Eq. 2.2, it becomes clear that the quasiparticles close to Δ have a stronger influence on the actual size of Δ. With the same quasiparticle density, but in a non-equilibrium distribution, it is thus possible to have an enhanced gap compared to thermal equilibrium. On top of that, the quasiparticle density itself can decrease, because quasiparticles at higher energies recombine faster than those close to Δ [29].

2.4.3 Non-equilibrium distribution of quasiparticles and phonons

Through the processes of quasiparticle scattering and recombination microwave absorption does not only create a non-equilibrium $f(E)$, but also a non-equilibrium $n(\Omega)$, the distribution of phonons in the film. The detailed kinetic equation approach to this problem was later developed by Chang and Scalapino [29, 60, 61], which results in a set of kinetic equations for $df(E)/dt$ and $dn(\Omega)/dt$, including the Eliashberg injection term $I_{qp}(E)$ as given in Eq. 2.42. This approach takes the energy dependence of the phonons explicitly into account as well. The equations are, for their length, presented in Appendix A. There are thus three systems involved (see Fig. 2.4): the quasiparticle (electron) system, described by $f(E)$, the phonons in the film, described by $n(\Omega)$ and a phonon bath, which is the phonon system of the substrate, for which a thermal distribution at the bath temperature is assumed, the Bose-Einstein distribution $n_{sub}(\Omega, T_{bath}) = 1/(\exp(\Omega/k_B T_{bath}) - 1)$. A steady state solution for $f(E)$ and $n(\Omega)$ can be obtained by iteratively solving the coupled system $df(E)/dt = dn(\Omega)/dt = 0$, together with the equation for the energy gap, Eq. 2.2. The numerical procedure presented in Ref. [62] has been used to obtain the results as shown in Section 2.4.4 and Chapter 8.

In the framework discussed above the dominant scattering mechanism is assumed to be electron-phonon interaction. In principle also inelastic electron-electron interaction (without recombination) could play a role in reducing the non-equilibrium microwave absorption effects. However, since the number of electrons exponentially decreases below T_c, this process is slower than electron-phonon interaction. Only close to T_c electron-electron interaction dominates [63, 64]. In the case of microwave absorption electron-electron scattering could play the role of reducing the peaks in $f(E)$ as shown in Fig. 2.7. However, the power deposited by microwave absorption has still to be released through electron-phonon interaction.

2.4.4 A non-equilibrium quasiparticle distribution at low temperature $T << T_c$

All of the microwave enhancement effects discussed in Section 2.4.2 were studied at temperatures close to T_c, where the enhancement effects are most pronounced. The effects of microwave absorption at $T/T_c \simeq 0.1 - 0.3$, relevant for our microresonator experiments, have not been investigated.

It is usually assumed that there is a limit to the sensitivity of microwave resonator detectors due to microwave power dissipation. The microwave power is assumed to create excess quasiparticles at low temperature [22]. The experimental evidence of this process is presented in Chapter 6 where we have measured a decrease in the number of quasiparticles and a corresponding increase in the quasiparticle recombination time for decreasing microwave power. These observations are consistent with an increasing effective temperature of the quasiparticle system, which can also be observed in the response of the resonator (lower quality factor and decreasing resonant frequency) as shown in Chapter 4. However, that does not answer the question what the microscopic mechanism behind this effect is. It was shown in Ref. [62] that the kinetic equations together with the Eliashberg microwave absorption equation explain the creation of excess quasiparticles at low temperature. Due to multiple microwave absorption events together with very slow electron-phonon interaction, a non-equilibrium $f(E)$ can be maintained that leads to an excess quasiparticle density. The question arises at which

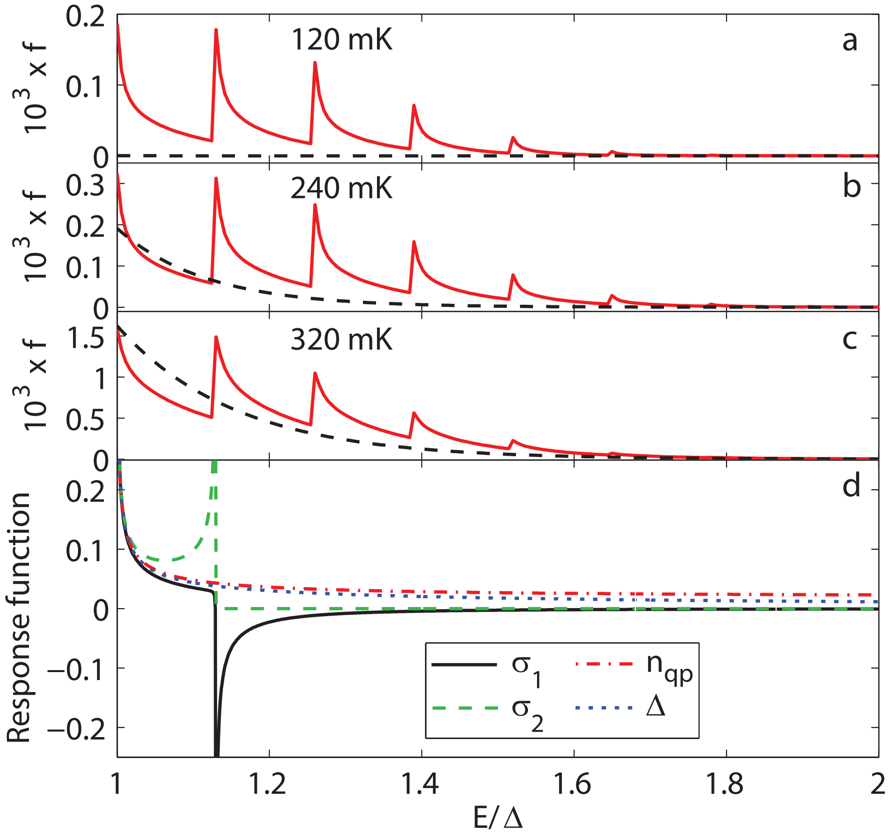

Figure 2.7: (a)-(c) The calculated non-equilibrium $f(E)$ due to microwave absorption at bath temperatures of 120, 240 and 320 mK (solid lines), for an aluminium microwave resonator at a microwave power of -72 dBm (calculations courtesy D. J. Goldie, see Chapter 8 for more details). The dashed lines show the Fermi-Dirac distribution for each bath temperature. (d) The response functions to $f(E)$ for σ_1, σ_2, n_{qp} and Δ as a function of energy, normalised to their (maximum) value at Δ.

point this ‘heating’ behaviour will turn into the enhancement effects discussed in the last section. In Chapter 8 we present measurements that show that for increasing microwave power, the quality factor increases for temperatures above 200 mK. The resonant frequency crosses over around 250 mK. These effects can be explained from a non-equilibrium $f(E)$, together with a different energy dependence of the observables.

The calculated non-equilibrium $f(E)$ due to microwave absorption is shown in Fig. 2.7 for three temperatures. The material parameters are chosen for a typical Al film and given in detail in Table 8.1. The quasiparticle distribution in thermal equilibrium at the bath temperature is shown for comparison. To show the different energy-dependences of Δ, n_{qp}, τ_{qp}, σ_1 and σ_2 we define response functions for these variables using Eqs. 2.2, 2.4, 2.11 and 2.12. Following Ref. [22], the response function K for a variable X is given by $X - X(T = 0) = \int_{\Delta}^{\infty} K_X f(E) dE$. The K_X for the four aforementioned variables are shown in Fig. 2.7d. For visibility, the density of states was broadened with a factor

$\Gamma/\Delta = 10^{-4}$.

At 120 mK, there is a very low density of quasiparticles in thermal equilibrium, with a long recombination lifetime. Microwave absorption has the effect of creating an excess quasiparticle population, which is reflected in a higher $f(E)$ at all energies and peaks at multiples of $\hbar\omega$. At a higher temperature there is a higher density of thermal quasiparticles and at 320 mK the main effect is redistribution over energies, whereas n_{qp} increases only a little. The most pronounced effect at that temperature is a decrease in the population at energies $\Delta > E > \hbar\omega$, which was the explanation of the enhancement effects close to T_c. At 320 mK temperature, there is still an excess quasiparticle density being created which partially compensates the enhancement effects. Therefore the enhancement of the energy gap at these temperatures is still very small. In Chapter 8 we show that these redistribution effects explain the temperature and power dependences of the quality factor, resonant frequency and quasiparticle lifetime in an Al microwave resonator.

A nonlinear resonator response due to heating

In the regime where excess quasiparticles are created, the effect of microwave absorption can be approximated by an effective temperature. The microwave dissipation in the quasiparticle system not only depends on the applied microwave power, but also on the detuning of the drive frequency with respect to the resonant frequency of the resonator, which changes as a function of temperature. In Chapter 4 the resonator response is modelled with a microwave dissipation that depends on the temperature and frequency. The electron-phonon interaction effectively cools the quasiparticle system and transports the absorbed microwave power to the bath. At high enough power the shapes of the dissipation and cooling curves give rise to non-linear behaviour with the possibility of a bistability between two different temperature states. Recently in Ref. [65] this model approach has been extended to the dynamical behaviour of the quasiparticle system under microwave heating. It has been derived that after a pulsed excitation, the decay time towards steady state can be strongly affected by this intrinsic nonlinearity. However, experimental evidence of this effect is not yet available. In view of the distribution functions in Fig. 2.7 the heating model is only a good approximation up to 200 mK (for aluminium).

2.4.5 Possible nonlinearities due to the current

It is well known that the current which can be carried by a superconductor has an upper limit, the critical current, which is directly related to the existence of a critical magnetic field. The critical current can be derived from energy considerations [1, 10]. In addition to redistribution of quasiparticles, the electromagnetic field affects the superconductor through the Cooper pairs. This effect is conventionally called the ‘pair breaking’ effect, because one of the electrons in the pair will have momentum $\mathbf{k}+\mathbf{q}$ and the other $-\mathbf{k}+\mathbf{q}$ [66], which breaks time-reversal symmetry. $\mathbf{q}$ is the additional momentum due to the applied field. The consequence is not only a reduction in Δ, but also a smeared density of states, where the divergent behaviour at $E = \Delta$ is removed. The density of states, measured with a tunnel junction in the presence of a DC current [67], is shown for several pair breaking strengths in Fig. 2.8a. A single depairing parameter in combination with the Usadel theory [68] describes the order parameter of the superconductor under pair breaking. Note that this 'pair breaking' mechanism is thus a weakening of the pairing energy of the Cooper pairs in the condensate, because the condensate consists of moving pairs, in contrast to the equilibrium ground state of Eq. 2.1. It is thus different from the pair breaking detection mechanism we investigate primarily in this thesis, which is based on breaking up a Cooper pair directly into quasiparticles by absorption of radiation with $\hbar\omega > 2\Delta$.

In Chapter 8, the experimental data on the electrodynamic response of Al is well described with a complex conductivity that includes a non-equilibrium quasiparticle distribution, as presented in Section 2.4.4. This correspondence indicates that the role of the current-induced broadening of the density of states is not dominant in the experiment. To estimate the actual maximum current in our experiment we can calculate the average current density from the internal microwave power in the resonator P_{int} by $j = \frac{\sqrt{4P_{int}/Z_0}}{Sd}$, with Z_0 the characteristic impedance and Sd the cross-sectional area. S is the width of the strip and d the thickness. The current density for a strip of 60 nm thick and 3 μm wide becomes then 2.5×10^5 A/cm^2 for the highest readout power of -64 dBm presented in Chapter 8 (where $P_{int} = -26$ dBm). However, the central strip of the resonator is wider than the penetration depth, which will cause a non-uniform current distribution, peaking at the edges of the strip. The current density as a function of position, x, can be approximated by [69]

$$j(x) = \begin{cases} \frac{c}{\sqrt{(a^2-p^2x^2)(b^2-p^2x^2)}}, & |x| \le a \\ 0, & a < |x| < b \\ -\frac{c}{\sqrt{(x^2-p^2a^2)(x^2-p^2b^2)}}, & |x| \ge b \end{cases} \tag{2.44}$$

where c is a constant. $1 - p \approx 0.67\lambda_\perp/a$ for $\lambda_\perp/a \ll 1$. In this definition a is half the central strip width $a = S/2$ and b is at the outer edge of the slot $b = S/2+W$, with W the width of the slot. Fig. 2.8b shows the current distribution from Eq. 2.44 for a $S = 3$ μm, $W = 2$ μm coplanar waveguide geometry with the material parameters of the sample used in Chapter 8: Al with $T_c = 1.17$ K, a thickness of 60 nm, $1/\sigma_N = 0.9$ $\mu\Omega$cm. The low temperature penetration depth in the dirty limit is given by $\lambda = \sqrt{\hbar/\mu_0\pi\Delta\sigma_N} \approx 92$ nm. We observe in Fig. 2.8b that the peak current is 2.3 times the average current density, $j_{peak} = 5.8 \times 10^5$ A/cm^2.

The critical current density can be calculated using $j_c = 0.75\Delta_0^{3/2}\sqrt{N_0\sigma_N/\hbar}$ [70], which has been experimentally tested [67, 70] for DC currents. For our samples this

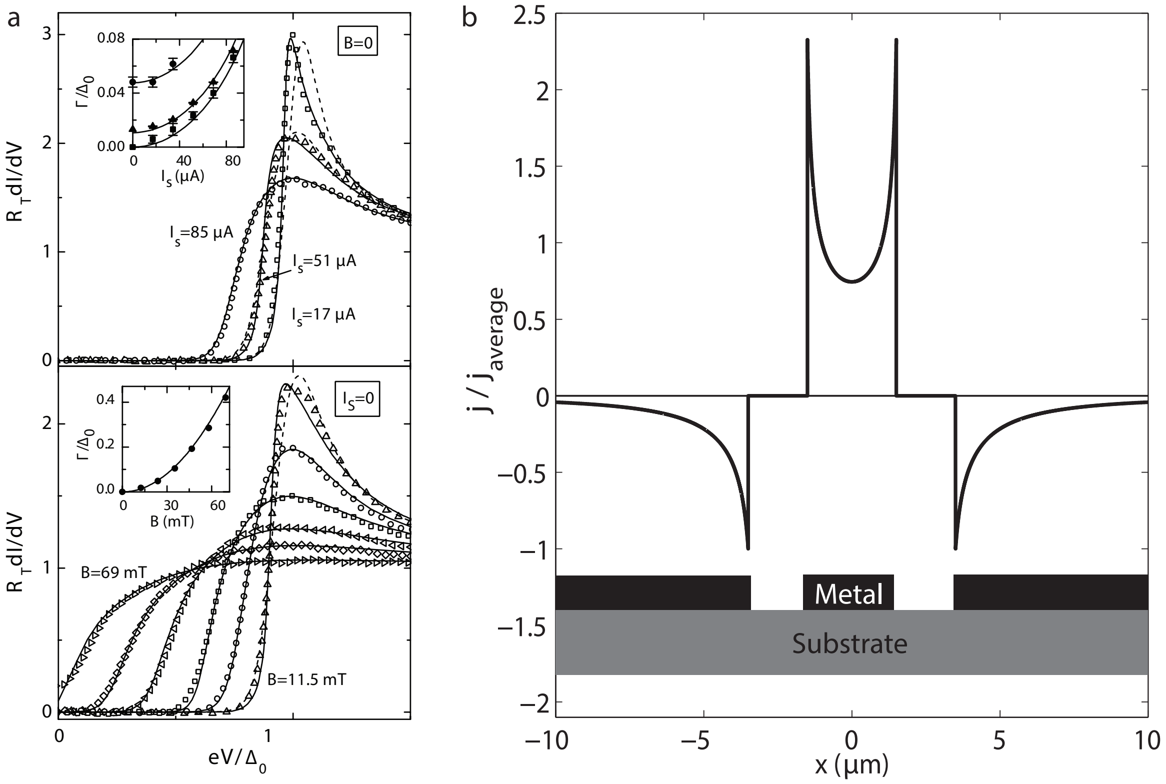

Figure 2.8: (a) The measured differential conductance of the probe tunnel junction, placed on an aluminium wire. The main effect of an applied current (top panel) or an applied magnetic field (bottom panel) is to broaden the density of states. The insets show the pair-breaking strength Γ needed to describe the measurements. Figure from Ref. [67]. (b) Current density distribution as a function of distance from the centre of an aluminium coplanar waveguide, normalised to the average current density in the central strip. The returning current runs through the groundplanes and the current is therefore negative in that region. The width of the central strip and the slots are 3 μm and 2 μm respectively, as shown in the schematic picture at the bottom.

equation results in $j_c = 4 \times 10^6$ A/cm^2. Thus only for the highest readout powers in our experiments the current becomes an appreciable fraction of the critical current, which could cause an additional non-linearity in the response of the superconductor due to the pair-breaking effect shown in Fig. 2.8a. The thus induced non-linearity causes a frequency shift in a microwave resonator, without much additional dissipation (much less than in the case of quasiparticle redistribution). The current dependent frequency shift is caused by the depairing, which causes a current dependent kinetic inductance. The kinetic inductance can be described as $L_K(j) = L_K(0)[1 + a(j/j_c)^2]$, with a a constant. The effect could also explain why the agreement between model and experiment in Fig. 8.1 is better for the quality factor than for the resonant frequency at the lowest temperatures. However, it cannot explain the cross-over behaviour between enhanced and depressed conductivity as a function of microwave power and temperature as described in Chapter 8. The dominant effect for our Al resonators is due to the redistribution of the quasiparticles over energy.

The nonlinear kinetic inductance without additional losses is the basis of travelling wave parametric amplifiers [71]. Parametric amplification was demonstrated with NbTiN, a material with a high normal state resistivity and a relatively high T_c, which has a much faster electron-phonon scattering rate than Al. In fact, if the redistribution effects with the emergence of excess quasiparticles would appear to the same extent in NbTiN, the parametric amplifier would have too much dissipation to work. The apparent difference between these two materials is due to a very different factor α_ω/τ as discussed in Section 2.4.2.

2.5 Absorption of pair breaking photons, $\hbar\omega > 2\Delta$

2.5.1 Intentional

The purpose of a detector is to detect radiation with the highest sensitivity (signal-to-noise) and the highest efficiency. To improve both properties, a necessary ingredient is the understanding of the photon absorption mechanism. In the experiments in Chapter 7 we use an antenna which launches the pair breaking signal as a travelling wave into a coplanar waveguide, which is discussed in more detail in Section 3.2.3. The absorption of the pair-breaking signal in the superconductor is mainly governed by σ_1. For frequencies $\hbar\omega < 2\Delta$ the first term in Eq. 2.11 dominates. Just above 2Δ the second term, which describes pair-breaking, rises rapidly and becomes dominant. σ_1 and σ_2 are plotted as function of frequency in Fig. 2.9a. The input parameters are those of the aluminium sample used in Chapter 7: $T_c = 1.24$ K, $\Delta = 188$ μeV and $T = T_c/8$. At 2Δ (90 GHz), σ_1 rises rapidly and starts to approach the normal state conductivity σ_N for higher energies. Close to the gap there is still a significant contribution of σ_2 to the total conductivity. The parameter which directly determines the absorption of the signal is the surface resistance R_s which can be calculated using Eq. 2.20. R_s is shown in Fig. 2.9b as a function of frequency (for $\rho_N = 2.2$ $\mu\Omega$cm). For comparison we show also the surface resistance in the normal state, using $\sigma_1 = \sigma_N$ and $\sigma_2 = 0$. The normal state conductivity gives a good approximation for energies far above the gap, for example for the 1.54 THz radiation we apply in Chapter 7.

Number of excited quasiparticles

We consider a photon-integrating detector (as opposed to a single photon counting detector), which detects the power of a steady stream of photons. In a pair-breaking detector like the kinetic inductance detector, the photon stream continuously breaks Cooper pairs into quasiparticles. The lifetime of each excitation is the quasiparticle recombination time given by Eq. 2.28. The process of recombination subsequently

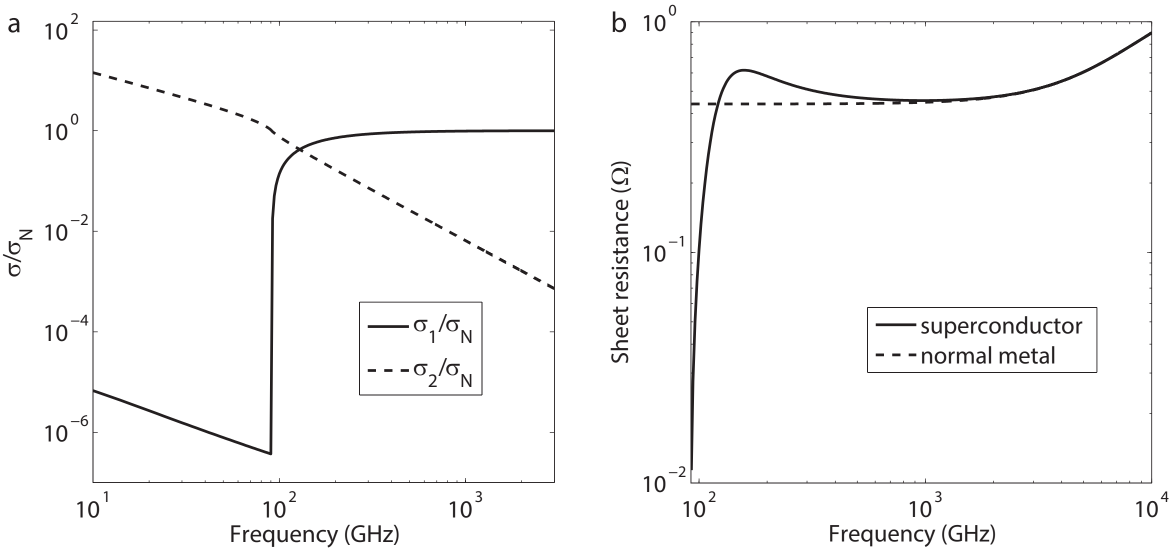

Figure 2.9: (a) The real and imaginary part of the complex conductivity as a function of frequency. The effect of Cooper pair breaking starts at a frequency of 90 GHz, corresponding to twice the gap energy for aluminium. (b) The sheet resistance as a function of frequency. The solid line includes superconductivity by calculating R_s using σ_1 and σ_2 from the Mattis-Bardeen equations as shown in (a). The dashed line is for a normal metal, where $\sigma = \sigma_N$. Note that for photon energies between 2Δ and 6Δ the normal metal resistance deviates significantly from that of the superconductor.

transports the power to the heat bath. These two processes maintain a steady state number of excited quasiparticles. In a simple, and often sufficient, description the radiation power P_{rad} is related to the steady state number of quasiparticles by

$$\eta_{opt}\eta_{pb}P_{rad} = \frac{N_{qp}\Delta}{\tau_{qp}}, \tag{2.45}$$

where η_{opt} is the optical efficiency, which is the fraction of the radiation power that is absorbed in the sensitive medium with respect to the incident power at the reference plane where P_{rad} is measured.

The pair breaking efficiency η_{pb} reflects that the detector is most sensitive to quasiparticles at an energy close to Δ. However when the frequency of the optical signal is significantly larger than 2Δ, there will also be quasiparticles at higher energies, mostly between Δ and 3Δ, which decrease the response of the complex conductivity to a change in the optical power $d\sigma/dP_{rad}$. For high energy (X-ray) photons $\hbar\omega >> 2\Delta$ it was shown in Ref. [72] that initially fast photo-electrons are created (with energy 10-20 eV), which by a down-conversion process involving stages of electron-electron and electron-phonon interaction, very rapidly cascades down in energy (much faster than τ_{qp}). The final stage of this process leaves quasiparticles with an average energy of 1.7Δ, which is finally released through recombination. The factor 1.7Δ would imply that $\eta_{pb} \simeq 0.59$. η_{pb} is assumed to approach 1 for $\hbar\omega$ close to 2Δ [22].

Although η_{pb} is conventionally called the 'pair breaking efficiency' it describes a reduction of the response, and not a reduction of the optical efficiency. This is most easily understood from a photon-counting perspective: if 10 photons would impinge on a detector with $\eta_{opt} = 1$ and $\eta_{pb} = 0.6$, the response will be 10 pulses with a height of 0.6. In contrast, a detector with $\eta_{opt} = 0.6$ and $\eta_{pb} = 1$ will show 6 pulses with height 1.

Non-equilibrium perspective

The factor η_{pb} in Eq. 2.45 arises because of the formulation in terms of N_{qp}. On a microscopic level, the absorption of pair breaking radiation leads to a non-equilibrium $f(E)$ in the superconductor, together with a change in Δ (Eq. 2.2). For sufficiently low energy photons that do not directly excite photo-electrons, but only break Cooper pairs in the superconductor, the resulting $f(E)$ can be calculated in steady state using the same kinetic equation approach as discussed in Section 2.4.1. The injection term is now the third term in Eq. 2.42 that describes pair breaking. The pair-breaking rate thus depends on the strength of the applied radiation field, which can be converted to absorbed power, in this case $P_{abs} = \eta_{opt} P_{rad}$. Note that the steady state approach takes account of the fact that the absorption (pair-breaking) process involves a non-equilibrium $f(E)$ in the superconductor. The responsivity of the detector will be determined by $d\sigma/dP_{rad}$, where σ, N_{qp} and τ_{qp} are determined by the non-equilibrium $f(E)$.

It was recently shown [73] that the resulting $f(E)$ using this procedure indeed gives rise to an η_{pb} of around 1 near the gap edge, which decreases to a around 0.6 for higher frequencies $\hbar\omega \gtrsim 4\Delta$. The exact $f(E)$, and thus η_{pb}, depends on the electron-phonon interaction time and the phonon escape time, and can therefore vary between materials and layer thicknesses. Gao et al. [20] have shown that the response of an Al resonator to pair-breaking radiation is similar to the response to temperature, which suggests that an effective temperature, together with η_{pb}, is a good description of the microwave response to pair-breaking radiation. An open problem is the influence of the microwave absorption on an experiment with pair-breaking radiation. This would require to include all terms of Eq. 2.42 with appropriate respective strengths in the kinetic equations.

Fluctuations in the photon stream - photon noise

The radiation power P_{rad} is not constant over time, it fluctuates due to the random arrival rate of the photons, which is a fundamental property of thermal radiation sources. Photon noise is thus the fundamental noise source for any power integrating detector and determines as such the sensitivity limit of an ideal detector. Photon noise limited detection was first demonstrated for microwave resonator detectors by Yates et al. [74]. The power spectral density of the power fluctuations in the photon stream is given by [75]

$$S_P = 2P_{rad}\hbar\omega(1 + \eta_{opt}B), \tag{2.46}$$

where $(1 + \eta_{opt}B)$ is the correction to Poissonian statistics due to photon bunching for a single mode, with B the mode occupation. Fig. 3.4b shows that the photon bunching contribution to the photon noise is negligible for the experiments presented in this thesis. The photon noise depends both on the radiation power and the frequency, and a detector sensitivity is thus only meaningful when these two numbers, together with the optical efficiency are specified. The hallmarks of photon noise in a microwave resonator are a flat noise spectrum as a function of frequency until a roll-off due to the quasiparticle recombination time, very similar to the spectrum due to generation-recombination noise. The roll-off frequency increases with increasing radiation power, because of the decreasing quasiparticle lifetime. How photon noise can be measured and described in a microwave resonator experiment is discussed in detail in Chapter 7, in direct comparison with experimental data.

2.5.2 Unintentional - excess quasiparticles

The pair breaking signal as discussed in the previous section is a quantity that should fulfill two requirements in an experiment: the power is well defined and the frequency is well defined. Both these requirements are compromised if the optical filtering is insufficient or in the presence of stray-light. The choice of filters and their position in the experimental setup will be discussed in Chapter 3. The problem of stray-light is not only present in optical experiments in which a controlled light source is required, but also in dark measurements without illumination. In a cryogenic system the lowest temperature is usually reached by cooling in different steps (e.g. 70 K, 4 K, 100 mK). If the lowest temperature stage is not well shielded from radiation, thermal radiation which is generated at the 4 K stage can reach the sample under study. In the case of a superconductor it will break Cooper pairs and create excess quasiparticles (in excess of the quasiparticles present due to the temperature). In microwave resonators both the quality factor and the quasiparticle recombination time are inversely proportional to the quasiparticle density and will thus be suppressed in the presence of excess quasiparticles due to stray-light (see Chapter 3 and Refs. [76–78]). The low limit that we can infer from our experiments is $n_{qp} \approx 10\ \mu\text{m}^{-3}$, currently limited by microwave readout power dissipation (Chapters 6 and 7).

Excess quasiparticles in superconducting qubits

In superconducting qubits, the presence of excess quasiparticles due to stray light will limit the coherence time (T_1) of the qubit, $T_1 \propto 1/n_{qp}$. This occurs because a quasiparticle can absorb or release energy and as such cause a transition of the qubit into its ground or excited state. The sensitivity of the qubit to quasiparticles depends on its design and sensitivity to charge [79]. Even in qubits based on the highly protected Majorana bound states, excess quasiparticles cause decoherence [80, 81]. In Refs. [82–85] the influence of quasiparticles, of both thermal and non-equilibrium origin, on the parity state of a particularly charge-sensitive qubit is discussed. However, not every quasiparticle tunnelling event that changes the parity of the qubit also induces decoherence. It was conjectured by Martinis et al. [86] that the presence of excess quasiparticles causes the saturation in T_1. This hypothesis was verified by deliberate injection of quasiparticles into the qubit, which can be achieved through the flux-control line of a qubit [87, 88]. A reduction of stray-light was achieved in our group by making the sample box more light tight and using coaxial filters [76], which later on evolved into the box-in-box concept discussed in Chapter 3. The quasiparticle lifetime does not depend anymore on the temperature of the environment. This concept has also been used to considerably improve the qubit coherence time [77]. A similar improvement can also be achieved by casting the whole qubit sample box into absorbing material [89]. Recently a measurement of the even-odd switching rate in a qubit was compared to the decoherence rate, which revealed that the quasiparticle tunnelling rate in the qubit does not limit the decoherence time T_1 [90]. More important for the comparison with our experiments is the low limit in the excess quasiparticle density that is inferred from this experiment: $n_{qp} < 0.1\ \mu\text{m}^{-3}$. A similarly low n_{qp} was obtained from a single-electron transistor experiment, which combined stray-light shielding with quasiparticle traps [91]. Both these experiments used aluminium as the material for the sensitive part of the device, which shows that the aluminium itself does not give rise to a significant excess quasiparticle density.

Interestingly one can reduce the influence of quasiparticle losses in microwave resonators by reducing the kinetic inductance fraction. Therefore, 3D cavities became recently popular in circuit QED experiments, where the field is mainly in the vacuum dielectric. The kinetic inductance fraction is only $10^{-5} - 10^{-6}$, which therefore, even with a lossy metal, can lead to Q-factors of 10^9 [92, 93]. In addition, the 3D embedding of the qubit may also reduce the influence of stray light. For microwave resonator detectors however, a high sensitivity to quasiparticles is required (high α_k). The only way to reduce the consequences of stray-light is then to eliminate it.

2.6 Choice of materials

Throughout this chapter we have seen several material dependent parameters that influence the responsivity and therewith the sensitivity of a superconducting microwave resonator detector. The choice of geometry and material is a trade-off of various aspects, such as noise and responsivity. In this section we first discuss the relevant material-dependent parameters to compare, after which we briefly review the choice of the metal and dielectric, mainly focussing on the metals Al and TiN and dielectric two-level-system noise.

The noise equivalent power is in general determined by the responsivity (signal) and the noise and given by

$$NEP = \sqrt{S_X} \left(\frac{dX}{dP_{rad}} \right)^{-1} \sqrt{1 + \omega^2 \tau^2}, \tag{2.47}$$

with τ the limiting timescale and X the observable, being either A or θ. The noise spectrum S_X is ideally photon noise limited and otherwise as low as possible. The responsivity can be divided into two factors: $\frac{dX}{dP_{rad}} = \frac{dX}{dN_{qp}} \frac{dN_{qp}}{dP_{rad}}$. dX/dN_{qp} is given by Equations 2.26 and 2.27. Using Eq. 2.45, dN_{qp}/dP_{rad} can be written as

$$\frac{dN_{qp}}{dP_{rad}} = \frac{\tau_{qp} \eta_{opt} \eta_{pb}}{\Delta} \propto \sqrt{\frac{\eta_{opt} \eta_{pb} \tau_0 N_0 V}{P_{rad}}}, \tag{2.48}$$

where the proportionality is derived using Eq. 2.29 and using the BCS relation $\Delta \simeq 1.76 k_B T_c$. It may seem strange that a bigger volume gives a higher dN_{qp}/dP_{rad}, but in a bigger volume the quasiparticle lifetime is longer for the same P_{rad}. For the *total* responsivity dX/dP_{rad} there is an additional factor $1/V$ from Eqs. 2.26 and 2.27, because the conductivity responds to a change in quasiparticle density. Therefore overall for increasing dX/dP_{rad} a small volume is desirable. Furthermore a high τ_0, a low N_0 (it occurs as well in the denominator of Eqs. 2.18 and 2.19), a high Q, and a high α_k enhance the responsivity dX/dP_{rad}. Next to these parameters related to the device physics, a material should also be easy to fabricate, reproducible and uniform over a large area.

Elemental superconductors - aluminium

Aluminium has the longest tradition in KID detectors. It shows a recombination time and electrodynamic response as expected by the predictions of Kaplan et al. [27] and Mattis-Bardeen [15] respectively. The fundamental limits originally associated with these detectors [22, 94], generation-recombination noise and photon noise were recently revealed in aluminium resonators, as shown in this thesis. Furthermore Al is routinely used in all kinds of applications. As shown in Table 2.1 it has a favourable gap energy, a very long τ_0, and a high enough quality factor (even up to 1×10^7 for Al grown with molecular beam epitaxy [95]). Furthermore it does not give rise to intrinsic excess quasiparticles as discussed in Section 2.5.2.

The quasiparticle recombination time for a BCS superconductor is directly related to the quasiparticle density (Eq. 2.29), which we demonstrate in Chapter 5. However, for most materials τ_{qp} can only be studied with the pulse-method. The low temperature saturation in τ_{qp} is not necessarily related to excess quasiparticles. Therefore Table 2.1 has an additional column showing the maximum measured τ_{qp} for each material. It was

Material	T_c (K)	Δ (μeV)	ρ_N ($\mu\Omega$cm)	λ_0 (nm)	τ_0 (ns)	$\tau_{qp,max}$	$Q_{i,max}$	References
Al	1.11	168	0.8	89	458	3.5 ms	3×10^6	Ch. 5,8
Ta	4.4	667	8.8	150	1.8	30 μs	1×10^6	[27, 96]
Nb	9.2	1395	6	45	0.15	1 ns	7×10^5	[19, 27, 97, 98]
TiN	0.7-4.5	100-650	100-1000	500-3000		200 μs	1×10^7	[99–101]
NbTiN	14.5	2200	100	275		1 ns	2×10^6	[19, 98]

Table 2.1: Typical parameters of various materials. Δ is calculated from T_c using the BCS relation. The values for Al are for the sputtered 40 nm thick film reported in Chapter 5, except for the maximum quality factor, which is for the film reported in Chapter 8. The properties of TiN vary widely because of the tunability of its properties through the composition and thickness. For NbTiN only the values for typical thick films are shown. In principle it has a similar tunability as TiN.

shown by Barends et al. [96] that impurities implanted in Al decrease the maximum recombination time.

Recombination in Ta has been shown to have the same dependence on impurities as Al [96]. The maximum, saturation recombination time for the cleanest films is however around 30 μs, much too short to be associated with external effects such as stray light (compared to several milliseconds for Al in the same setup). In view of the $Q_{i,max}$ and $\tau_{qp,max}$, Ta is thus only suitable for applications involving high optical powers.

Nb has been used for a first generation of microwave resonators, but it is not suitable as a microresonator detector because of its fast recombination. Already at modest temperatures τ_{qp} saturates at around 1 ns [98].

Table 2.1 is an overview of typical parameters for thin films of the various materials, which is meant to compare between the materials, not to give the absolute maximum of every parameter ever achieved. The maximum quality factors are compared in the many microwave photon regime, which is typically used for detectors, and for microwave frequencies of 3-8 GHz.

Disordered superconductors - TiN

It was shown by Leduc et al. [99] that TiN is a promising material for microresonator detectors because of its high Q_i and high penetration depth, which can give an α_k close to 1 (α_k ≈0.3 for Al in a similar geometry). The high α_k also helps to reduce the volume for the same resonant frequency. $\tau_{qp,max}$ is 10 times lower than for Al. Both for sputtered TiN [99, 102] and atomic layer deposited (ALD) TiN [100, 101], the T_c can be varied from 0.7 to 4.5 K. However, the electrodynamic response of TiN, especially the frequency response, does not behave according to the predictions of Mattis and Bardeen. We studied the response of a range of ALD grown TiN films, where the resistivity increased with decreasing thickness (see Coumou et al. [101]). Fig. 2.10a

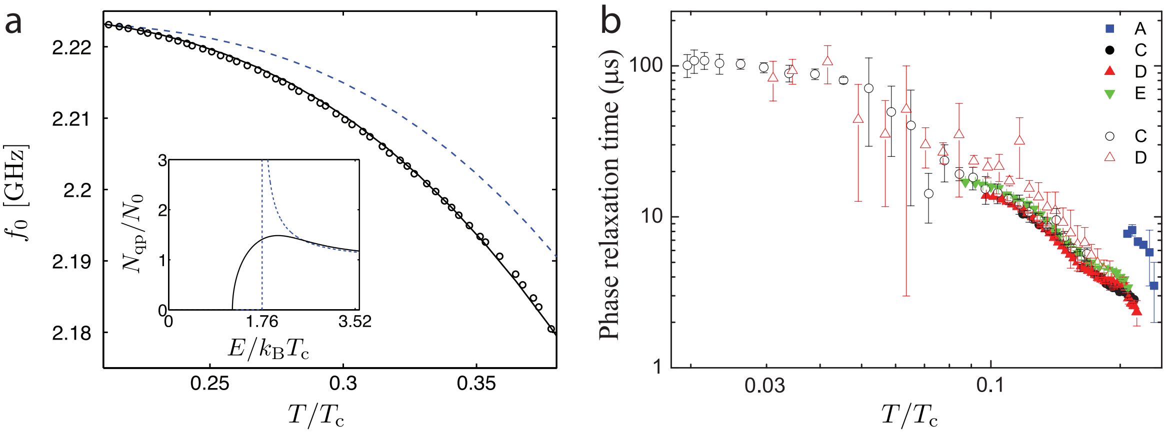

Figure 2.10: (a) The resonant frequency as a function of normalised temperature of a microwave resonator made from a 6 nm thick TiN film. The dashed line is the prediction of the response from the Mattis-Bardeen theory, based on a BCS quasiparticle density of states (inset). The solid line in the inset is the density of states in the presence of a pair-breaking parameter, which results in a modified frequency response (solid line main panel). Figure from Driessen et al. [100]. (b) The measured relaxation time from a pulse excitation for four different TiN films, with A the most disordered (T_c = 1.5 K, ρ_N = 380 $\mu\Omega$cm) and E the least disordered film (T_c = 3.6 K, ρ_N = 120 $\mu\Omega$cm). The open/closed symbols represent measurements in two different setups. Figure from Coumou et al. [101].

shows the frequency response of a 6 nm TiN film with a T_c of 1.5 K and ρ_N = 380 $\mu\Omega$cm. The response cannot be described with the Mattis-Bardeen theory, which is discussed in depth by Driessen et al. [100].

From another point of view TiN is a material that can be classified as a disordered superconductor. In this class of materials, the electron mean free path is so small that localisation effects play a role in the emergence of superconductivity. For ALD deposited films, the disorder increases with decreasing thickness. It has been shown by local tunnelling spectroscopy that in TiN films similar to the one used for Fig. 2.10a, the energy gap and the density of states are not homogeneous but rather show spatial variations over a scale of 50 nm [103]. In the description of the electrodynamic response of TiN, one can introduce a smeared density of states, described with a pair breaking parameter analogous to the effect of a strong current (as in Fig. 2.8a). Such a modified theory describes the electrodynamic response well, as shown in Fig. 2.10. However it is still a homogeneous description of a spatially inhomogeneous property. Recent microwave resonator measurements on TiN films combined with local tunneling spectroscopy on the same films shows that, for the most disordered films, the density of states required to describe the electrodynamic response is not consistent with the tunnelling spectra [104].

Fig. 2.10b shows the measured pulse-decay times for ALD TiN films with varying disorder, which we interpret as the quasiparticle recombination time [101]. We obtain a similar $\tau_{qp,max} \approx 100\ \mu$s as Leduc et al. [99]. More importantly the temperature dependence of the measured times is much weaker than in Eq. 2.28 (with any value of τ_0), and cannot be interpreted in the same framework. In experiments by Gao et al. [105] it was shown that the pulse-decay measured in the resonator amplitude and phase direction results in different decay times at low temperatures. All these observations show that disordered superconductors and their electrodynamic response are more complicated than for a BCS-superconductor such as Al. So far the fundamental noise limits have not been reached with TiN. A consistent description of the quasiparticle dynamics, the microwave response and the absorption of pair breaking radiation in a superconductor with a non-homogeneous order parameter is still not available.

Dielectric layers - two level systems

The resonant frequency and the losses of a microwave resonator are determined by the inductance (current, magnetic field) and by the capacitance (electric field). The current can only flow in the metal part and thus probes the superconductor with its quasiparticle system. In the section of the resonator where the electric field is the strongest, the response of the resonator is dominated by the dielectric environment of the resonator. This environment consists of vacuum, the substrate and other spurious dielectric layers. In the latter two, the dielectric constant varies due to changes in the occupation of dipole two-level-systems (TLS), which are especially abundant in amorphous layers. These TLS can have the effects of a temperature dependent shift of the resonant frequency, excess noise and a limit to the quality factor due a loss tangent at microwave frequencies. TLS have a number of properties related to the choice of materials and experimental conditions:

- The TLS losses and the noise decrease if the microwave power is increased. The noise level scales with $P_{int}^{-1/2}$ [106, 107], with P_{int} the internal power of the resonator. This power dependence is consistent with a model assuming a surface distribution of TLS [108].

- The TLS losses and noise decrease for bigger structures. It is thus advantageous to use wider CPW lines [107, 108] and bigger elements in a lumped element geometry [109].

- Most TLS exist in surface layers, in an oxide on top of the metal or at the metal-substrate interface [17, 110–112]. The top oxide layer can be avoided to a large extent by using a material that does not oxidize well, such as NbTiN [107] (the noise level is 7 dB lower than for Al on the same substrate) or TiN [113]. TLS at the substrate-metal interface can be removed by hydrogen passivation of the substrate before the deposition of the metal [107]. A dip in hydrofluoric acid (HF) is used for that purpose. A high-resistivity crystalline Si substrate with hydrogen passivation is the best choice. The effect of the remaining interface, the

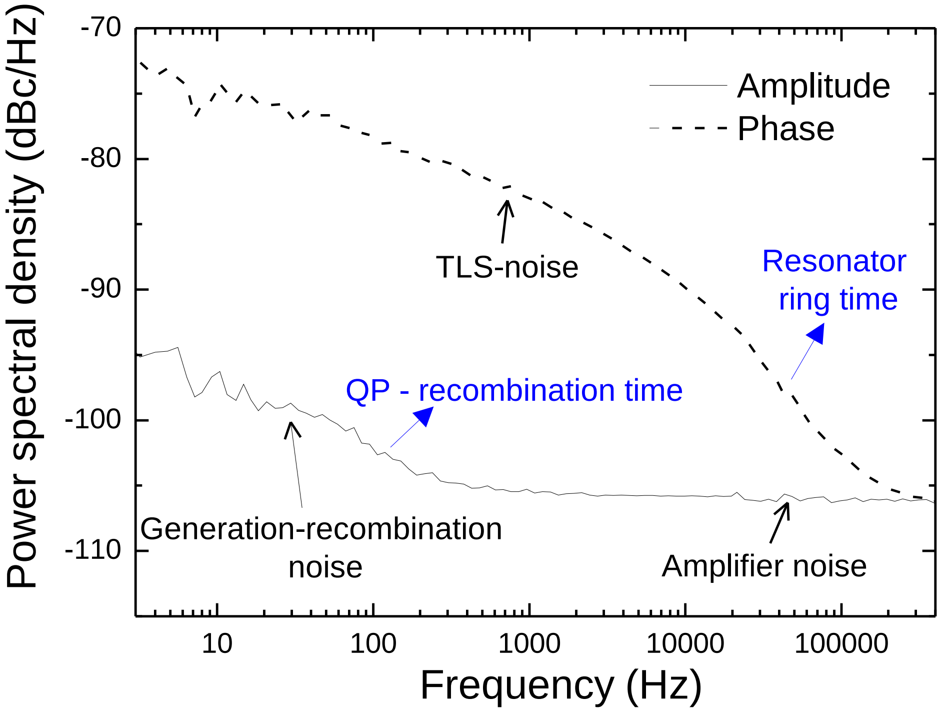

Figure 2.11: The measured amplitude and phase power spectral density as a function of frequency. The measurement was performed on an aluminium coplanar waveguide resonator at a temperature of 120 mK and shows most of the noise sources discussed in this chapter as indicated. The two time scales that cause a roll-off in the spectrum are indicated in blue. See for the details of the measurement Chapter 5.

substrate-air interface, can be reduced by etching trenches in the substrate, which reduces the noise by another 7 dB [111]. The TLS losses ($1/Q_i$) are reduced as well [110, 114].

- The TLS noise level [115] and the losses [110] decrease for higher temperatures.

For a long time TLS-noise was only observed in the phase direction of the response, corresponding to fluctuations in the dielectric constant. Because TLS also cause losses, one would expect fluctuations in the amplitude (dissipation) direction as well. In experiments by Gao et al. [116] the amplitude noise was shown to be lower than the vacuum noise, except for low frequencies, which suggested the absence of TLS noise in the dissipation direction. It was recently suggested by Neill et al. [117] that there is TLS noise in the dissipation direction as well, which is strongly power dependent. At high microwave powers (which are used for detector purposes) the difference in the phase and amplitude TLS-noise levels is large, whereas at the single microwave photon level they are of the same order of magnitude. For the high microwave powers we use in the experiments in this thesis, TLS-noise in the amplitude direction is therefore not visible.

In Refs. [17, 19] a broader discussion of relevant literature is provided. There are thus a number of conflicting design choices for a resonator detector. For a high response a small volume is better, but a reduction in size introduces more TLS losses and noise. A higher temperature reduces the TLS-noise, but reduces the quasiparticle response. In this thesis the amplitude readout is used, which is dominated by quasiparticle fluctuations for aluminium resonators. Fig. 2.11 shows power spectral density of the amplitude and phase noise, with the relevant noise contributions. Next to generation-recombination noise and TLS-noise there is a white noise contribution due to the amplifier. Note that in a device in which the TLS-noise is much lower, the generation-recombination noise will also show up in the phase spectrum. At low frequencies there is an additional $1/f$ component, which is most likely due to the electronics, but $1/f$ noise can also have a wide variety of origins [118].

Hybrid devices

A way to combine the best of both worlds, the low noise of NbTiN and the high sensitivity of Al, is to use a combination of both materials. NbTiN by itself has a low responsivity and a high gap energy. Since the sensitivity to TLS losses and noise is the largest at the capacitive end of a resonator, that end is made of NbTiN and could also be larger. The sensitivity to quasiparticles is at maximum at the inductive end, where the current is the highest, which should therefore contain an Al section. These devices show particularly low phase noise (due to the NbTiN) and are photon-noise limited in amplitude for radiation powers of 100 fW and higher as demonstrated by Yates et al. [74] and therefore well suited for ground based observations. They are even photon noise limited in phase readout as shown by Janssen et al. [119], which is convenient because the response in the phase direction is higher (Fig. 2.3). Another advantage of these two materials is the difference in energy gap between NbTiN and Al (1.1 THz vs. 90 GHz), which confines the quasiparticles created by pair breaking to the Al sensitive region.

Instrument requirements

When the detector is photon-noise limited with a high optical efficiency, the fundamental sensitivity limit is reached in principle. But even then there are parameters that can be optimised for the particular application. For instance τ_{qp} determines the speed of the detector, which is especially important for photon counting experiments. The speed can be increased by using a material with lower τ_0 or by choosing a smaller volume. Furthermore the noise-level due to the readout electronics has to be lower than the photon-noise level, and the number of bits per channel has to be large enough to distinguish the photon noise level from the carrier. It is therefore beneficial to choose a material and geometry with high responsivity, which thus enhances the photon-noise level and reduces the complexity of the readout electronics.

References

[1] J. R. Hook and H. E. Hall, *Solid State Physics*, John Wiley & Sons, Inc., 2^{nd} edition, 2005.

[2] D. Pines and P. Nozières, *The Theory of Quantum Liquids: Volume 1*, W. A. Benjamin, Inc., 1966.

[3] C. A. Reynolds, B. Serin, W. H. Wright, and L. B. Nesbitt, *Superconductivity of Isotopes of Mercury*, Phys. Rev. **78**, 487 (1950).

[4] E. Maxwell, *Isotope Effect in the Superconductivity of Mercury*, Phys. Rev. **78**, 477 (1950).

[5] L. N. Cooper, *Bound Electron Pairs in a Degenerate Fermi Gas*, Phys. Rev. **104**, 1189 (1956).

[6] J. Bardeen, L. N. Cooper, and J. R. Schrieffer, *Theory of Superconductivity*, Phys. Rev. **108**, 1175 (1957).

[7] A. L. Fetter and J. D. Walecka, *Quantum Theory of Many-Particle Systems*, Dover Publications, Inc., New York, 2003.

[8] R. E. Glover and M. Tinkham, *Conductivity of Superconducting Films for Photon Energies between* 0.3 *and* $40kT_c$, Phys. Rev. **108**, 243 (1957).

[9] H. Kamerlingh Onnes, *Further experiments with Liquid Helium G. On the electrical resistance of Pure Metals etc. VI. On the Sudden Change in the Rate at which the Resistance of Mercury Disappears*, Comm. Phys. Lab. Univ. Leiden , 124c (1911).

[10] M. Tinkham, *Introduction to Superconductivity*, McGraw-Hill, New York, 2^{nd} edition, 1996.

[11] F. London and H. London, *The Electromagnetic Equations of the Supraconductor*, Proc. R. Soc. Lond. A **149**, 71 (1935).

[12] C. J. Gorter and H. B. G. Casimir, *On supraconductivity 1*, Physica **1**, 306 (1934).

[13] A. B. Pippard, *An Experimental and Theoretical Study of the Relation between Magnetic Field and Current in a Superconductor*, Proc. R. Soc. London A. **216**, 547 (1953).

[14] J. Pearl, *Current distribution in superconducting films carrying quantized fluxoids*, Appl. Phys. Lett. **5**, 65 (1964).

[15] D. C. Mattis and J. Bardeen, *Theory of the anomalous skin effect in normal and superconducting metals*, Phys. Rev. **111**, 412 (1958).

[16] M. Dressel and G. Grüner, *Electrodynamics of solids*, Cambridge University Press, 2002.

[17] J. Gao, *The Physics of Superconducting Microwave Resonators*, PhD thesis, California Institute of Technology, 2008.

[18] J. P. Turneaure, J. Halbritter, and H. A. Schwettman, *The surface impedance of superconductors and normal conductors: The Mattis-Bardeen theory*, J. Superconductivity **4**, 341 (1991).

[19] R. Barends, *Photon-detecting Superconducting Resonators*, PhD thesis, Delft University of Technology, 2009.

[20] J. Gao, J. Zmuidzinas, A. Vayonakis, P. Day, B. Mazin, and H. Leduc, *Equivalence of the effects on the complex conductivity of superconductor due to temperature change and external pair breaking*, J. Low Temp. Phys. **151**, 557 (2008).

[21] C. S. Owen and D. J. Scalapino, *Superconducting State under the Influence of External Dynamic Pair Breaking*, Phys. Rev. Lett. **28**, 1559 (1972).

[22] J. Zmuidzinas, *Superconducting Microresonators: Physics and Applications*, Ann. Rev. Condens. Matter Phys. **3**, 169 (2012).

[23] W. Henkels and C. Kircher, *Penetration depth measurements on type II superconducting films*, IEEE Trans. Magn. **13**, 63 (1977).

[24] R. L. Kautz, *Picosecond pulses on superconducting striplines*, J. Appl. Phys. **49**, 308 (1978).

[25] J. P. Turneaure and I. Weissman, *Microwave Surface Resistance of Superconducting Niobium*, J. Appl. Phys. **39**, 4417 (1968).

[26] B. A. Mazin, *Microwave kinetic inductance detectors*, PhD thesis, California Institute of Technology, 2004.

[27] S. B. Kaplan, C. C. Chi, D. N. Langenberg, J. Chang, S. Jafarey, and D. J. Scalapino, *Quasiparticle and phonon lifetimes in superconductors*, Phys. Rev. B **14**, 4854 (1976).

[28] H. K. Leung, J. P. Carbotte, D. W. Taylor, and C. R. Leavens, *Multiple-plane wave calculation of the electron-phonon interaction in Al*, Canadian J. of Phys. **54**, 1585 (1976).

[29] J.-J. Chang and D. J. Scalapino, *Kinetic-equation approach to nonequilibrium superconductivity*, Phys. Rev. B **15**, 2651 (1977).

[30] S. B. Kaplan, *Acoustic matching of superconducting films to substrates*, J. Low Temp. Phys. **37**, 343 (1979).

[31] N. Vercruyssen, R. Barends, T. M. Klapwijk, J. T. Muhonen, M. Meschke, and J. P. Pekola, *Substrate-dependent quasiparticle recombination time in superconducting resonators*, Appl. Phys. Lett. **99**, 062509 (2011).

[32] D. C. Moore, S. R. Golwala, B. Bumble, B. Cornell, P. K. Day, H. G. LeDuc, and J. Zmuidzinas, *Position and energy-resolved particle detection using phonon-mediated microwave kinetic inductance detectors*, Appl. Phys. Lett. **100**, 232601 (2012).

[33] O. Quaranta, T. W. Cecil, L. Gades, B. Mazin, and A. Miceli, *X-ray photon detection using superconducting resonators in thermal quasi-equilibrium*, Supercond. Sci. Technol. **26**, 105021 (2013).

[34] V. Mitin, L. Reggiani, and L. Varani, *Generation-Recombination Noise in Semiconductors*, in *Noise and fluctuations control in electronic devices*, edited by A. Balandin, American Scientific Publishers, 2002.

[35] C. M. Wilson, L. Frunzio, and D. E. Prober, *Time-resolved measurements of thermodynamic fluctuations of the particle number in a nondegenerate Fermi gas*, Phys. Rev. Lett. **87**, 067004 (2001).

[36] C. M. Wilson and D. E. Prober, *Quasiparticle number fluctuations in superconductors*, Phys. Rev. B **69**, 094524 (2004).

[37] C. M. Wilson, *Optical/UV Single Photon Spectrometers using Superconducting Tunnel Junctions*, PhD thesis, Yale University, 2002.

[38] K. M. van Vliet and J. R. Fassett, *Fluctuations due to electronic transitions and transport in solids*, in *Fluctuation phenomena in solids*, edited by R. E. Burgess, Academic, New York, 1965.

[39] A. Rothwarf and B. N. Taylor, *Measurement of Recombination Lifetimes in Superconductors*, Phys. Rev. Lett. **19**, 27 (1967).

[40] R. Barends, J. J. A. Baselmans, S. J. C. Yates, J. R. Gao, J. N. Hovenier, and T. M. Klapwijk, *Quasiparticle relaxation in optically excited high-Q superconducting resonators*, Phys. Rev. Lett. **100**, 257002 (2008).

[41] K. M. van Vliet, *Nonthermal Equilibrium Fluctuations of Electrons and Holes*, Phys. Rev. **133**, A1182 (1964).

[42] M. Lax, *Fluctuations from the Nonequilibrium Steady State*, Rev. Mod. Phys. **32**, 25 (1960).

[43] S. Sridhar and J. E. Mercereau, *Nonequilibrium dynamics of quasiparticles in superconductors*, Phys. Rev. B **34**, 203 (1986).

[44] R. V. Carlson and A. M. Goldman, *Propagating Order-Parameter Collective Modes in Superconducting Films*, Phys. Rev. Lett. **34**, 11 (1975).

[45] A. Schmid and G. Schön, *Collective Oscillations in a Dirty Superconductor*, Phys. Rev. Lett. **34**, 941 (1975).

[46] A. V. Sergeev, V. V. Mitin, and B. S. Karasik, *Ultrasensitive hot-electron kinetic-inductance detectors operating well below the superconducting transition*, Appl. Phys. Lett. **80**, 817 (2002).

[47] G. M. Eliashberg, *Film superconductivity stimulated by a high-frequency field*, JETP Lett. **11**, 114 (1970).

[48] B. I. Ivlev, S. G. Lisitsyn, and G. M. Eliashberg, *Nonequilibrium excitations in superconductors in high-frequency fields*, J. Low Temp. Phys. **10**, 449 (1973).

[49] J. E. Mooij and T. M. Klapwijk, *Nonlinear electrodynamics in microwave-stimulated superconductivity*, Phys. Rev. B **27**, 3054 (1983).

[50] A. F. G. Wyatt, V. M. Dmitriev, W. S. Moore, and F. W. Sheard, *Microwave-Enhanced Critical Supercurrents in Constricted Tin Films*, Phys. Rev. Lett. **16**, 1166 (1966).

[51] A. H. Dayem and J. J. Wiegand, *Behavior of Thin-Film Superconducting Bridges in a Microwave Field*, Phys. Rev. **155**, 419 (1967).

[52] T. M. Klapwijk and J. E. Mooij, *Microwave-enhanced superconductivity in aluminium films*, Physica B+C **81**, 132 (1976).

[53] T. M. Klapwijk, J. N. van den Bergh, and J. E. Mooij, *Radiation-stimulated superconductivity*, J. Low Temp. Phys. **26**, 385 (1977).

[54] T. M. Klapwijk, *Superconducting microbridges and radiation-stimulated superconductivity*, PhD thesis, Technische Hogeschool Delft, 1977.

[55] J. E. Mooij, N. Lambert, and T. M. Klapwijk, *T_c enhancement!*, Solid State Comm. **36**, 585 (1980).

[56] T. Kommers and J. Clarke, *Measurement of Microwave-Enhanced Energy Gap in Superconducting Aluminum by Tunneling*, Phys. Rev. Lett. **38**, 1091 (1977).

[57] R. E. Horstman and J. Wolter, *Gap enhancement in narrow superconducting tunneljunctions induced by homogeneous microwave currents*, Phys. Lett. **82A**, 43 (1981).

[58] J. A. Pals, K. Weiss, P. M. T. M. van Attekum, R. E. Horstman, and J. Wolter, *Non-equilibrium superconductivity in homogeneous thin films*, Phys. Rep. **89**, 324 (1982).

[59] J. Wolter and R. E. Horstman, *Determination of the quasiparticle energy distribution in superconducting tunneljunctions under microwave irradiation*, Phys. Lett. **86A**, 185 (1981).

[60] J.-J. Chang and D. J. Scalapino, *Gap enhancement in superconducting thin films due to microwave irradiation*, J. Low Temp. Phys. **29**, 477 (1977).

[61] J.-J. Chang and D. Scalapino, *Nonequilibrium superconductivity*, J. Low Temp. Phys. **31**, 1 (1978).

[62] D. J. Goldie and S. Withington, *Non-equilibrium superconductivity in quantum-sensing superconducting resonators*, Supercond. Sci. Technol. **26**, 015004 (2013).

[63] P. Santhanam and D. E. Prober, *Inelastic electron scattering mechanisms in clean aluminum films*, Phys. Rev. B **29**, 3733 (1984).

[64] T. M. Klapwijk, P. A. van der Plas, and J. E. Mooij, *Electron-electron scattering in dirty three-dimensional aluminum films*, Phys. Rev. B **33**, 1474 (1986).

[65] S. E. Thompson, S. Withington, D. J. Goldie, and C. N. Thomas, *Dynamical behaviour of superconducting microresonators with readout-power heating*, Supercond. Sci. Technol. **26**, 095009 (2013).

[66] J. Bardeen, *Critical fields and currents in superconductors*, Rev. Mod. Phys. **34**, 667 (1962).

[67] A. Anthore, H. Pothier, and D. Esteve, *Density of states in a superconductor carrying a supercurrent*, Phys. Rev. Lett. **90**, 127001 (2003).

[68] K. D. Usadel, *Generalized Diffusion Equation for Superconducting Alloys*, Phys. Rev. Lett. **25**, 507 (1970).

[69] J. R. Clem, *Inductances and attenuation constant for a thin-film superconducting coplanar waveguide resonator*, J. Appl. Phys **113**, 013910 (2013).

[70] J. Romijn, T. M. Klapwijk, M. J. Renne, and J. E. Mooij, *Critical pair-breaking current in superconducting aluminum strips far below* T_c, Phys. Rev. B **26**, 3648 (1982).

[71] B. H. Eom, P. K. Day, H. G. LeDuc, and J. Zmuidzinas, *A wideband, low-noise superconducting amplifier with high dynamic range*, Nature Phys. **8**, 623 (2012).

[72] A. G. Kozorezov, A. F. Volkov, J. K. Wigmore, A. Peacock, A. Poelaert, and R. den Hartog, *Quasiparticle-phonon downconversion in nonequilibrium superconductors*, Phys. Rev. B **61**, 11807 (2000).

[73] D. J. Goldie, *Non-equilibrium Superconductivity in Kinetic Inductance Detectors for THz Photon Sensing*, 24th International Symposium on Space Terahertz Technology, 2013, This work has recently been extended: T. Guruswamy, D. J. Goldie, S. Withington, *Quasiparticle generation efficiency in superconducting thin-films*, a preprint of which is available at http://arxiv.org/abs/1401.1937.

[74] S. J. C. Yates, J. J. A. Baselmans, A. Endo, R. M. J. Janssen, L. Ferrari, P. Diener, and A. M. Baryshev, *Photon noise limited radiation detection with lens-antenna coupled microwave kinetic inductance detectors*, Appl. Phys. Lett. **99**, 073505 (2011).

[75] R. W. Boyd, *Photon bunching and the photon-noise-limited performance of infrared detectors*, Infrared Phys. **22**, 157 (1982).

[76] J. J. A. Baselmans and S. J. C. Yates, *Long quasiparticle lifetime in Aluminium Microwave Kinetic Inductance Detectors using coaxial stray light filters*, AIP Conference Proceedings **1185**, 160 (2009).

[77] R. Barends, J. Wenner, M. Lenander, Y. Chen, R. C. Bialczak, J. Kelly, E. Lucero, P. O'Malley, M. Mariantoni, D. Sank, H. Wang, T. C. White, Y. Yin, J. Zhao, A. N. Cleland, J. M. Martinis, and J. J. A. Baselmans, *Minimizing quasiparticle generation from stray infrared light in superconducting quantum circuits*, Appl. Phys. Lett. **99**, 113507 (2011).

[78] J. Baselmans, S. Yates, P. Diener, and P. de Visser, *Ultra low background cryogenic test facility for far-infrared radiation detectors*, J. Low Temp. Phys. **167**, 360 (2012).

[79] J. Clarke and F. K. Wilhelm, *Superconducting quantum bits*, Nature **453**, 1031 (2008).

[80] D. Rainis and D. Loss, *Majorana qubit decoherence by quasiparticle poisoning*, Phys. Rev. B **85**, 174533 (2012).

[81] B. van Heck, A. R. Akhmerov, F. Hassler, M. Burrello, and C. W. J. Beenakker, *Coulomb-assisted braiding of Majorana fermions in a Josephson junction array*, New Journal of Physics **14**, 035019 (2012).

[82] J. Aumentado, M. W. Keller, J. M. Martinis, and M. H. Devoret, *Nonequilibrium quasiparticles and 2e periodicity in single-Cooper-pair transistors*, Phys. Rev. Lett. **92**, 066802 (2004).

[83] A. J. Ferguson, N. A. Court, F. E. Hudson, and R. G. Clark, *Microsecond resolution of quasiparticle tunneling in the single-Cooper-pair transistor*, Phys. Rev. Lett. **97**, 106603 (2006).

[84] B. S. Palmer, C. A. Sanchez, A. Naik, M. A. Manheimer, J. F. Schneiderman, P. M. Echternach, and F. C. Wellstood, *Steady-state thermodynamics of nonequilibrium quasiparticles in a Cooper-pair box*, Phys. Rev. B **76**, 054501 (2007).

[85] M. D. Shaw, R. M. Lutchyn, P. Delsing, and P. M. Echternach, *Kinetics of nonequilibrium quasiparticle tunneling in superconducting charge qubits*, Phys. Rev. B **78**, 024503 (2008).

[86] J. M. Martinis, M. Ansmann, and J. Aumentado, *Energy decay in superconducting Josephson-junction qubits from nonequilibrium quasiparticle excitations*, Phys. Rev. Lett. **103**, 097002 (2009).

[87] M. Lenander, H. Wang, R. C. Bialczak, E. Lucero, M. Mariantoni, M. Neeley, A. D. O'Connell, D. Sank, M. Weides, J. Wenner, T. Yamamoto, Y. Yin, J. Zhao, A. N. Cleland, and J. M. Martinis, *Measurement of energy decay in superconducting qubits from nonequilibrium quasiparticles*, Phys. Rev. B **84**, 024501 (2011).

[88] G. Catelani, J. Koch, L. Frunzio, R. J. Schoelkopf, M. H. Devoret, and L. I. Glazman, *Quasiparticle relaxation of superconducting qubits in the presence of flux*, Phys. Rev. Lett. **106**, 077002 (2011).

[89] A. D. Córcoles, J. M. Chow, J. M. Gambetta, C. Rigetti, J. R. Rozen, G. A. Keefe, M. B. Rothwell, M. B. Ketchen, and M. Steffen, *Protecting superconducting qubits from radiation*, Appl. Phys. Lett. **99**, 181906 (2011).

[90] D. Ristè, C. C. Bultink, M. J. Tiggelman, R. N. Schouten, K. W. Lehnert, and L. DiCarlo, *Millisecond charge-parity fluctuations and induced decoherence in a superconducting transmon qubit*, Nature Comm. **4**, 1913 (2013).

[91] O.-P. Saira, A. Kemppinen, V. F. Maisi, and J. P. Pekola, *Vanishing quasiparticle density in a hybrid Al/Cu/Al single-electron transistor*, Phys. Rev. B **85**, 012504 (2012).

[92] H. Paik, D. I. Schuster, L. S. Bishop, G. Kirchmair, G. Catelani, A. P. Sears, B. R. Johnson, M. J. Reagor, L. Frunzio, L. Glazman, and R. J. Schoelkopf, *Observation of high coherence in Josephson junction qubits measured in a three dimensional circuit QED architecture*, Phys. Rev. Lett. **107**, 240501 (2011).

[93] M. Reagor, H. Paik, G. Catelani, L. Sun, C. Axline, E. Holland, I. M. Pop, N. A. Masluk, T. Brecht, L. Frunzio, M. H. Devoret, L. Glazman, and R. J. Schoelkopf, *Reaching 10 ms single photon lifetimes for superconducting aluminum cavities*, Appl. Phys. Lett. **102**, 192604 (2013).

[94] P. K. Day, H. G. LeDuc, B. A. Mazin, A. Vayonakis, and J. Zmuidzinas, *A broadband superconducting detector suitable for use in large arrays*, Nature **425**, 817 (2003).

[95] A. Megrant, C. Neill, R. Barends, B. Chiaro, Y. Chen, L. Feigl, J. Kelly, E. Lucero, M. Mariantoni, P. J. J. O'Malley, D. Sank, A. Vainsencher, J. Wenner, T. C. White, Y. Yin, J. Zhao, C. J. Palmstrøm, J. M. Martinis, and A. N. Cleland, *Planar superconducting resonators with internal quality factors above one million*, Appl. Phys. Lett. **100**, 113510 (2012).

[96] R. Barends, S. van Vliet, J. J. A. Baselmans, S. J. C. Yates, J. R. Gao, and T. M. Klapwijk, *Enhancement of quasiparticle recombination in Ta and Al superconductors by implantation of magnetic and nonmagnetic atoms*, Phys. Rev. B **79**, 020509(R) (2009).

[97] G. Vardulakis, *Superconducting Kinetic Inductance Detectors, Theory, Simulations & Experiments*, PhD thesis, University of Cambridge, 2007.

[98] R. P. S. M. Lobo, J. D. LaVeigne, D. H. Reitze, D. B. Tanner, Z. H. Barber, E. Jacques, P. Bosland, M. J. Burns, and G. L. Carr, *Photoinduced time-resolved electrodynamics or superconducting metals and alloys*, Phys. Rev. B **72**, 024510 (2005).

[99] H. G. Leduc, B. Bumble, P. K. Day, B. H. Eom, J. Gao, S. Golwala, B. A. Mazin, S. McHugh, A. Merrill, D. C. Moore, O. Noroozian, A. D. Turner, and J. Zmuidzinas, *Titanium nitride films for ultrasensitive microresonator detectors*, Appl. Phys. Lett. **97**, 102509 (2010).

[100] E. F. C. Driessen, P. C. J. J. Coumou, R. R. Tromp, P. J. de Visser, and T. M. Klapwijk, *Strongly Disordered TiN and NbTiN s-Wave Superconductors Probed by Microwave Electrodynamics*, Phys. Rev. Lett. **109**, 107003 (2012).

[101] P. C. J. J. Coumou, M. R. Zuiddam, E. F. C. Driessen, P. J. de Visser, J. J. A. Baselmans, and T. M. Klapwijk, *Microwave Properties of Superconducting Atomic-Layer Deposited TiN Films*, IEEE Trans. Appl. Supercond. **23**, 7500404 (2013).

[102] M. R. Vissers, J. Gao, J. S. Kline, M. Sandberg, M. P. Weides, D. S. Wisbey, and D. P. Pappas, *Characterization and in-situ monitoring of sub-stoichiometric adjustable superconducting critical temperature titanium nitride growth*, Thin Solid Films **548**, 485 (2013).

[103] B. Sacépé, C. Chapelier, T. I. Baturina, V. M. Vinokur, M. R. Baklanov, and M. Sanquer, *Disorder-induced inhomgeneities of the superconducting state close to the superconductor-insulator transition*, Phys. Rev. Lett. **101**, 157006 (2008).

[104] P. C. J. J. Coumou, E. F. C. Driessen, J. Bueno, C. Chapelier, and T. M. Klapwijk, *Electrodynamic response and local tunneling spectroscopy of strongly disordered superconducting TiN films*, Phys. Rev. B **88**, 180505(R) (2013).

[105] J. Gao, M. R. Vissers, M. O. Sandberg, F. C. S. da Silva, S. W. Nam, D. P. Pappas, D. S. Wisbey, E. C. Langman, S. R. Meeker, B. A. Mazin, H. G. Leduc, J. Zmuidzinas, and K. D. Irwin, *A titanium-nitride near-infrared kinetic inductance photon-counting detector and its anomalous electrodynamics*, Appl. Phys. Lett. **101**, 142602 (2012).

[106] J. Gao, J. Zmuidzinas, B. A. Mazin, H. G. LeDuc, and P. K. Day, *Noise properties of superconducting coplanar waveguide microwave resonators*, Appl. Phys. Lett. **90**, 102507 (2007).

[107] R. Barends, H. L. Hortensius, T. Zijlstra, J. J. A. Baselmans, S. J. C. Yates, J. R. Gao, and T. M. Klapwijk, *Noise in NbTiN, Al and Ta superconducting resonators on silicon and sapphire substrates*, IEEE Trans. on Appl. Supercond. **19**, 936 (2009).

[108] J. Gao, M. Daal, J. M. Martinis, A. Vayonakis, J. Zmuidzinas, B. Sadoulet, B. A. Mazin, P. K. Day, and H. G. Leduc, *A semiempirical model for two-level system noise in superconducting microresonators*, Appl. Phys. Lett. **92**, 212504 (2008).

[109] O. Noroozian, J. Gao, J. Zmuidzinas, H. G. LeDuc, and B. A. Mazin, *Two-level system noise reduction for Microwave Kinetic Inductance Detectors*, AIP Conference Proceedings **1185**, 148 (2009).

[110] R. Barends, N. Vercruyssen, A. Endo, P. J. de Visser, T. Zijlstra, T. M. Klapwijk, P. Diener, S. J. C. Yates, and J. J. A. Baselmans, *Minimal resonator loss for circuit quantum electrodynamics*, Appl. Phys. Lett. **97**, 023508 (2010).

[111] R. Barends, N. Vercruyssen, A. Endo, P. J. de Visser, T. Zijlstra, T. M. Klapwijk, and J. J. A. Baselmans, *Reduced frequency noise in superconducting resonators*, Appl. Phys. Lett. **97**, 033507 (2010).

[112] J. Wenner, R. Barends, R. C. Bialczak, Y. Chen, J. Kelly, E. Lucero, M. Mariantoni, A. Megrant, P. J. J. O'Malley, D. Sank, A. Vainsencher, H. Wang, T. C. White, Y. Yin, J. Zhao, A. N. Cleland, and J. M. Martinis, *Surface loss simulations of superconducting coplanar waveguide resonators*, Appl. Phys. Lett. **99**, 113513 (2011).

[113] M. R. Vissers, J. Gao, D. S. Wisbey, D. A. Hite, C. C. Tsuei, A. D. Corcoles, M. Steffen, and D. P. Pappas, *Low loss superconducting titanium nitride coplanar waveguide resonators*, Appl. Phys. Lett. **97**, 232509 (2010).

[114] M. R. Vissers, J. S. Kline, J. Gao, D. S. Wisbey, and D. P. Pappas, *Reduced microwave loss in trenched superconducting coplanar waveguides*, Appl. Phys. Lett. **100**, 082602 (2012).

[115] S. Kumar, J. Gao, J. Zmuidzinas, B. A. Mazin, H. G. LeDuc, and P. K. Day, *Temperature dependence of the frequency and noise of superconducting coplanar waveguide resonators*, Appl. Phys. Lett. **92**, 123503 (2008).

[116] J. Gao, L. R. Vale, J. A. B. Mates, D. R. Schmidt, G. C. Hilton, K. D. Irwin, F. Mallet, M. Castellanos-Beltran, K. W. Lehnert, J. Zmuidzinas, and H. G. LeDuc, *Strongly quadrature-dependent noise in superconducting micro-resonators measured at the vacuum-noise limit*, Appl. Phys. Lett. **98**, 232508 (2011).

[117] C. Neill, A. Megrant, R. Barends, Y. Chen, B. Chiaro, J. Kelly, J. Y. Mutus, P. J. J. O'Malley, D. Sank, J. Wenner, T. C. White, Y. Yin, A. N. Cleland, and J. M. Martinis, *Fluctuations from edge defects in superconducting resonators*, Appl. Phys. Lett. **103**, 072601 (2013).

[118] S. Kogan, *Electronic Noise and Fluctuations in Solids*, Cambridge University Press, 1996.

[119] R. M. J. Janssen, J. J. A. Baselmans, A. Endo, L. Ferrari, S. J. C. Yates, A. M. Baryshev, and T. M. Klapwijk, *High optical efficiency and photon noise limited sensitivity of microwave kinetic inductance detectors using phase readout*, Appl. Phys. Lett. **103**, 203503 (2013).

Chapter 3

How to measure the intrinsic limits

3.1 Dark environment

A superconducting resonator is an extremely sensitive device, due to the low excitation energy of the superconductor and the high quality factors that can be reached in such a resonator. In Chapter 2, we have seen that aluminium has a low gap energy and long quasiparticle lifetime, and is as such an excellent material to detect very tiny signals. For example for space-based imaging with these devices, the required Noise Equivalent Power (NEP) is about 3×10^{-19} WHz$^{-1/2}$, corresponding to a radiation power of around 50 aW at 1.5 THz. In a laboratory test bed for those detectors one should be able to reach those conditions. Therefore any stray-light, in particular due to hotter stages of the setup, has to be reduced to a level well below the desired radiation power. In this section we describe how we achieve a dark environment to test the superconducting resonators [1]. Section 3.2 describes how a controlled photon source is introduced to measure the response to radiation. We discuss how radiation is received by the antenna and absorbed in the sensitive part of the detector. In Section 3.3 we review how the resonator response is related to the measured transmission of the embedding circuit. In Section 3.4 the measurement setup is presented and the analysis of the noise measurements is discussed. Section 3.5 provides an overview of the sample fabrication and mounting.

3.1.1 Cryostat

The cryogenic system is a pulse tube pre-cooled adiabatic demagnetisation refrigerator (ADR). The pulse tube cooler has an intermediate stage at 50 K and reaches a base temperature of 3.2 K. The ADR consists of a ferric ammonium alum (FAA) salt pill and a gadolinium gallium garnet (GGG) crystal, surrounded by superconducting wires to

---

Parts of this chapter were published as: Jochem Baselmans, Stephen Yates, Pascale Diener and Pieter de Visser, *Journal of Low Temperature Physics* **167**, 360-366 (2012); and as part of the supplementary information published with Chapters 7 and 8.

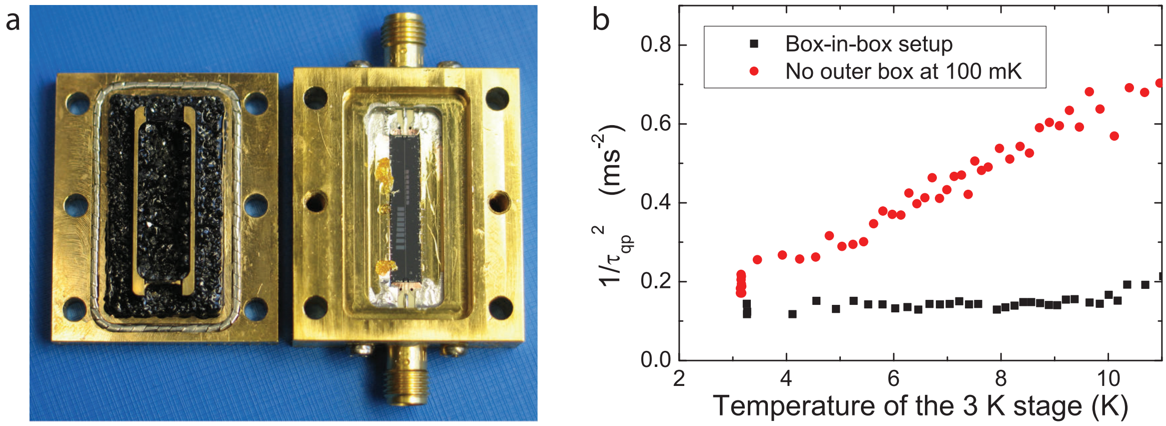

Figure 3.1: (a) Photograph of the sample holder for dark experiments. A sample with Al microwave resonators is mounted in the holder. The lid is coated with a layer of black epoxy with SiC grains and equipped with an EMI gasket. (b) $1/\tau_{qp}^2$ in an Al microwave resonator as a function of the temperature of the 3 K stage of the cryostat (τ_{qp} is the quasiparticle recombination time). The sample temperature was kept at 100 mK. The red dots are measurements with only the light-tight sample box and the coax cable filters. The black squares are measurements in the full box-in-box configuration. Figure from Ref. [1].

create a magnetic field that aligns the spins. Cooling occurs when the magnetic field is turned off and the spins start to randomise. The GGG crystal reaches a temperature of 450 mK after a recharge of the magnet, which slowly increases to about 800 mK at the end of the hold time. We call this stage the 500 mK stage. The GGG stage serves as an intermediate state towards the coldest stage (FAA), which can reach a temperature of 30 mK. The system is usually used at 100 mK, which increases the hold time of the ADR (to around 36 hours) and is low enough to measure the Al superconducting resonators. An outer cryoperm shield and an inner superconducting lead-tin coated shield are used to shield the sample from magnetic fields, especially from the high magnetic field that is needed to recharge the ADR. Both shields also surround the cable feed-throughs with tubes. The aspect ratio of those tubes is 3.5, high enough to not limit the shielding.

3.1.2 Box-in-box configuration

In early experiments on Al superconducting resonators in the ADR system, the measured quasiparticle recombination time at low temperature saturates at around 400 μs [2]. In these experiments no care was taken to shield the sample from radiation from the 3 K stage. If the sample is kept at 100 mK, but the outer stage is heated by switching of the pulse-tube cooler, the quasiparticle recombination time changes drastically (it decreases a factor 5 from 3 K to 9 K), showing its sensitivity to the environment.

A first improvement was achieved by coating the inside of the sample holder with absorber consisting of black Stycast 2850FT with 1 mm SiC grains. All holes and slits in the sample box were covered with Al tape. This improved the recombination time to about 1 ms and showed a shallower slope when measured as a function of the temperature of the 3 K stage. A second change involved the use of light absorbing labyrinths and an EMI gasket between the sample holder and its lid (Fig. 3.1a). The lid is coated on the inner side with an approximately 3 mm thick layer of carbon loaded epoxy with 1 mm SiC grains [3]. The absorber layer needs to be thick enough to absorbed the radiation of the lowest frequency that is able to break Cooper pairs (90 GHz for Al, a wavelength of 3.8 mm). To eliminate stray light entering through the coax cables that are used for the microwave measurements, homemade coax cable filters were designed, which are described in detail below.

The measured recombination time with this sample box and the coax cable filters in place is shown in Fig. 3.1b as red dots. All of these actions did not completely remove the response of the quasiparticle recombination time to a changing 3 K stage temperature. Therefore an additional box was introduced at 100 mK, to surround the sample box. This box-in-box concept essentially creates a 100 mK environment for the sample box instead of the previous 3 K environment [1]. Fig. 3.3 shows the box-in-box configuration for optical experiments. Both the outer box and the inner sample box are made out of gold plated copper. For the dark measurements the box at 100 mK is closed with a lid which is equipped with labyrinths filled with carbon loaded epoxy, which consists of 3% by weight carbon powder in Epotek-920 epoxy. The lid is coated on the inner side with a similar 3 mm layer of carbon loaded epoxy as the lid of the sample box. A separate labyrinth with carbon-loaded epoxy is used to introduce a 2 mm diameter hole to be able to evacuate the box. The coaxial cables for the microwave measurements enter the light-tight box through coax cable filters that are glued into the box with silver loaded epoxy. All the dark measurements presented in this thesis were performed in this box-in-box configuration.

Coax cable filters

The coax cable filters are homemade and consist of a 2 mm inner diameter gold plated Cu tube with a 0.25 mm diameter Cu wire as the central connector. The dielectric consists of a mixture of 15 grams of black Stycast with 1.2 gram of 24LV catalyst and 2.8 grams of bronze powder with 0.5 μm diameter particles from Canano Technologies. Sub-micron bronze powder is expected to give a cut-off frequency in the GHz range [4]. To fabricate the filter we use a microwave cable connector (Radiall R125.055.000) on one side and a 90 degree SMA panel launcher (Radiall R125.462.001W) on the other side. To insert the dielectric, the first connector is mounted and the central Cu wire is put under tension to keep it centred. The dielectric mixture is injected using a syringe. The Stycast-bronze powder ratio was optimised to give a dielectric constant of 6.22, which gives a 50 Ω characteristic impedance of the filter. A photograph of the result is shown in Fig. 3.2a. The measured transmission of the filter at room temperature

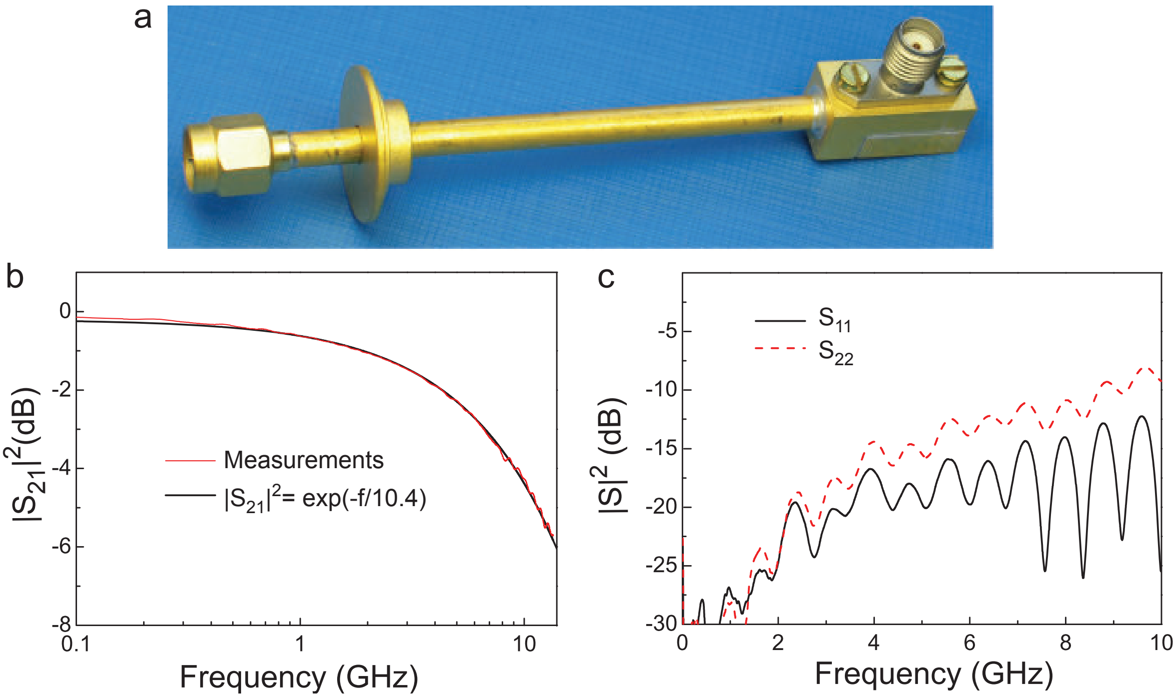

Figure 3.2: (a) Measured transmission $|S_{21}|^2$ as a function of frequency of one of the coax cable filters. The data can be fitted with a single exponential decay. (b) Reflection at both ends of the filter, $|S_{11}|^2$ and $|S_{22}|^2$ as a function of frequency. Port 1 is the 90 degree connector at the right, which is mounted in the light-tight box. Port 2 corresponds to the left connector.

is shown in Fig. 3.2b. The result can be fitted with a single exponential decay with a characteristic frequency of 10.4 GHz. If we extrapolate the result, the attenuation at 90 GHz is -38 dB, which indicates that stray-light that can break Cooper pairs is attenuated very efficiently. The reflection of the microwave signal in the frequency range of interest is lower than -10 dB as shown in Fig. 3.2c.

LED-pulse excitation

The quasiparticle recombination time can be experimentally probed using either a measurement of quasiparticle fluctuations or by measuring the decay after a pulsed excitation. The first method is most reliable (Chapter 5), but so far quasiparticle fluctuations have only been measured in Al devices. Next to that it is useful to compare the results of both methods. For the pulse-method we use a fast LED pulse from a GaAsP LED (HP5082-440, 655 nm or 1.9 eV), the light of which is guided towards the sample with an optical fibre. The LED is mounted at the 3 K stage of the cryostat. The light is coupled to a 40 cm long, 0.5 mm diameter PMMA (Polymethylmethacrylaat or Perspex) fibre. Care has to be taken not to create a stray-light leak through the fibre. The fibre is therefore taped to the outer 100 mK box over a length of 20 cm to allow for a good thermalisation. The fibre attenuates radiation around 1 THz efficiently, with an absorption coefficient of 10 cm^{-1}, but becomes less effective down to 100 GHz, around the gap edge of Al is (< 0.1 cm^{-1}) [5]. A review of 100 GHz - 1 THz properties of various materials can be found in Ref. [6]. To reject radiation below those frequencies the fibre ends in front of a 150 μm diameter hole in the lid of the outer box. This hole acts as a waveguide with a high-pass waveguide cut-off at 1.2 THz for the mode with the lowest frequency. For this TE_{11} mode the cut-off frequency is $f_{cut-off} = \frac{1.84c}{2\pi r}$, with c the speed of light and r the radius [7]. A short piece of identical fibre is mounted on the other side of the waveguide and fed into the sample holder, ending directly above the sample.

3.1.3 Verification

To test the system, a chip with Al resonators is mounted into the sample holder, a photograph of which is shown in Fig. 3.1a. The resonators are halfwave coplanar waveguide resonators patterned in a sputter-deposited 50 nm Al film, similar to those used in Chapter 5. The quasiparticle recombination time is measured with the LED-pulse method as a function of the temperature of the 3 K stage, while the sample and light-tight box are kept at 100 mK. The measured quasiparticle recombination time is shown in Fig. 3.1b. We observe that the recombination time does not change with increasing 3 K stage temperature, which demonstrates that the box-in-box configuration effectively shields stray light [1]. For comparison the data from the same measurement without the outer 100 mK box are shown as red dots in Fig. 3.1b, which shows a clear temperature dependence (here the light-tight sample box and the coax cable filters were already installed).

From the measurements of the quasiparticle recombination time and the number of quasiparticles presented in Chapter 6, we can estimate an upper bound for the stray-light level in the setup. From measurements of quasiparticle fluctuations we obtain $\tau_{qp} = 3.5$ ms and $N_{qp} = 17\times10^4$ at 100 mK (Fig. 6.3), corresponding to a quasiparticle density $n_{qp} = 17$ $\mu\mathrm{m}^{-3}$. In these measurements the 3 K stage temperature was constant at 3.2 K. Using Equation 2.45, the absorbed power to maintain this quasiparticle number is 0.2 fW. Note that in this experiment N_{qp} was limited by microwave power absorption, there was no sign of saturation due to stray light. The upper bound is thus limited by the sensitivity of the detector. If we assume that stray-light is only generated by the 3 K stage of the setup we can improve the estimate of the maximum stray-light power. In Fig. 3.1b the recombination time is constant up to 10 K. Based on the measurement without the outer box (red dots in Fig. 3.1b), the absorbed stray light power scales linearly with temperature ($1/\tau_{qp}^2 \propto P_{abs}$), which results in an upper limit of 0.06 fW of stray light at 3.2 K. However there is no saturation in the measured lifetime as a function of microwave readout power (Figs. 6.3 and 7.5), which suggest that the stray-light power is much smaller than 0.06 fW. Note that the linear dependence we observe in the absorbed power in the detector (Fig. 3.2b) is the result of a complex combination of radiating parts with different emissivity and a frequency dependent absorption of the black epoxy layers (they absorb more efficiently at higher frequencies).

The same sample was measured as well in a dilution refrigerator, which has an additional shield at its base temperature (10 mK). In that system also a τ_{qp} of 3 ms was measured. In the same fridge measurements on quasiparticle tunnelling in qubits showed that $n_{qp} < 0.04\ \mu\text{m}^{-3}$ [8], two orders of magnitude lower than what our device can measure, which indicates that the main stray light problem is solved by a shield at the base temperature. A box-in-box configuration similar to ours was used in Ref. [9] in an ADR cryostat to eliminate the effect of stray light on qubits and resonators, where the stray-light induced quasiparticle density was reduced to $n_{qp} < 0.2\ \mu\text{m}^{-3}$.

3.2 Controlled terahertz characterisation

To measure the response and sensitivity of the detector to radiation, the device has to be exposed to that radiation. In a cryogenic setup the most convenient way to irradiate the detector is to use a cryogenic blackbody with a variable temperature, combined with filters to select the frequency band of interest. There are two main requirements to the setup. Firstly the radiation frequency should be well defined, which requires the out-of-band rejection of the filters to be good enough to filter the undesired frequencies. Secondly, only this radiation should reach the sample, thus the stray light rejection discussed in the previous section is required. These requirements can be tested by studying the response as a function of absorbed power and by comparing the optical efficiency with a simulation of the lens-antenna system. The following discussion of the setup focuses on the experimental characterisation of an aluminium microwave resonator irradiated with photons in a band around 1.54 THz, the main results of which are discussed in Chapter 7.

3.2.1 Experimental definition of the 1.54 THz band

The setup is based upon the same box-in-box configuration described above, but now with access to a thermal photon source through a series of filters, as shown in Fig. 3.3a. The photon source used in the experiment is a blackbody radiator, which is formed by a 2.5 mm thick, 40 mm diameter copper cone, coated with carbon loaded epoxy (EPOTEK 920 1LB part A, with 3% by weight carbon black and 3% by weight EPOTEK 920 1LB part B), which is covered with 1 mm SiC grains. The cone is coupled to the 3 K stage with a 18 mm long 0.3 mm diameter Cu wire to increase the speed of the blackbody. The blackbody is heated with three resistors to increase the uniformity of the temperature profile. The temperature of the blackbody is varied in the experiment from 3.2 - 25 K. 3.2 K is the minimum base temperature of the pulse tube cooler. There are three stacks of metal-mesh filters, with eight filters in total (QMC Instruments, Cardiff), the characteristics of which are shown in Fig. 3.3b. The

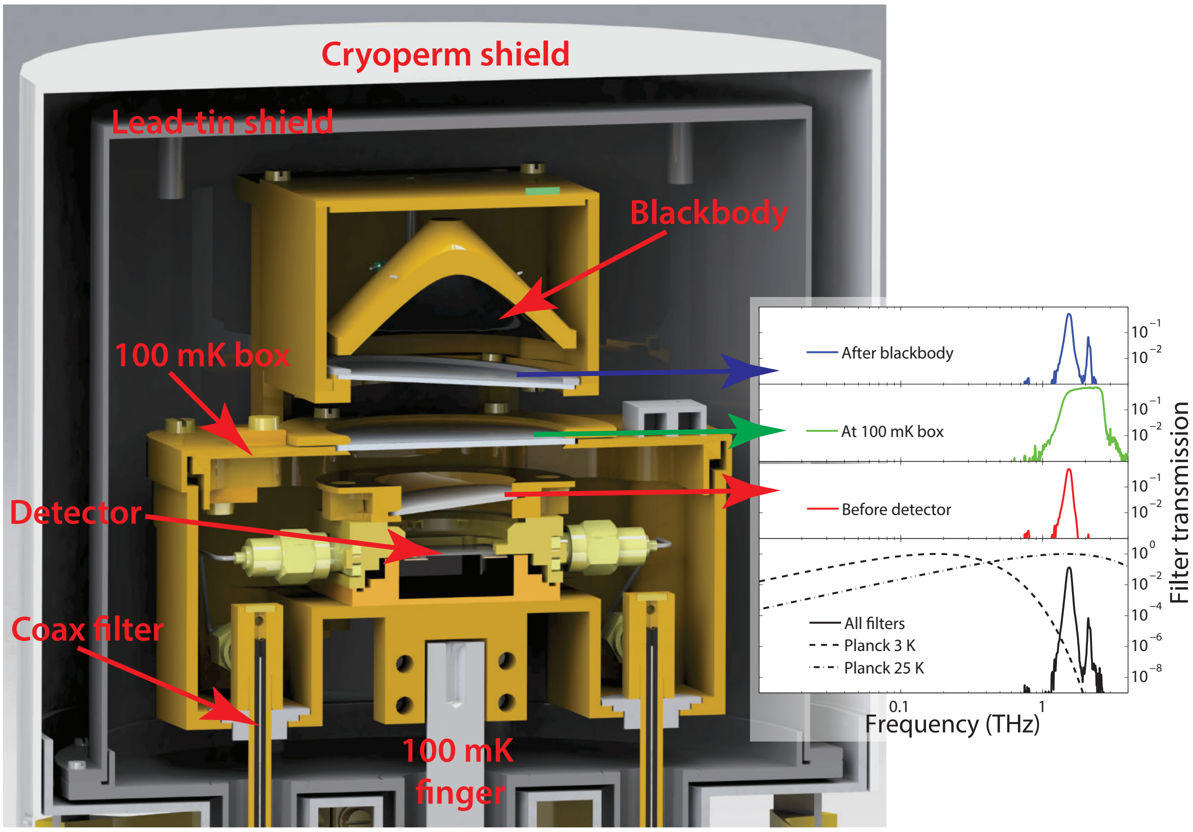

Figure 3.3: (a) A cross-section of the measurement setup, including the optical filters and blackbody. (b), Filter transmission characteristics of the three stacks of optical filters in the setup. The first and third set have a low-pass, a band pass and a high-pass filter. The second set (which closes the outer 100 mK box) has only a high- and a low-pass filter. The bottom panel shows the total transmission of these eight filters. The dashed and dash-dotted curves are the normalised spectral radiance (Planck's law) at blackbody temperatures of 3 and 25 K.

measured transmission of the whole filter stack as a function of optical frequency, $\Theta(F)$, is shown in Fig. 3.3b (bottom panel).

Since there is no aperture limitation in between the blackbody and the detector, the optical throughput is assumed to be $\lambda^2 = (c/F)^2$, with λ the wavelength and c the speed of light. We assume a single-mode detector. The total radiation power that arrives in front of the lens of the detector can now be calculated by numerically integrating Planck's law over the throughput and the measured filter characteristic at each blackbody temperature T_{BB}. The radiation power is here given for one polarisation.

$$P_{rad}(T_{BB}) = \int_0^\infty \frac{\Theta(F) hF dF}{\exp(hF/k_b T_{BB}) - 1}, \tag{3.1}$$

where h is Planck's constant and k_B Boltzmann's constant. The optical window around 1.54 THz, together with the blackbody temperature range of 3-25 K gives a large tuning range in radiation power, more than eight orders of magnitude, as shown in Fig. 3.4a.

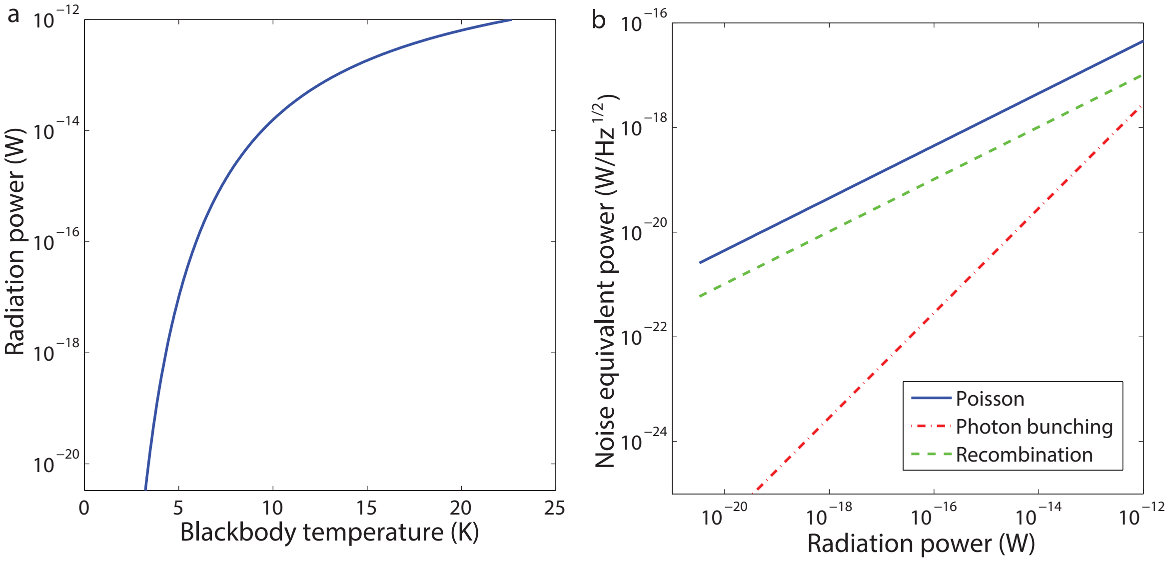

Figure 3.4: **a**, Radiation power in the filter transmission band as a function of blackbody temperature. **b**, The noise equivalent power as a function of radiation power. The three lines are the contributions to the optical NEP due to the Poisson statistics of the photon stream, due to the photon bunching statistics, and due to the random recombination of quasiparticles.

With the present device, we can verify the radiation power down to 0.1 fW using the measured quasiparticle recombination time (Chapter 7). The filtering of the out-of-band blackbody radiation is only sufficient with all three filter stacks installed. We have performed several experiments without the last filter (before the detector). In those experiments we see evidence for heating of the 100 mK box filter, which is reradiating its absorbed power. The experiments are described in detail in Bueno et al. [10].

The radiation power, calculated by Eq. 3.1, allows to calculate the different contributions to the noise equivalent power. The photon-noise NEP is given by

$$NEP_{photon} = \sqrt{\frac{2P_{rad}hF + 2P_{rad}hF\eta_{opt}B + 2\Delta P_{rad}/\eta_{pb}}{\eta_{opt}}}, \tag{3.2}$$

where the first term is due to the Poisson statistics of the photon stream, the second term due to photon bunching (giving a correction to Poisson statistics) and the third term is the recombination noise of the quasiparticles. $B = 1/(\exp(hF/k_BT_{BB}) - 1)$ is the mode occupation [11], which also depends on the blackbody temperature. η_{opt} is the optical efficiency, the fraction of power that is absorbed in the detector. For multi-mode absorption the optical efficiency and occupation of each mode have to be included. The second term in Eq. 3.2 is much smaller than the Poisson term over the whole range of measured powers, as shown in Fig. 3.4b. The third term, the recombination noise, is also shown in Fig. 3.4b, which shows that the contribution due to recombination noise is small compared to photon noise, as discussed in the main article. The lines in Fig. 3.4b are calculated with $\eta_{opt} = 100\%$. In the experiment in Chapter 7 $\eta_{opt} = 48\%$.

The photon-bunching contribution depends much stronger on power than the term due to Poisson statistics. Interestingly, the optical efficiency η_{opt} drops out of the NEP equation if $\eta_{opt}B >> 1$. This situation occurs at much higher powers than we are interested in (above 1 nW), but it would be easier to obtain at lower frequencies.

Right in front of the detector, after the last optical filter, we place a polariser to select the polarization for which the antenna is designed. The polariser consists of a copper wire grid on top of a 1.5 μm thick Mylar film. The grid lines are 10 μm wide and the spacing between the lines is 20 μm.

3.2.2 1.54 THz antenna-lens system

The radiation power is focused by an elliptical silicon lens of 2 mm in diameter onto the antenna, which is in the second focus of the lens [13]. A schematic of the lens is shown in Fig. 3.5a. The major and minor axis of the ellipse are $b = 1.037$ mm and $a = 0.992$ mm respectively, and $c = 0.303$ mm. The lens has an anti-reflection coating of 130 μm of Parylene C, with a refractive index of 1.62 [14]. The anti-reflection coating is not optimised for 1.54 THz as shown in Fig. 3.5c (we took a lens with a coating optimised for 350 GHz). The antenna is an in-line X-slot antenna, designed to receive radiation in a broad band around 1.54 THz as described in Ref. [12], which is shown in Fig. 3.5b. The antenna launches the radiation as a travelling wave onto the coplanar waveguide on both sides of the antenna. The antenna, with impedance Z_A, together with the transmission lines with characteristic impedance Z_0, can be represented in a circuit as shown in Fig. 3.5d [12]. We assume that all radiation will be absorbed in the waveguide, it will not be reflected back to the antenna, which is represented by matched loads on both sides. This assumption is verified in Section 3.2.3. Note that the antenna impedance should be twice Z_0 for optimal matching and power transfer.

To obtain the optical efficiency, a simulation in CST Microwave Studio is performed of the whole structure: the lens with the coating, the antenna and a piece of coplanar waveguide transmission line. The aperture is chosen to be 30 degrees, the angle from which the detector can see the blackbody (single side angle). The optical efficiency is shown as a function of frequency in Fig. 3.5c. The total efficiency is the multiplication of the front-to-back ratio, the spill over losses, the efficiency of an impedance mismatch between the antenna and the CPW line and the reflection losses at the anti-reflection coated lens surface. All together, we expect an efficiency of 48% for one polarisation in the filter transmission band around 1.54 THz, which is in good agreement with the measured optical efficiency of 48±8% (see Chapter 7). Note that this antenna was not designed to have a perfect optical efficiency, but to have a large bandwidth. The agreement of the measured optical efficiency with the CST-simulation shows that the power flow in the optical system is understood.

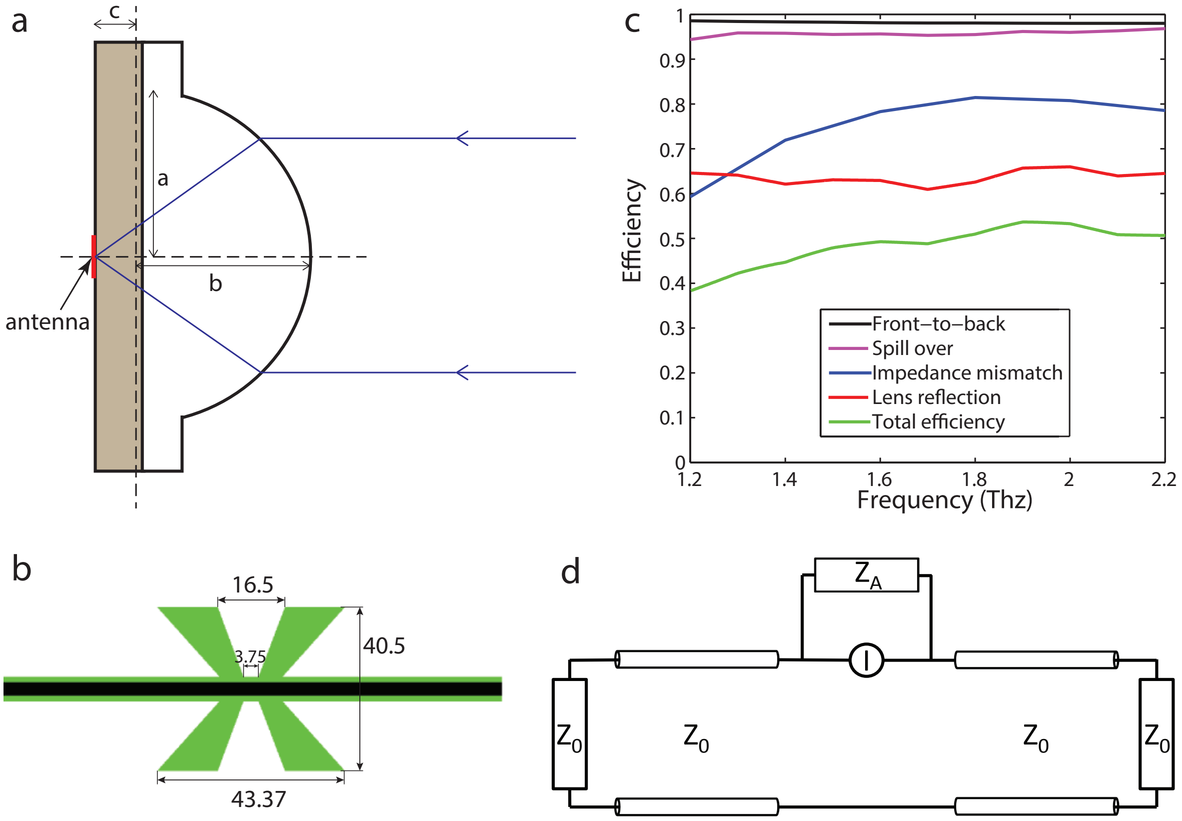

Figure 3.5: (a), Schematic of the extended elliptical lens with which radiation is focused onto the antenna. The white piece is made of the lens material (silicon), the grey area is the substrate which is glued onto the lens-array. The dimensions are given in the text. The dashed lines cross where the major and minor axes intersect. (b), A drawing of the in line X-slot antenna with short pieces of transmission line on both sides. The central line of the coplanar waveguide is shown in black, the groundplane in white and the substrate in green. The dimension are in μm. The width of the central line is 3 μm and the CPW slots are 1.5 μm wide. (c), The optical efficiency of the antenna-lens system as a function of frequency as calculated with CST Microwave Studio. The total efficiency is the multiplication of the front-to-back ratio, the spill over efficiency, the efficiency of an impedance mismatch between the antenna and the CPW line and the reflection losses at the anti-reflection coated lens surface. Simulation courtesy Nuria Llombart. (d), The equivalent circuit of the antenna and the coplanar waveguide transmission lines following Ref. [12]. The antenna is represented by its Norton equivalent circuit with impedance Z_A and a current source. It is coupled to a transmission line with characteristic impedance Z_0, which ends on both sides in a matched load Z_0.

3.2.3 Absorption of pair-breaking radiation in the resonator line

The assumption of a matched load in the circuit representation of the antenna-CPW system requires that the pair-breaking wave is absorbed completely before it can return to the antenna. Therefore we need to calculate the attenuation of the pair-breaking signal in the CPW waveguide. The attenuation constant α depends on the sheet resistance R_s, which can be calculated using the Mattis-Bardeen equations for the complex conductivity (Eqs. 2.11 and 2.12) together with Eq. 2.20, which was discussed in Section 2.5 for pair breaking radiation. We distinguish the sheet resistance of the central conductor $R_{s,c}$ and the groundplane $R_{s,g}$. The attenuation constant (of the wave amplitude) is given by [15, 16]

$$\alpha = \frac{R_{s,c}g_c + R_{s,g}g_g}{2Z_0}, \tag{3.3}$$

where g_c and g_g are the geometry factors for the central line and the ground plane respectively, which are presented as Eqs. 3.7 and 3.8. Z_0 is the characteristic impedance of the waveguide. We leave the discussion of those three parameters to the next section, to make that a complete treatment of the microwave properties of a CPW. We are now in the position to calculate the attenuation constant for the 1.54 THz radiation for the device presented in Chapter 7. The central strip of the CPW is $S = 3$ μm wide and the gaps are $W = 1.5$ μm wide. The energy gap is $\Delta = 188$ μeV. The central line is made of Al with $d = 50$ nm and $\rho_N = 2.2$ $\mu\Omega$cm, and the groundplanes of Al with $d = 100$ nm and $\rho_N = 0.28$ $\mu\Omega$cm. We calculate the sheet impedance at 1.54 THz (see Fig. 2.9), which results in $R_{s,c} = 0.46$ Ω, $R_{s,g} = 0.13$ Ω and $Z_0 = 51$ Ω. The attenuation constant is 1.5×10^3/m, which is more conventionally expressed as a power attenuation of 13 dB/mm (using $20 \cdot \log_{10}(\exp(-\alpha \cdot 1 \text{ mm}))$). The distance from the antenna to the end of the resonator is more than 4 mm on both sides, thus the assumption that all radiation from the antenna is absorbed is justified.

The relative absorption in the central line compared to the groundplane is given by $R_{s,c}g_c/(R_{s,c}g_c + R_{s,g}g_g)$, which is 90% for this particular device. There are two reasons why it is important that most of the pair-breaking radiation is absorbed in the central line. Firstly, within the typical recombination lifetime of quasiparticles in Al, quasiparticles can diffuse over several millimetres before recombination. Quasiparticles created in the groundplane will therefore be quickly lost from the responsive regime (approximately the microwave penetration depth). Therefore the central line of the resonator is isolated to confine the quasiparticles. Secondly, because of the different sheet resistances of the central line and groundplane, the microwave response of the central line is 20 times larger (see Section 3.3.1).

The approach to calculate the attenuation as presented in this section was verified using microwave simulations of the same structures in SONNET. To compare both methods the surface resistance in the normal state was taken (see Fig. 2.9). For various dimensions the agreement in the attenuation constant between the Sonnet simulations and the approach in this section is better than 0.5 dB/mm.

3.3 Microwave resonator and circuit

To measure the response of a microwave resonator it has to be embedded in a microwave circuit. In the experiments described in Chapters 5-8 we have used halfwave coplanar waveguide (CPW) resonators, which are capacitively coupled to a through transmission line, which is a CPW line as well. A photograph of such a resonator is shown in Fig. 5.1b. The resonator is 8-10 mm long and has two open ends as to isolate the central strip of the resonator from its groundplane. The advantage of using CPW resonators is that only one metal deposition step on top of a crystalline substrate is needed and the fabrication is therefore relatively easy. For microstrip resonators for example, one needs two metal depositions steps, and most importantly a deposited dielectric. Moreover, pair-breaking radiation can be coupled into the CPW using an antenna as explained in the previous section. Therefore the CPW detector and the structure that receives the radiation can be optimised independently.

In this section the impedance of the CPW resonator, the microwave transmission S_{21} and the internal power is derived, which shows how those quantities are related to the complex conductivity of the superconductor (Section 2.2.3). Such a derivation has been given before for quarterwave and in-line, halfwave resonators [17–20], but not explicitly for the capacitively coupled halfwave resonators used here. The results are similar up to numerical factors.

3.3.1 Coplanar waveguide

The resonant frequency of a distributed resonator, such as a CPW resonator, is determined by its length l and its phase velocity v_{ph}. The phase velocity is determined by the kinetic inductance L_k, geometric inductance L_g and capacitance C_l per unit length and given by $v_{ph} = 1/\sqrt{C_l(L_g + L_k)}$. A half wavelength resonator resonates at a wavelength $\lambda_{res} = 2l$. Using $\lambda_{res} = 2\pi v_{ph}/\omega_0$, the angular resonant frequency ω_0 is given by

$$\omega_0 = \frac{2\pi}{2l\sqrt{(L_g + L_k)C_l}}. \tag{3.4}$$

Note that the resonant frequency of a lumped element LC-resonator is different: $\omega_0 = 1/\sqrt{LC}$.

Along a CPW an electromagnetic field travels predominantly in the quasi transverse electromagnetic (quasi-TEM) mode. The current flows mainly at the edges of the central line and ground planes. The penetration of the current into the superconductor depends on the penetration depth, which was discussed in Section 2.4.5. In Fig. 2.8 we showed that the current in the groundplanes is equal and opposite to the current in the central line (even mode). The effective dielectric constant for a CPW is $\epsilon_{eff} \approx (1+\epsilon_{subs})/2$, approximately half the dielectric constant of the substrate. The capacitance and the geometric inductance per unit length for a CPW with central line width S and slots of width W are then given by [15]

$$L_g = \frac{\mu_0}{4}\frac{K(k')}{K(k)}, \tag{3.5}$$

$$C_l = 4\epsilon_0\epsilon_{eff}\frac{K(k)}{K(k')}, \tag{3.6}$$

where $k = S/(S+2W) = a/b$ (a and b were used in Section 2.4.5). $k'^2 = 1-k^2$, and K is the complete elliptic integral of the first kind.

The characteristic impedance of the CPW is given by $Z_0 = \sqrt{L/C_l}$, where L includes both geometric and kinetic inductance. For the through transmission lines we usually use a central line width of 10 μm and slots of 6 μm, which results in $Z_0 \approx 50$ Ω, to match the impedance of the coaxial cables in the setup. For materials with a high resistivity, the total inductance can be dominated by the kinetic inductance. Therefore any variation in the material properties can give significant changes in Z_0, which makes it difficult to fabricate a 50 Ω line. For Al, the kinetic inductance for these dimensions and a film thickness of 40 nm is only 10% of the total inductance, and one obtains relatively easily the desired Z_0.

The kinetic inductance, L_k, is due to the inertia of the Cooper pairs in the superconductor and is determined by both the geometry of the waveguide and the surface impedance of the superconductor L_s, which we introduced in Section 2.2.3. The geometry factors for the central line g_c and the groundplanes g_g are given by [15]

$$g_c = \frac{1}{4S(1-k^2)K^2(k)}\left[\pi + \ln\left(\frac{4\pi S}{d}\right) - k\ln\left(\frac{1+k}{1-k}\right)\right], \tag{3.7}$$

$$g_g = \frac{k}{4S(1-k^2)K^2(k)}\left[\pi + \ln\left(\frac{4\pi(S+2W)}{d}\right) - \frac{1}{k}\ln\left(\frac{1+k}{1-k}\right)\right], \tag{3.8}$$

where d is the film thickness and $g = g_c + g_g$. The kinetic inductance is thus given by $L_k = g_c L_{s,c} + g_g L_{s,g}$, where $L_{s,c}$ and $L_{s,g}$ are the sheet inductances of the central line and the groundplane. The approximations behind these expressions give a limiting range of validity: $d < S/20$ and $k < 0.8$. In essence, the metal thickness should be much smaller than the width of the central line and the width of the gaps of the CPW. Eqs. 3.7 and 3.8 are equivalent to the expressions derived [16] and tested [21] for superconducting CPWs. Agreement to within 10% was also found for CPW superconducting resonators [19, 22]. The kinetic inductance fraction is now given by

$$\alpha_k = \frac{L_k}{L_k + L_g}. \tag{3.9}$$

For a high response of the resonant frequency to a change in the complex conductivity it is thus beneficial to have a high α_k (see also Eq. 2.24).

As an example we take the properties of the Al resonator reported in Chapter 5: $S = 3$ μm, $W = 2$ μm and $d = 40$ nm, which results in $g_c/(g_c + g_g) = 0.72$. The response is thus primarily determined by the central line of the CPW. The Al properties are $\rho_N = 0.8$ $\mu\Omega$cm and $\Delta = 168$ μeV, both for the groundplane and central line. Using the Mattis-Bardeen equations Eqs. 2.11 and 2.12 (with $\omega = 2\pi \cdot 6.6$ GHz), we calculate the surface inductance from Eq. 2.20, $L_s = 0.266$ pH, which results in $\alpha_k = 0.2$.

The participation ratio of the central line is enhanced in the sample that is used for the measurements in Chapter 7. Here $S = 3$ μm and $W = 1.5$ μm and $\Delta = 188$ μeV. The central line is made of Al with $d = 50$ nm and $\rho_N = 2.2$ $\mu\Omega$cm, and the groundplanes of Al with $d = 100$ nm and $\rho_N = 0.28$ $\mu\Omega$cm. If we use these different properties in Eqs. 3.7 and 3.8 and calculate $L_{s,c} = 0.512$ pH and $L_{s,g} = 0.065$, the resulting kinetic inductance fraction is $\alpha_k = 0.28$. Now the participation ratio has to be scaled with the different L_s as well: $L_{s,c}g_c/(L_{s,c}g_c + L_{s,g}g_g) = 0.95$. The microwave response of the central line is therefore about 20 times higher than the response of the groundplane for the double Al layer resonator. For this particular experiment this is even more beneficial, because the pair-breaking radiation is also predominantly absorbed in the central line of the resonator (see Section 3.2.3). Note that Eqs. 3.7 and 3.8 are derived using a conformal mapping technique with an equal thickness for the groundplane and central conductor. However, the thickness of both layers and their thickness difference are much smaller than the dimensions of the CPW. Therefore the distribution of the transverse electric and magnetic fields will not change much compared to planes of equal thickness.

Experimentally α_k can be determined in several ways, as pointed out by Gao [19]. First the measured resonant frequency can be compared to the calculated resonant frequency where only the geometrical inductance is taken into account. α_k is now derived as $\alpha_k = 1 - (\omega_0^{meas}/\omega_0^{calc})^2$. The second method is based on a measurement of the fractional resonant frequency shift as a function of temperature. α_k can be obtained from a fit of Eq. 2.24 to the measured $\delta\omega_0/\omega_0$ using the calculated $\delta\sigma_2(T)/\sigma_2(0)$ from the Mattis-Bardeen equations. For α_k close to one this linearized approach breaks down and $\omega_0(T)$ has to be calculated using 3.4. The measured Q_i can be used in the same way, together with Eq. 2.25.

3.3.2 Impedance of a coupled halfwave resonator

The circuit we consider here is shown in Fig. 3.6. The resonator, with impedance Z_{line} is capacitively coupled to a transmission line with a capacitance C. The readout line has an impedance Z_0.

The input impedance of a halfwave transmission line resonator with two open ends

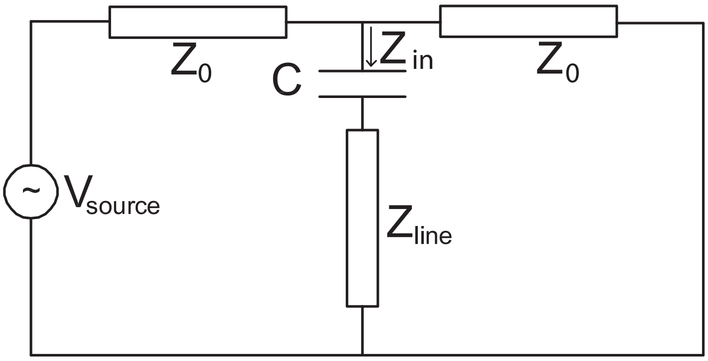

Figure 3.6: The microwave circuit considered for the analysis in this section.

is given by [23]

$$Z_{line} = Z_0 \coth(\alpha + i\beta)l = Z_0 \frac{1 + i\tan\beta l \tanh\alpha l}{\tanh\alpha l + i\tan\beta l}, \tag{3.10}$$

where l is the length of the line. $\gamma = \alpha + i\beta$ is the complex propagation constant. We assume that the characteristic impedance of the resonator is also Z_0. At a wavelength of twice the length, $l = \lambda/2$, close to the resonant frequency $\omega_{1/2}$ (that is: the resonant frequency of the half wavelength line without coupler), with $\omega = \omega_{1/2} + \delta\omega$,

$$\begin{aligned} \beta l &= \pi + \tfrac{\pi\delta\omega}{\omega_{1/2}}, && (3.11)\\ \tan\beta l &= \tan\tfrac{\pi\delta\omega}{\omega_0} \approx \tfrac{\delta\omega\pi}{\omega_{1/2}}. && (3.12) \end{aligned}$$

We can rewrite Eq. 3.10, also using that $\tanh\alpha l \approx \alpha l$ and $i\tan\beta l \tanh\alpha l \approx \alpha l \frac{\pi\delta\omega}{\omega_{1/2}}$ as

$$Z_{line} = \frac{Z_0}{\alpha l + i\frac{\delta\omega\pi}{\omega_{1/2}}}. \tag{3.13}$$

We now define the internal quality factor of this halfwave resonator as $Q_i = \frac{\alpha}{2\beta}$, which leads to $\alpha l = \frac{\beta l}{2Q_i} = \frac{\pi}{2Q_i}(1 + \frac{\delta\omega}{\omega_{1/2}})$. Therefore we get

$$Z_{line} = Z_0 \frac{2Q_i/\pi}{\left(1 + \frac{\delta\omega}{\omega_{1/2}}\right) + i2Q_i\frac{\pi\delta\omega}{\omega_{1/2}}} = Z_0 \frac{\frac{2Q_i}{\pi} - 4i\frac{Q_i^2}{\pi}\frac{\delta\omega}{\omega_{1/2}}}{1 + 4Q_i^2\left(\frac{\delta\omega}{\omega_{1/2}}\right)^2}, \tag{3.14}$$

where we have used $\frac{\delta\omega}{\omega_{1/2}} << 1$.

We add a capacitive coupler, coupling the halfwave resonator to the transmission line with a capacitance C. Now the impedance looking into the capacitance is given by

$$Z_{in} = Z_{line} + \frac{1}{i\omega C} = Z_0 \frac{\frac{2Qi}{\pi} - 4i\frac{Q_i^2}{\pi}\frac{\delta\omega}{\omega_{1/2}} - \frac{i}{\omega C Z_0}\left(1 + 4Q_i^2\left(\frac{\delta\omega}{\omega_{1/2}}\right)^2\right)}{1 + 4Q_i^2\left(\frac{\delta\omega}{\omega_{1/2}}\right)^2} \tag{3.15}$$

The added capacitance will cause the resonant frequency of the line and coupler, ω_0, to deviate from the resonant frequency of the line only, $\omega_{1/2}$. The new criterion for resonance will be that the imaginary part of Eq. 3.15 vanishes, $\mathrm{Im}(Z_{in}) = 0$, the solutions of which are

$$\frac{\delta\omega}{\omega_{1/2}} = \frac{\omega C Z_0}{2Q_i}\left(-\frac{Q_i}{\pi} \pm \sqrt{\frac{Q_i^2}{\pi} - \frac{1}{\omega^2 C^2 Z_0^2}}\right) \approx -\frac{\omega C Z_0}{\pi} \vee 0. \tag{3.16}$$

The approximation here requires that $\frac{1}{\omega^2 C^2 Z_0^2} << Q_i^2/\pi$, which holds for all practical cases. We take the first solution, which lowers the resonant frequency and makes the line slightly inductive. We can now rewrite our equations for small deviations with respect to the new resonant frequency (of the halfwave line *and* coupler) ω_0 using

$$\frac{\delta\omega}{\omega_{1/2}} = \frac{\delta\omega}{\omega_0} - \sqrt{1/\pi Q_c}. \tag{3.17}$$

Eq. 3.15 can be rewritten with the new definition of the resonant frequency as

$$\frac{Z_{in}}{Z_0} = \frac{2Q_i\sqrt{\frac{Q_c}{\pi}}\frac{\delta\omega}{\omega_0} - i\sqrt{\frac{1}{\pi Q_c}}}{1 + 2iQ_i\left(\frac{\delta\omega}{\omega_0} - \sqrt{\frac{1}{\pi Q_c}}\right)}. \tag{3.18}$$

Coupling quality factor

We will now first derive the coupling quality factor Q_c. The energy stored in the line at resonance is $\frac{1}{2}C_l l V_{line}^2$, where V_{line} is the voltage over the line. If we divide the voltage V_L over the coupler and the halfwave line, we get $V_{line} = \frac{Z_{in}}{Z_{line}}V_L$. The current is given by $I = V_L/Z_{in} = V_{line}/Z_{line}$. The 'dissipated' power in the throughline is

$$P_{diss}^c = |I|^2\frac{Z_0}{2} = \frac{V_{line}^2}{|Z_{line}|^2}\frac{Z_0}{2}. \tag{3.19}$$

The superscript c is to denote that it is the power that is lost through the coupler.

At resonance, $\omega = \omega_0$, we get from above that $|Z_{line}| = \frac{1}{\omega C}$. Furthermore we can write the capacitance of the line to be $C_l l = \frac{l}{v_{ph} Z_0}$, where v_{ph} is the phase velocity and we assume again that the characteristic impedance is Z_0. At the first resonance of the circuit we can write $\omega C_l l = \frac{\omega l}{v_{ph} Z_0} = \frac{2\pi l}{\lambda Z_0} = \frac{\pi}{Z_0}$, where λ is the wavelength. Now

$$Q_c = \frac{\omega E}{P_{diss}^c} = \frac{\omega \frac{1}{2} C_l l V_{line}^2}{\frac{V_{line}^2 Z_0/2}{|Z_{line}|^2}} = \frac{\omega C_l |Z_{line}|^2}{Z_0} = \frac{\pi}{\omega^2 C^2 Z_0^2}. \tag{3.20}$$

Note that the result is a factor of 2 different compared to a quarterwave resonator [20].

3.3.3 Transmission of the resonant circuit

The forward transmission of the circuit S_{21} is given by [23]

$$S_{21} = \frac{2}{2 + \frac{Z_0}{Z}} = \frac{Q/Q_i + 2iQ\frac{\delta\omega}{\omega_0}}{1 + 2iQ\frac{\delta\omega}{\omega_0}}, \tag{3.21}$$

where Q is the loaded quality factor, which is given by

$$Q = \frac{Q_i Q_c}{Q_i + Q_c}. \tag{3.22}$$

The magnitude of S_{21} is given by

$$|S_{21}|^2 = \frac{S_{21,min}^2 + 4Q^2\left(\frac{\delta\omega}{\omega_0}\right)^2}{1 + 4Q^2\left(\frac{\delta\omega}{\omega_0}\right)^2} = 1 + \frac{S_{21,min}^2 - 1}{1 + 4Q^2\left(\frac{\delta\omega}{\omega_0}\right)^2}, \tag{3.23}$$

where $S_{21,min}$ is the transmission on resonance, $S_{21,min} = \frac{Q}{Q_i}$. This is a result that is very commonly used to extract the quality factors and the resonant frequency from the resonance curves.

In experiments we are interested in small changes of the real and imaginary part of the response. The real and imaginary part of S_{21} are derived from Eq. 3.21 and given by

$$\mathrm{Re}(S_{21}) = \frac{S_{21}^{min} + 4Q^2\left(\frac{\delta\omega}{\omega_0}\right)^2}{1 + 4Q^2\left(\frac{\delta\omega}{\omega_0}\right)^2} \approx \frac{Q}{Q_i}, \tag{3.24}$$

$$\mathrm{Im}(S_{21}) = \frac{2Q\frac{\delta\omega}{\omega_0}(1 - S_{21}^{min})}{1 + 4Q^2\left(\frac{\delta\omega}{\omega_0}\right)^2} \approx 2Q\frac{\delta\omega}{\omega_0}(1 - S_{21}^{min}), \tag{3.25}$$

where for the approximation the first order in $\frac{\delta\omega}{\omega_0}$ is taken. For small changes Eq. 3.24 can be used to derive $\delta\mathrm{Re}(S_{21}) = -\frac{Q_c Q_i}{(Q_c+Q_i)^2}\frac{\delta Q_i}{Q_i}$.

Impedance mismatch of transmission line and coax cables

When the characteristic impedance of the on-chip through transmission line is not matched to the impedance of the microwave cables (50 Ω), the impedance mismatch causes additional reflections of the microwave signal at both ends of the through transmission line. This effect distorts the resonance curve from the ideal Lorentzian profile and one needs an additional parameter to describe the resonance curve [24, 25]. Usually for Al transmission lines, the impedance is predictable and can be designed to match 50 Ω. The resonance curves can then be described with Eq. 3.23.

3.3.4 Microwave power dissipation in the quasiparticle system

In Fig. 3.6 the load of this circuit is Z_{in}, through which a current I_L flows and over which a voltage V_L is applied. Therefore

$$I_L = \frac{V_{source}}{2Z_{in} + Z_0} = \frac{V_{source}/Z_{in}}{2 + \frac{Z_0}{Z_{in}}}. \tag{3.26}$$

The dissipated power in the load is now given by

$$P_{abs} = |I_L|^2 \mathrm{Re}(Z_{in}) = \frac{V_{source}^2 \mathrm{Re}(Z_{in})}{|2Z_{in} + Z_0|^2} = \frac{4Z_0 P_{read} \mathrm{Re}(Z_{in})}{|2Z_{in} + Z_0|^2}, \tag{3.27}$$

where we take $P_{read} = \frac{V_{source}^2}{4Z_0}$ to be the *readout power* on the throughline.

We now focus on the dissipated power at resonance. On resonance, $\frac{Z_{in}}{Z_0} = \frac{Q_c}{2Q_i}$. Therefore

$$P_{abs} = \frac{2Z_0^2 P_{read} \frac{Q_c}{Q_i}}{Z_0^2 \left(\frac{Q_c}{Q_i} + 1\right)^2} = \frac{P_{read}}{2} \frac{4Q^2}{Q_i Q_c}. \tag{3.28}$$

At critical coupling $Q_i = Q_c$, which results in $P_{abs} = P_{read}/2$.

So far we have assumed that there is only one source of dissipation associated with Q_i. We can refine this assumption by adding an additional source of loss. It is always possible to write this loss as a quality factor, say Q_i^*. We define Q_i^{qp} as the quality factor due to dissipation in the quasiparticle system. Then

$$\frac{1}{Q} = \frac{1}{Q_c} + \frac{1}{Q_i^*} + \frac{1}{Q_i^{qp}} = \frac{1}{Q_c} + \frac{1}{Q_i}, \tag{3.29}$$

and therefore the dissipated power in the quasiparticle system P_{abs}^{qp} is given by

$$P_{abs}^{qp} = P_{abs} \frac{Q_i}{Q_i^{qp}} = \frac{P_{read}}{2} \frac{4Q^2}{Q_i Q_c} \frac{Q_i}{Q_i^{qp}}, \tag{3.30}$$

where we assumed to be on resonance (Eq. 3.28). This equation has been reported [26], but it is important to notice that this derivation shows that one can consistently derive P_{abs} from parameters that are obtained from a fit to the resonance curve as given by Eq. 3.23. P_{abs}^{qp} will be an important parameter in Chapter 8 where the effect of microwave absorption on the quasiparticle system is considered.

3.3.5 Internal power in the resonator

To relate the readout power on the throughline, P_{read} to the microwave field or current in the resonator, one needs to know the internal power of the resonator P_{int}. We consider here the internal power at resonance and for the case the characteristic impedance of the halfwave line is Z_0. Then

$$V_{line} = V_L \frac{Z_{line}}{Z_{in}} = V_{source} \frac{Z_{line}}{Z_{in}} \frac{1}{1 + \frac{Z_0}{Z_{in}}} = V_{source} \frac{Q}{\omega C Z_0 Q_c} \tag{3.31}$$

and therefore

$$V_{line}^2 = V_{source}^2 \frac{Q^2}{Q_c} \frac{1}{\pi} = 4 Z_0 P_{read} \frac{Q^2}{\pi Q_c}. \tag{3.32}$$

Using these relations the internal power is given by[1]

$$P_{int} = \frac{\omega E}{2\pi} = \frac{\frac{1}{2}\omega\ C_l l V_{line}^2}{2\pi} = \frac{V_{line}^2}{4Z_0} = \frac{1}{\pi} \frac{Q^2}{Q_c} P_{read}. \tag{3.33}$$

For a quarterwave resonator, $P_{int} = \frac{2}{\pi} \frac{Q^2}{Q_c} P_{read}$.

If the characteristic impedance of the resonator $Z_l \neq Z_0$, this has to be carried through the whole derivation. The result is that Q_c changes to

$$Q_c = \frac{\pi}{\omega^2 C^2 Z_0 Z_l}. \tag{3.34}$$

The internal power and the dissipated power (Eqs. 3.28 and 3.33) do not change, because the difference in characteristic impedance between the throughline and the resonator is already taken into account through Q_c.

3.3.6 The resonance circle, amplitude and phase

The microwave transmission S_{21} of an aluminium microwave resonator is shown in Figure 3.7 at a radiation power of 34 fW, a bath temperature of 120 mK and a microwave power, $P_{read} = -90$ dBm. The transmission is calibrated for the gain, losses and phase shift of the readout circuitry by a calibration measurement of S_{21} at a temperature of 600 mK, where the resonator features are suppressed by quasiparticle losses and only the throughline transmission is measured. A measurement of the transmission with a frequency sweep is shown as a solid line, which is a circle in the complex plane. The resonant frequency is at the point where the circle crosses the x-axis, where $\mathrm{Im}(S_{21}) = 0$ and $S_{21} = S_{21,min}$.

To calculate the amplitude and phase with respect to the resonance circle we define the centre point of the circle $x_c = (1 + S_{21,min})/2$ and thus $1 - x_c = Q/2Q_c$. The amplitude A and phase θ are now given by

$$A = \frac{\sqrt{(\mathrm{Re}(S_{21}) - x_c)^2 + \mathrm{Im}(S_{21})^2}}{1 - x_c} \approx \frac{\mathrm{Re}(S_{21}) - x_c}{1 - x_c}, \tag{3.35}$$

$$\tan(\theta) = \frac{\mathrm{Im}(S_{21})}{x_c - \mathrm{Re}(S_{21})}. \tag{3.36}$$

---

[1] The stored energy E can be converted into a number of stored microwave photons as $E/\hbar\omega = 2\pi P_{int}/\hbar\omega^2$, which is a common way to express the microwave field strength in a resonator.

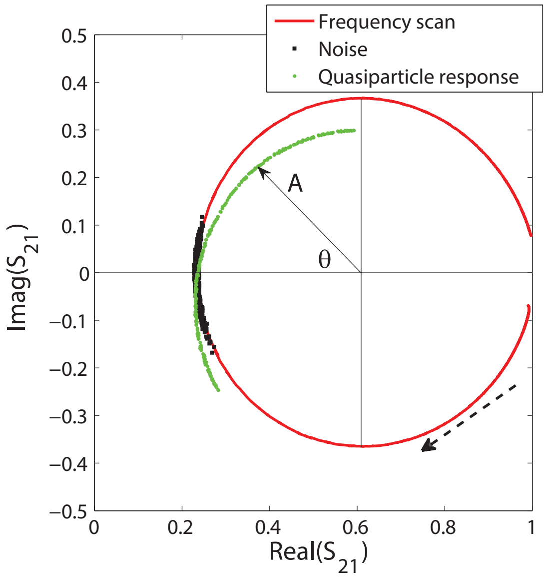

Figure 3.7: The real and imaginary part of the microwave transmission of an Al microwave resonator. The red solid line shows the measurements of a frequency sweep at constant radiation power (34 fW), which trace out a circle in the complex plane. The dashed arrow indicates increasing frequency. The amplitude A and phase θ are defined with respect to the circle. The black squares are measurements as a function of time (noise) at a constant frequency, the resonant frequency. The green dots show the response at a constant frequency when the number of quasiparticles is changed by varying the radiation power from 22 to 82 fW.

Near the equilibrium resonant frequency ω_0, using Eqs. 3.24 and 3.25 together with $\delta A = A - 1$ and the small angle approximation $\tan(\theta) \approx \theta$ the amplitude and phase response are given by

$$\delta A = \frac{-\delta \mathrm{Re}(S_{21})}{1 - x_c} = \frac{2Q}{Q_i}\frac{\delta Q_i}{Q_i}, \tag{3.37}$$

$$\theta = \frac{\mathrm{Im}(S_{21})}{x_c - \mathrm{Re}(S_{21})} = -4Q\frac{\delta\omega}{\omega_0}. \tag{3.38}$$

These equations are generally valid, regardless of the mechanism that dominates δQ_i and $\delta\omega$. Under the assumption that the complex conductivity of the superconductor dominates the response, Eqs. 2.24 and 2.25 describe δQ_i and $\delta\omega$, and therefore

$$\delta A = -\alpha_k \beta Q \frac{\delta\sigma_1}{\sigma_2}, \tag{3.39}$$

$$\theta = -\alpha_k \beta Q \frac{\delta\sigma_2}{\sigma_2}, \tag{3.40}$$

from which the equations for dA/dN_{qp} and $d\theta/dN_{qp}$ (Eqs. 2.26 and 2.27) can be readily derived. Fig. 3.7 shows how the amplitude and phase respond to a change in the quasiparticle number, which is here induced through a variation in the radiation power. This trajectory is also called the 'quasiparticle trajectory'. In Chapter 7 the experiment is described in detail. Fig. 7.2 shows how the resonance dip $S_{21}(\omega)$, the resonance circle and the amplitude and phase response evolve with increasing radiation power.

There are several advantages in using the amplitude and phase defined with respect to the resonance circle. Firstly, the reactive (σ_2) and the dissipative part (σ_1) of the response of the superconductor show up in only the phase and amplitude direction respectively. Therefore the response of the condensate, σ_2, can be separated from the response of the quasiparticles, σ_1. Secondly, the noise of the (HEMT) amplifier is of equal magnitude in amplitude and phase and uncorrelated. Furthermore, the noise of dielectric two level systems (TLS) occurs predominantly as frequency fluctuations, and is therefore only measurable in the phase direction. Therefore, the amplitude response, in which the HEMT noise dominates, can be used to study quasiparticle fluctuations, also if the phase-noise is dominated by TLS-noise.

Fig. 3.7 shows that when the phase-noise is dominated by TLS-noise (which is the case for that measurement), the noise blob (the time domain data in the complex plane) develops in the direction of the circle. When both the amplitude and phase noise are dominated by quasiparticle fluctuations the noise blob will be oriented along the quasiparticle trajectory.

3.4 Microwave measurement

3.4.1 Microwave setup

To measure the microwave response of the resonators we use a microwave setup that contains electronics at room temperature and in the cryostat, a schematic overview of which is presented in Fig. 3.8. Right after the generator (Agilent E8257D), the microwave signal is split into two. One part goes as a local oscillator reference to the IQ-mixer (Miteq IRM0218LC1Q). The other part goes into the cryostat, along the sample and ends up at the other port of the IQ-mixer. The output is digitised with a 2-channel ADC with self-adjusting anti-aliasing filter (National Instruments PXI-5922) at a maximum rate of 2 MHz. The IQ-mixer requires a constant reference signal. Therefore the generator power is kept constant and the desired signal level at the sample is set by adjusting the variable attenuators (Aeroflex/Weinschel 8310). The IQ-mixer has to be calibrated for phase imbalance, gain imbalance and DC offsets. The calibration can be done using the IQ-mixer in heterodyne mode by applying signals from two frequency-locked oscillators to the input ports of the IQ-mixer, with a frequency difference of 100 kHz for example. The calibration procedure is explained in detail in Ref. [20].

In the cryostat the signal is attenuated at each temperature stage to reduce thermal noise of the previous temperature stage. To that end, the total attenuation from room temperature to the sample temperature should be more than the temperature ratio (40

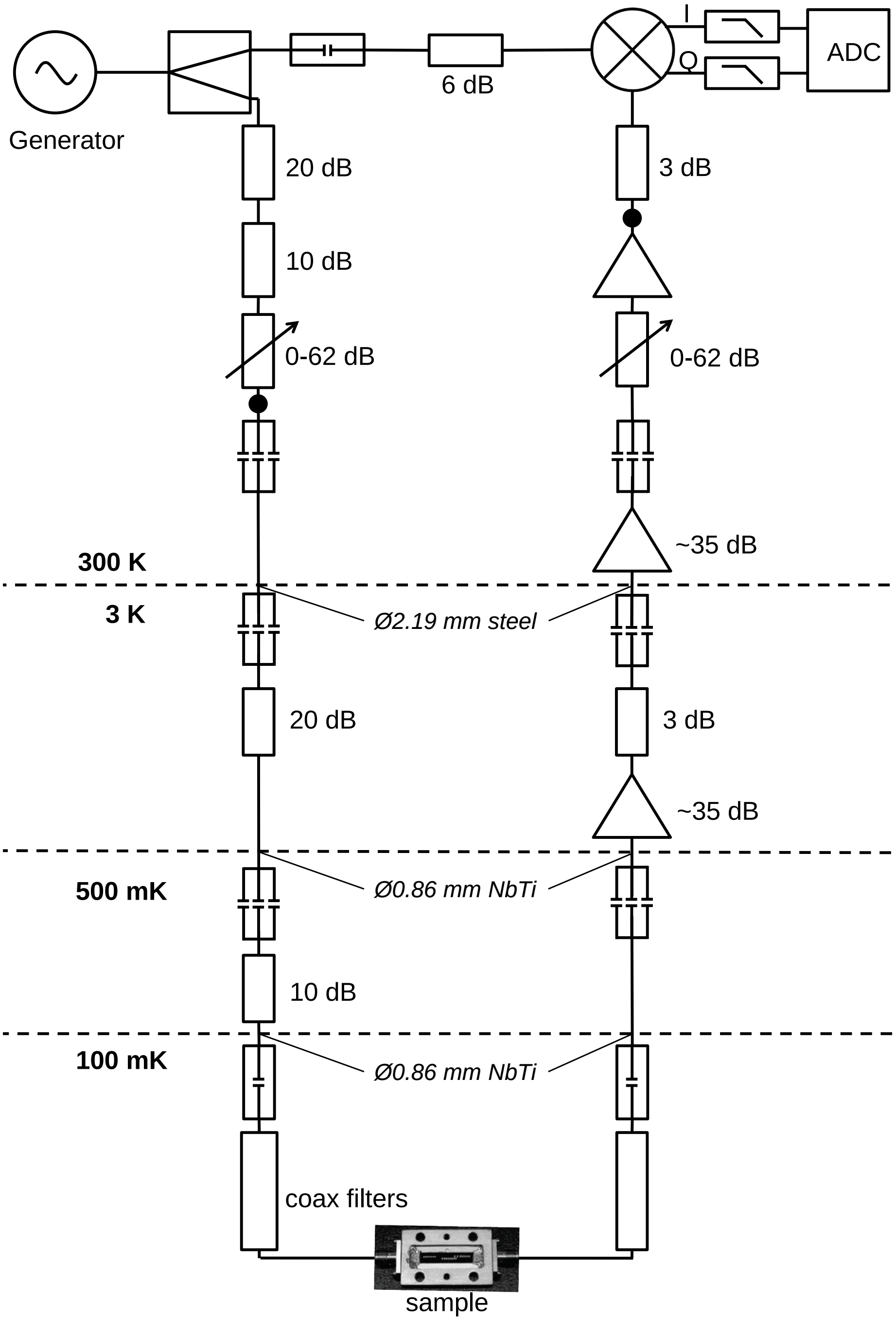

Figure 3.8: The microwave components in the readout system. The signal from the generator is first split and then fed into the cryostat using flexible SMA cables. In the cryostat it is attenuated at each temperature stage and interrupted with double and single DC blocks. The signal enters the 100 mK box through the coax filters. The signal which leaves the sample box is amplified at the 3 K stage and at room temperature before it is mixed with a copy of the original signal in an IQ mixer. Alternatively the signal generator and IQ mixer can be replaced by a vector network analyser (VNA) for quick characterisation. The VNA replaces the complete system above the thick black dots.

dB going from 300 K to 30 mK). From 300 K, 2.19 mm diameter steel coax cables are used to reach the 3 K stage, with an additional thermal strap at 50 K. Double or single DC-blocks are introduced at each stage, introducing an interruption of the galvanic connection to reduce the thermal conductivity between the temperature stages. 20 dB attenuation is introduced at 3 K and another 10 dB attenuation at 500 mK. Each attenuator is thoroughly attached to its stage for thermalisation. The cables between the 3 K stage and the 500 mK stage are 12 cm long, 0.86 mm diameter NbTi coax cables (Coax Co.). Between the 500 mK and 100 mK stage the same cables of 9 cm length are used. These cables have low microwave losses, because NbTi is a superconductor. They also have a low thermal conductivity, which reduces the thermal loading on the 100 mK stage. The thermal loading through these two cables from 500 mK to 100 mK is 7 nW. Before entering the light-tight box the signal passes through the coax cable low-pass filters at 100 mK, the characteristics of which are shown in Fig. 3.2. Inside the 100 mK box, the connection from the coax filter to the sample box is made using 0.86 mm Cu cables. After the sample there is an identical coax cable filter. The signal is amplified with a low noise high-electron-mobility transistor (HEMT) amplifier with a noise temperature of 3-4 K (CITCRYO4-12A Wadefalk/Weinreb), which is mounted on the 3 K stage. At room temperature there are two additional amplifiers (MITEQ AFS5-02001200-30-10P-5 and MITEQ AMF-4F-02000800-15-10P).

The noise of the HEMT amplifier dominates the system noise for our system. In Fig. 6.1 we observe a noise floor for both amplitude and phase of -106 dBc/Hz at 6.62 GHz. The unit dBc/Hz means the noise with respect to the carrier, which is here the resonance circle. The system noise level in A or θ is related to the (single sideband) system noise temperature T_{noise} as [20]

$$S_{A,\theta}^{system} = \frac{k_B T_{noise}}{r_c^2 P_{read}}, \tag{3.41}$$

with P_{read} the microwave readout power, which is -75 dBm for this measurement. $r_c = Q/2Q_c = (1 - S_{21,min})/2 \leq 0.5$ is the radius of the resonance circle. The factor $1/r_c^2$ arises because the noise referred to the resonance circle has first to be translated to noise referred to the transmission S_{21} (for both the unit dBc/Hz is used). For the measurement in Fig. 6.1, Eq. 3.41 results in $T_{noise} = 7$ K. The main contribution is due to the HEMT amplifier, which has a noise temperature of 3-3.5 K at 6.6 GHz (dependent on the exact bias settings of the amplifier). In between the sample and amplifier is the output coax filter which attenuates 3 dB at this frequency (Fig. 3.2b), and thus the amplifier contribution to the system noise is about 6-7 K, which is consistent with the measured noise level.

Additionally there is thermal noise from each stage before the sample. The output power P_{out} of each attenuator with gain $G < 1$ is related to its input power P_{in} as given by

$$P_{out} = GP_{in} + (1 - G)k_B T_a, \tag{3.42}$$

with T_a the physical temperature of the attenuator. The noise power from each temperature stage is attenuated by all subsequent attenuators (see Barends [20] for a more detailed treatment). Room temperature noise is attenuated to the 0.15 K level as well as the noise from the 3 K attenuator. The attenuator at 500 mK contributes for 0.25 K (because of the 3 dB attenuation of the coax filter). The last attenuator before the sample is the coax filter at 100 mK. The output coax filter attenuates the thermal noise by another 3 dB. These contributions would now sum op to ~0.5 K at the input of the amplifier, which is already small compared to the HEMT-noise. However, the resonator itself acts as well as a bandpass filter for these noise contributions. Thus on-resonance and in the band of the resonator this thermal noise is attenuated by an amount corresponding to the depth of the resonance dip. Often a measurement off-resonance (i.e. far away from the resonator-dip) is performed to estimate the system noise level. For a representative system noise measurement, the difference in transmitted power on- and off-resonance has to be compensated.

The setup with the IQ-mixer is used for most of the measurements. For quick characterisation we alternatively switch to a Vector Network Analyser (VNA), Agilent PNA-L N5230A. The VNA replaces all electronics above the thick black dots in Fig. 3.8 and is particularly useful for rapid S_{21} frequency sweep measurements.

3.4.2 Noise measurement

Prior to each noise measurement a frequency sweep is performed to obtain the resonance circle and in particular the resonant frequency of the resonator under the conditions of the noise measurement. The noise measurement itself consists of two time-domain traces of the IQ-response at the resonant frequency at two different sampling rates, to reduce the amount of data. One time domain stream is sampled for 40 seconds at 50 kHz, the second stream for 0.5 s at 2 MHz. The IQ-response is translated into amplitude and phase using Eqs. 3.35 and 3.36.

The spectral properties of noise are described by the power spectral density. The Wiener-Khinchin theorem states that for a random process that is wide sense stationary (the first and second moment are independent of time), the power spectral density is the Fourier transform of the autocorrelation function of that process [27]. For any process x the power spectral density S_x is real valued and $S_x(\omega) \geq 0$. The correlation function of such a process, R_x only depends on the time difference u: $\langle x(t)x^*(t-u)\rangle = R_x(u)$. The power spectral density, S_x, is now given by

$$S_x(\omega) = 2\int_{-\infty}^{\infty} R_x(u)\exp(-i\omega u)du. \tag{3.43}$$

The factor of two arises because we consider here only positive frequencies, i.e. a double sideband spectrum with the same total spectral power. For quasiparticle number fluctuations with variance $\left\langle \Delta N_{qp}^2 \right\rangle = N_{qp}$, a characteristic timescale τ and $R_N(u) =$

$\left\langle \Delta N_{qp}^2 \right\rangle \exp\left(-\frac{u}{\tau}\right)$ (Eq. 2.32), we have seen that $S_N = \frac{4N_{qp}\tau}{1+\omega^2\tau^2}$. The same factor of two arises here because of the single sided spectrum. The additional factor of two is due to the even correlation function in this particular process.

In the same way, the cross power spectral density $S_{x,y}(\omega)$ is the Fourier transform of the cross-correlation function $R_{x,y}(u) = \langle x(t)y(t-u)\rangle$. The cross power spectral density is generally a complex quantity, which describes the statistical relationship between x and y in the frequency domain. $S_{x,y}(\omega) = 0$ if x and y are orthogonal. $S_{x,y}$ is real if the correlated components in x and y occur without time delay. For the microwave resonator measurements reported in this thesis we use the cross power spectral density of the amplitude and phase of the resonator response. Most of the unwanted contributions to the noise spectra are uncorrelated (amplifier noise, dielectric two-level system noise). Fluctuations in the number of quasiparticles however cause a correlated response in the resonator amplitude and phase, because both σ_1 (amplitude) and σ_2 (phase) change at the same time upon a quasiparticle generation or recombination event. We observe that quasiparticle fluctuations indeed occur as a real, negative component of $S_{A,\theta}$ (see Fig. 6.1).

In practice, the power spectral density and the cross power spectral density are calculated from the measured time domain data using the Matlab functions *pwelch* and *cpsd* respectively, which are based on a Fast Fourier Transform (FFT) method. The spectra obtained from the 40 s time trace and from the 0.5 s time trace are stitched at 20 kHz.

3.4.3 Cosmic ray hits

In principle the spectrum of the noise is meant to represent the equilibrium properties of the noise process. However, the 40 s time streams are sometimes subject to large glitches. These have to be removed from the time-domain data to obtain a good estimate of the spectrum of the noise process. In practice we cut the time domain trace into 32 pieces and throw pieces with hits away. The spectrum is than calculated for each single piece. The total spectrum is obtained by averaging the spectra of the not-rejected pieces.

One type of glitch is rare. It involves only a single data point and originates from possible electronic glitches. These peaks are easily rejected in the first rejection step described below. The second type of peak involves the creation of quasiparticles by cosmic ray hits, which can either be direct substrate hits causing large peaks every 20-30 s (usually 1 or 2 per 40 s), or hits in the metal sample box next to the sample, which can create a shower of lower energy particles that cause smaller hits (one every 5-10 s). Fig. 5.2c shows examples of both a large and small hit. The evidence that quasiparticles are created in these events is the fact that the decay-time of the hits is the quasiparticle recombination time, which is alternatively measured from the noise spectrum or using an LED-pulse. The rejection of time-domain pieces containing hits is done in two steps. First the standard deviation is estimated using the whole 40 s of data. Pieces with hits bigger than 5 times the standard deviation are rejected, which removes the first type of single-point glitches and the large cosmic ray hits. In a second step, we filter the data using a moving average filter with a time constant $\tau_{qp}/2$, which enhances the signal-to-noise ratio of peaks with a characteristic decay time of τ_{qp}. The standard deviation is recalculated based on the filtered time trace, and pieces with peaks are rejected using the same criterion. The drawback of the method is that to get a spectrum at low frequencies, one would have to integrate much longer, because the time stream is cut in 32 pieces. To use the time domain data more effectively, peaks could also be removed based on a peak-shape template, which only takes out the time domain points that are actually in the peak. The 0.5 s time stream, sampled at 2 MHz, is treated in the same way, but usually no hits occur in this short timeframe.

In experiments by Swenson et al. [28] a similar hit rate of one in every 5-20 seconds was found, in a similar experimental configuration. In that experiment an array of five similar superconducting microwave resonators was read out simultaneously with a frequency multiplexed readout. The measurements show that all resonators get excited by a single cosmic ray hit, which indicates that the cosmic ray is absorbed in the substrate. The excited phonons spread throughout the substrate and create quasiparticle excitations in the superconductor, which results in a signal in the resonator detectors. Interestingly the difference in arrival time at each pixel is a measure of the phonon-velocity in the substrate. Cosmic rays are especially problematic for space-based systems with large arrays of detectors, because the hit rate is expected to be $1/\text{cm}^2/\text{s}$ in a typical orbit. An extensive study on cosmic ray hits in the Planck instrument, which also uses low temperature detectors, can be found in Ref. [29].

3.4.4 Response to radiation

The response to radiation requires several measurements to be done. For each step in blackbody temperature, the voltage of the blackbody heater is first set, after which we wait 10 minutes for the temperature to stabilise. When the temperature is stabilised, first a frequency-sweep is performed to measure the resonance circle and to determine the resonant frequency and quality factors (using Eq. 3.23) at that blackbody power. Secondly a noise measurement is performed. The time domain data is processed as explained in Section 3.4.2 to obtain a spectrum of the noise. Thirdly the responsivity is obtained from a measurement of the IQ-response at the resonant frequency while sweeping the blackbody temperature in a small range around the temperature of interest. The response is integrated for 500 ms at each point. The responsivity (dA/dP_{rad}) is than obtained by a linear fit to the measured response in the range where the response is linear. This fit-range differs widely from low to high radiation power, and therefore the fit-ranges are determined manually and chosen to be small enough to be in the linear regime and large enough to have a small uncertainty. In particular at low

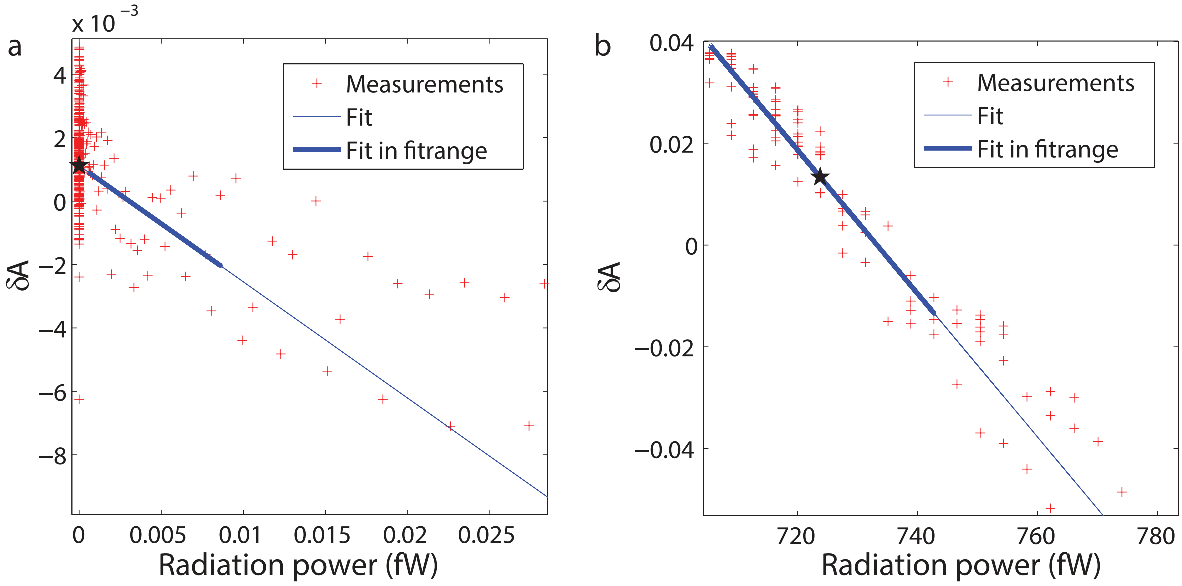

Figure 3.9: (a), Response of the resonator amplitude δA as a function of radiation power. The power for which the response is estimated is the lowest radiation power: 3 zW. Because there is only noise and no response at that radiation power, the fit range is extended to 0.3 aW - 9 aW, indicated by the thick blue line. The thin line shows how a linear response would continue over a larger range. The black star indicates the 3 zW point. (b), The response of the resonator at the highest radiation power: 724 fW (at the black star). The fit range to obtain the responsivity is here 705 - 743 fW.

radiation powers $P_{rad} < 0.1$ fW the quasiparticle number saturates and is determined by the absorbed microwave readout power (which is reflected in a saturation in the NEP below 0.1 fW in Fig. 7.1c). Because of the 500 ms integration time in the response measurement, we start to see response already at $P_{rad} > 0.3$ aW. For even lower P_{rad}, dA/dP_{rad} can thus only be estimated by going to somewhat higher powers. This is illustrated in Fig. 3.9a for the lowest radiation power $P_{rad} = 3$ zW.

In the limit where the absorbed radiation power dominates the number of quasiparticles, dA/dP_{rad} is more easily obtained since the response changes both below and above the P_{rad} of interest. Therefore the fit-range can be much smaller. An example is shown in Fig. 3.9b for the highest radiation power of 724 fW. More details on the experiment are given in Chapter 7.

3.5 Fabrication

The aluminium resonators reported in Chapters 5 - 8 are fabricated in the cleanroom at SRON in Utrecht. The fabrication starts with a 2 inch c-plane sapphire wafer (CrysTec GmbH), which is first cleaned for 5 min in an aqua regia bath at 60 °C. Aluminium is sputter-deposited in the LLS sputtering system, which is equipped with a cryopump and a load-lock, at a power of 800 W and a pressure of 5 mTorr (Ar). The background pressure of the system is better than 2×10^{-7} mbar. These settings result in a growth rate of 0.4 nm/s. Next the substrate is treated with HDMS (hexamethyldisilazane, which promotes adhesion of the resist), before the photoresist AZ6612 is deposited, which is subsequently baked for 60 s on a hot plate at 110 °C. A 4-inch carrier wafer is now applied and both wafers are baked another 60 s at 110 °C. The carrier wafer is used to enable alignment of the mask that is used for the photolithography. The resist is exposed for 5.5 s to UV light using contact lithography and developed in AZ developer for 45 s. To remove unwanted leftovers of the resist, a reactive ion etch is applied using an O_2 plasma for 15 s. The aluminium is etched for 375 s in a mixture of phosphoric acid, acetic acid, water, and nitric acid (PAWN). Acetone is spinned onto the wafer to remove the resist. Single-layer devices (such as in Chapter 5) are finished now. The times mentioned here are for a 150 nm thick Al layer.

For the double layer device as used in Chapter 7, the first (groundplane) layer is deposited and patterned as described above. Right after the last cleaning step of the first layer, the second Al layer is sputtered. Note that the second layer also covers the first layer where it is not etched. The lithography process is the same as above, except that the PAWN etch is applied now for 105 s. The only patterns for this layer are the central lines of the CPW resonators, the groundplane is thus also partially etched away. For a deposited 150 nm groundplane layer and a 50 nm second layer, the groundplane was etched away down to 100 nm, which thus also removes a possible interface layer between the two Al layers. During dicing the wafer is protected by a layer of AZ6612 resist, baked for 30 s at 110 °C, which is removed before mounting the sample for measurements. Samples for dark experiments are glued into the sample box using GE varnish and are wire bonded with 25 μm Al wire bonds (Fig. 3.1a).

For the samples that are exposed to radiation, a lens-array is mounted on top of the detector chip and the lens-centres are aligned to the antennas. To that end the detector chip is mounted with 4 small flat springs into the sample holder, with the patterned side facing downwards. The sample holder is placed on an x-y-rotation stage of a microscope and aligned for rotation. Note that sapphire is transparent and therefore the Al pattern on the back side can be used for alignment. The lens-array is put onto the chip and is aligned for rotation and subsequently in the x-y direction using a second translation stage. The lens-array is glued onto the chip by putting two droplets of cyanoacrylate glue (Bison superglue) at the sides, which spreads under the lens-array due to capillary action, and left to dry for 10 minutes. The alignment accuracy is typically 10 μm.

References

[1] J. Baselmans, S. Yates, P. Diener, and P. de Visser, *Ultra low background cryogenic test facility for far-infrared radiation detectors*, J. Low Temp. Phys. **167**, 360

(2012).

[2] J. J. A. Baselmans and S. J. C. Yates, *Long quasiparticle lifetime in Aluminium Microwave Kinetic Inductance Detectors using coaxial stray light filters*, AIP Conference Proceedings **1185**, 160 (2009).

[3] T. Klaassen, M. Diez, J. Blok, C. Smorenburg, K. Wildeman, and G. Jakob, *Optical Characterization of Absorbing Coatings for Sub-millimeter Radiation*, Proceedings of the 12th International Symposium on Space Terahertz Technology, San Diego, California, USA , p400 (2001).

[4] F. P. Milliken, J. R. Rozen, G. A. Keefe, and R. H. Koch, *50 Ω characteristic impedance low-pass metal powder filters*, Rev. Sci. Instrum. **78**, 024701 (2007).

[5] M. Halpern, H. P. Gush, E. Wishnow, and V. D. Cosmo, *Far infrared transmission of dielectrics at cryogenic and room temperatures: glass, Fluorogold, Eccosorb, Stycast, and various plastics*, Appl. Opt. **25**, 565 (1986).

[6] J. W. Lamb, *Miscellaneous data on materials for millimetre and submillimetre optics*, Int. J. Infrared Millim. Waves **17**, 1997 (1996).

[7] W. C. Elmore and M. A. Heald, *Physics of Waves*, Dover Publications, Inc., New York, 1985.

[8] D. Ristè, C. C. Bultink, M. J. Tiggelman, R. N. Schouten, K. W. Lehnert, and L. DiCarlo, *Millisecond charge-parity fluctuations and induced decoherence in a superconducting transmon qubit*, Nature Comm. **4**, 1913 (2013).

[9] R. Barends, J. Wenner, M. Lenander, Y. Chen, R. C. Bialczak, J. Kelly, E. Lucero, P. O'Malley, M. Mariantoni, D. Sank, H. Wang, T. C. White, Y. Yin, J. Zhao, A. N. Cleland, J. M. Martinis, and J. J. A. Baselmans, *Minimizing quasiparticle generation from stray infrared light in superconducting quantum circuits*, Appl. Phys. Lett. **99**, 113507 (2011).

[10] J. Bueno, P. J. de Visser, J. J. A. Baselmans, and S. Doyle, *Study on optical filter heating in background limited detector experiments*, submitted to J. Low Temp. Phys. (2013).

[11] R. W. Boyd, *Photon bunching and the photon-noise-limited performance of infrared detectors*, Infrared Phys. **22**, 157 (1982).

[12] A. Iacono, A. Freni, A. Neto, and G. Gerini, *In-line X-slot element focal plane array of Kinetic Inductance Detectors*, in *Proceedings of the European Conference on Antennas and Propagation*, Rome, Italy, 2011.

[13] D. Filipovic, S. Gearhart, and G. Rebeiz, *Double-slot antennas on extended hemispherical and elliptical silicon dielectric lenses*, IEEE Trans. on Microwave Theory and Tech. **41**, 1738 (1993).

[14] M. Ji, C. Musante, S. Yngvesson, A. J. Gatesman, and J. Waldman, *Study Of Parylene As Anti-Reflection Coating For Silicon Optics At THz Frequencies*, Proceedings of the 11th International Symposium on Space Terahertz Technology, Ann Arbor, Michigan, USA , p398 (2000).

[15] R. E. Collin, *Foundations of Microwave Engineering*, John Wiley & Sons, Inc., 2^{nd} edition, 2001.

[16] C. L. Holloway and E. F. Kuester, *A quasi-closed form expression for the conductor loss of CPW lines, with an investigation of edge shape effects*, IEEE Trans. Microwave Theory Tech. **43**, 2695 (1995).

[17] B. A. Mazin, *Microwave kinetic inductance detectors*, PhD thesis, California Institute of Technology, 2004.

[18] G. Vardulakis, *Superconducting Kinetic Inductance Detectors, Theory, Simulations & Experiments*, PhD thesis, University of Cambridge, 2007.

[19] J. Gao, *The Physics of Superconducting Microwave Resonators*, PhD thesis, California Institute of Technology, 2008.

[20] R. Barends, *Photon-detecting Superconducting Resonators*, PhD thesis, Delft University of Technology, 2009.

[21] J. Booth and C. Holloway, *Conductor loss in superconducting planar structures: calculations and measurements*, IEEE Trans. Microwave Theory Techn. **47**, 769 (1999).

[22] J. Gao, J. Zmuidzinas, B. Mazin, P. Day, and H. Leduc, *Experimental study of the kinetic inductance fraction of superconducting coplanar waveguide*, Nucl. Instr. Meth. in Phys. Research Sec. A **559**, 585 (2006).

[23] D. M. Pozar, *Microwave Engineering*, John Wiley & Sons, Inc., 2^{nd} edition, 1998.

[24] M. S. Khalil, M. J. A. Stoutimore, F. C. Wellstood, and K. D. Osborn, *An analysis method for asymmetric resonator transmission applied to superconducting devices*, J. Appl. Phys. **111**, 054510 (2012).

[25] A. Megrant, C. Neill, R. Barends, B. Chiaro, Y. Chen, L. Feigl, J. Kelly, E. Lucero, M. Mariantoni, P. J. J. O'Malley, D. Sank, A. Vainsencher, J. Wenner, T. C. White, Y. Yin, J. Zhao, C. J. Palmstrøm, J. M. Martinis, and A. N. Cleland, *Planar superconducting resonators with internal quality factors above one million*, Appl. Phys. Lett. **100**, 113510 (2012).

[26] J. Zmuidzinas, *Superconducting Microresonators: Physics and Applications*, Ann. Rev. Condens. Matter Phys. **3**, 169 (2012).

[27] S. Kogan, *Electronic Noise and Fluctuations in Solids*, Cambridge University Press, 1996.

[28] L. J. Swenson, A. Cruciani, A. Benoit, M. Roesch, C. S. Yung, A. Bideaud, and A. Monfardini, *High-speed phonon imaging using frequency-multiplexed kinetic inductance detectors*, Appl. Phys. Lett. **96**, 263511 (2010).

[29] Planck collaboration: P. A. R. Ade et al., *Planck 2013 results X. Energetic particle effects: characterization, removal, and simulation*, arXiv:1303.5071v2, to be published in Astr. & Astroph. (2013).

Chapter 4

Readout-power heating and hysteretic switching between thermal quasiparticle states in Kinetic Inductance Detectors

A model is presented for readout-power heating in Kinetic Inductance Detectors. It is shown that the power dissipated by the readout signal can cause the temperature of the quasiparticle system in the superconducting resonator to switch between well-defined states. At low readout powers, only a single solution to the heat balance equation exists, and the resonance curve merely distorts as the readout power is increased. At high readout powers, three states exist, two of which are stable, and the resonance curve shows hysteretic switching. The power threshold for switching depends on the geometry and material used, but is typically around -70 dBm for aluminium resonators. A comprehensive set of simulations is reported, and a detailed account of the switching process is given. Experimental results are also shown, which are in strong qualitative agreement with the simulations. The general features of the model are independent of the precise cooling function, and are even applicable for resonators on suspended, thermally isolated, dielectric membranes, where an increase in quasiparticle lifetime is expected. We discuss various extensions to the technique, including the possibility of recovering the cooling function from large-signal measurements of the resonance curve.

This chapter was published as P. J. de Visser, S. Withington and D. J. Goldie, *Journal of Applied Physics* **108**, 114504 (2010).

4.1 Introduction

Kinetic Inductance Detectors (KIDs) are being developed extensively for large-format astronomical imaging [1]. They come in a variety of forms, but the basic device comprises a microwave (f_0 <10 GHz) superconducting thin-film resonator on a sapphire, quartz, or silicon substrate. The superconducting material is usually Al, Ta, or Nb, having a critical temperature, T_c, of approximately 1 K, 4 K, and 9 K respectively. When an infrared, optical, or x-ray photon is absorbed, the surface impedance changes, and the resonant frequency shifts. By monitoring the transmission amplitude and phase, at a single readout frequency, highly sensitive detectors can be made. KIDs can be packed into large-format imaging arrays by lightly coupling thousands of resonators to a single, through transmission line, which can be read out using software-defined radio techniques.

A key issue when optimising the performance of KIDs is decreasing the amount of noise. It is desirable to maximise the microwave readout power, so that the transmission amplitude and phase can be recorded with a high signal-to-noise ratio, and the sensitivity of the detector is enhanced. In fact, when using phase readout, excess noise is seen, which scales inversely with the square root of power [2, 3]. This noise is often attributed to two-level systems, originating from the refractive index of the substrate or native oxide, fluctuating as a consequence of the movement of uncoordinated, lightly bound, atoms. Amplitude readout is sometimes used to minimise this problem [4, 5]. Unfortunately, as the readout power is increased above a certain threshold, the resonant curve begins to distort, and eventually begins switching hysteretically as the readout frequency is swept up and down. This behaviour is seen in all devices, although the exact power level at which the distortion appears varies from material to material. It can also vary between films of notionally identical material manufactured by different groups.

The power handling capability of superconducting resonators is also important from the point of view of detector linearity, because as the incident photon rate increases, the density of non-equilibrium quasiparticles increases.

In this paper, we present a model describing non-linear behaviour in KIDs due to microwave-readout heating. As power is applied, the temperature of the quasiparticle system rises until a balance is reached between the rate at which microwave energy is dissipated in the resonator, and the rate at which energy is transferred from the quasiparticle system of the superconductor to the phonon system of the substrate. We present simulations showing that our model accounts for the functional form of what is seen experimentally, and gives rise to multiple temperature states. These states manifest themselves as hysteretic switching in the resonance curves.

Non-linearities in superconducting films and resonators are widely studied in the context of high-T_c superconductors for different applications [6], with critical temperatures ranging from 9 K (Niobium) to 87 K (YBCO). Non-linear behaviour is found to originate from thermal instabilities due to local hot spots [7, 8] and vortices [9–11] leading to a power-dependent surface impedance [12, 13]. Other effects involve a Kerr nonlinearity [14–16] or weak links in the film [17, 18], leading to a nonlinear inductance at high current density. Intermodulation measurements can indicate which mechanism causes non-linearities [14, 19]. In most mechanisms, the superconductor film quality plays a crucial role in the power handling [6].

Quasiparticle heating is sometimes mentioned, but neglected due to the relatively high thermal conductivity of high-T_c superconductors. Where thermal effects play a role, they are caused by local heating due to film inhomogeneities [8, 20] or measured by an external resonant probe [21]. We emphasize that some of these effects may still be present in low-T_c resonators, but the temperature-state switching described here is likely to dominate at the very low operating temperatures, $T_c/10$, of KIDs, especially where $T_c \approx$1-2 K. Another global heating model, based on the substrate thermal conductivity, was previously described [22]. Data presented in this reference was taken on resonators using more than 8 orders of magnitude more power and at temperatures from 40-70 K, which makes it a totally different regime than we study in this paper.

Non-linear resonators can also be used for parametric amplifiers [15, 16] or intermodulation amplifiers [23]. This is usually done by introducing a non-linear element in the resonator. The Josephson bifurcation amplifier is a well-known example. For a review, see Ref. [24] and references therein. Interestingly, this amplifier could be useful to enhance the sensitivity of the readout of KIDs [5].

The paper is structured as follows: In Sec. 4.2 the proposed theory of readout-power heating in superconducting resonators is described, and then in Sec. 4.3 simulations are reported. In Sec. 4.4, experimental results are presented, which indicate that the simulations have the correct general forms. Finally, in the Discussion and Conclusion we reflect on the findings and describe various ways in which the study might be taken forward.

4.2 Theory

4.2.1 Superconducting microstrip resonators

The microscopic picture of the electrodynamic response of superconductors was developed by Mattis and Bardeen [25]. According to this theory, the complex conductivity, $\sigma = \sigma_1 - i\sigma_2$, describing the response of both Cooper pairs and quasiparticles to a time-varying electric field is given by

$$\begin{aligned}\frac{\sigma_1}{\sigma_N} &= \frac{2}{\hbar\omega}\int_{\Delta}^{\infty}[f(E)-f(E+\hbar\omega)]g_1(E)dE \\ &+ \frac{1}{\hbar\omega}\int_{min(\Delta-\hbar\omega,-\Delta)}^{-\Delta}[1-2f(E+\hbar\omega)]g_1(E)dE, \qquad (4.1)\\ \frac{\sigma_2}{\sigma_N} &= \frac{1}{\hbar\omega}\int_{max(\Delta-\hbar\omega,-\Delta)}^{\Delta}[1-2f(E+\hbar\omega)]g_2(E)dE, \qquad (4.2)\end{aligned}$$

where

$$\begin{aligned} g_1(E) &= \frac{E^2+\Delta^2+\hbar\omega E}{(E^2-\Delta^2)^{1/2}[(E+\hbar\omega)^2-\Delta^2]^{1/2}}, \qquad (4.3)\\ g_2(E) &= \frac{E^2+\Delta^2+\hbar\omega E}{(\Delta^2-E^2)^{1/2}[(E+\hbar\omega)^2-\Delta^2]^{1/2}}, \qquad (4.4)\end{aligned}$$

and $f(E)$ is the Fermi function. σ_N the normal-state conductivity, and ω the angular frequency. To determine the conductivity as a function of temperature, it is necessary to know how the energy gap, $\Delta(T)$, changes with temperature. It can be calculated by numerically inverting the integral equation

$$\frac{1}{N(0)V_{sc}} = \int_{\Delta(T)}^{\hbar\omega_D}\frac{1-2f(\epsilon)}{\sqrt{\epsilon^2-\Delta^2(T)}}d\epsilon, \qquad (4.5)$$

where $N(0)$ is the single-spin density of states at the Fermi surface, V_{sc} is the scattering parameter or potential energy describing phonon exchange, $\hbar$ is the reduced Planck's constant, ω_D is the Debye frequency, T is the temperature, ϵ the energy relative to the Fermi level, and k_B is Boltzmann's constant.

The surface impedance of a superconducting film can be calculated from the complex conductivity. For arbitrary thicknesses t, the surface impedance Z_s, in the dirty limit, is given by [26]

$$Z_s = \sqrt{\frac{i\mu_0\omega}{\sigma}}\coth(\sqrt{i\omega\mu_0\sigma}t), \qquad (4.6)$$

where μ_0 is the permeability of free space, and σ the complex conductivity.

Knowing the geometry of the resonator, and the surface impedance as a function of temperature, it is possible to calculate the microwave loss as a function of temperature. Unfortunately, calculating the loss of a thin-film transmission line is more difficult than calculating the characteristic impedance and modal propagation constant, because it is necessary to know the detailed way in which the induced current penetrates into, and flows around, the waveguiding structure. To explore the basic properties of the model, it is beneficial to use a microstrip geometry so that we can take advantage of the equations developed by Yassin and Withington [27]. These equations, based on conformal mapping, allow the loss to be calculated accurately and analytically. Using them results in the propagation constant, $\gamma = \alpha + i\beta$, which includes the losses, and the characteristic impedance of the line, Z_0.

The input impedance of a shorted transmission line, Z_{line}, is

$$Z_{line} = Z_0 \tanh \gamma l = Z_0 \tanh \left(\frac{\beta}{2Q_i} + i\beta \right) l, \tag{4.7}$$

where l is the length of the line. For an ideal line $\alpha = 0$, and so when $l = \lambda/4$, the input impedance $Z_{line} \to \infty$. We have expressed the result in terms of the internal quality factor $Q_i = \beta/(2\alpha)$, which describes the losses. Obviously, an ideal line has an infinite Q_i.

The resonator is capacitively coupled at its open end to a readout line. A schematic of the relevant circuit components is given in Fig. 4.1. The capacitance of the gap, C_g, loads the resonator, and so at resonance the line is not exactly $\lambda/4$ long. Rather, resonance occurs when the capacitive impedance looking into the gap is equal in magnitude to the inductive impedance looking into the resonator. The total series impedance, as seen by the readout line, is given by

$$Z_L = \frac{1}{i\omega C_g} + Z_0 \tanh \gamma l, \tag{4.8}$$

where the second term is given by Eq. 4.7. In reality, the whole element consists of a through transmission line with the gap and resonator connected in parallel at some intermediate position. The forward scattering parameter between the input and output ports, S_{21}, becomes

$$S_{21} = \frac{2}{2 + Z_{trl}/Z_L}, \tag{4.9}$$

where Z_{trl} is the characteristic impedance of the through line, and Z_L the impedance looking into the coupling gap, as given by Eq. 4.8. S_{21} can be written in terms of its amplitude $|S_{21}|$ and phase θ, according to $|S_{21}|e^{i\theta}$, which are the quantities recorded by the readout electronics.

4.2.2 Power dissipation

Now we are able to calculate the amplitude and phase of the resonance curve as a function of temperature. For temperatures well below T_c, the losses are exceedingly small, but nevertheless finite, and therefore the resonator absorbs power. The quality factor of the resonator can be defined as $1/Q = 1/Q_c + 1/Q_i$, where Q_c is the coupling quality factor. At low temperatures, the Mattis and Bardeen theory predicts that the internal quality factor, Q_i, should increase exponentially as the temperature is lowered. Measurements show, however, the internal quality factor saturates at values of around 10^5 - 10^6 at $T/T_c \approx 0.2$ for our resonators, which means that an additional dissipative mechanism is present. The source of this loss may be due to excess quasiparticles [28],

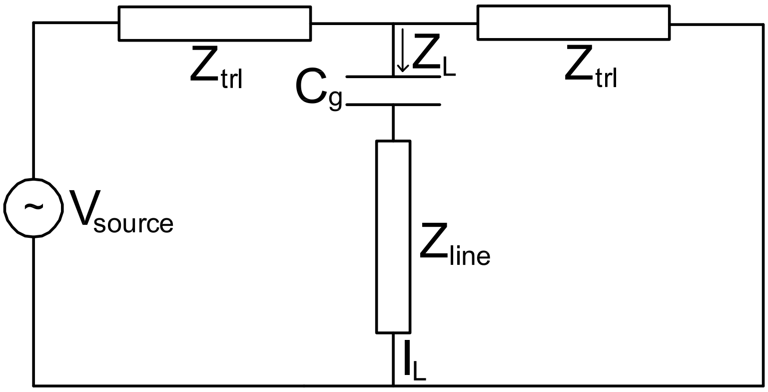

Figure 4.1: Circuit schematic of the resonator, with Z_L the loaded impedance of the resonator, Z_{line} the resonator impedance without coupling gap, C_g the capacitance of the coupling gap, V_{source} the voltage of the source, I_L the current in the load and Z_{trl} the impedance of the througline.

loss at the surface of the superconductor, or in the dielectric material, but the exact origin is not known [29, 30]. To make an improved estimate of the dissipated power, we take this saturation into account by modifying the internal quality factor in Eq. 4.7 by

$$\frac{1}{Q_i} = \frac{1}{Q_{i,MB}} + \frac{1}{Q_{sat}}, \tag{4.10}$$

where Q_{sat} is the saturation quality factor and $Q_{i,MB}$ the quality factor following the Mattis-Bardeen equations. In the calculations presented here we assume that the additional loss is due to quasiparticles, which is reasonable since we are interested in high readout powers, and dielectric loss saturates at power levels well before non-linearities occur [30, 31]. This refinement is not central to the model, and changes the results very little, but it does ensure that the model is consistent with what is seen experimentally.

Finally, we need to calculate the power dissipated in the resonator, which proceeds as follows. The power available from a microwave source, which we shall call the *readout power*, is taken conventionally to be

$$P_{readout} = \frac{V_{source}^2}{4Z_{trl}}, \tag{4.11}$$

where V_{source} is the Thévenin equivalent circuit voltage of the source. If this source is connected to the through transmission line of a KID, and the through line is terminated with a matched load, the current, I_L, flowing into the parallel component representing the coupling gap and resonator is given by

$$I_L = V_{source}\frac{1/Z_L}{Z_{trl}/Z_L + 2}, \tag{4.12}$$

Parameter	Symbol	Value
Strip length	l	4 mm
Strip width	w	3 μm
Film thickness	t	200 nm
Dielectric height	h	200 nm
Gap capacitance	C_g	5 fF
Relative permittivity of dielectric	ϵ_r	11
Throughline impedance	Z_{trl}	20 Ω
Designed resonant frequency	f_0	4.26302 GHz

Table 4.1: Parameters of the microstrip resonators simulated.

where Z_L is the parallel load impedance, which is given by Eq. 4.8. Finally, the power dissipated in the load, P_{diss}, which is actually the power dissipated in the resonator because the coupling gap is lossless, is given by

$$P_{diss} = |I_L|^2 R_L, \tag{4.13}$$

where R_L is the resistance of the load, which is given by the real part of Eq. 4.8.

The dissipated power depends on how much power is coupled into the resonator, and therefore peaks at the resonant frequency. The resonant frequency is temperature dependent, and therefore the dissipated power is temperature dependent. In fact, we can define a resonant temperature for a particular readout frequency. This effect is shown in Fig. 4.2, where the dissipated power has been calculated for an Al microstrip resonator as a function of temperature, for different readout frequencies. The geometrical factors used in the simulation are listed in Table 4.1, and the parameters of Al were taken to be $N_0 V_{sc} = 0.17$, $T_D = 420$ K, and $\rho = 2.4$ $\mu\Omega$cm [32]. The simulations were carried out with a readout power of 2 nW (-57 dBm) and a bath temperature 120 mK.

We observe that the resonant temperature falls as the readout frequency is increased, as expected, because the resonant frequency always falls as the temperature is increased. At the highest readout frequencies, where the zero-temperature resonant frequency is approached, a plateau appears as a direct consequence of the saturation of the quality factor, Eq. 4.10.

4.2.3 Heat transport

The energy absorbed by the resonator leads to a heating of the quasiparticle system, which cools by transferring energy to the phonon system of the superconductor, and from the phonon system of the superconductor to the phonon system of the substrate. Equilibrium is established, for a particular readout frequency and readout power, when these rates are equal. The rate of heat loss will certainly increase as the temperature of the quasiparticles increases relative to that of the phonons, but what is the functional form of this relationship?

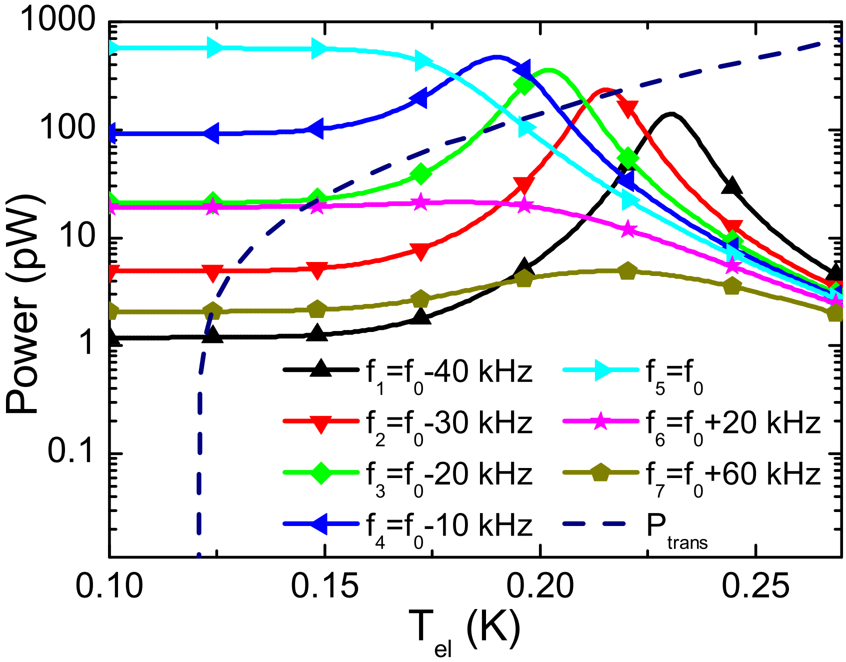

Figure 4.2: Power dissipated in an Al microstrip resonator as a function of temperature for different readout frequencies. The low temperature resonance frequency $f_0 = 4.26302$ GHz. The readout power is -57 dBm. The dashed line shows the electron-phonon cooling power as a function of temperature according to $P_{e-ph} = V\Sigma(T_{el}^5 - T_{ph}^5)$, for a phonon temperature of 120 mK.

In the case of a metal, the rate of energy transport, from electrons to phonons, is described by the power law [33]

$$P_{e-ph} = V\Sigma(T_{el}^5 - T_{ph}^5), \tag{4.14}$$

where T_{el} is the electron temperature, T_{ph} the phonon temperature, and V the interaction volume. Σ is a material constant, and in the calculations reported in this paper, we used a value of $\Sigma = 0.2 \times 10^9$ Wm^{-3}K^{-5} for Al, as measured using a Coulomb-blockade electrometer [34]. The volume was calculated through $V = wtl$, where w and l are the width and length of the microstrip line, and t is the thickness of the film. For an Al microstrip with the dimensions given in Table 4.1, $V\Sigma = 480$ nWK^{-5}. The dashed line in Fig. 4.2 shows the power transported by electron-phonon coupling as a function of temperature, for a phonon temperature of 120 mK.

The system comes into equilibrium where the heating and cooling curves cross, and it is seen that multiple solutions can exist. As will be described, these different solutions give rise to hysteretic switching. A key point, however, is that although we might question whether Eq. 4.14 has the correct functional form for a superconductor, and whether the interaction volume should be reduced to account for the current density varying along the length of the resonator, the qualitative behaviour remains unchanged.

Widely varying cooling curves result in the same generic behaviour. We have carried out simulations using exponential cooling functions, and the same behaviour is seen.

A further complication is that the Kapitza boundary conductance between the phonon system of the film and the phonon system of the substrate might affect the functional form of the cooling. Kapitza coupling is described by the power law

$$P_{Kap} \;=\; A\Sigma_{Kap}(T^4 - T^4_{bath}), \tag{4.15}$$

where $A = wl$ is the area of the microstrip line, and Σ_{Kap} depends on the materials used. In general, this conductance needs to be added in series with that of the quasiparticle-phonon coupling. From Ref. [35] we estimate Σ_{Kap} to be 850 $\mathrm{Wm^{-2}K^{-4}}$ and $A\Sigma_{Kap} = 10\ \mu\mathrm{WK^{-4}}$, and therefore in the simulations that follow, we assume that the Kapitza conductance can be neglected.

A further possibility is that resonators are fabricated on thin (<1 μm) silicon nitride membranes for the purpose of increasing the quasiparticle lifetime, which has certain potential advantages for KIDs. The thermal transport properties of suspended membranes have been studied extensively in the context of low-noise Transition Edge Sensors. The thermal conductance of a mesoscopic dielectric support depends on a number of factors, including the dimensionality of the phonon system, which effectively varies with temperature. The power flow from a suspended membrane to the bath is described by

$$P_{mem} \;=\; K(T^n - T^n_{bath}), \tag{4.16}$$

where K is a geometry-dependent factor, and n the power-law coefficient, which has been shown by a number of groups to have a value in the range $3 - 4$, depending on the geometry and material used [36, 37]. Over the temperature range 50 - 300 mK, structures can be produced that have thermal conductances in the range 0.1 $\mathrm{pWK^{-1}}$ to 500 $\mathrm{pWK^{-1}}$.

The key point about this discussion is that, for all of the mechanisms listed, the relationship between power flow and temperature takes the form of a simple power law. Thus, although the quantitative details will differ, Fig. 4.2 indicates that the different cooling functions will give rise to the same general behaviour.

4.2.4 Steady state temperature

To this point we have said nothing about how the equilibrium temperature can be determined numerically. Calculating the steady-state temperature for different readout frequencies and power levels is equivalent to finding the intersection points of the heating and cooling curves in Fig. 4.2. For low readout power levels, the curves have only one intersection point, which occurs at temperatures very close to the bath temperature, and ideally, one would always operate a KID in this way.

For the readout power used in Fig. 4.2 (2 nW), however, the number of intersection points depends on the readout frequency. For the lowest frequencies, f_1 and lower, there is only one intersection point, which is close to the bath temperature. For high frequencies, f_4 and higher, there is again only one intersection point, but now it is significantly above the bath temperature. Frequencies in between show three intersection points, implying that there are three different solutions to the heat balance equation.

It is easy to show that the highest and lowest temperature solutions are stable, but the middle one is not. Imagine that some external source of energy, or fluctuation such as generation-recombination noise, causes the temperature of the quasiparticle system to increase or decrease impulsively. Inspection of Fig. 4.2 shows that for the highest and lowest solutions, the temperature will relax back to its equilibrium state after the impulse has finished. The middle point, however, will either flip to the upper solution, because heating dominates cooling, or to the lower solution, because cooling dominates heating, respectively.

In our simulation software, the steady-state temperatures were calculated, for every frequency, using a root-finding algorithm. The algorithm searches for the temperature that reduces the error $\xi(T) = P_{diss} - P_{e-ph}$ to zero. The iterative procedure

$$T_{k+1} \quad = \quad T_k - \gamma \frac{\partial T}{\partial \xi} \xi(T_k), \tag{4.17}$$

where T_k is the temperature at iteration k, is particularly effective because it has a quadratic rate of convergence near the solution. γ is a multiplicative constant having a value of between 0 and 1; typically 0.7. It determines the size of the step taken at each iteration, and its value does not affect the final solution, but only the rate and stability with which the solution is found. Almost any guess can be used to initiate the procedure, but in the case where some parameter is varied, say the readout frequency or readout power, the solution of the previous calculation can be used as the starting point of the next calculation.

For low power levels the implementation of the algorithm is straightforward since there is only one solution to the steady-state temperature, which is close to the bath temperature. In the case of multiple solutions, then by using the solution of the previous calculation, say when sweeping the frequency, as the starting guess of the next calculation, the procedure will follow the desired root in a smooth manner. Only when a root ceases to exist will the procedure switch to an available solution. Sweeping up or down in frequency leads to jumps, which as will be seen are hysteretic.

A calculation was performed using the algorithm described above for the Al resonator of Section 4.2.2, with a phonon temperature of 120 mK. The resulting quasiparticle temperature and transmission amplitude are plotted as a function of frequency in Figures 4.3 and 4.4. The markers used are the same as those of Fig. 4.2, in the sense that a given symbol marks the point on Fig. 4.3, and Fig. 4.4, where the corresponding frequency curve of Fig. 4.2 has a solution by crossing the cooling curve. The

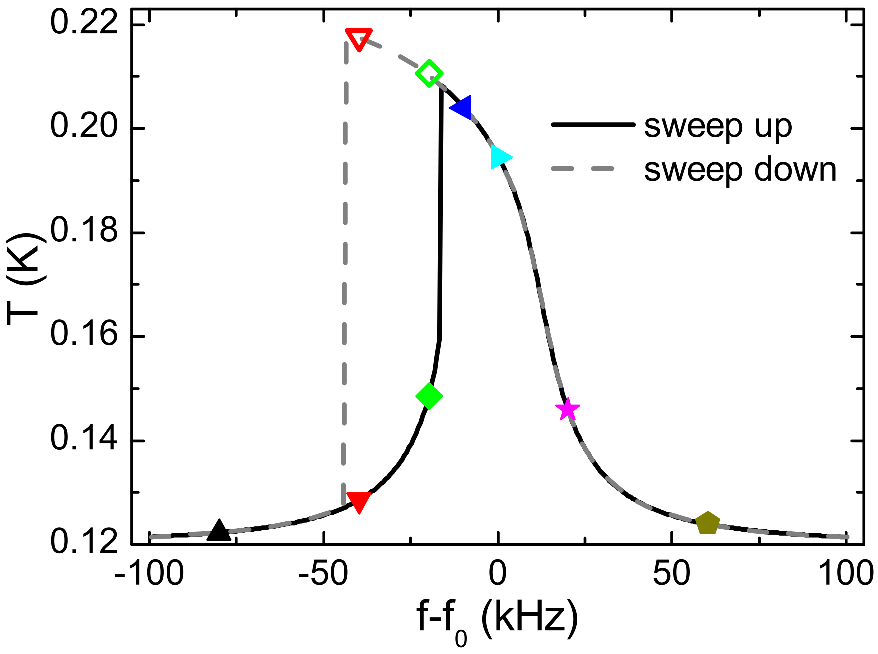

Figure 4.3: Steady-state temperature of the quasiparticles due to readout-power heating, assuming quasiparticle-phonon limited cooling. The markers correspond to the points of intersection of the heating and cooling curves in Fig. 4.2. The filled/open symbols show when the temperature is in the first/second stable state. The low temperature resonance frequency $f_0 = 4.26302$ GHz.

solid symbols correspond to tracing the solution when the frequency is increasing (the low-temperature solutions), and the open symbols to the case when the frequency is decreasing (the high-temperature solutions).

The origin of the hysteresis in the resonance curve can be explained by comparing Fig. 4.2 with Figures 4.3 and 4.4. Sweeping up in frequency means starting at a frequency f_1 or lower, which has only one solution, close to the bath temperature. When the frequency is increased to f_2, three solutions are possible, of which only the lowest and highest are stable, as discussed previously. If there are no large noise fluctuations, it can be assumed that at f_2 the system will remain in the low temperature state (indicated with a '▼'). The same situation prevails at f_3, as indicated by the symbol '♦'. By f_4 the low-temperature state is unavailable, and the system switches to the high-temperature state, as indicated with the symbol '◄'. As a consequence, the resonance curve, Fig. 4.4, has a sharp downward transition. For frequencies f_5 to f_7, the steady-state temperature decreases again, which completes the resonance curve for sweeping up in frequency. It is also clear that the noise spectrum of the readout signal will be altered significantly in the region close to the transition, an effect that is seen experimentally.

Sweeping down in frequency means starting at a frequency f_7 or higher, giving

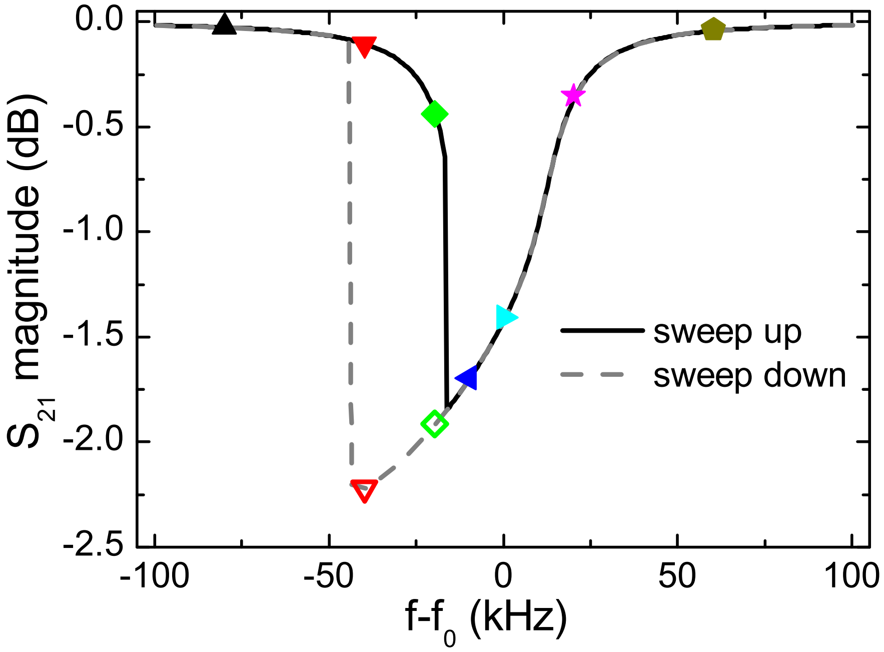

Figure 4.4: The resonator response curves, $|S_{21}|$, corresponding to the temperature curves in Fig. 4.3.

a steady-state temperature close to the phonon temperature. Frequencies f_6, f_5 and f_4 show an increasing temperature, until the region is reached where three solutions are available, f_3. Again, assuming that the temperature noise levels are small, the quasiparticle system will initially be in the high-temperature state, marked with the symbol '$\Diamond$' in Fig. 4.2. By the time f_2 is reached, as marked by the symbol '∇', a noise fluctuation is able to drive the instantaneous temperature below the middle state, and the system switches to the low-temperature state, as shown in Fig. 4.3. The noise is no longer sufficient to switch it back. Interestingly, the overall Q of the resonator influences the exact frequency at which switching occurs. Finally, as the frequency comes down to f_1 and lower, only the low-temperature state is available, and the cycle is completed.

So far, σ_1 and σ_2 are calculated in every iteration step by numerically integrating Equations 4.1 and 4.2, and Δ is calculated by numerical inversion of Eq. 4.5. At low temperatures and frequencies, $\hbar\omega, kT \ll 2\Delta$, the integrals for σ_1 and σ_2 can be expressed analytically [38]. If one would also take a fixed value for Δ, P_{diss} can be expressed analytically. The steady state temperature still needs to be solved with a non-linear solver, but the procedure will be much faster. This analytical approach gives results reasonably close to the numerical strategy for $T/T_c < 0.2$. Since we did not want to limit ourselves to a certain temperature range, we used the full numerical approach for the calculations presented in this paper. We also performed a full set of simulations using the analytical formulae, which shows they are accurate to within 10% for the operation temperature and overestimate the power handling by only 3 dB, provided

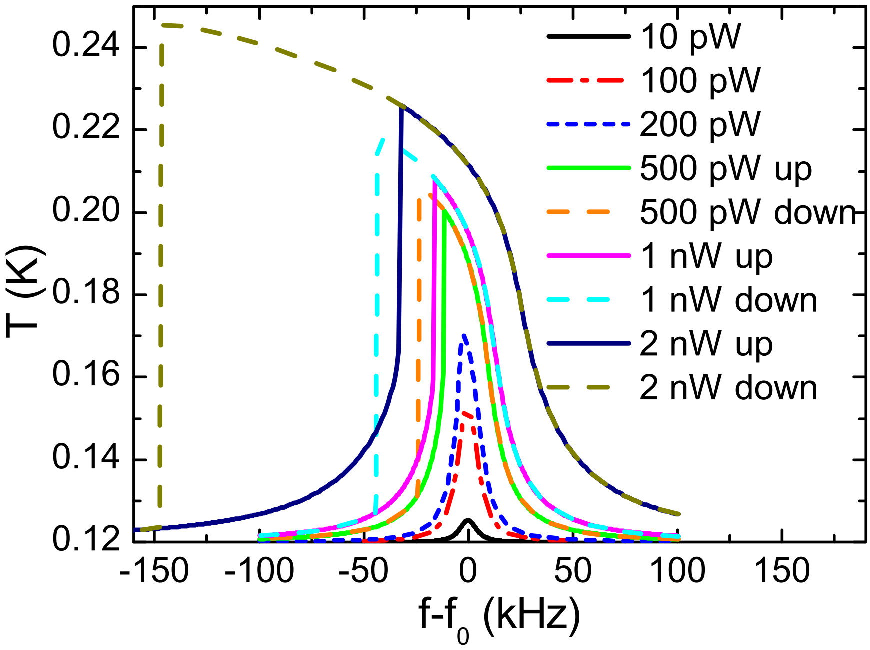

Figure 4.5: Calculated steady-state temperature of the quasiparticle system due to microwave heating for an Al microstrip resonator, shown as a function of frequency for different readout power levels and with $f_0 = 4.26302$ GHz.

the temperature does not exceed $T/T_c = 0.2$.

4.3 Extended simulations

In this section we present an extended set of simulations, which explore additional features of the model.

4.3.1 Switching and hysteresis in the resonance curve

We have still to consider how the shape of the resonance curve changes as the readout power level is increased. In Figures 4.5 and 4.6 the steady-state quasiparticle temperature and transmission amplitude of the Al resonator described previously are shown as a function of frequency for a set of readout powers. It can be seen that below 10 pW the internal temperature rise is small, and the resonance curve shows a deep symmetrical response. At 100 pW the quasiparticle temperature at resonance is already 30 mK above the phonon temperature, making the resonance curve less pronounced. At 200 pW there is a 50 mK temperature rise, and the resonance curve becomes asymmetrical. By 500 pW switching with hysteresis appears, with the hysteresis becoming more pronounced as the power is increased further.

Since the phonon temperature appears in the power law for heat transport, Eq. 4.14,

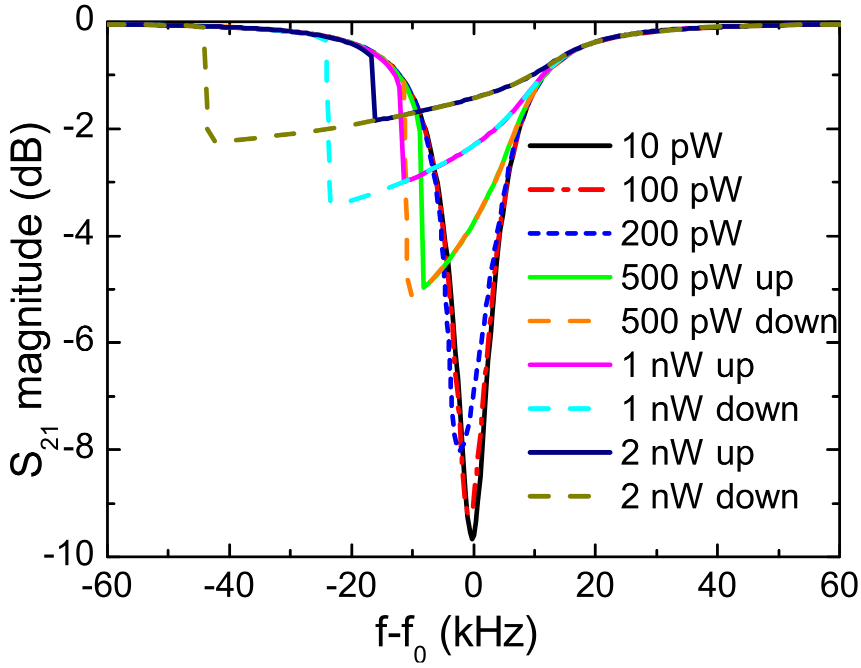

Figure 4.6: The resonator response curves, $|S_{21}|$, corresponding to the temperature curves in Fig. 4.5.

the power at which sufficient heating occurs for switching, decreases slightly if the phonon temperature is increased for the same resonator. If the phonon temperature is increased from 80 mK to 150 mK, switching occurs for the Al resonator at half the power level. The power threshold for switching will increase if the electron-phonon coupling (Σ) is stronger.

The power at which switching occurs increases with approximately the thickness squared in the simulations. The thickness dependence of the surface impedance and the thickness dependence in the heat transport law, Eq. 4.14, contribute to this dependence. In Fig. 4.6 for a 100 nm film, switching occurs at -63 dBm (500 pW) where for a 40 nm film, the switching occurs at -71 dBm and for 250 nm at -59 dBm. The power handling decreases if the length of the resonator decreases (and the resonance frequency increases), because the dissipation volume decreases. In the frequency region of interest (1-10 GHz) there is no significant resonance frequency dependence if one leaves out the change in dissipation volume.

A higher conductivity of the film, σ_N (or a lower resistivity ρ), will lead to a decrease in resistive losses and therefore the power handling will be larger.

In general, the dissipated power into the quasiparticle system can be related to the readout power and quality factors by [4] $P_{diss} = P_{readout}\frac{2Q^2}{Q_iQ_c}\chi_{qp}$, valid at resonance, where $\chi_{qp} = Q_i/Q_{i,qp}$ is the fraction of the dissipated power that goes into the quasiparticle system. In this paper we assumed $\chi_{qp} = 1$ as discussed in Sec. 4.2.2. This formula implies that the maximum readout power absorption occurs when $Q_i = Q_c$. If the quality factor is limited by coupling ($Q \approx Q_c << Q_i$), a lower Q_i will give a higher dissipation, leading to switching at lower readout powers.

4.3.2 Niobium and Tantalum

The simulations reported so far have been limited to Al. Other materials, such as Nb ($T_c \approx 9$ K) and Ta ($T_c \approx 4$ K), are also interesting for KIDs, and so it is beneficial to explore their behaviour. In fact we have performed a full set of simulations for these materials, and found the same general behaviour as for Al.

Looking at the power law for quasiparticle-phonon limited heat transport, Eq. 4.14, we expect that for higher T_c materials, more power is needed to set-up a significant temperature difference. Superconducting resonators are operated ideally at $T \approx T_c/10$ [1]. For a Nb resonator with the same geometry as in Table 4.1, but with $N_0V_{sc} = 0.306$, $T_D = 228$ K, $\rho = 14$ $\mu\Omega$cm, and a phonon temperature of 1 K, the power needed to get sufficient heating for switching is 10μW (-20 dBm), assuming the same quasiparticle-phonon coupling. For a Ta resonator with the same geometry, and $N_0V_{sc} = 0.25$, $T_D = 247$ K, $\rho = 13$ $\mu\Omega$cm, and a phonon temperature of 0.4 K, the power needed for switching is 300 nW (-35 dBm), assuming the same quasiparticle-phonon coupling. Inspection of Eq. 4.14 shows that for a material with a higher T_c, the power that can be transported by electron-phonon coupling can be much higher, before a temperature of $T_c/5$ is reached. Therefore, the model predicts a higher power handling for materials with a higher T_c. The mentioned power levels for Nb and Ta are sufficiently high that another mechanism may cause the resonator to saturate, before the heating described here comes into effect. A detailed experimental study is needed before this question can be answered, but it is interesting to note that Nb resonators show, experimentally, the same general behaviour as our simulations predict [39].

4.3.3 Resonators on membranes

In Section 4.2.3, we mentioned the possibility of fabricating superconducting resonators on suspended silicon nitride membranes. The heat transported through thin legs can be described by $P_{mem} = K(T^n - T^n_{bath})$, with $K = 10$ pW/K^n as an achievable but low value and n is about 3. The quasiparticle-phonon coupling and Kapitza coupling will generally be much greater, and therefore the most significant temperature difference will be between the membrane and bath. Using this new power law, with a bath temperature of 120 mK, the steady-state temperature of a membrane-supported Al KID was calculated for a number of readout power levels. The curves are the same as those in Fig. 4.6, only the power levels are different. Hysteretic switching is present for power levels of 200 fW and higher, which is three orders of magnitude lower than for the quasiparticle-phonon limited heat transport, but high enough to operate as a detector.

4.4 Experimental results

To illustrate the key features of readout-power heating, we present a set of experimental results that are characteristic of the behaviour seen in many low-T_c materials, measured by a number of different groups. A 100 nm thick Al film was sputtered onto an R-plane sapphire substrate under ultra high vacuum conditions. The critical temperature of the film T_c was 1.228 K, the low temperature resistivity ρ was 0.63 $\mu\Omega$cm, and the residual resistance ratio 5.2. A coplanar thin-film waveguide (CPW) resonator was used in the experiment, and therefore we can only make a qualitative comparison with the simulations. The chip was cooled in a cryostat with an Adiabatic Demagnetization Refrigerator to a bath temperature of 81mK, and the complex transmission S_{21} was measured using a cooled HEMT amplifier and a vector network analyzer.

$|S_{21}|$ is shown as a function of frequency in Fig. 4.7, for a range of readout power levels. Below -81 dBm, at the chip, the resonance curve was independent of the incident readout power, and it is in this range that a KID would normally be operated. A decrease in the absolute amplitude of the noise was observed as the readout power was increased, which is a well-known phenomenon. As the readout power was increased further, up to -70 dBm, the curve distorted, which is a sign of heating, because the resonance frequency shifts in the same direction as when the bath temperature is increased. Crucially at -69 dBm a discontinuity appeared. Although not shown here, because different apparatus had to be used to avoid blanking of the readout signal during frequency sweeping, it has also been confirmed that the resonance curves are hysteretic with the frequency interval between the switching events in the two sweep directions increasing as the power level is increased. It was also observed that the spectrum of the noise fluctuations on $|S_{21}|$ changed markedly when the device was read out at a single frequency close to one of the discontinuities. All of these observations are consistent with the phenomena predicted by our simple model.

4.5 Discussion

The major assumption behind the simple model developed in this paper is that the quasiparticle distribution under microwave absorption can be described as a thermal distribution at elevated temperature. Secondly, that the limited electron-phonon transport, which leads to the elevated temperature, can be described by a power law. Although the non-linear behaviour is well described by this model, the description of the microwave absorption can be refined, to correctly account for the microscopic properties of the superconductor. The microwave field in the resonator varies along the length of the resonator and therefore microwave absorption will have a spatial dependence. Eliashberg and coworkers formulated the rate with which the quasiparticle distribution is changed by the vector pontential of the microwave field [40, 41]. Given this rate of change, the framework of Chang and Scalapino [42] provides a way to calculate

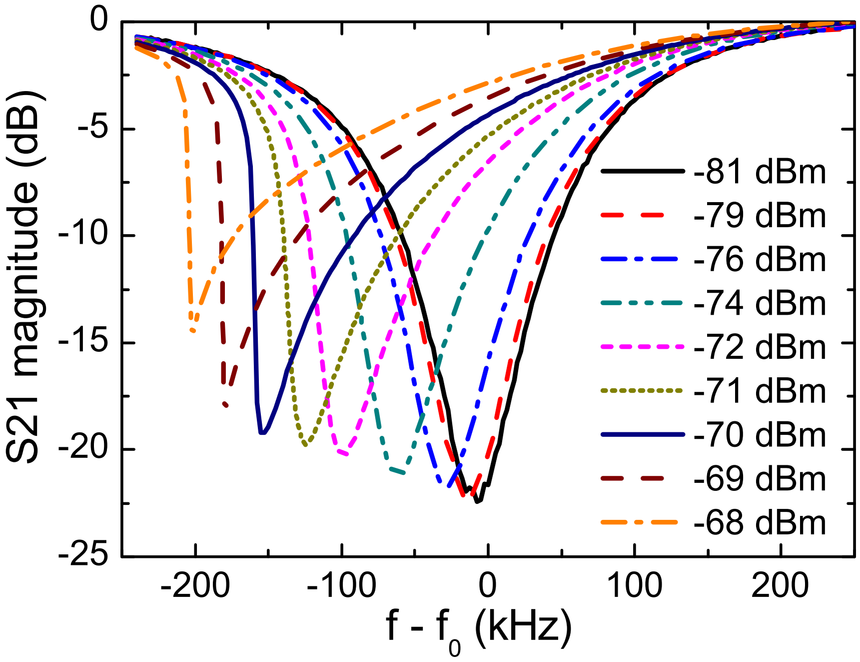

Figure 4.7: Experimental resonance curves of an Al coplanar waveguide resonator for different readout power levels. The bath temperature was 81 mK and $f_0 = 4.55929$ GHz.

the steady state quasiparticle- and phonon distributions in the superconductor if the electron-phonon coupling and the phonon escape time in the film are known. In future research, we will include this framework, together with the spatially varying field, into the model and compare it with the thermal approximation we made here. The framework may also be used to model and optimize the detector sensitivity [4].

Because the work reported here was undertaken to establish the principles of the approach, the simulations were carried out using the loss equations of a microstrip line, which are particularly straightforward to use. Similarly accurate equations for coplanar line are not readily available. Also, we have used a cooling curve that was formulated for normal metals rather than superconductors, and therefore it is not possible to perform a detailed numerical comparison. It is essential to appreciate, however, that the key elements of the model follow directly from the general shape of the power-absorption curve of the resonator, and the general shape of the cooling curve of the quasiparticle system; the observed behaviour does not depend in a critical way on experimental parameters. The current distributions, and therefore the losses in the two geometries, are not dramatically different, and therefore we would expect the power levels at which the effects are seen to be of the same order of magnitude.

We also assumed a volume $V = wtl$ in which the microwave power is dissipated and the electron-phonon transport takes place. The microwave field only extends about the distance of the penetration depth into the metal, which is around 80 nm for Al, of the order of the film thickness. However, the quasiparticle diffusion time on the scale of the strip width (3 μm) is less than a nanosecond. Since the relaxation processes are slower, the assumption of uniform electron-phonon transport over the strip crossection is justified. On the length of the strip, the current distribution is proportional to $cos^2(x)$, with x the coordinate along the length of the strip. Since this is a smoothly rising function, we estimate the error of taking the whole length of the strip to be a factor of two at maximum.

We have assumed that dielectric loss is not present at any significant level, but we did restrict the Q_i to some maximum value Q_{sat}, and it is known that dielectric loss decreases with increased power [30]. If dielectric loss, or even radiation loss, is present then we might expect switching to occur at a slightly higher readout power. Power dissipation in the superconductor and the dielectric could be distinguished in the model. From the simulations we would expect that switching, in the case of quasiparticle-phonon limited transport, for a 100 nm thick film, to be present for powers higher than -63 dBm (500 pW), whereas we get a value of -69 dBm (125 pW) from the measurements presented in Fig. 4.7. Given the assumptions made, these are pleasingly similar. We are currently carrying out a detailed quantitative study, comparing simulated resonance curves with experimental measurements on films having different thicknesses (10 nm - 100 nm), and these will be reported shortly.

The resonance curves presented in Fig. 4.7 are representative of all of the superconducting resonators we have measured over a number of years: many Nb, Ta, and Al resonators on a variety of substrates, in a number of different cryogenic systems. Although the results are quantitatively different they are all qualitatively the same. The only difference was in a single measurement on a Nb resonator, when two discontinuities where seen when sweeping the frequency in the same direction [39]. This observation can now be understood in terms of an inadvertent double-dip on the power absorption curve of the resonant circuit, leading to 3 stable and 2 unstable quasiparticle temperature states.

If it is demonstrated that the mechanism described in this paper is responsible for the observed behaviour of KIDs, as distinct from say exceeding the critical current at the edges of the film, where the current density is high, then the heating model will be of considerable importance. For example, it is interesting to observe that if we can calculate the power absorption curve of the resonator accurately, then it should be possible to recover, from large-signal measurements of resonance curves, the precise functional form of the quasiparticle-phonon cooling function, which would be of great interest in its own right. Both the distortion of the resonance curve, and the frequencies of the switching events, can be used to uncover information about the microscopic physics involved.

An alternative approach is to measure the scattering parameters, both S_{11} and S_{21}, as a function of bath temperature for low readout powers, and thereby calculate the absorbed power as a function of bath temperature. Assuming that the observed heating is the same as when power is absorbed by the quasiparticle system directly, then the cooling curve can be recovered from high readout-power measurements at the bath base temperature, without the need for microwave simulations.

4.6 Conclusions

We have presented a model for non-linear behaviour due to readout-power heating in Kinetic Inductance Detectors. It has been shown that the power dissipated in a superconducting resonator, as a function of temperature, has a peak such that when combined with a typical monotonically increasing cooling curve, leads to two stable and one unstable quasiparticle temperature states. The exact form of the cooling curve, whether due to quasiparticle-phonon coupling or Kapitza boundary effects, does not change the general form of what is seen: at low power levels, the intrinsic behaviour of the resonator is measured, at medium power levels, the resonance curve distorts, and at high power levels, switching appears. The switching is hysteretic in the frequency domain, and the frequency difference between the transition points increases as the readout power is increased. All of these effects are seen in both the simulations and in experiments.

Not only is our model potentially important for optimising the behaviour of KIDs, it may also open the door to interesting physics. For example, it should be possible to recover the precise functional form of the cooling mechanism. The work also shows that it should be possible to operate resonators on suspended membranes, and therefore it should be possible to study the way in which the cooling changes as a function of the dimensionality of the phonon system of the substrate.

Intriguingly, using the hysteresis, it may be possible to make a photon-counting detector that latches after an event has occurred, and which is then reset by offsetting the frequency of the readout source.

This work was carried out during three months a visit of Pieter de Visser to the Department of Physics at the University of Cambridge, which was partially financed by an Erasmus grant. We thank T. M. Klapwijk for valuable discussion.

References

[1] P. K. Day, H. G. LeDuc, B. A. Mazin, A. Vayonakis, and J. Zmuidzinas, *A broadband superconducting detector suitable for use in large arrays*, Nature **425**, 817 (2003).

[2] J. Gao, M. Daal, J. M. Martinis, A. Vayonakis, J. Zmuidzinas, B. Sadoulet, B. A. Mazin, P. K. Day, and H. G. Leduc, *A semiempirical model for two-level system noise in superconducting microresonators*, Appl. Phys. Lett. **92**, 212504 (2008).

[3] R. Barends, H. L. Hortensius, T. Zijlstra, J. J. A. Baselmans, S. J. C. Yates, J. R.

Gao, and T. M. Klapwijk, *Noise in NbTiN, Al and Ta superconducting resonators on silicon and sapphire substrates*, IEEE Trans. on Appl. Supercond. **19**, 936 (2009).

[4] H. G. Leduc, B. Bumble, P. K. Day, B. H. Eom, J. Gao, S. Golwala, B. A. Mazin, S. McHugh, A. Merrill, D. C. Moore, O. Noroozian, A. D. Turner, and J. Zmuidzinas, *Titanium nitride films for ultrasensitive microresonator detectors*, Appl. Phys. Lett. **97**, 102509 (2010).

[5] J. Gao, L. R. Vale, J. A. B. Mates, D. R. Schmidt, G. C. Hilton, K. D. Irwin, F. Mallet, M. Castellanos-Beltran, K. W. Lehnert, J. Zmuidzinas, and H. G. LeDuc, *Strongly quadrature-dependent noise in superconducting micro-resonators measured at the vacuum-noise limit*, Appl. Phys. Lett. **98**, 232508 (2011).

[6] A. V. Velichko, M. J. Lancaster, and A. Porch, *Nonlinear microwave properties of high T_c thin films*, Supercond. Sci. Technol. **18**, R24 (2005).

[7] A. Gurevich and R. Mints, *Self-heating in normal metals and superconductors*, Rev. Mod. Phys. **59**, 941 (1987).

[8] J. Wosik, L.-M. Xie, K. Nesteruk, D. Li, J. H. Miller, and S. A. Long, *Power handling capabilities of superconducting YBCO thin films: thermally induced nonlinearity effects*, J. of Supercond. **10**, 97 (1997).

[9] P. Lahl and R. Wördenweber, *Fundamental microwave-power-limiting mechanism of epitaxial high-temperature superconducting thin-film devices*, J. Appl. Phys. **97**, 113911 (2005).

[10] M. A. Golosovsky, H. J. Snortland, and M. R. Beasley, *Nonlinear microwave properties of superconducting Nb microstrip resonators*, Phys. Rev. B **51**, 6462 (1995).

[11] B. Abdo, E. Sergev, O. Shtempluch, and E. Buks, *Escape rate of metastable states in a driven NbN superconducting microwave resonator*, J. Appl. Phys. **101**, 083909 (2007).

[12] D. E. Oates, P. Nguyen, G. Dresselhaus, M. S. Dresselhaus, C. W. Lam, and S. M. Ali, *Measurements and modeling of linear and nonlinear effects in striplines*, J. of Supercond. **5**, 361 (1992).

[13] J. H. Oates, R. T. Shin, D. E. Oates, M. J. Tsuk, and P. P. Nguyen, *A nonlinear transmission line model for superconducting stripline resonators*, IEEE Trans. on Appl. Supercond. **3**, 17 (1993).

[14] T. Dahm and D. J. Scalapino, *Theory of intermodulation in a superconducting microstrip resonator*, J. Appl. Phys. **81**, 2002 (1997).

[15] B. Yurke and E. Buks, *Performance of cavity-parametric amplifiers: employing Kerr nonlinearities, in the presence of two-photon loss*, J. Lightwave Technol. **24**, 5054 (2006).

[16] E. A. Tholén, A. Ergül, E. M. Doherty, F. M. Weber, F. Grégis, and D. B. Haviland, *Nonlinearities and parametric amplification in superconducting coplanar waveguide resonators*, Appl. Phys. Lett. **90**, 253509 (2007).

[17] C. C. Chin, D. E. Oates, G. Dresselhaus, and M. S. Dresselhaus, *Nonlinear electrodynamics of superconducting NbN and Nb thin films at microwave frequencies*, Phys. Rev. B **45**, 4788 (1992).

[18] G. Ghigo, R. Gerbaldo, L. Gozzelino, F. Laviano, G. Lopardo, E. Monticone, C. Portesi, and E. Mezzetti, *Local thermal bistability in MgB_2 microwave coplanar resonators: Opposite jumpwise response to weak-link switching and to vortex avalanches*, Appl. Phys. Lett. **94**, 052505 (2009).

[19] R. Monaco, A. Andreone, and F. Palomba, *Intermodulation measurements in Nb superconducting microstrip resonators*, J. Appl. Phys. **88**, 2898 (2000).

[20] J. Wosik, L. M. Xie, R. Grabovickic, T. Hogan, and S. A. Long, *Microwave power handling capability of HTS superconducting thin films: weak links and thermal effects induced limitation*, IEEE Trans. on Appl. Supercond. **9**, 2456 (1999).

[21] J. Kermorvant, C. J. van der Beek, J.-C. Mage, B. Marcilhac, Y. Lemaître, J. Briatico, R. Bernard, and J. Villegas, *Joule heating and high frequency nonlinear effects in the surface impedance of high T_c superconductors*, J. Appl. Phys. **106**, 023912 (2009).

[22] L. F. Cohen, A. L. Cowie, A. Purnell, N. A. Lindop, S. Thiess, and J. C. Gallop, *Thermally induced nonlinear behaviour of HTS films at high microwave power*, Supercond. Sci. Technol. **15**, 559 (2002).

[23] B. Abdo, E. Segev, O. Shtempluck, and E. Buks, *Intermodulation gain in nonlinear NbN superconducting microwave resonators*, Appl. Phys. Lett. **88**, 022508 (2006).

[24] R. Vijay, M. H. Devoret, and I. Siddiqi, *Invited review article: the Josephson bifurcation amplifier*, Rev. Sci. Instr. **80**, 111101 (2009).

[25] D. C. Mattis and J. Bardeen, *Theory of the anomalous skin effect in normal and superconducting metals*, Phys. Rev. **111**, 412 (1958).

[26] R. L. Kautz, *Picosecond pulses on superconducting striplines*, J. Appl. Phys. **49**, 308 (1978).

[27] G. Yassin and S. Withington, *Electromagnetic models for superconducting millimetre-wave and sub-millimetre-wave microstrip transmission lines*, J. Phys. D. Appl. Phys. **28**, 1983 (1995).

[28] J. M. Martinis, M. Ansmann, and J. Aumentado, *Energy decay in superconducting Josephson-junction qubits from nonequilibrium quasiparticle excitations*, Phys. Rev. Lett. **103**, 097002 (2009).

[29] R. Barends, J. J. A. Baselmans, J. N. Hovenier, J. R. Gao, S. J. C. Yates, T. M. Klapwijk, and H. F. C. Hoevers, *Niobium and tantalum high-Q resonators for photon detectors*, IEEE Trans. on Appl. Supercond. **17**, 263 (2007).

[30] J. Gao, M. Daal, A. Vayonakis, S. Kumar, J. Zmuidzinas, B. Sadoulet, B. A. Mazin, P. K. Day, and H. G. Leduc, *Experimental evidence for a surface distribution of two-level systems in superconducting lithographed microwave resonators*, Appl. Phys. Lett. **92**, 152505 (2008).

[31] R. Barends, N. Vercruyssen, A. Endo, P. J. de Visser, T. Zijlstra, T. M. Klapwijk, P. Diener, S. J. C. Yates, and J. J. A. Baselmans, *Minimal resonator loss for circuit quantum electrodynamics*, Appl. Phys. Lett. **97**, 023508 (2010).

[32] R. D. Parks, *Superconductivity*, volume 2, Marcel Dekker Inc. New York, 1^{st} edition, 1969.

[33] F. C. Wellstood, C. Urbina, and J. Clarke, *Hot-electron effects in metals*, Phys. Rev. B **49**, 5942 (1994).

[34] R. L. Kautz, G. Zimmerli, and J. M. Martinis, *Self-heating in the Coulomb-blockade electrometer*, J. Appl. Phys. **73**, 2386 (1993).

[35] E. T. Swartz and R. O. Pohl, *Thermal boundary resistance*, Rev. Mod. Phys. **61**, 605 (1989).

[36] T. Kühn, D. V. Anghel, J. P. Pekola, M. Manninen, and Y. M. Galperin, *Heat transport in ultrathin dielectric membranes and bridges*, Phys. Rev. B **70**, 125425 (2004).

[37] K. Rostem, D. J. Goldie, S. Withington, D. M. Glowacka, V. N. Tsaneva, and M. D. Audley, *On-chip characterization of low-noise microstrip-coupled transition edge sensors*, J. Appl. Phys. **105**, 084509 (2009).

[38] J. Gao, J. Zmuidzinas, A. Vayonakis, P. Day, B. Mazin, and H. Leduc, *Equivalence of the effects on the complex conductivity of superconductor due to temperature change and external pair breaking*, J. Low Temp. Phys. **151**, 557 (2008).

[39] G. Vardulakis, *Superconducting Kinetic Inductance Detectors, Theory, Simulations & Experiments*, PhD thesis, University of Cambridge, 2007.

[40] G. M. Eliashberg, *Film superconductivity stimulated by a high-frequency field*, JETP Lett. **11**, 114 (1970).

[41] B. I. Ivlev, S. G. Lisitsyn, and G. M. Eliashberg, *Nonequilibrium excitations in superconductors in high-frequency fields*, J. Low Temp. Phys. **10**, 449 (1973).

[42] J.-J. Chang and D. J. Scalapino, *Kinetic-equation approach to nonequilibrium superconductivity*, Phys. Rev. B **15**, 2651 (1977).

Chapter 5

Number fluctuations of sparse quasiparticles in a superconductor

We have directly measured quasiparticle number fluctuations in a thin film superconducting Al resonator in thermal equilibrium. The spectrum of these fluctuations provides a measure of both the density and the lifetime of the quasiparticles. We observe that the quasiparticle density decreases exponentially with decreasing temperature, as theoretically predicted, but saturates below 160 mK to 25-55 μm^{-3}. We show that this saturation is consistent with the measured saturation in the quasiparticle lifetime, which also explains similar observations in qubit decoherence times.

This chapter was published as P. J. de Visser, J. J. A. Baselmans, P. Diener, S. J. C. Yates, A. Endo, and T. M. Klapwijk, *Physical Review Letters* **106**, 167004 (2011).

5.1 Introduction

In a superconductor the density of unpaired electrons (quasiparticles) should vanish when approaching zero temperature [1]. This crucial property promises long decoherence times for superconducting qubits [2] and long relaxation times for highly sensitive radiation detectors [3]. However, relaxation times for resonators [4, 5] and qubit decoherence times [6–8] were shown to saturate at low temperature. Recent modeling [8, 9] suggests that non-equilibrium quasiparticles are the main candidate for this saturation, which was tested qualitatively by injecting quasiparticles into a qubit [10]. A direct measurement of the number of quasiparticles and the energy decay rate in equilibrium at low temperatures would provide new insight in superconductivity at low temperatures, crucially needed in the aforementioned fields.

At finite temperature, it follows from thermodynamics that the density of quasiparticles fluctuates around an average value that increases exponentially with temperature [11]. Here we report a measurement of the spectrum of these fluctuations in a single aluminium superconducting film ($T_c = 1.1$ K) in equilibrium, for temperatures from 300 mK to 100 mK. The number fluctuations show up as fluctuations in the complex conductivity of the film, probed with a microwave resonator. The spectrum of these fluctuations provides a direct measure of the number of quasiparticles in the superconductor. We observe that the quasiparticle density decreases exponentially with decreasing temperature until it saturates at 25-55 μm^{-3} below 160 mK. We prove that the measured saturation of the quasiparticle lifetime to 2.2 ms below 160 mK is consistent with the saturation in quasiparticle density. In addition, our experiment shows that it is possible to reach the fundamental generation-recombination noise limit in detectors based on Al resonators.

5.2 Quasiparticle number fluctuations in thermal equilibrium

In a superconductor in thermal equilibrium, the density of quasiparticles per unit volume is given by

$$n_{qp} = 2N_0\sqrt{2\pi k_B T\Delta}\,\exp(-\Delta/k_B T), \tag{5.1}$$

valid at $k_B T < \Delta$, with N_0 the single spin density of states at the Fermi level ($1.72 \times 10^{10}\ \mu\text{m}^{-3}\text{eV}^{-1}$ for Al), k_B Boltzmann's constant, T the temperature and Δ the energy gap of the superconductor. Two quasiparticles with opposite spins and momenta can be generated from a Cooper pair by a phonon with an energy larger than the energy gap. When two quasiparticles recombine into a Cooper pair, a phonon is emitted. These processes, schematically depicted in Fig. 5.1a, are random processes in equilibrium. Assuming a thermal distribution of quasiparticles and phonons at low temperature, the

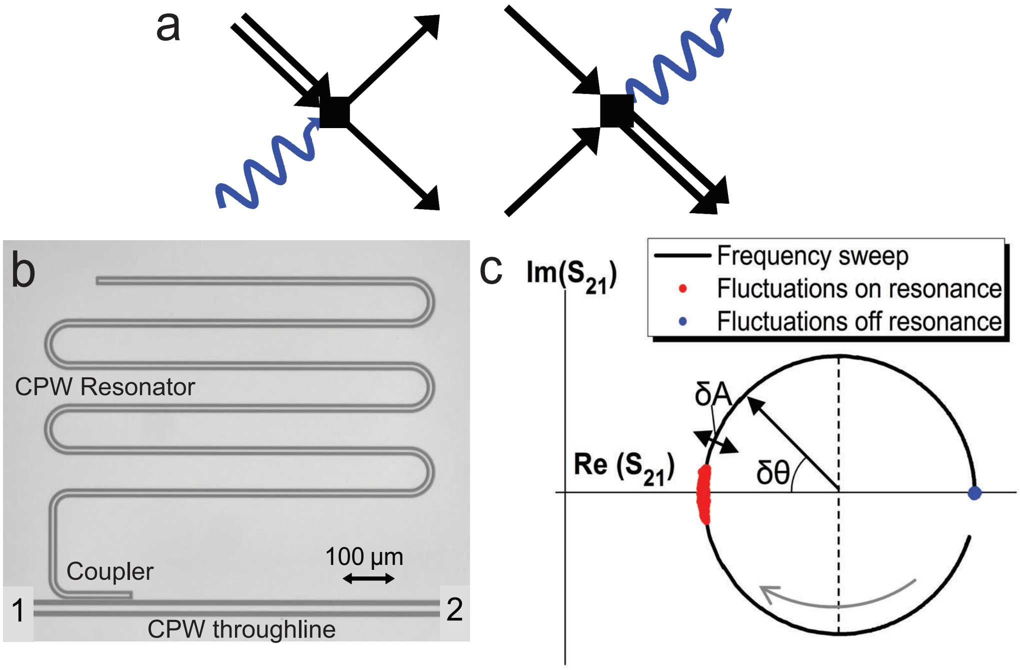

Figure 5.1: (a) Schematic of the process of generation (left) and recombination (right) of quasiparticles in a superconductor. The single arrow symbolises a quasiparticle, the double arrow a Cooper pair and the wavy arrow a phonon. (b) A microscope picture of the microwave resonator, two times reduced in length for visibility. The open ends set the half wavelength resonance condition. The coplanar waveguide (CPW) through line is used for the microwave excitation and readout (from contact 1 to 2) of the resonator. (c) The real and imaginary parts of the complex transmission S_{21} as a function of frequency around the resonant frequency. The gray arrow indicates the direction of increasing frequency. We define a resonator amplitude A and phase θ with respect to the resonance circle centre as indicated. In red, the measured fluctuations in S_{21} at the resonant frequency are shown. The fluctuations far off-resonance are shown in blue, which are used as a calibration for system noise contributions.

average quasiparticle recombination time is given by [12]

$$\tau_r = \frac{\tau_0}{\sqrt{\pi}} \left(\frac{k_B T_c}{2\Delta}\right)^{5/2} \sqrt{\frac{T_c}{T}} \exp(\Delta/k_B T) = \frac{\tau_0}{n_{qp}} \frac{N_0 (k_B T_c)^3}{2\Delta^2}, \tag{5.2}$$

where T_c is the critical temperature of the superconductor and τ_0 a material dependent, characteristic electron-phonon interaction time. Eqs. 5.1 and 5.2 predict a very low quasiparticle density and consequently a very long quasiparticle lifetime at temperatures $T < T_c/10$.

The process of random generation and recombination of charge carriers is a well-studied phenomenon in solid state physics, in particular in semiconductors, but has hardly been studied in superconductors. In one earlier experiment, this generation-recombination noise was identified in the current fluctuations through a tunnel barrier connected to a small Al quasiparticle box [13], although only down to an intermediate 210 mK. The general theory of quasiparticle number fluctuations in a superconductor [11, 13] connects the frequency dependence of the fluctuations to the microscopic dynamics of quasiparticle generation and recombination. The dominant timescale of these processes is the recombination time of a quasiparticle (τ_r is about 1 ms in an Al film [4]), because the phonon pair breaking time and the phonon escape time are both much shorter, about 10^{-10} s based on a film thickness of 40 nm [12, 14]. In thermal equilibrium, the generation and recombination rates are equal and the variance of the random number fluctuations $\sigma^2 = \left\langle \delta N_{qp}^2 \right\rangle = N_{qp} = n_{qp}V$, with V the volume of the system. The power spectral density of these fluctuations shows a Lorentzian spectrum, given by

$$S_N(\omega) = \frac{4N_{qp}\tau_r}{1+(\omega\tau_r)^2}, \tag{5.3}$$

with ω the angular frequency. Eqs. 5.1 and 5.2 show that the product $N_{qp}\tau_r$ is constant over temperature, whereas the total integrated power spectral density increases exponentially with temperature. This is because the bandwidth of the fluctuations increases exponentially with temperature as well, as it scales with $1/\tau_r^2$. We emphasise that this property is unique for quasiparticle generation-recombination noise in a superconductor.

5.3 Quasiparticle fluctuations in a microwave resonator

We measure the quasiparticle number fluctuations using a high-quality microwave resonator. The high frequency response of the superconductor is controlled by the quasiparticle density through the complex conductivity $\sigma_1 - i\sigma_2$. The real part, σ_1, is resistive and denotes the conductivity by quasiparticles. The imaginary part, σ_2, is inductive and due to the superconducting condensate, the Cooper pairs [15]. Quasiparticle number fluctuations will show up as fluctuations in the complex conductivity. To measure the complex conductivity, a 40 nm thick Al film was patterned into microwave resonators. The film was sputter-deposited onto a C-plane sapphire substrate. The critical temperature is 1.11 K, from which the energy gap $\Delta = 1.76k_BT_c = 168$ μeV. The low temperature resistivity $\rho = 0.8$ $\mu\Omega$cm and the residual resistance ratio RRR = 5.2. The film was patterned by wet etching into distributed, half wavelength, coplanar waveguide resonators, with a defined central line width of 3.0 μm and gaps of 2.0 μm wide (Fig. 5.1b). The resonator under consideration shows its lowest order resonance at 6.61924 GHz and has a central strip volume of 1.0×10^3 μm^3. The resonance curve at 100 mK shows a coupling limited quality factor of 3.87×10^4. The samples are cooled in a pulse tube pre-cooled adiabatic demagnetization refrigerator. The cold stage is surrounded by a superconducting magnetic shield inside a cryoperm shield. Special care has been taken to make the setup light tight, such that no excess quasiparticles are created by stray light. The sample is mounted inside a light tight holder which itself is placed inside another light tight box (also at base temperature), to prevent radiation leaking in via the coax cable connectors. Radiation absorber, consisting of carbon black, epoxy and SiC grains is placed inside both the sample holder and the outer box. The outer box is equipped with special coax cable filters that attenuate all frequencies above 10 GHz exponentially (see Ref. [16] for details). The system is proven to be light tight by measuring the quasiparticle lifetime as a function of the 4 K-stage temperature while keeping the sample at base temperature. Within the measurement accuracy (15%), there was no change in the lifetime, indicating that the stray-light power at the chip is negligible. For the lifetime measurements the sample is illuminated with a short pulse of light from a GaAsP LED (see Ref. [4]), fibre coupled to the sample via a 0.15 mm waveguide (a 1 THz high pass filter) to prevent pair breaking radiation from the 4 K environment to reach the sample[1].

The complex transmission of the microwave circuit is measured with a quadrature mixer and traces out a circle in the complex plane. The microwave signal is amplified at 4 K with a high electron mobility transistor (HEMT) amplifier and with a room temperature amplifier, before it is mixed with a copy of the original signal [3, 17]. We define a resonator amplitude and phase with respect to the resonance circle, as depicted in Fig. 5.1c. The resonator amplitude predominantly responds to changes in σ_1 [18] (therefore also called dissipation direction). The responsivity of the resonator amplitude to quasiparticles $dA/dN_{qp} = -2\alpha Q\kappa/V$, with Q the quality factor of the resonator, α the fraction of kinetic inductance over the total inductance and $\kappa = \frac{\delta\sigma_1/\sigma_2}{\delta n_{qp}}$, which depends only weakly on temperature. The amplitude responsivity was determined experimentally as described in Ref. [17]. dA/dN_{qp} is measured to be almost temperature independent. For similar resonators it is known that the sensitivity in phase is limited by two-level fluctuators [19, 20] and that the sensitivity in amplitude is up to a factor 10 better, limited by the HEMT amplifier [17].

The power spectral density due to quasiparticle number fluctuations in the resonator *amplitude* is given by

$$S_A(\omega) = S_N(\omega)\frac{(dA/dN_{qp})^2}{1+(\omega\tau_{res})^2}, \tag{5.4}$$

where τ_{res} is the resonator ringtime given by $\tau_{res} = \frac{Q}{\pi f_0}$. In this experiment $\tau_r \gg \tau_{res} \approx 2$ μs, meaning that the roll-off in the noise spectrum will be determined solely by τ_r. Using Eqs. 5.1-5.4, with $\tau_0 = 438$ ns [12] and a measured $dA/dN_{qp} = 5.0 \times 10^{-7}$, we expect $S_A = -99.3$ dBc/Hz. This is a high value compared to other superconductors like Ta and Nb, due to the large τ_0 in Al [12].

We have measured the fluctuations in the resonator amplitude in equilibrium at the resonant frequency using a microwave power of -77 dBm. The power spectral density,

---

[1] The fibreglass is opaque at 1 THz, but more transparent below 300 GHz.

corrected for system noise, is shown in Fig. 5.2a for various temperatures, which is the central result of this paper. In Fig. 5.2b the system noise spectrum is shown, which is subtracted from the spectrum measured on resonance, to get the corrected spectra in Fig. 5.2a. Parts of the time domain signal where large energy impacts are observed, are removed from the analysis as shown in Fig. 5.2c, because they distort the dynamic equilibrium. These impacts do not appear in the system noise signal and decay within a time τ_r, which shows they are events that create quasiparticles, for example cosmic ray hits [21] or local radioactivity.

In Fig. 5.2a we observe that the measured power spectral density of the fluctuations has a constant level for all temperatures. The roll-off in the spectra can be described with a single timescale that decreases with temperature. From these two properties we conclude that we directly observe quasiparticle number fluctuations.

5.4 The equilibrium quasiparticle recombination time

The recombination time, τ_r, is extracted from the measured noise spectra and shown as the black squares in Fig. 5.3 as a function of temperature. At temperatures from 180-300 mK, we find the expected exponential temperature dependence. Eq. 5.2 is used to fit for the characteristic electron-phonon interaction time τ_0 and we find a value of 458±10 ns, in reasonable agreement with other studies [12, 22]. Due to the phonon trapping effect, which we cannot estimate accurately, the measured τ_0 may differ from the pure electron-phonon time [14, 22]. At temperatures below 150 mK we measure a temperature independent quasiparticle recombination time of 2.2 ms, which is among the longest reported for a thin superconducting film. Alternatively, the recombination time is measured by monitoring the restoration of equilibrium after a short pulse of optical photons [4], which is shown by the filled circles in Fig. 5.3. The lifetimes obtained from the noise spectra are equal to the lifetimes from the pulse measurement up to 220 mK, indicating that both measurements really probe quasiparticle recombination in equilibrium. The lifetime from the noise spectra agrees well with theory (full line) up to 300 mK. The lifetime from the pulse method shows a deviation from theory, which we always observe in Al on sapphire resonators. The deviation between the two sets of experimental data calls thus for a future analysis of the physical processes in the pulse method.

5.5 Measuring the number of quasiparticles

We combine the level of the power spectral density (Fig. 5.2) *and* the quasiparticle lifetime obtained from the roll-off in this spectral density (Fig. 5.3) to obtain the number of quasiparticles, N_{qp}, by using Eqs. 5.3 and 5.4, together with the measured values of dA/dN_{qp}. The result is plotted in Fig. 5.4 with the black squares. As a cross

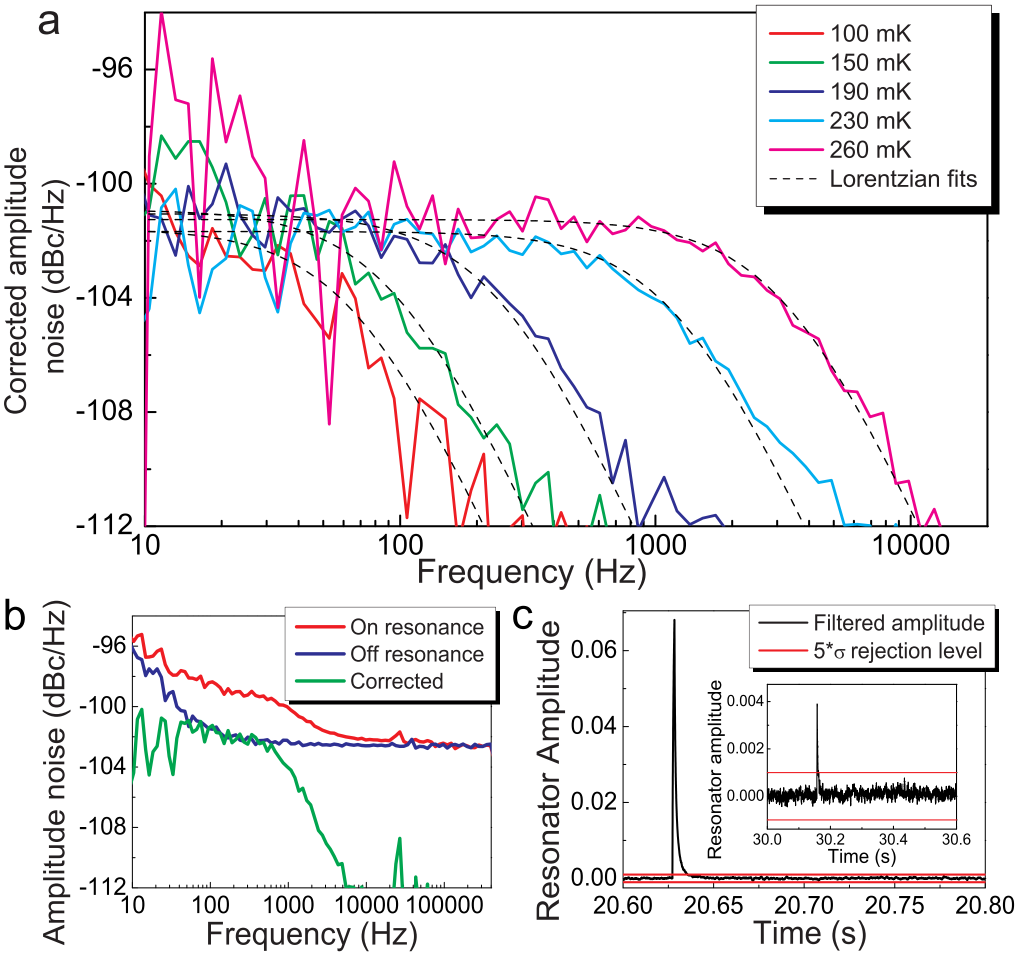

Figure 5.2: (a) Corrected power spectral density of the resonator amplitude fluctuations as a function of frequency, calibrated for system noise contributions as depicted in (b). The spectra are plotted for six different temperatures. Note that the spectral density is temperature independent up to the roll-off frequency. The Lorentzian fits, plotted as dashed lines, show that the spectra can be described with a single timescale. (b) The noise spectrum on resonance is corrected for system noise contributions by subtracting the system noise from the raw data. The system noise is obtained by taking a calibration measurement at a frequency far from the resonant frequency as indicated in Fig. 5.1c. (c) Part of the time trace of the resonator amplitude. High energy impacts are observed every 20-30 s. Smaller impacts (inset) happen every 5-10 s. The time trace is filtered with a moving average filter with a time constant $\tau_r/2$. Parts with impacts larger than 5 times the standard deviation (0.43 eV) are rejected.

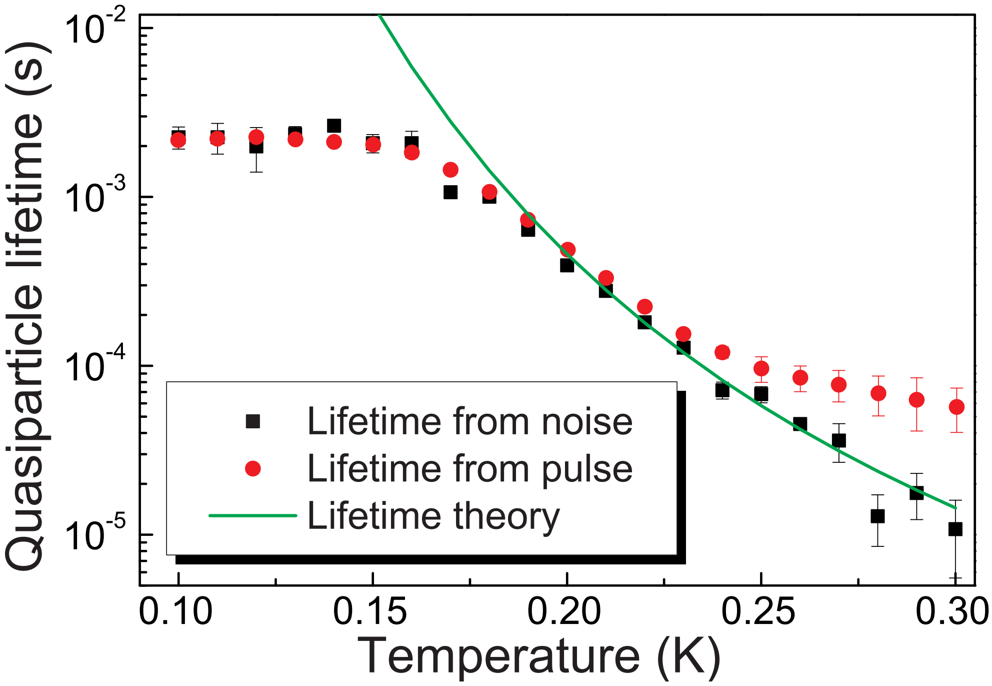

Figure 5.3: The quasiparticle lifetime, obtained from the roll-off frequency of the resonator amplitude noise spectrum (Fig. 5.2), as a function of temperature. The solid line is the lifetime, calculated from theory. Additionally the lifetime is determined with a short pulse of light. The exponential decay of the excitation is fit and the obtained decay time is plotted as a function of temperature. The measurements show consistently that the lifetime saturates to about 2.2 ms below 160 mK. The error bars represent statistical uncertainties obtained from the fitting procedure.

check, we convert the quasiparticle lifetime measured from the noise roll-off directly into quasiparticle number by using Eq. 5.2, which is shown in Fig. 5.4 with red triangles. We assume that the relevant volume is the central strip volume of the resonator. The quasiparticle number, obtained via these two methods consistently shows a saturation, giving a low temperature quasiparticle density of 25-55 μm^{-3}. We conclude that the quasiparticle lifetime saturation is due to a saturation in the quasiparticle density, consistent with the conjecture of Martinis et al. [8].

5.6 Discussion

The question remains what the source of the non-thermal (in view of Eq. 5.1) quasiparticle density below 160 mK is. In literature, it is usually referred to as non-equilibrium quasiparticle density, which is inferred from saturating tunnel rates [6, 23] and attributed to electromagnetic noise [24, 25] and radiation [26] or, if the first two are eliminated, to cosmic rays, local radioactivity, slow heat release or stray light [8]. In our experiment, excess quasiparticles due to cosmic ray hits are excluded as shown in Fig.

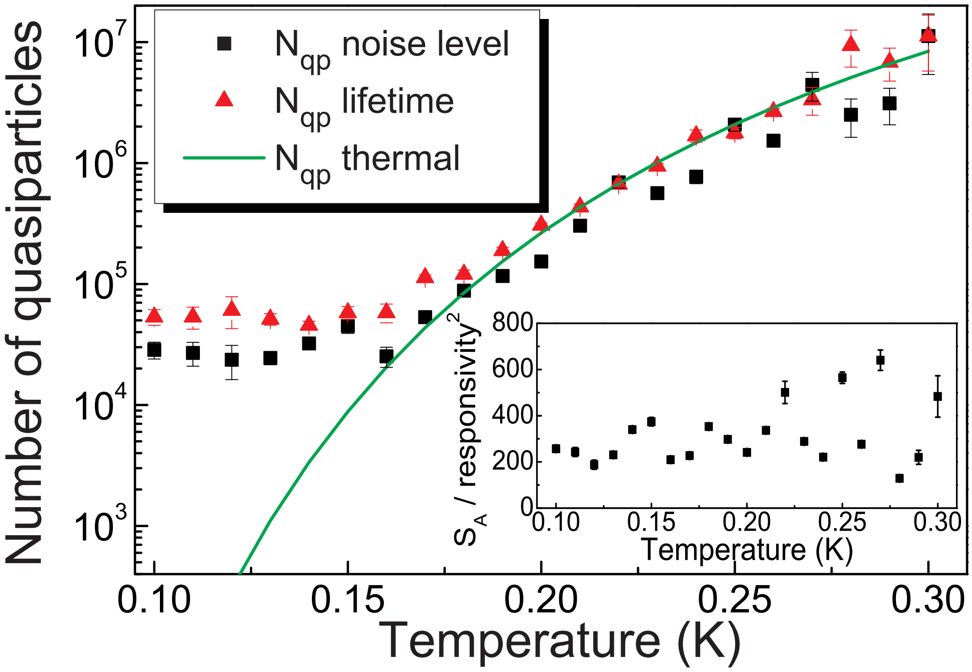

Figure 5.4: The number of quasiparticles as determined from the noise level as a function of temperature. The inset shows that the noise level (S_A) divided by the responsivity is almost temperature independent. The error bars indicate combined statistical uncertainties. Alternatively, the number of quasiparticles in the superconductor is determined from the measured quasiparticle lifetimes. The number of quasiparticles saturates at around 30,000-50,000 below 160 mK, where an exponential decrease is expected (solid line).

5.2c. Local radioactivity is also excluded as far as it generates similar distinguishable events. The sample box and coaxial cables are thoroughly shielded from stray light, validated by the observation that τ_r is independent of the 4 K-stage temperature, as explained before. Additionally, if there would still be stray-light, it would cause an additional photon shot noise [4] contribution, which decreases with increasing temperature, due to the decreasing quasiparticle lifetime. The observed temperature independent noise level therefore excludes stray light. We cannot completely exclude quasiparticle generation by the microwave signal. The microwave power range over which we can measure the quasiparticle fluctuations is only 4 dB due to limitations in resonator power handling and amplifier noise temperature. Over this range the quasiparticle density is power independent.

For radiation detectors, the noise equivalent power (NEP) is a common way to express the sensitivity. From the noise level and lifetime measurements we determine [3] an electrical NEP of 3.3×10^{-19} WHz$^{-1/2}$ due to generation-recombination noise, not taken into account the system noise, which will increase the NEP by about a factor of two. For Al resonators with this geometry and the observed remnant quasiparticle density, this is the fundamental limit to the sensitivity. A significant improvement is only possible if one could reduce the remnant quasiparticle density or the resonator volume.

We would like to thank Y.J.Y. Lankwarden for fabricating the devices. A. Endo is financially supported by NWO (Veni grant 639.041.023) and the Netherlands Research School for Astronomy (NOVA).

References

[1] M. Tinkham, *Introduction to Superconductivity*, McGraw-Hill, New York, 2^{nd} edition, 1996.

[2] J. Clarke and F. K. Wilhelm, *Superconducting quantum bits*, Nature **453**, 1031 (2008).

[3] P. K. Day, H. G. LeDuc, B. A. Mazin, A. Vayonakis, and J. Zmuidzinas, *A broadband superconducting detector suitable for use in large arrays*, Nature **425**, 817 (2003).

[4] R. Barends, J. J. A. Baselmans, S. J. C. Yates, J. R. Gao, J. N. Hovenier, and T. M. Klapwijk, *Quasiparticle relaxation in optically excited high-Q superconducting resonators*, Phys. Rev. Lett. **100**, 257002 (2008).

[5] R. Barends, S. van Vliet, J. J. A. Baselmans, S. J. C. Yates, J. R. Gao, and T. M. Klapwijk, *Enhancement of quasiparticle recombination in Ta and Al superconductors by implantation of magnetic and nonmagnetic atoms*, Phys. Rev. B **79**, 020509(R) (2009).

[6] J. Aumentado, M. W. Keller, J. M. Martinis, and M. H. Devoret, *Nonequilibrium quasiparticles and 2e periodicity in single-Cooper-pair transistors*, Phys. Rev. Lett. **92**, 066802 (2004).

[7] M. D. Shaw, R. M. Lutchyn, P. Delsing, and P. M. Echternach, *Kinetics of nonequilibrium quasiparticle tunneling in superconducting charge qubits*, Phys. Rev. B **78**, 024503 (2008).

[8] J. M. Martinis, M. Ansmann, and J. Aumentado, *Energy decay in superconducting Josephson-junction qubits from nonequilibrium quasiparticle excitations*, Phys. Rev. Lett. **103**, 097002 (2009).

[9] G. Catelani, J. Koch, L. Frunzio, R. J. Schoelkopf, M. H. Devoret, and L. I. Glazman, *Quasiparticle relaxation of superconducting qubits in the presence of flux*, Phys. Rev. Lett. **106**, 077002 (2011).

[10] M. Lenander, H. Wang, R. C. Bialczak, E. Lucero, M. Mariantoni, M. Neeley, A. D. O'Connell, D. Sank, M. Weides, J. Wenner, T. Yamamoto, Y. Yin, J. Zhao, A. N. Cleland, and J. M. Martinis, *Measurement of energy decay in superconducting qubits from nonequilibrium quasiparticles*, Phys. Rev. B **84**, 024501 (2011).

[11] C. M. Wilson and D. E. Prober, *Quasiparticle number fluctuations in superconductors*, Phys. Rev. B **69**, 094524 (2004).

[12] S. B. Kaplan, C. C. Chi, D. N. Langenberg, J. Chang, S. Jafarey, and D. J. Scalapino, *Quasiparticle and phonon lifetimes in superconductors*, Phys. Rev. B **14**, 4854 (1976).

[13] C. M. Wilson, L. Frunzio, and D. E. Prober, *Time-resolved measurements of thermodynamic fluctuations of the particle number in a nondegenerate Fermi gas*, Phys. Rev. Lett. **87**, 067004 (2001).

[14] S. B. Kaplan, *Acoustic matching of superconducting films to substrates*, J. Low Temp. Phys. **37**, 343 (1979).

[15] D. C. Mattis and J. Bardeen, *Theory of the anomalous skin effect in normal and superconducting metals*, Phys. Rev. **111**, 412 (1958).

[16] J. J. A. Baselmans and S. J. C. Yates, *Long quasiparticle lifetime in Aluminium Microwave Kinetic Inductance Detectors using coaxial stray light filters*, AIP Conference Proceedings **1185**, 160 (2009).

[17] J. Baselmans, S. J. C. Yates, R. Barends, Y. J. Y. Lankwarden, J. R. Gao, H. Hoevers, and T. M. Klapwijk, *Noise and sensitivity of aluminum kinetic inductance detectors for sub-mm astronomy*, J. Low Temp. Phys. **151**, 524 (2008).

[18] R. Barends, *Photon-detecting Superconducting Resonators*, PhD thesis, Delft University of Technology, 2009.

[19] J. Gao, J. Zmuidzinas, B. A. Mazin, H. G. LeDuc, and P. K. Day, *Noise properties of superconducting coplanar waveguide microwave resonators*, Appl. Phys. Lett. **90**, 102507 (2007).

[20] J. Gao, M. Daal, A. Vayonakis, S. Kumar, J. Zmuidzinas, B. Sadoulet, B. A. Mazin, P. K. Day, and H. G. Leduc, *Experimental evidence for a surface distribution of two-level systems in superconducting lithographed microwave resonators*, Appl. Phys. Lett. **92**, 152505 (2008).

[21] L. J. Swenson, A. Cruciani, A. Benoit, M. Roesch, C. S. Yung, A. Bideaud, and A. Monfardini, *High-speed phonon imaging using frequency-multiplexed kinetic inductance detectors*, Appl. Phys. Lett. **96**, 263511 (2010).

[22] C. C. Chi and J. Clarke, *Quasiparticle branch mixing rates in superconducting aluminum*, Phys. Rev. B **19**, 4495 (1979).

[23] A. J. Ferguson, N. A. Court, F. E. Hudson, and R. G. Clark, *Microsecond resolution of quasiparticle tunneling in the single-Cooper-pair transistor*, Phys. Rev. Lett. **97**, 106603 (2006).

[24] W. Kuo, C. S. Wu, J. H. Shyu, and C. D. Shen, *Parity effect in a superconducting island in a tunable dissipative environment*, Phys. Rev. B **74**, 184522 (2006).

[25] B. S. Palmer, C. A. Sanchez, A. Naik, M. A. Manheimer, J. F. Schneiderman, P. M. Echternach, and F. C. Wellstood, *Steady-state thermodynamics of nonequilibrium quasiparticles in a Cooper-pair box*, Phys. Rev. B **76**, 054501 (2007).

[26] O. Naaman and J. Aumentado, *Narrow-band microwave radiation from a biased single-Cooper-pair transistor*, Phys. Rev. Lett. **98**, 227001 (2007).

Chapter 6

Microwave-induced excess quasiparticles in superconducting resonators measured through correlated conductivity fluctuations

We have measured the number of quasiparticles and their lifetime in aluminium superconducting microwave resonators. The number of excess quasiparticles below 160 mK decreases from 72 to 17 μm^{-3} with a 6 dB decrease of the microwave power. The quasiparticle lifetime increases accordingly from 1.4 to 3.5 ms. These properties of the superconductor were measured through the spectrum of correlated fluctuations in the quasiparticle system and condensate of the superconductor, which show up in the resonator amplitude and phase respectively. Because uncorrelated noise sources vanish, fluctuations in the superconductor can be studied with a sensitivity close to the vacuum noise.

This chapter was published as P. J. de Visser, J. J. A. Baselmans, S. J. C. Yates, P. Diener, A. Endo, and T. M. Klapwijk, *Applied Physics Letters* **100**, 162601 (2012).

6.1 Introduction

The promise of a long quasiparticle lifetime and a long coherence time makes superconducting circuits popular for use in radiation detection and quantum computation. At low temperature the number of quasiparticles in a superconductor should decrease exponentially. Excess quasiparticles were recently suggested to limit the coherence time of superconducting qubits [1–6] and the tunnelling rate in single-electron transistors [7]. Recently, the quasiparticle lifetime in a high-quality aluminium superconducting resonator [8] was shown to be consistent with an excess quasiparticle population inferred from noise measurements [9]. There is a vivid debate on the question of the origin of those excess quasiparticles [1–7, 9], which mainly focuses on reducing the influence of the environment on the devices under study. Here we show for superconducting aluminium resonators that the environment is well enough under control in our experimental setup to reveal a new source of quasiparticles, namely the microwave readout power of these devices. We show that the saturation in the number of quasiparticles at low temperature (100-150 mK), as inferred from noise measurements, decreases from 72 to 17 μm^{-3} with a 6 dB decrease of the microwave power. The quasiparticle lifetime increases accordingly from 1.4 to 3.5 ms.

6.2 Microwave response to quasiparticle fluctuations in two quadratures

Microwave resonators are popular devices in radiation detection [10] and circuit quantum electrodynamics [11]. The two quadratures of the microwave field in such a resonator are proportional to the real and imaginary part of the conductivity of the superconductor $\sigma_1 - i\sigma_2$. The real part corresponds to dissipation in the quasiparticle system and the imaginary part to the kinetic inductance of the condensate [12]. We have shown recently that the real part of the conductivity shows quasiparticle number fluctuations [9]. When two quasiparticles recombine, a Cooper pair is formed and when a Cooper pair is broken it leaves two quasiparticles. Therefore, the superconducting condensate fluctuates as well, and one would expect to see these fluctuations in the reactive response of the microwave resonator. However, this reactive response is obscured by the response of two-level fluctuators in the dielectrics surrounding the resonator [13]. Therefore, we study here the correlation between the dissipative and reactive part of the conductivity in an aluminium resonator. We observe correlated fluctuations in the dissipative and reactive parts of the response, which proves the correlated nature of fluctuations in the quasiparticle system and the condensate. The correlation results in a measurement of fluctuations in the superconductor down to the vacuum noise level, even with a conventional amplifier. The number of quasiparticles and their lifetime are extracted from the fluctuation spectra.

In thermal equilibrium, the average number of quasiparticles per unit volume in a superconductor follows an exponential temperature dependence: $n_{qp} \propto \sqrt{\Delta k_B T} \exp(-\Delta/k_B T)$. The average quasiparticle lifetime has the inverse temperature dependence [14]: $\tau_{qp} \propto \sqrt{1/\Delta k_B T} \exp(\Delta/k_B T)$. Δ is the energy gap of the superconductor, T the temperature and k_B Boltzmann's constant. Two quasiparticles with opposite spins and momenta can be generated from a Cooper pair by a phonon with an energy larger than 2Δ. When two quasiparticles recombine into a Cooper pair, a phonon is emitted. These processes are random processes in equilibrium and lead to fluctuations of the number of quasiparticles around the average. The power spectral density of these fluctuations shows a Lorentzian spectrum, given by [15]

$$S_N(f) = \frac{4N_{qp}\tau_{qp}}{1 + (2\pi f \tau_{qp})^2}, \tag{6.1}$$

with f the frequency and $N_{qp} = n_{qp}V$, with V the volume of the system. Since the temperature dependences of N_{qp} and τ_{qp} are exactly opposite, $N_{qp}\tau_{qp}$ is constant over temperature. This formulation was verified through fluctuations in the quasiparticle current of a Cooper pair box [16]. Recently we have observed these fluctuations in the dissipative response of a microwave resonator [9]. As discussed above, equilibrium fluctuations in the number of quasiparticles should coincide with fluctuations in the condensate, which should show up in the reactive response of the resonator.

To measure the complex conductivity, a 40 nm thick Al film was sputter-deposited onto a c-plane sapphire substrate. The critical temperature is 1.11 K, from which the energy gap $\Delta = 1.76 k_B T_c = 168$ μeV. The film was patterned by wet etching into half wavelength, coplanar waveguide resonators. The resonator has a central strip volume of $1.0 \cdot 10^3$ μm^3 and resonates at 6.62 GHz. The sample is cooled in a pulse tube pre-cooled adiabatic demagnetization refrigerator to 100 mK, with a box-in-box configuration and coax cable filters for thorough stray light shielding, crucial for these measurements. More details on the setup are given in Ref. [17].

The complex transmission of the microwave circuit is measured with a quadrature mixer as a function of frequency and traces out a circle in the complex plane. The resonator amplitude, A, measured from the circle center, is proportional to σ_1 and therefore called the dissipation quadrature. The phase, θ, is proportional to σ_2 and is also called the frequency quadrature. The responsivities of amplitude and phase to a change in the number of quasiparticles are determined experimentally as described in Ref. [18], which leads to $dA/dN_{qp} = -5 \times 10^{-7}$ and $d\theta/dN_{qp} = 4 \times 10^{-6}$ at 100 mK. At the end of this Letter we will discuss the reliability of this method for a readout-power dependent quasiparticle density. The *cross* power spectral density due to correlated quasiparticle number fluctuations in the resonator amplitude and phase is given by

$$S_{A,\theta}(f) = S_N(f)\frac{dA \cdot d\theta/dN_{qp}^2}{1 + (2\pi f \tau_{res})^2}, \tag{6.2}$$

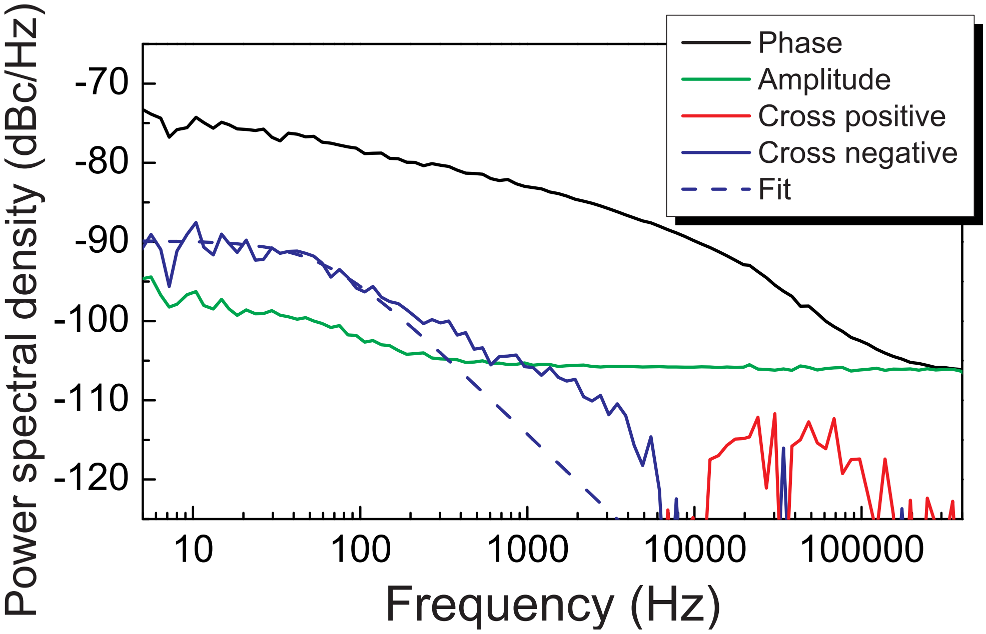

Figure 6.1: Amplitude, phase and cross power spectral densities of the resonator as a function of frequency at 120 mK and a microwave power of −75 dBm. Because of the log-scale the positive and negative parts of the cross power spectral density are plotted separately. The dashed line is a single-timescale Lorentzian fit.

which is only different from the amplitude or phase power spectral density by the responsivity factor, which would be $(dA/dN_{qp})^2$ and $(d\theta/dN_{qp})^2$ for the amplitude and phase spectra respectively. τ_{res} is the resonator ringtime given by $\tau_{res} = \frac{Q}{\pi f_0} \approx 2$ μs. Because the amplitude responsivity to quasiparticles is negative, we expect that the correlation of the quasiparticle fluctuations in amplitude and phase is negative.

6.3 Correlated fluctutations

We have measured the fluctuations in the resonator amplitude and phase as a function of time at the resonant frequency. Occasionally peaks occur in the time domain data due to high energy impacts, which are filtered out of the spectral analysis as discussed in Ref. [9]. The power spectral densities of amplitude and phase are calculated by taking the Fourier transform of the autocorrelation of the time domain signals. The cross power spectral density is calculated by Fourier transforming the cross-correlation function of amplitude and phase. If the direction of the fluctuations with respect to the resonant circle in the complex plane is offset, one may convert phase noise into the amplitude direction. By simulating different orientations, we estimate the statistical error in the orientation to be ±0.28°, which leads to an uncertainty of ±0.7 dB in the level of the cross power spectum.

The amplitude, phase and cross power spectral densities at 120 mK are shown as a function of frequency in Fig. 6.1. We first compare the different spectra. To start with, the phase noise is orders of magnitude higher than the amplitude noise, which is due to the response of two-level-system (TLS) fluctuators in the dielectrics to the electric field [13]. Therefore observing quasiparticle fluctuations in the phase-only spectrum is nearly impossible. The flat level of -106 dBc/Hz is due to the amplifier noise and attenuation in between the sample and the (HEMT) amplifier and corresponds to a system noise temperature of 7 K. It was recently shown for similar microwave resonators that there is no TLS noise in the amplitude down to the vacuum noise [19]. Therefore, if the system noise is subtracted, the quasiparticle signature becomes visible in the amplitude spectrum [9]. The cross power spectrum shows no TLS noise or amplifier noise, which shows that these contributions are uncorrelated.

We now look closer at the cross power spectral density. Part of the cross power spectrum (up to 10 kHz) is negative (blue) as expected for quasiparticle fluctuations. This part of the spectrum is real, meaning that the quasiparticle fluctuations enter amplitude and phase without relative delay. A small part at higher frequency has equal real and imaginary parts, of which the real part is positive (red). The negative part consists of two roll-offs. The first roll-off is at the quasiparticle lifetime ($\tau \approx 2$ ms, $f \approx 80$ Hz) as shown by the dashed line in Fig. 6.1. As a function of temperature, the lifetime from the cross spectra is the same as from amplitude-only spectra (Ref. [9]), consistent with the framework of quasiparticle number fluctuations. The difference in the level of the cross and amplitude spectra (10 ± 1) is due to the difference in amplitude and phase responsivity. The first conclusion of this Letter is that the correlated noise in the amplitude and phase of the resonator is due to correlated fluctuations in the quasiparticle system and the superconducting condensate.

The second roll-off in Fig. 6.1 is at a shorter timescale ($\tau \approx 100$ μs, $f \approx 1.5$ kHz) and has a much lower (a factor 25) noise level. We interpret this second roll-off in the spectrum as a signature of phonon fluctuations. This phenomenon requires a more extensive discussion which we will publish separately (in this thesis this discussion is presented in Appendix B). The positive part of the spectrum is small and only visible close to the resonator ring-time (which also determines the roll-off frequency of the phase spectrum), which we attribute to phase-amplitude mixing due to slight detuning from the resonant frequency during the measurement [20]. The sign of this contribution varies between different resonators, where the quasiparticle contribution is always negative.

We observe that around 10 kHz the spectral density drops to below -120 dBc/Hz, which corresponds to the vacuum noise $\frac{1}{2}hf/k_B$. Note that the vacuum noise is not a physical limit here, but only used for comparison. Thus correlating amplitude and phase means a factor of 25 improvement with respect to the amplifier noise level when measuring amplitude or phase only, proving the high sensitivity of this method in measuring quasiparticle fluctuations. For microwave resonators used as photon detectors

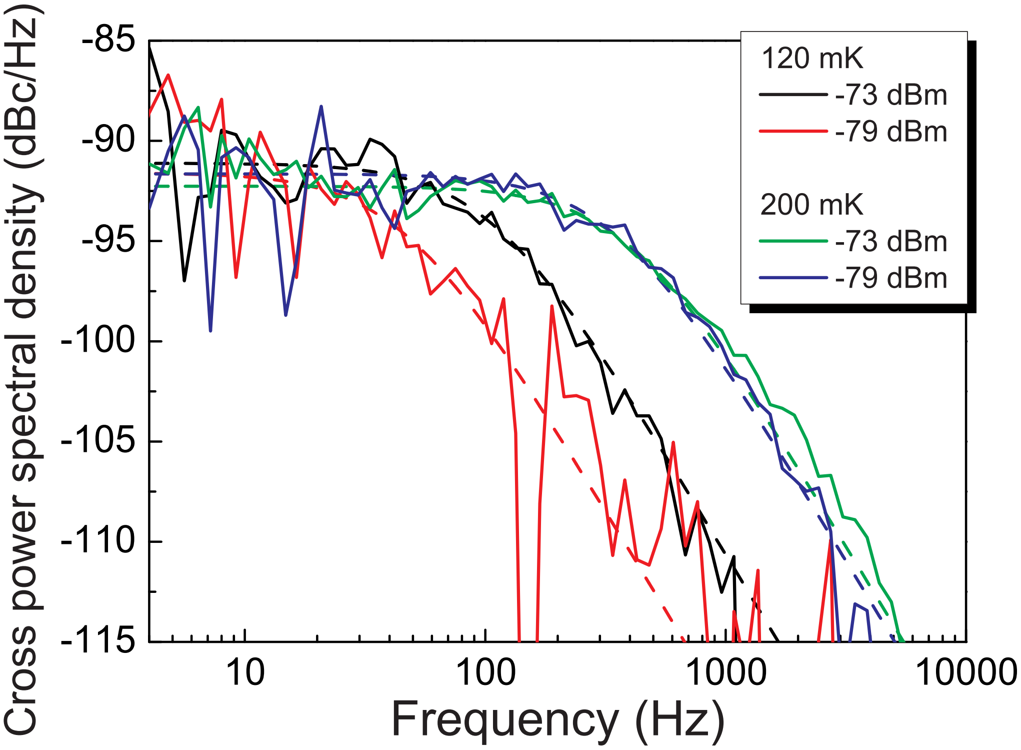

Figure 6.2: Cross power spectral density of the resonator amplitude and phase as a function of frequency at two different microwave powers and temperatures of 120 and 200 mK. The dashed lines are single-timescale Lorentzian fits.

and limited by uncorrelated noise, we envision an improvement in sensitivity if one reads out the detector by correlating the amplitude and phase signal.

6.4 Excess quasiparticles due to the microwave readout power

In Figure 6.2 cross spectra are shown at 120 mK and 200 mK for two different microwave readout powers. We observe that at 120 mK the roll-off frequency increases with increasing microwave power. This behaviour is observed up to 190 mK. At 200 mK, the spectra at different powers are similar, which marks the point where thermal quasiparticles start to dominate. We extract the number of quasiparticles from the cross power spectral density by using Eqs. 6.1 and 6.2 and the quasiparticle lifetimes as determined from the roll-off frequency of the spectra. The number of quasiparticles and the quasiparticle lifetime are plotted for four different readout powers as a function of temperature in Fig. 6.3a. The error bars represent statistical errors as obtained from the fits and, for N_{qp}, the orientation uncertainty described above. The level at which the number of quasiparticles saturates clearly decreases with decreasing readout

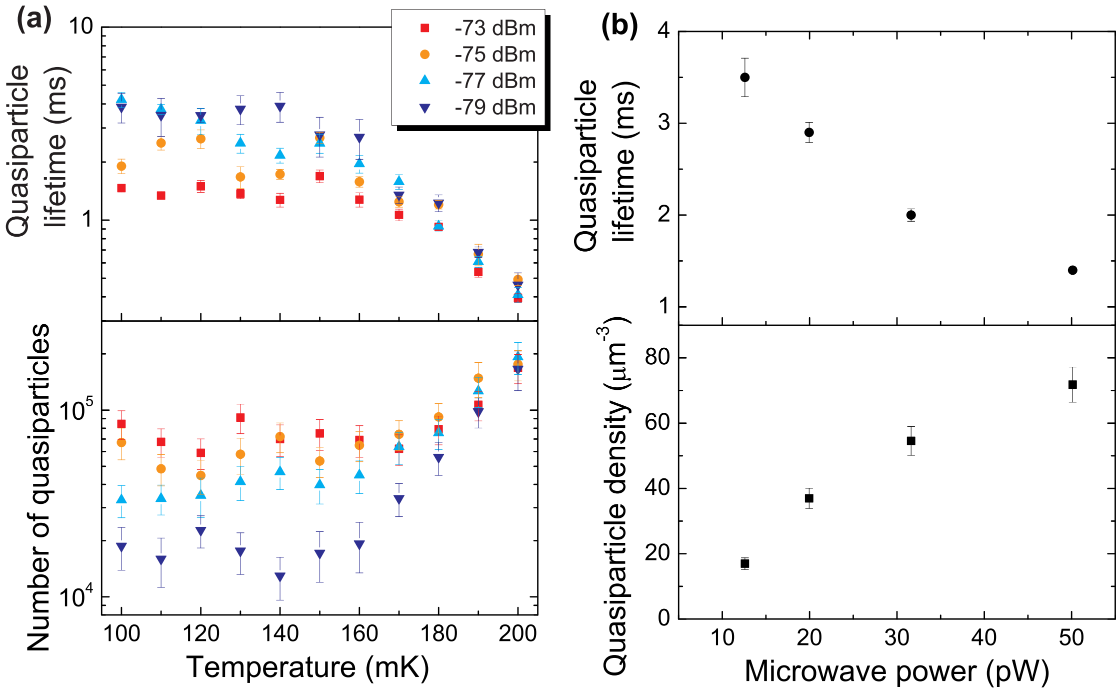

Figure 6.3: (a) Number of quasiparticles and the quasiparticle lifetime as a function of temperature for four different microwave readout powers. (b) Quasiparticle density and quasiparticle lifetime as a function of readout power. Each point is a weighted average of the values from 100-150 mK as shown in (a).

power. The quasiparticle lifetime increases with decreasing power, consistent with the decreasing number of quasiparticles. To get a better estimate of the saturation levels, we average n_{qp} and τ_{qp} from 100-150 mK and plot the averages as a function of power in Fig. 6.3b. We conclude that the microwave readout signal is the main source of excess quasiparticles at low temperature for superconducting resonators.

In the broader field of superconducting quantum circuits [1–7] excess quasiparticles are mainly attributed to environmental effects, which we strongly reduce by shielding our sample box and filtering the cables [17]. The fact that we reveal a microwave power dependence of the number of quasiparticles proves that our setup is light-tight to at least the lowest measured quasiparticle density (less than 0.1 fW of stray-light [17]). We note that since qubits are operated in the limit of a few microwave photons, it is unlikely that the excess quasiparticles in these systems are also due to the microwave power.

In the simplest picture, the power that is needed to create a certain number of quasiparticles is given by $P_{qp} = N_{qp}\Delta/\tau_{qp}$. Based on P_{qp} and an estimate of the power that is dissipated in the quasiparticle system, P_{diss}, we can ascribe an efficiency η_{read} to the process of quasiparticle creation due to the microwave readout power given by $\eta_{read} = P_{qp}/P_{diss}$. P_{diss} is given by $P_{diss} = \chi_c\chi_{qp}P_{read}/2$, with P_{read} the applied microwave power (*not* the internal power in the resonator). $\chi_c = \frac{4Q^2}{Q_c Q_i}$ is the coupling efficiency and $\chi_{qp} = Q_i/Q_{i,qp}$ is the fraction of dissipated power that goes into the quasiparticle system. For this resonator the coupling quality factor is $Q_c = 3.9 \times 10^4$ and the internal quality factor is $Q_i = 1.65 \times 10^5$ at 100 mK and, which hardly change with power. Since we can measure the number of quasiparticles, we can estimate the quality factor due to quasiparticles, $Q_{i,qp}$, for each power, which ranges from 6×10^5 at $P_{read} = -73$ dBm to 4×10^6 at $P_{read} = -79$ dBm. Given these numbers we calculate $\eta_{read} = 3.3 \pm 1.3 \times 10^{-4}$. The sensitivity of microwave resonators used as kinetic inductance detectors is usually expressed by the noise equivalent power (NEP). The NEP due to quasiparticle number fluctuations [21] can be expressed as $NEP = \frac{2\Delta}{\eta}\sqrt{N_{qp}/\tau_{qp}} = \frac{2}{\eta}\sqrt{\eta_{read} P_{diss} \Delta}$, with $\eta \approx 0.6$ a conversion efficiency of optical energy into quasiparticles. The measured value of η_{read} is pleasingly low in this context. At the lowest measured readout power we get $NEP = 2 \times 10^{-19}$ W/Hz$^{-1/2}$.

So far we have not touched upon the mechanism with which the readout signal leads to excess quasiparticles. We may explain the excess quasiparticles by Joule heating due to the microwave power, leading to an elevated steady state temperature of the quasiparticle system. To that end, we use the model described in Ref. [22], in which heat transport is assumed to be limited by electron-phonon coupling. The model parameters are the same as the measured parameters of our device[1]. We find that η_{read} ranges from 1×10^{-4} at the lowest readout power of -79 dBm to 9×10^{-4} at -73 dBm. Experimentally η_{read} is constant within the uncertainty. Thus the order of magnitude of η_{read} in the simulations agrees with the measurements, but the power dependence is different.

6.5 Discussion

The question remains how quasiparticle creation by the microwave field can be understood microscopically. A microscopic picture could be a change of the quasiparticle distribution function due to microwave absorption [23–25] and consequently a change in the complex conductivity [25, 26] or an altered density of states due to the microwave field [27]. The redistribution of quasiparticles could lead to Cooper pair breaking. The next step to unravel the physical mechanism of the microwave power dependent quasiparticle density will therefore be a comparison of these models to resonator measurements. In this context we note that in Fig. 6.3b, the product $N_{qp}\tau_{qp}$ is not completely constant as a function of readout power. Our analysis here is based on thermal quasiparticles, from which we derive the responsivity to quasiparticles. As the quasiparticle distribution may be non-thermal, the complex conductivity and therefore the responsivity to the number of quasiparticles may change. This could affect the derivation of

---

[1] We have changed the characteristic impedance equations for a microstrip geometry, used in the original model, into equations for a coplanar waveguide geometry.

N_{qp} from the noise level. The measurement of τ_{qp} is fairly rigid, since it is obtained from the roll-off frequency only.

6.6 Summary

In summary, we have measured correlated fluctuations in the quasiparticle system and condensate of a superconductor, which show up in the amplitude and phase of an aluminium microwave resonator respectively. From the correlated noise spectra, we determine the number of quasiparticles and their lifetime, which both saturate at temperatures below 160 mK. The level of this saturation is microwave power dependent, showing that the microwave readout power leads to excess quasiparticles.

We would like to thank Y.J.Y. Lankwarden for fabricating the devices. A.E. is financially supported by NWO (Veni grant 639.041.023) and JSPS Fellowship for Research Abroad.

References

[1] J. M. Martinis, M. Ansmann, and J. Aumentado, *Energy decay in superconducting Josephson-junction qubits from nonequilibrium quasiparticle excitations*, Phys. Rev. Lett. **103**, 097002 (2009).

[2] G. Catelani, J. Koch, L. Frunzio, R. J. Schoelkopf, M. H. Devoret, and L. I. Glazman, *Quasiparticle relaxation of superconducting qubits in the presence of flux*, Phys. Rev. Lett. **106**, 077002 (2011).

[3] H. Paik, D. I. Schuster, L. S. Bishop, G. Kirchmair, G. Catelani, A. P. Sears, B. R. Johnson, M. J. Reagor, L. Frunzio, L. Glazman, and R. J. Schoelkopf, *Observation of high coherence in Josephson junction qubits measured in a three dimensional circuit QED architecture*, Phys. Rev. Lett. **107**, 240501 (2011).

[4] M. Lenander, H. Wang, R. C. Bialczak, E. Lucero, M. Mariantoni, M. Neeley, A. D. O'Connell, D. Sank, M. Weides, J. Wenner, T. Yamamoto, Y. Yin, J. Zhao, A. N. Cleland, and J. M. Martinis, *Measurement of energy decay in superconducting qubits from nonequilibrium quasiparticles*, Phys. Rev. B **84**, 024501 (2011).

[5] R. Barends, J. Wenner, M. Lenander, Y. Chen, R. C. Bialczak, J. Kelly, E. Lucero, P. O'Malley, M. Mariantoni, D. Sank, H. Wang, T. C. White, Y. Yin, J. Zhao, A. N. Cleland, J. M. Martinis, and J. J. A. Baselmans, *Minimizing quasiparticle generation from stray infrared light in superconducting quantum circuits*, Appl. Phys. Lett. **99**, 113507 (2011).

[6] A. D. Córcoles, J. M. Chow, J. M. Gambetta, C. Rigetti, J. R. Rozen, G. A. Keefe, M. B. Rothwell, M. B. Ketchen, and M. Steffen, *Protecting superconducting qubits from radiation*, Appl. Phys. Lett. **99**, 181906 (2011).

[7] O.-P. Saira, A. Kemppinen, V. F. Maisi, and J. P. Pekola, *Vanishing quasiparticle density in a hybrid Al/Cu/Al single-electron transistor*, Phys. Rev. B **85**, 012504 (2012).

[8] R. Barends, J. J. A. Baselmans, S. J. C. Yates, J. R. Gao, J. N. Hovenier, and T. M. Klapwijk, *Quasiparticle relaxation in optically excited high-Q superconducting resonators*, Phys. Rev. Lett. **100**, 257002 (2008).

[9] P. J. de Visser, J. J. A. Baselmans, P. Diener, S. J. C. Yates, A. Endo, and T. M. Klapwijk, *Number fluctuations of sparse quasiparticles in a superconductor*, Phys. Rev. Lett. **106**, 167004 (2011).

[10] P. K. Day, H. G. LeDuc, B. A. Mazin, A. Vayonakis, and J. Zmuidzinas, *A broadband superconducting detector suitable for use in large arrays*, Nature **425**, 817 (2003).

[11] A. Wallraff, D. I. Schuster, A. Blais, L. Frunzio, R.-S. Huang, J. Majer, S. Kumar, S. M. Girvin, and R. J. Schoelkopf, *Strong coupling of a single photon to a superconducting qubit using circuit quantum electrodynamics*, Nature **431**, 162 (2004).

[12] D. C. Mattis and J. Bardeen, *Theory of the anomalous skin effect in normal and superconducting metals*, Phys. Rev. **111**, 412 (1958).

[13] J. Gao, J. Zmuidzinas, B. A. Mazin, H. G. LeDuc, and P. K. Day, *Noise properties of superconducting coplanar waveguide microwave resonators*, Appl. Phys. Lett. **90**, 102507 (2007).

[14] S. B. Kaplan, C. C. Chi, D. N. Langenberg, J. Chang, S. Jafarey, and D. J. Scalapino, *Quasiparticle and phonon lifetimes in superconductors*, Phys. Rev. B **14**, 4854 (1976).

[15] C. M. Wilson and D. E. Prober, *Quasiparticle number fluctuations in superconductors*, Phys. Rev. B **69**, 094524 (2004).

[16] C. M. Wilson, L. Frunzio, and D. E. Prober, *Time-resolved measurements of thermodynamic fluctuations of the particle number in a nondegenerate Fermi gas*, Phys. Rev. Lett. **87**, 067004 (2001).

[17] J. Baselmans, S. Yates, P. Diener, and P. de Visser, *Ultra low background cryogenic test facility for far-infrared radiation detectors*, J. Low Temp. Phys. **167**, 360 (2012).

[18] J. Baselmans, S. J. C. Yates, R. Barends, Y. J. Y. Lankwarden, J. R. Gao, H. Hoevers, and T. M. Klapwijk, *Noise and sensitivity of aluminum kinetic inductance detectors for sub-mm astronomy*, J. Low Temp. Phys. **151**, 524 (2008).

[19] J. Gao, L. R. Vale, J. A. B. Mates, D. R. Schmidt, G. C. Hilton, K. D. Irwin, F. Mallet, M. Castellanos-Beltran, K. W. Lehnert, J. Zmuidzinas, and H. G. LeDuc,

Strongly quadrature-dependent noise in superconducting micro-resonators measured at the vacuum-noise limit, Appl. Phys. Lett. **98**, 232508 (2011).

[20] J. Zmuidzinas, J. Gao, P. K. Day, and H. G. LeDuc, unpublished.

[21] P. J. de Visser, J. J. A. Baselmans, P. Diener, S. J. C. Yates, A. Endo, and T. M. Klapwijk, *Generation-Recombination Noise: The Fundamental Sensitivity Limit for Kinetic Inductance Detectors*, J. Low Temp. Phys. **167**, 335 (2012).

[22] P. J. de Visser, S. Withington, and D. J. Goldie, *Readout-power heating and hysteretic switching between thermal quasiparticle states in kinetic inductance detectors*, J. Appl. Phys. **108**, 114504 (2010).

[23] B. I. Ivlev, S. G. Lisitsyn, and G. M. Eliashberg, *Nonequilibrium excitations in superconductors in high-frequency fields*, J. Low Temp. Phys. **10**, 449 (1973).

[24] T. M. Klapwijk and J. E. Mooij, *Microwave-enhanced superconductivity in aluminium films*, Physica B+C **81**, 132 (1976).

[25] J.-J. Chang and D. J. Scalapino, *Kinetic-equation approach to nonequilibrium superconductivity*, Phys. Rev. B **15**, 2651 (1977).

[26] G. Catelani, L. I. Glazman, and K. E. Nagaev, *Effect of quasiparticle injection on the ac response of a superconductor*, Phys. Rev. B **82**, 134502 (2010).

[27] A. Anthore, H. Pothier, and D. Esteve, *Density of states in a superconductor carrying a supercurrent*, Phys. Rev. Lett. **90**, 127001 (2003).

Chapter 7

Fluctuations in the electron system of a superconductor exposed to a photon flux

In a superconductor, in which electrons are paired, the density of unpaired electrons should become zero when approaching zero temperature. Therefore radiation detectors based on breaking of pairs promise supreme sensitivity, which we demonstrate using an aluminium superconducting microwave resonator. We show that the resonator also enables the study of the response of the electron system of the superconductor to pair-breaking photons, microwave photons and varying temperatures. A large range in radiation power (at 1.54 THz) can be chosen by carefully filtering the radiation from a blackbody source. We identify two regimes. At high radiation power, fluctuations in the electron system caused by the random arrival rate of the photons are resolved, giving a straightforward measure of the optical efficiency ($48 \pm 8\%$) and showing an unprecedented detector sensitivity. At low radiation power fluctuations are dominated by excess quasiparticles, the number of which is measured through their recombination lifetime.

This chapter was published as P. J. de Visser, J. J. A. Baselmans, J. Bueno. N. Llombart and T. M. Klapwijk, *Nature Communications* **5**, 3130 (2014). The supplementary material submitted with this article is presented in Appendix C. Part of the Methods section in the article is presented in Chapter 3 and is referenced as such in this chapter.

7.1 Introduction

In a superconductor well below its critical temperature, the majority of the electrons is bound in a condensate of Cooper pairs. The further the superconductor is cooled down, the closer it gets to its ground state, where all the quasiparticles are condensed to pairs. Due to the low gap energy, the superconductor is sensitive to disturbances from the environment to which it couples. In most experiments this sensitivity is undesirable, but it is particularly suited for detection of radiation. The superconductor can interact with its environment due to either photons or phonons. Photons with an energy higher than the energy gap break up Cooper pairs into quasiparticles. The change in the number of quasiparticles and Cooper pairs changes the electrodynamic response of the superconductor, which can be measured using a microwave resonator [1]. Quasiparticles give rise to microwave losses and the Cooper pairs to a kinetic inductance [2]. In steady state, the number of quasiparticles fluctuates in time around a constant average value. A measurement of the spectrum of these fluctuations allows for a characterisation of the quasiparticle system when exposed to pair-breaking photons, microwave photons or to changes in the bath temperature. The characteristic timescale of the fluctuations, the quasiparticle recombination time, is inversely proportional to the number of quasiparticles [3], and is therefore a measure of this number. These fluctuation phenomena are a monitor of the superconducting state and reveal the physical mechanisms that are at the heart of pair breaking in a superconductor.

We study these processes in a superconducting pair breaking detector formed by a 50 nm thick Al film. The ideal pair breaking detector can either count single photons while its sensitivity is limited by Fano noise, or is photon integrating and limited by photon noise, the noise from the photon source itself [4]. In both cases a high optical efficiency is required. The principle of radiation detection due to pair breaking with superconducting microwave resonators was proposed in 2003 [1, 5]. Since then the most important source of excess noise [1], due to dielectric two level systems, has been thoroughly studied [6–9]. Here we report on an all-aluminium antenna-coupled microwave resonator detector (Fig. 7.1a), which is limited only by fluctuations in the electron system that are fundamentally connected to the physical process of pair breaking.

We use a blackbody with a variable temperature (3-25 K) and eight optical filters, which define an optical band around 1.54 THz, as shown schematically in Fig. 7.1b. The radiation power can be changed from 3×10^{-21} W to 7×10^{-13} W. At powers ranging from 0.1 - 700 fW, the sensitivity is only limited by the random arrival rate of the photons, which is evident through the measured power dependence of the noise equivalent power (NEP) as shown in Fig. 7.1c. At lower radiation powers, we observe a power-independent NEP. This is consistent with generation-recombination noise due to the presence of excess quasiparticles [10, 11]. Excess quasiparticles are a general concern for superconducting devices [12–18]. In this case they are generated by the microwave readout power [19, 20]. As shown in Fig. 7.1c, they impose a lower limit to the NEP of this detector of $3.8 \pm 0.6 \times 10^{-19}$ WHz$^{-1/2}$, which is the lowest reported so far for this type of detectors.

7.2 Design of the experiment.

The detector is based on a lens-antenna coupled superconducting microwave resonator. The resonator is an open ended half wave, coplanar waveguide resonator, where the central strip (with a width of 3 μm) is isolated from the ground plane. The resonators all have different lengths and therefore different resonant frequencies, enabling the read-out of all resonators using a single coaxial line. Radiation is focused by a silicon lens to an X-slot antenna [21], optimised for broad band detection from 1.4-2.8 THz. Radiation coupled to the antenna is launched as a travelling wave into the waveguide [21], where it is absorbed by breaking Cooper pairs (the gap energy $\Delta = 188$ μeV). The created quasiparticles, which can diffuse over several millimetres before they recombine, are confined to the central strip. The central strip layer is 50 nm thick, and the groundplane layer 100 nm. The thin central strip layer gives higher response and ensures that most of the radiation is absorbed in that central strip, due to its higher resistance (see Methods). The thick groundplane reduces antenna losses. An advantage of the geometry, shown in Fig. 7.1a, is that it can also be used at other radiation frequencies by only changing the antenna.

The sample is cooled in a pulse tube precooled adiabatic demagnetization refrigerator. The sample stage is carefully shielded from stray light from the 3 K stage of the cooler, using a box-in-a-box concept with optical filters at each stage, as well as coax cable filters in the outer box [22]. The photon source is a blackbody with a variable temperature between 3 and 25 K (see Section 3.2). The system is schematically depicted in Fig. 7.1b. Eight optical filters in series define an optical bandpass of 0.1 THz centred around 1.54 THz. Three filter stacks are essential to eliminate filter heating. The filter transmission of the three filter stages is shown in Fig. 7.2a. The curves of spectral radiance for high and low blackbody temperature indicate a large tuning range in radiation power (P_{rad}). In fact, P_{rad} can be varied between 3 zW (1 zW $= 10^{-21}$ W) and 1 pW (Fig. 3.4). Practically this experiment allows us to switch from a regime where the number of quasiparticles is fully determined by the radiation to a regime with a negligible number of optically created quasiparticles. We put a polarising wire grid just before the detector to make sure the detector only receives radiation in the polarisation direction of the antenna.

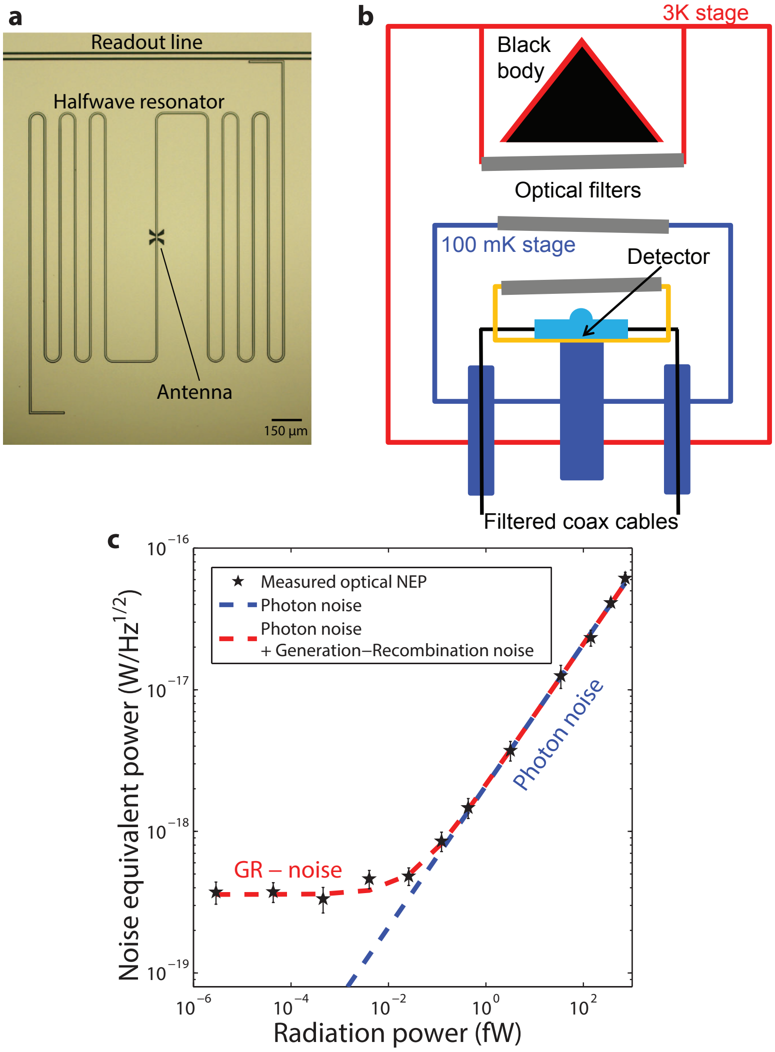

Figure 7.1: Overview of the experiment and main results. **a**, A picture of one antenna-coupled microwave resonator. It consists of a half wavelength coplanar waveguide microwave resonator with two open ends, capacitively coupled to a microwave readout line. In the middle it has an X-slot antenna to receive optical radiation. The ground plane and central strip of the resonator are respectively 100 and 50 nm thick layers of aluminium. **b**, Schematic of the setup for measurements at various radiation powers. A blackbody with a variable temperature illuminates the lens-antenna coupled resonators through three stacks of filters, which define a passband around 1.54 THz. Because of the box-in-box configuration at 100 mK and the coax cable filters, the device is well shielded from stray light. **c**, The optical sensitivity, expressed in Noise Equivalent Power (NEP) as a function of radiation power at a frequency of 20 Hz. We observe two regimes: above 0.1 fW the NEP increases with $\sqrt{P_{\mathrm{rad}}}$, indicative of photon noise, whereas below 0.1 fW the NEP saturates. The blue line is the photon noise limit as a function of power, with the optical efficiency (48%) taken into account. For the red dashed line, the generation-recombination noise limit due to excess quasiparticles is taken into account, based on a quasiparticle recombination time of 3 ms. The error bars (1 s.d.) are combined statistical uncertainties from the noise level and responsivity.

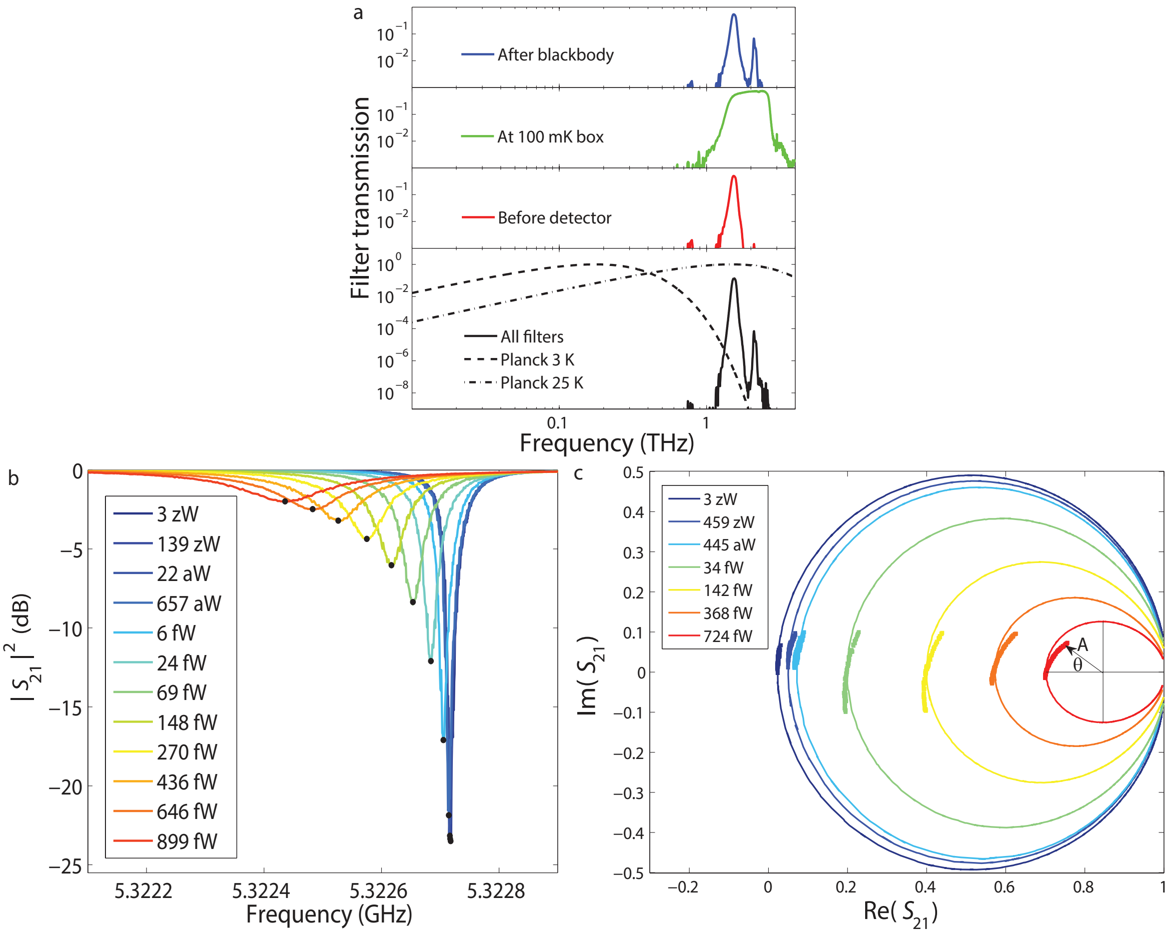

Figure 7.2: Response to radiation. **a**, Filter transmission characteristics of the three stacks of optical filters in the setup (Fig. 7.1b). The first and third set of filters have a low-pass, a band-pass and a high-pass filter. The second set (at the 100 mK box) has only a high- and a low-pass filter. In the bottom panel the total transmission of these eight filters is shown. We also show the normalised spectral radiance (Planck's law) at two blackbody temperatures, which demonstrate the large tunability in radiation power in this spectral range. Note that especially for low blackbody temperatures only a fraction 10^{-6} of the total power is in the spectral range of interest. The rejection of the rest of the power requires the eight consecutive filters. **b**, The magnitude of the microwave transmission $|S_{21}|^2$, measured as a function of frequency for various radiation powers as shown in the legend. At higher power, more quasiparticles are created, which give a higher resistance and inductance and therefore lead to a lower resonant frequency and a shallower dip. The dots show the resonant frequency at each power. **c**, The resonance circle for a selection of radiation powers (legend), measured as a function of frequency (lines). The squares show the response upon a small change in the radiation power measured at constant frequency, the resonant frequency of each circle. In the last circle we show how that response is translated into an amplitude, A, and a phase, θ.

7.3 Operation principle

The number of quasiparticles is measured through a measurement of the complex conductivity of the superconductor. The real part of the conductivity, σ_1, is due to the quasiparticles and resistive. The imaginary part, σ_2, is due to the kinetic inductance of the Cooper-pair condensate [2]. When the radiation power or the bath temperature is increased, more quasiparticles are generated, which changes both σ_1 and σ_2. The kinetic inductance increases, which leads to a lower resonant frequency $f_0 = 1/2l\sqrt{(L_\mathrm{g} + L_\mathrm{k})C}$, where l is the length of the resonator, L_g the geometrical inductance, L_k the kinetic inductance and C the capacitance of the line, all per unit length. The losses at microwave frequencies also increase, leading to a shallower resonance. Measurements of the resonance curves for various radiation powers are shown in Fig. 7.2b. In a practical detection scheme one typically uses an amplitude, A, and a phase, θ, referred to the resonance circle in the complex plane [6], as shown in Fig. 7.2c. The amplitude response originates from a change in resistance, whereas the phase changes due to the kinetic inductance. We have only used the amplitude response in this experiment, because the phase-noise is too high for this resonator (see Section C.1).

The NEP is a convenient quantity to compare the spectra of quasiparticle fluctuations in different regimes, as shown in Fig. 7.1c. The NEP of the resonator amplitude is experimentally determined from a measurement of the noise spectrum (S_A) and the responsivity to radiation (dA/dP_rad) and given by

$$NEP(f) = \sqrt{S_A(f)} \left(\frac{dA}{dP_\mathrm{rad}}\right)^{-1} \sqrt{1 + (2\pi f \tau_\mathrm{qp})^2}, \tag{7.1}$$

with P_rad the radiation power and f the modulation frequency. dA/dP_rad is obtained experimentally by a linear fit to a measurement of A where P_rad was slowly varied around the power of interest (see Section 3.4.4). The measured microwave response upon a change in P_rad is shown in Fig. 7.2c. The last factor in Eq. 7.1 arises because the quasiparticle system cannot respond to fluctuations that are faster than the quasiparticle recombination time, τ_qp.

7.4 Photon-induced quasiparticle fluctuations

If the average number of quasiparticles is dominated by the absorbed optical photons, the number of quasiparticles fluctuates in time due to two contributions. One is fundamental to every power-integrating detector and due to the random arrival rate of the photons, which induce a random generation of quasiparticles. The power spectral density of fluctuations in the resonator amplitude due to this photon noise is given by [4]

$$S_A^\mathrm{P}(f) = 2hFP_\mathrm{rad}(1 + \eta_\mathrm{opt}B)\frac{(dA/dP_\mathrm{rad})^2}{1 + (2\pi f \tau_\mathrm{qp})^2}, \tag{7.2}$$

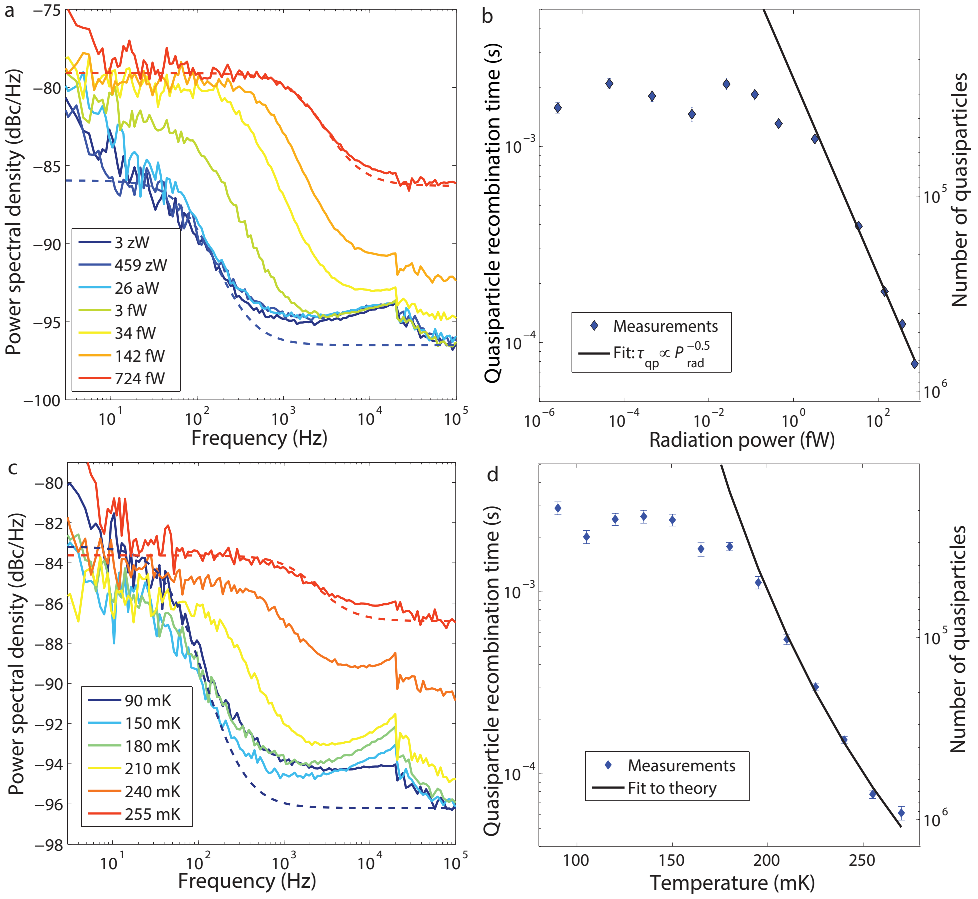

Figure 7.3: Quasiparticle fluctuations. **a**, Power spectral density of the resonator amplitude as a function of frequency for different radiation powers at a constant bath temperature of 120 mK and a constant microwave readout power of -88 dBm. Lorentzian fits to the spectra at the lowest and highest temperatures (dashed lines) show how the quasiparticle recombination time can be extracted from the spectra. A noise floor due to amplifier noise is added to the fitted roll-off. **b**, The quasiparticle recombination time as a function of radiation power obtained from the roll-off frequency in the measured spectra. The error bars denote statistical uncertainties from the fitting procedure (1 s.d.). The line is a power law fit to the last five points (where τ_{qp} does not saturate): $\tau_{\mathrm{qp}} \propto P_{\mathrm{rad}}^{-0.50\pm0.03}$. The right axis shows the number of quasiparticles corresponding to the measured recombination time. **c**, Power spectral density of the resonator amplitude as a function of frequency for different bath temperatures at a microwave readout power of -88 dBm. As expected the level of the spectrum stays constant and the roll-off frequency increases with increasing temperature, corresponding to a decreasing recombination time. At the highest two temperatures, the spectral level starts to rise, because the amplifier noise starts to dominate. **d**, Quasiparticle recombination time as a function of temperature as extracted from the spectra. The error bars are 1 s.d. The solid line is the theoretical expectation for the recombination time from Ref. [3]. The right axis shows the number of quasiparticles corresponding to the measured recombination time.

where the first term is the spectrum of the photon (power) fluctuations and the second term describes the resonator response upon a change in the radiation power. F is the frequency of the optical photons and h Planck's constant. The factor $(1+\eta_{\mathrm{opt}}B)$ is the correction to Poissonian statistics due to photon bunching for a single mode, with η_{opt} the optical efficiency and B the mode occupation [23]. The photon bunching contribution is negligible for the here measured power range (Fig. 3.4b). Eq. 7.2 is valid as long as $\tau_{\mathrm{qp}} \gg \tau_{\mathrm{res}}$, which holds in this experiment since the response time of the resonator, given by $\tau_{\mathrm{res}} = Q/\pi f_0$, is 6 μs. Q is the quality factor of the resonator.

Because of the pair-breaking nature of the radiation absorption a second noise mechanism arises due to random recombination of the quasiparticles that are generated by the photons. This is half the generation-recombination noise that arises in thermal equilibrium [24], because generation noise is already contained in Eq. 7.2. The spectrum is given by

$$S_A^{\mathrm{R}}(f) = \frac{2N_{\mathrm{qp}}\tau_{\mathrm{qp}}}{1+(2\pi f\tau_{\mathrm{qp}})^2}\left(\frac{dA}{dN_{\mathrm{qp}}}\right)^2, \tag{7.3}$$

with N_{qp} the number of quasiparticles and dA/dN_{qp} the responsivity of A to a change in N_{qp}. Quasiparticle number fluctuations can be converted to power fluctuations through $\eta_{\mathrm{pb}}\eta_{\mathrm{opt}}P_{\mathrm{rad}} = N_{\mathrm{qp}}\Delta/\tau_{\mathrm{qp}}$. η_{opt} is the optical efficiency, the efficiency with which power in front of the lens is absorbed in the detector. $\eta_{\mathrm{pb}} \approx 0.57$ is the pair breaking efficiency [25], the efficiency with which absorbed radiation power is converted into quasiparticles. For small changes in the quasiparticle number, $dP_{\mathrm{rad}}/dN_{\mathrm{qp}} = \Delta/(\tau_{\mathrm{qp}}\eta_{\mathrm{pb}}\eta_{\mathrm{opt}})$ and therefore $dA/dP_{\mathrm{rad}} = \tau_{\mathrm{qp}}\eta_{\mathrm{pb}}\eta_{\mathrm{opt}}/\Delta \cdot (dA/dN_{\mathrm{qp}})$. From Eqs. 7.2 and 7.3, the relative contribution of photon noise compared to recombination noise is given by $hF(1+mB)\eta_{\mathrm{pb}}\eta_{\mathrm{opt}}/\Delta = 10$ at all P_{rad}, for $F = 1.54$ THz and $\eta_{\mathrm{opt}} = 0.5$.

The NEP due to photon noise and recombination noise (Eqs. 7.1-7.3), for $f < 1/(2\pi\tau_{\mathrm{qp}})$, is given by

$$NEP_{\mathrm{photon}} = \sqrt{\frac{2P_{\mathrm{rad}}hF(1+\eta_{\mathrm{opt}}B) + 2\Delta P_{\mathrm{rad}}/\eta_{\mathrm{pb}}}{\eta_{\mathrm{opt}}}}, \tag{7.4}$$

which is shown as the blue dashed line in Fig. 7.1c. The three contributions in Eq. 7.4 are compared in Fig. 3.4b.

In thermal equilibrium N_{qp} is related to τ_{qp} through

$$N_{\mathrm{qp}} = \frac{1}{\tau_{\mathrm{qp}}}\frac{\tau_0 N_0 (k_{\mathrm{B}}T_{\mathrm{c}})^3 V}{2\Delta^2}, \tag{7.5}$$

where N_0 is the single spin density of states at the Fermi level, V the volume, k_{B} Boltzmann's constant, and τ_0 the characteristic electron-phonon interaction time [3]. We take $N_0 = 1.72 \times 10^{10}$ μm^{-3}eV^{-1} and $V = 0.6 \times 10^3$ μm^3, half the volume of the central strip of the resonator (see Methods). In this experiment Eq. 7.5 can be applied under the assumption that the response of the resonator amplitude is dominated by quasiparticle generation and recombination. We have shown earlier in a similar aluminium device that N_{qp} and τ_{qp} are related by Eq. 7.5 for thermally generated quasiparticles. This equation is also expected to hold in non-equilibrium conditions due to optical excitations [26] or microwave readout power dissipation at low bath temperatures [20].

The fluctuations in the resonator amplitude were measured as a function of radiation power at a constant bath temperature of 120 mK (Section 3.4.2). The resulting power spectral densities are shown in Fig. 7.3a for a selection of radiation powers and a constant microwave readout power (the power on the readout line) of -88 dBm. We observe that the spectra show a roll-off, the frequency of which increases as a function of radiation power, due to the decreasing quasiparticle recombination time. The other phenomena in the noise spectrum at higher frequencies (the bump at 20 kHz, a second higher frequency roll-off and amplifier noise, see Fig. C.3) are understood and can be accounted for (see Section C.2). The quasiparticle recombination times from the roll-off in the spectra are shown as a function of radiation power in Fig. 7.3b. N_{qp}, calculated using Eq. 7.5 is shown on the right axis. Since $\eta_{\mathrm{pb}}\eta_{\mathrm{opt}}P_{\mathrm{rad}} = N_{\mathrm{qp}}\Delta/\tau_{\mathrm{qp}}$ and $N_{\mathrm{qp}} \propto 1/\tau_{\mathrm{qp}}$ (Eq. 7.5), τ_{qp} is expected to scale as $\tau_{\mathrm{qp}} \propto P_{\mathrm{rad}}^{-1/2}$. A fit to the measured recombination time as a function of P_{rad} results in $\tau_{\mathrm{qp}} \propto P_{\mathrm{rad}}^{-0.50\pm0.03}$, which agrees very well with the expected behaviour. Within the measurement accuracy the same coefficient is measured for other microwave readout powers. The quasiparticle recombination time saturates below about 0.1 fW. This saturation in the recombination time is commonly observed [27] but not yet understood for all materials. Here the saturation is consistent with the presence of excess quasiparticles, which we have demonstrated in measurements on a very similar Al resonator [11].

7.5 Phonon-induced quasiparticle fluctuations

Excess quasiparticles give rise to quasiparticle number fluctuations [11, 19]. To verify that the spectra in the saturation regime show these fluctuations, we change the number of quasiparticles by varying the number of phonons (the bath temperature) at the same microwave power. The amplitude spectrum is shown for bath temperatures ranging from 90-255 mK in Fig. 7.3c. The blackbody temperature is kept at 3.2 K, so there are less than 100 quasiparticles due to the radiation power in the sensitive volume. The amplitude spectrum due to quasiparticle fluctuations can be described as [10, 11] $S_A^{\mathrm{GR}}(f) = 2S_A^{\mathrm{R}}(f)$, because here both generation and recombination are considered. The noise level, which is proportional to $N_{\mathrm{qp}}\tau_{\mathrm{qp}}$, is expected to be constant as a function of temperature (see Eq. 7.5), which we indeed observe in Fig. 7.3c. We assume here that dA/dN_{qp} is constant for this temperature range [26]. The quasiparticle recombination time extracted from these spectra is plotted as a function of temperature in Fig. 7.3d.

We observe the same saturation level in the recombination time as in Fig. 7.3b where the radiation power was changed. $\tau_0 = 303 \pm 14$ ns is obtained from a fit to the measured τ_{qp} as a function of temperature [3, 11]. τ_0 is slightly different from earlier results (458 ns [11]), which could be due to the higher resistivity and T_c of the Al [3].

We have now verified that the noise spectra in the regime of low radiation power (below 0.1 fW) are consistent with quasiparticle number fluctuations. The optical NEP due to quasiparticle number fluctuations is given by

$$NEP_{\mathrm{GR}} = \frac{2\Delta}{\eta_{\mathrm{pb}}\eta_{\mathrm{opt}}}\sqrt{\frac{N_{\mathrm{qp}}}{\tau_{\mathrm{qp}}}}. \tag{7.6}$$

Using this equation, the saturation of the NEP in Fig. 7.1c is consistent with the measured saturation in the quasiparticle recombination time (Fig. 7.3b) and the number of quasiparticles inferred from that measurement.

If we return to the photon induced fluctuations in Fig. 7.3a, we observe that the noise level becomes also constant at the highest radiation powers. This constant level is expected when Eqs. 7.2 and 7.3 are rewritten in terms of $N_{\mathrm{qp}}\tau_{\mathrm{qp}}$. The noise level is higher than in Fig. 7.3c, because there is both photon noise and recombination noise.

7.6 Noise equivalent power

The measured NEP, obtained by using Eq. 7.1 together with the measured S_A, dA/dP_{rad} and τ_{qp}, is shown for various radiation powers in Fig. 7.4. The NEP measurement was done at a range of microwave readout powers. The results shown in Figs. 7.1c and 7.4 are at the readout power with the minimum NEP for that radiation power. The measured dA/dP_{rad} and S_A that constitute the NEP are shown in Fig. C.1. Note that the levels of these S_A are different from those in Fig. 7.3a because of the strong dependence of dA/dP_{rad} on the microwave readout power.

The measured optical NEP at 20 Hz is shown as a function of radiation power in Fig. 7.1c as our main result. At radiation powers of 0.1 fW and higher, the NEP scales with $\sqrt{P_{\mathrm{rad}}}$, as expected from the photon noise limit given by Eq. 7.4. In this regime, the optical efficiency is obtained by fitting Eq. 7.4 to the measured NEP. The result is shown as the blue line in Fig. 7.1c, which gives $\eta_{\mathrm{opt}} = 0.48 \pm 0.08$ for a single polarisation, consistent with electromagnetic simulations of the antenna (see Section 3.2.2).

Below 0.1 fW, the NEP saturates at $3.8 \pm 0.6 \times 10^{-19}$ WHz$^{-1/2}$. We have seen that generation-recombination noise due to excess quasiparticles dominates the noise spectra in this regime. From the measured recombination time (3 ms, see Fig. 7.5b), we calculate N_{qp} using Eq. 7.5. The sum of Eqs. 7.4 and 7.6 is shown as the red dashed line in Fig. 7.1c and gives a good account of the measured NEP. The limit of 3.8×10^{-19} WHz$^{-1/2}$ is in good agreement with predictions based on dark experiments [19].

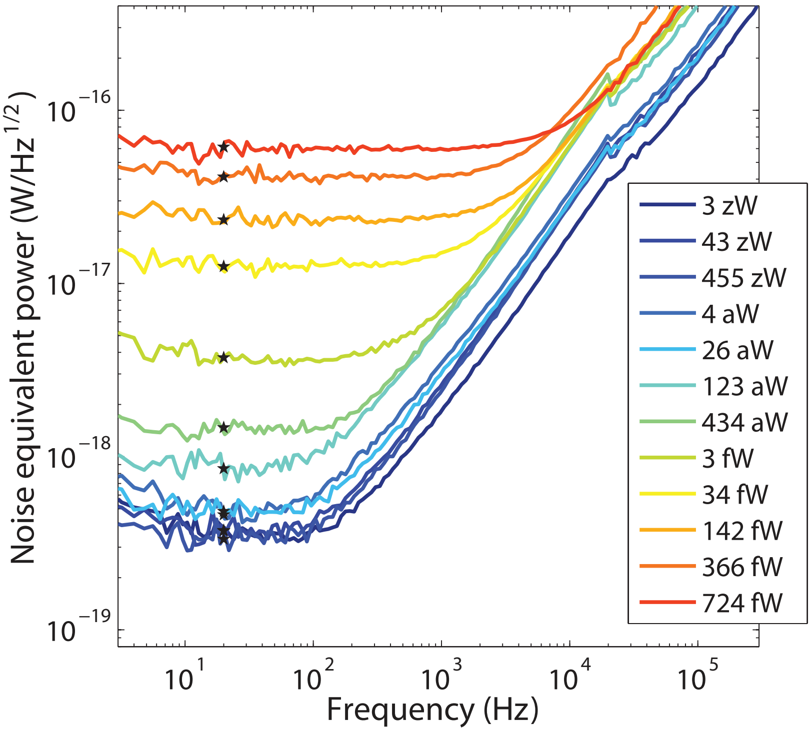

Figure 7.4: Noise equivalent power. Measured optical noise equivalent power (NEP) in the resonator amplitude as a function of frequency for different radiation powers. The corner frequency of each spectrum corresponds to the quasiparticle recombination time as plotted in Fig. 7.3b. The stars indicate the NEP at the reference frequency of 20 Hz, which is chosen well within the quasiparticle roll-off. These are the NEP values shown in Fig. 7.1c. The measurements shown are taken at the readout power that gives the minimum NEP for that radiation power.

7.7 Excess quasiparticles due to the readout power

From recent dark experiments [19] (without blackbody source) and simulations [20] we expect that the excess quasiparticles at low radiation power are due to microwave readout power dissipation. In an optical experiment excess quasiparticles should lead to a decrease in the optical response. The measured responsivity is shown in Fig. 7.5a as a function of P_{read}. Indeed, the responsivity decreases with increasing P_{read}, consistent with excess quasiparticles due to microwave absorption. A power law fit to the responsivity versus readout power results in $dA/P_{\mathrm{rad}} \propto P_{\mathrm{read}}^{-0.4\pm0.1}$. Fig. 7.5b shows τ_{qp}, extracted from the noise spectra, as a function of P_{read}. τ_{qp} increases when P_{read} decreases, which is also consistent with quasiparticle generation by the microwave readout signal [19, 20]. A fit to the measured data gives $\tau_{\mathrm{qp}} \propto P_{\mathrm{read}}^{-0.2\pm0.05}$.

Microwave absorption leads to a strong non-equilibrium quasiparticle distribution in aluminium microwave resonators, which was recently shown in calculations [20] and experimentally [28]. The complex conductivity is shown to be more sensitive to the

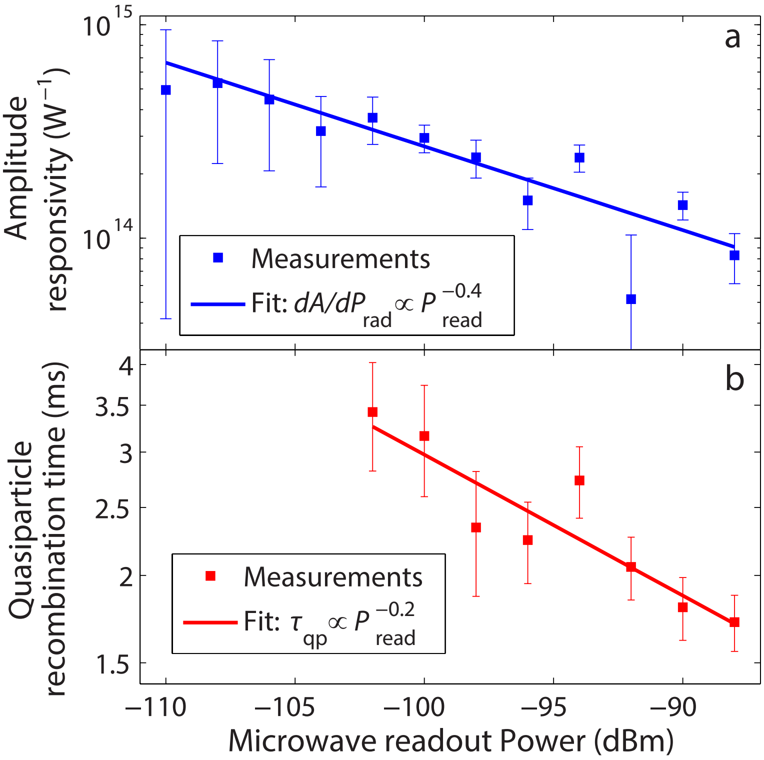

Figure 7.5: Readout power dependence. **a**, The optical responsivity, as obtained from a fit to the measured amplitude response, as a function of microwave readout power. The error bars denote statistical uncertainties from the fitting procedure (1 s.d.). The line is a power law fit to the data: $dA/dP_{\mathrm{rad}} \propto P_{\mathrm{read}}^{-0.4\pm0.1}$. **b**, The quasiparticle recombination time as obtained from the roll-off in the noise spectra as a function of microwave readout power. The error bars are 1 s.d. Below -102 dBm, the roll-off due to the recombination time is not visible anymore. The line is a fit to the data with a power law coefficient of $\tau_{\mathrm{qp}} \propto P_{\mathrm{read}}^{-0.2\pm0.1}$. All data is measured at a radiation power of 3 zW and a bath temperature of 120 mK.

details of the non-equilibrium quasiparticle distribution than τ_{qp}. Therefore the different exponents for dA/dP_{rad} and τ_{qp} in Fig. 7.5 are not surprising. An extension of the work in Ref. [20], including pair breaking radiation, would be needed to understand the data in Fig. 7.5. If we make two assumptions we can get a rough estimate of how the observables in Fig. 7.5 scale with P_{read}. We assume that the absorbed microwave power is proportional to P_{read} and that η_{read}, the efficiency with which the readout power is converted to quasiparticles, is constant. In that case, the optical responsivity is expected to scale with readout power as $dA/P_{\mathrm{rad}} \propto P_{\mathrm{read}}^{-0.5}$ in the regime where the readout power dominates the number of quasiparticles, and $\tau_{\mathrm{qp}} \propto P_{\mathrm{read}}^{-0.5}$ (see Section C.3 for a derivation). Although the scaling of dA/dP_{rad} is in reasonable agreement with the measurements, the approximation does not cover the different exponents for responsivity and τ_{qp}. A more detailed theoretical treatment of this problem is required.

7.8 Discussion

At higher radiation powers, where the noise spectrum is dominated by photon noise, the optical responsivity also changes with readout power. In this regime ($P_{\mathrm{rad}} > 1$ fW) however, the measured photon noise NEP stays the same, as expected from Eq. 7.4 (see Fig. C.5). Therefore, when photon-noise dominates the noise spectrum, one can safely use high readout powers to suppress amplifier noise (see Sec. C.4).

At the lowest readout power where τ_{qp} was determined, $P_{\mathrm{read}} = -102$ dBm, the quasiparticle recombination time is 3.5 ms, which corresponds to a quasiparticle density $n_{\mathrm{qp}} = 24\ \mu\mathrm{m}^{-3}$. This density is still high in comparison with the lowest reported values for superconducting qubits and Cooper pair transistors [17, 18] (less than 0.1 $\mu\mathrm{m}^{-3}$), but inherent to the relatively high microwave powers we need in this type of experiments. The measured limit in optical NEP due to excess quasiparticles is comparable to the lowest observed optical NEP in other detectors for similar wavelengths [29–31].

A reduction in N_{qp} is possible by using a parametric amplifier with high bandwidth and dynamic range [32]. This allows a reduction of the readout power by about a factor 10. In the current design however, the detector would become too slow for practical use at low readout power due to the long recombination time. The most feasible route towards lower NEP with aluminium, the most reliable material so far, is to choose geometries in which the active volume is dramatically reduced, which could also be the route towards single photon counting at terahertz frequencies.

7.9 Methods

Sample design. A layer of aluminium with a thickness of 100 nm is sputtered onto a sapphire substrate and serves as the ground plane for the microwave resonators. The microwave resonator is a coplanar waveguide resonator with a central strip width of 3 μm and slit widths of 1.5 μm. The central strip of the resonator is made of a second layer of 50 nm thick Al. The critical temperature of the 50 nm layer is measured to be $T_c = 1.24$ K, from which the energy gap $\Delta = 1.76 k_B T_c = 188\ \mu$eV. From the normal state resistivity ($\rho = 2.2\ \mu\Omega$cm for the central strip and 0.28 $\mu\Omega$cm for the groundplane) the skin depth for radiation at 1.54 THz is 60 nm in the central strip and 21 nm in the groundplane. The X-slot antenna would be ineffective for a layer thinner than the skin depth, therefore the groundplane layer is 100 nm thick. The microwave sheet resistance of the central line is 0.46 Ω and that of the ground plane 0.13 Ω. Taking this effect into account, together with the participation ratios of the central line and the ground plane [33], we estimate that 90% of the radiation is absorbed in the central line.

The current distribution along the length of the resonator peaks at the antenna and decreases as $\sin(x)$ to zero at the open ends. Therefore the responsivity changes with $\sin^2(x)$. Since the diffusion length within a typical quasiparticle recombination lifetime of 2 ms is more than half the resonator length, optically created quasiparticles can move into the non-responsive regime. Therefore for calculating the number of quasiparticles in the sensitive volume, we take half the central strip volume, $V = 0.6 \times 10^3\ \mu\text{m}^3$.

Acknowledgements
We would like to thank Y.J.Y. Lankwarden for fabricating the devices and S.J.C. Yates for contributing to the experimental setup. This work has been supported as part of a collaborative project, SPACEKIDS, funded via grant 313320 provided by the European Commission under Theme SPA.2012.2.2-01 of Framework Programme 7.

References

[1] P. K. Day, H. G. LeDuc, B. A. Mazin, A. Vayonakis, and J. Zmuidzinas, *A broadband superconducting detector suitable for use in large arrays*, Nature **425**, 817 (2003).

[2] D. C. Mattis and J. Bardeen, *Theory of the anomalous skin effect in normal and superconducting metals*, Phys. Rev. **111**, 412 (1958).

[3] S. B. Kaplan, C. C. Chi, D. N. Langenberg, J. Chang, S. Jafarey, and D. J. Scalapino, *Quasiparticle and phonon lifetimes in superconductors*, Phys. Rev. B **14**, 4854 (1976).

[4] S. J. C. Yates, J. J. A. Baselmans, A. Endo, R. M. J. Janssen, L. Ferrari, P. Diener, and A. M. Baryshev, *Photon noise limited radiation detection with lens-antenna coupled microwave kinetic inductance detectors*, Appl. Phys. Lett. **99**, 073505 (2011).

[5] J. Zmuidzinas, *Superconducting Microresonators: Physics and Applications*, Ann. Rev. Condens. Matter Phys. **3**, 169 (2012).

[6] J. Gao, J. Zmuidzinas, B. A. Mazin, H. G. LeDuc, and P. K. Day, *Noise properties of superconducting coplanar waveguide microwave resonators*, Appl. Phys. Lett. **90**, 102507 (2007).

[7] J. Gao, M. Daal, J. M. Martinis, A. Vayonakis, J. Zmuidzinas, B. Sadoulet, B. A. Mazin, P. K. Day, and H. G. Leduc, *A semiempirical model for two-level system noise in superconducting microresonators*, Appl. Phys. Lett. **92**, 212504 (2008).

[8] R. Barends, H. L. Hortensius, T. Zijlstra, J. J. A. Baselmans, S. J. C. Yates, J. R. Gao, and T. M. Klapwijk, *Contribution of dielectrics to frequency and noise of NbTiN superconducting resonators*, Appl. Phys. Lett. **92**, 223502 (2008).

[9] R. Barends, N. Vercruyssen, A. Endo, P. J. de Visser, T. Zijlstra, T. M. Klapwijk, and J. J. A. Baselmans, *Reduced frequency noise in superconducting resonators*, Appl. Phys. Lett. **97**, 033507 (2010).

[10] C. M. Wilson, L. Frunzio, and D. E. Prober, *Time-resolved measurements of thermodynamic fluctuations of the particle number in a nondegenerate Fermi gas*, Phys. Rev. Lett. **87**, 067004 (2001).

[11] P. J. de Visser, J. J. A. Baselmans, P. Diener, S. J. C. Yates, A. Endo, and T. M. Klapwijk, *Number fluctuations of sparse quasiparticles in a superconductor*, Phys. Rev. Lett. **106**, 167004 (2011).

[12] J. M. Martinis, M. Ansmann, and J. Aumentado, *Energy decay in superconducting Josephson-junction qubits from nonequilibrium quasiparticle excitations*, Phys. Rev. Lett. **103**, 097002 (2009).

[13] G. Catelani, J. Koch, L. Frunzio, R. J. Schoelkopf, M. H. Devoret, and L. I. Glazman, *Quasiparticle relaxation of superconducting qubits in the presence of flux*, Phys. Rev. Lett. **106**, 077002 (2011).

[14] M. Lenander, H. Wang, R. C. Bialczak, E. Lucero, M. Mariantoni, M. Neeley, A. D. O'Connell, D. Sank, M. Weides, J. Wenner, T. Yamamoto, Y. Yin, J. Zhao, A. N. Cleland, and J. M. Martinis, *Measurement of energy decay in superconducting qubits from nonequilibrium quasiparticles*, Phys. Rev. B **84**, 024501 (2011).

[15] M. Zgirski, L. Bretheau, Q. L. Masne, H. Pothier, D. Esteve, and C. Urbina, *Evidence of long-lived quasiparticles trapped in superconducting point contacts*, Phys. Rev. Lett. **106**, 257003 (2011).

[16] R. Barends, J. Wenner, M. Lenander, Y. Chen, R. C. Bialczak, J. Kelly, E. Lucero, P. O'Malley, M. Mariantoni, D. Sank, H. Wang, T. C. White, Y. Yin, J. Zhao, A. N. Cleland, J. M. Martinis, and J. J. A. Baselmans, *Minimizing quasiparticle generation from stray infrared light in superconducting quantum circuits*, Appl. Phys. Lett. **99**, 113507 (2011).

[17] O.-P. Saira, A. Kemppinen, V. F. Maisi, and J. P. Pekola, *Vanishing quasiparticle density in a hybrid Al/Cu/Al single-electron transistor*, Phys. Rev. B **85**, 012504 (2012).

[18] D. Ristè, C. C. Bultink, M. J. Tiggelman, R. N. Schouten, K. W. Lehnert, and L. DiCarlo, *Millisecond charge-parity fluctuations and induced decoherence in a superconducting transmon qubit*, Nature Comm. **4**, 1913 (2013).

[19] P. J. de Visser, J. J. A. Baselmans, S. J. C. Yates, P. Diener, A. Endo, and T. M. Klapwijk, *Microwave-induced excess quasiparticles in superconducting resonators measured through correlated conductivity fluctuations*, Appl. Phys. Lett. **100**, 162601 (2012).

[20] D. J. Goldie and S. Withington, *Non-equilibrium superconductivity in quantum-sensing superconducting resonators*, Supercond. Sci. Technol. **26**, 015004 (2013).

[21] A. Iacono, A. Freni, A. Neto, and G. Gerini, *In-line X-slot element focal plane array of Kinetic Inductance Detectors*, in *Proceedings of the European Conference on Antennas and Propagation*, Rome, Italy, 2011.

[22] J. Baselmans, S. Yates, P. Diener, and P. de Visser, *Ultra low background cryogenic test facility for far-infrared radiation detectors*, J. Low Temp. Phys. **167**, 360 (2012).

[23] R. W. Boyd, *Photon bunching and the photon-noise-limited performance of infrared detectors*, Infrared Phys. **22**, 157 (1982).

[24] C. M. Wilson and D. E. Prober, *Quasiparticle number fluctuations in superconductors*, Phys. Rev. B **69**, 094524 (2004).

[25] A. G. Kozorezov, A. F. Volkov, J. K. Wigmore, A. Peacock, A. Poelaert, and R. den Hartog, *Quasiparticle-phonon downconversion in nonequilibrium superconductors*, Phys. Rev. B **61**, 11807 (2000).

[26] J. Gao, J. Zmuidzinas, A. Vayonakis, P. Day, B. Mazin, and H. Leduc, *Equivalence of the effects on the complex conductivity of superconductor due to temperature change and external pair breaking*, J. Low Temp. Phys. **151**, 557 (2008).

[27] R. Barends, S. van Vliet, J. J. A. Baselmans, S. J. C. Yates, J. R. Gao, and T. M. Klapwijk, *Enhancement of quasiparticle recombination in Ta and Al superconductors by implantation of magnetic and nonmagnetic atoms*, Phys. Rev. B **79**, 020509(R) (2009).

[28] P. J. de Visser, D. J. Goldie, P. Diener, S. Withington, J. J. A. Baselmans, and T. M. Klapwijk, *Evidence of a Nonequilibrium Distribution of Quasiparticles in the Microwave Response of a Superconducting Aluminum Resonator*, Phys. Rev. Lett. **112**, 047004 (2014).

[29] B. S. Karasik and R. Cantor, *Demonstration of high optical sensitivity in far-infrared hot-electron bolometer*, Appl. Phys. Lett. **98**, 193503 (2011).

[30] M. D. Audley, G. de Lange, J.-R. Gao, P. Khosropanah, M. Ridder, L. Ferrari, W. M. Laauwen, M. Ranjan, P. D. Mauskopf, D. Morozov, and N. A. Trappe, *Measurements of the optical performance of bolometers for SPICA / SAFARI*, Proc. of SPIE **8452**, 84520B (2012).

[31] K. J. Stone, K. G. Megerian, P. K. Day, P. M. Echternach, J. Bueno, and N. Llombart, *Real time quasiparticle tunneling measurements on an illuminated quantum capacitance detector*, Appl. Phys. Lett. **100**, 263509 (2012).

[32] B. H. Eom, P. K. Day, H. G. LeDuc, and J. Zmuidzinas, *A wideband, low-noise superconducting amplifier with high dynamic range*, Nature Phys. **8**, 623 (2012).

[33] C. L. Holloway and E. F. Kuester, *A quasi-closed form expression for the conductor loss of CPW lines, with an investigation of edge shape effects*, IEEE Trans. Microwave Theory Tech. **43**, 2695 (1995).

Chapter 8

Evidence of a nonequilibrium distribution of quasiparticles in the microwave response of a superconducting aluminium resonator

In a superconductor absorption of photons with an energy below the superconducting gap leads to redistribution of quasiparticles over energy and thus induces a strong non-equilibrium quasiparticle energy distribution. We have measured the electrodynamic response, quality factor and resonant frequency, of a superconducting aluminium microwave resonator as a function of microwave power and temperature. Below 200 mK, both the quality factor and resonant frequency decrease with increasing microwave power, consistent with the creation of excess quasiparticles due to microwave absorption. Counterintuitively, above 200 mK, the quality factor and resonant frequency increase with increasing power. We demonstrate that the effect can only be understood by a non-thermal quasiparticle distribution.

This chapter was published as P. J. de Visser, D. J. Goldie, P. Diener, S. Withington, J. J. A. Baselmans, and T. M. Klapwijk, *Physical Review Letters* **112**, 047004 (2014).

8.1 Introduction

A superconductor can be characterised by the density of states, which exhibits an energy gap due to Cooper pair formation, and the distribution function of the electrons, which in thermal equilibrium is the Fermi-Dirac distribution. When a superconductor is driven by an electromagnetic field, nonlinear effects in the electrodynamic response can occur, which are usually assumed to be due to a change in the density of states, the so called pair breaking mechanism[1]. These nonlinear effects can be described along the lines of a current dependent superfluid density $n_s(T,j) \propto n_s(T)\,[1-(j/j_c)^2]$, where j is the actual current density, j_c the critical current density and T the temperature. Observations such as the nonlinear Meissner effect [1] and nonlinear microwave conductivity [2, 3] can be explained by a broadening of the density of states and a decreased n_s. The quasiparticles are assumed to be in thermal equilibrium and a Fermi-Dirac distribution $f(E) = 1/(\exp(E/k_BT)+1)$ is assumed, with E the quasiparticle energy and k_B Boltzmann's constant.

Here we demonstrate that a microwave field also has a strong effect on $f(E)$ in the superconductor, and induces a nonlinear response. We present measurements of the electrodynamic response, quality factor and resonant frequency, of an Al superconducting resonator (at 5.3 GHz) as a function of temperature and microwave power at low temperatures $T_c/18 < T < T_c/3$. The response measurements, complemented with quasiparticle recombination time measurements, are explained consistently by a model based on a microwave-induced non-equilibrium $f(E)$.

Redistribution of quasiparticles [4, 5] due to microwave absorption [6, 7] has been shown earlier to cause enhancement of the critical current [8, 9], the critical temperature (T_c) and the energy gap [10]. These enhancement effects are most pronounced close to T_c and were observed for temperatures $T > 0.8T_c$. A representation of gap suppression and gap enhancement is shown in the inset to Fig. 8.1b [9]. The consequences of the redistribution of quasiparticles for the electrodynamic response were only studied theoretically for $T > 0.5T_c$ [11]. Redistribution of quasiparticles also explains [12] the microwave power dependent number of quasiparticles in microwave resonators at low temperatures, which we have recently measured [13]. These quasiparticles impose a limit for detectors for astrophysics based on microwave resonators [14, 15]. Related phenomena have been reported in superconducting-normal metal devices [16, 17], terahertz pulse experiments [18] and holographic superconductivity [19].

8.2 Microwave power dependent Q and f_0

To measure the microwave response, microwave resonators were patterned into a 60 nm thick Al film, which was sputter deposited on a sapphire substrate. T_c was mea-

---

[1] This pair breaking mechanism is different from direct Cooper pair breaking by e.g. photons.

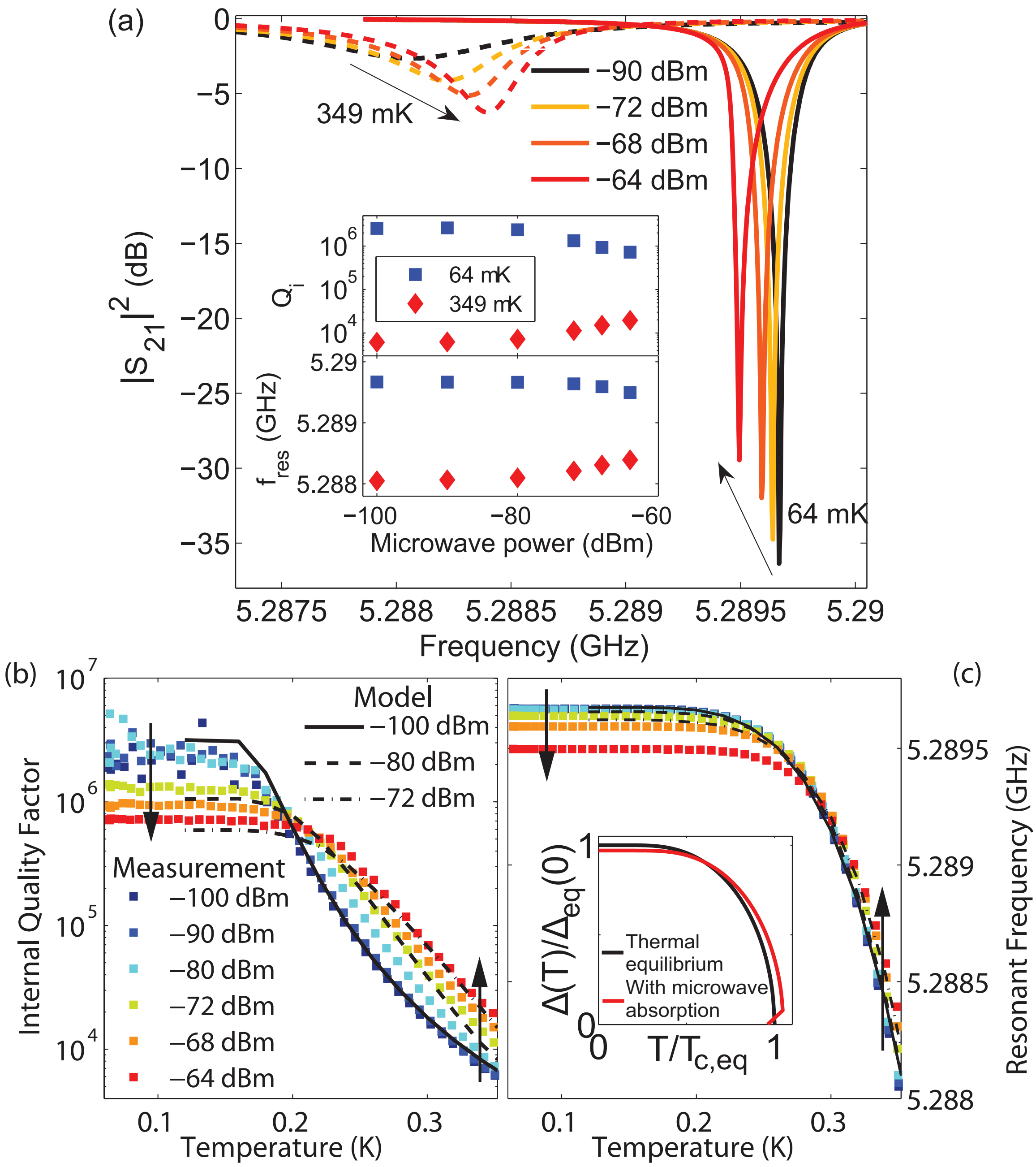

Figure 8.1: (a) The measured microwave transmission $|S_{21}|^2$ as a function of frequency for sample A. The solid lines are taken for four different microwave readout powers (P_{read}) at a temperature of 64 mK. The dashed lines are taken at 349 mK. The same colour coding applies. The arrows indicate increasing P_{read}. The inset shows the internal quality factor and resonant frequency as determined from the S_{21} measurements as a function of P_{read}. (b),(c) The measured internal quality factor and resonant frequency as a function of temperature for various P_{read} (the same legend applies). The arrows indicate increasing P_{read}. Simulation results are shown as lines. The inset is a representation of the effect of microwave absorption on the energy gap Δ. The temperature is normalised to the equilibrium T_c.

sured to be 1.17 K, from which the energy gap at zero temperature is taken to be $\Delta = 1.76k_BT_c = 177$ μeV. The low temperature resistivity was 0.9 $\mu\Omega$cm. The film was patterned by wet etching into distributed, half-wavelength, coplanar waveguide resonators, which are capacitively coupled to a transmission line. With readout power, P_{read}, we will mean the incident microwave power on the through transmission line. The presented measurements were performed on a resonator with a length of 9.84 mm and a central strip volume of 1770 μm^3 (sample A). Sample B is similar and will be introduced later. Further details are given in Table 8.1. The half-wavelength geometry was chosen because it has an isolated central strip, which prevents quasiparticle outdiffusion. The samples were cooled in a pulse tube precooled adiabatic demagnetization refrigerator. Care was taken to make the sample stage light-tight as described in Ref. [20], which is crucial to eliminate excess quasiparticles due to straylight. The complex transmission S_{21} of the microwave circuit was measured with a vector network analyser. The microwave signal was amplified at 4 K with a high electron mobility transistor amplifier and with a room temperature amplifier.

We have measured the microwave transmission S_{21} for various P_{read} as a function of temperature. A selection of resonance curves is shown in Fig. 8.1a. We kept P_{read} below the bifurcation regime [21, 22]. By fitting a Lorentzian curve to the resonance curve (Eq. 3.23), we extracted the resonant frequency (f_{res}) and the internal quality factor (Q_i), which are plotted for 64 and 349 mK as a function of P_{read} in the inset in Fig. 8.1a[2]. Q_i is higher when the resonance curve is deeper. Q_i and f_{res} are shown for several microwave powers as a function of temperature in Fig. 8.1b and c. Two distinct regimes appear. At low temperatures both Q_i and f_{res} decrease with increasing microwave power, which is consistent with a higher effective electron temperature. At the highest temperatures however, both Q_i and f_{res} increase with increasing power, which contradicts with a heating model [21] and also cannot be explained by a pair-breaking effect where the density of states broadens due to the current [23]. The pair-breaking mechanism would induce a downward frequency shift without dissipation [3] and might play a role at the highest P_{read} at the lowest temperatures.

8.3 Redistribution of quasiparticles

We have modelled the effect of absorption of microwave photons on the quasiparticle distribution function, $f(E)$, by using a set of kinetic equations. Absorption of a microwave photon with energy $\hbar\omega$ causes quasiparticles at an energy E to move to an energy $E + \hbar\omega$. The rate with which quasiparticles at energy E absorb photons with

---

[2] At 64 mK, a P_{read} of -64 (-100) dBm leads to a stored energy of 0.55 fJ (0.11 aJ), corresponding to 1.6×10^8 (3.1×10^4) photons.

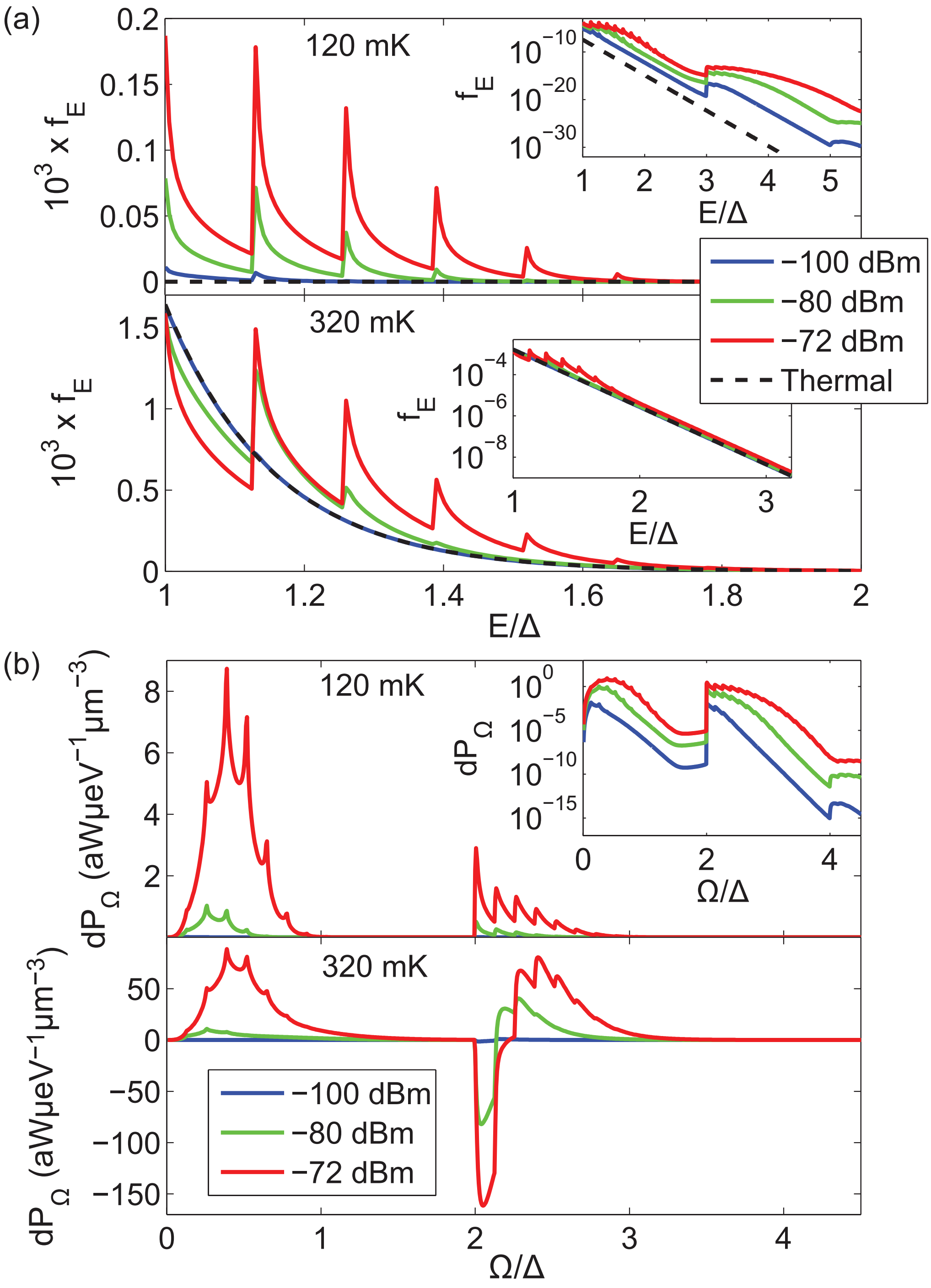

Figure 8.2: (a) The calculated quasiparticle distribution as a function of normalised energy. The two different panels are for temperatures of 120 and 320 mK. The insets show the same distributions on a log-scale. (b) The phonon power flow from the film to the substrate as a function of normalised energy, for 120 mK (the inset shows the same lines on a log-scale) and 320 mK. dP is zero in thermal equilibrium.

energy $\hbar\omega$ can be described with an injection term $I_{qp}(E,\omega)$ [6, 7], which is given by

$$\begin{aligned} I_{qp}(E,\omega) &= 2B\left[h_1(E,E+\hbar\omega)\left(f(E+\hbar\omega)-f(E)\right)\right. \\ &- \left. h_1(E,E-\hbar\omega)\left(f(E)-f(E-\hbar\omega)\right)\right], \end{aligned} \tag{8.1}$$

with $h_1(E,E') = \left(1+\frac{\Delta^2}{EE'}\right)\rho(E')$. $\rho(E)$ is the density of states, which is given by $\rho(E) = E/\sqrt{E^2-\Delta^2}$. B relates the injection rate to the microwave field strength [12, 24]. The thus created change in $f(E)$, is counteracted by electron-phonon scattering and quasiparticle recombination, which depend both on $f(E)$ and on $n(\Omega)$, the phonon distribution in the film (Ω is the phonon energy). In steady state the microwave power that is absorbed by the quasiparticle system is transported through the phonon system of the film and is released in the phonon system of the substrate, the heat bath. We solve the full nonlinear kinetic equations as presented in Ref. [4], together with Eq. 8.1, in steady state, $df(E)/dt = dn(\Omega)/dt = 0$ for all energies, with a self-consistency equation for Δ, given by

$$\frac{1}{N_0 V_{BCS}} = \int_{\Delta}^{\Omega_D} \frac{1-2f(E)}{\sqrt{E^2-\Delta^2}}dE, \tag{8.2}$$

with N_0 the single spin density of states at the Fermi level, Ω_D the Debye energy and V_{BCS} the effective pairing potential. The numerical procedure is explained in Ref. [12].

8.3.1 Effect on complex conductivity

The complex conductivity $\sigma = \sigma_1 - i\sigma_2$, describing the response of both Cooper pairs and quasiparticles to a time-varying electric field with $\hbar\omega < 2\Delta$, is given by [25]

$$\frac{\sigma_1}{\sigma_N}(\omega) = \frac{2}{\hbar\omega}\int_{\Delta}^{\infty}[f(E)-f(E+\hbar\omega)]g_1(E)dE, \tag{8.3}$$

$$\frac{\sigma_2}{\sigma_N}(\omega) = \frac{1}{\hbar\omega}\int_{\Delta-\hbar\omega}^{\Delta}[1-2f(E+\hbar\omega)]g_2(E)dE, \tag{8.4}$$

where $g_1(E) = h_1(E,E+\hbar\omega)\rho(E)$ and $g_2(E) = h_1(E,E+\hbar\omega)E/\sqrt{\Delta^2-E^2}$. σ_N is the normal-state conductivity and ω the angular frequency. Eqs. 8.3 and 8.4 show the role of $f(E)$ in determining the conductivity. In a microwave resonator f_{res} is proportional to the imaginary part of the conductivity, σ_2, and Q_i is proportional to σ_2/σ_1, which connects these observables to $f(E)$.

8.3.2 Absorbed microwave power

Since I_{qp} is proportional to the field strength squared, we need to know the microwave field in the resonator for a certain P_{read}. We solve this problem by using the absorbed microwave power in the quasiparticle system, P_{abs}. For the experiment P_{abs} can be calculated by

$$P_{abs} = \frac{P_{read}}{2}\frac{4Q^2}{Q_iQ_c}\frac{Q_i}{Q_{i,qp}}. \tag{8.5}$$

The loaded quality factor Q is given by $Q = \frac{Q_iQ_c}{Q_c+Q_i}$ and Q_c is the coupling quality factor. $Q_c = \pi/(\omega C_g Z_0)^2$, with C_g the coupling capacitance and Z_0 the characteristic impedance of the transmission line. See Section 3.3.4 for a derivation. The calculated P_{abs} based on the measured quality factors is shown in Fig. 8.3. Since Q_i depends strongly on temperature, P_{abs} is more than an order of magnitude higher at 300 mK (where $Q_i = Q_c$) than at 100 mK, which is a crucial ingredient to model the measurements in Fig. 8.1. The factor $Q_i/Q_{i,qp}$ in Eq. 8.5 arises when Q_i is not limited by quasiparticle dissipation. Here we take $Q_i/Q_{i,qp} = 1$. P_{abs} is calculated per unit volume, where the volume is taken to be twice that of the central strip of the resonator, to roughly account for the groundplane of the waveguide, in which power will be absorbed as well. In the calculations we adjust the constant B in Eq. 8.1, such that $P_{abs} = 4N_0 \int_\Delta^\infty I_{qp} E\rho(E)dE$.

8.3.3 Quasiparticle and phonon distribution functions

The simulations where performed for a frequency of 5.57 GHz. The resulting non-equilibrium quasiparticle distributions are shown in Fig. 8.2a for three readout powers for temperatures of 120 and 320 mK. A structure with sharp peaks at multiples of $\hbar\omega/\Delta$ shows up due to microwave photon absorption. At 120 mK, the driven distribution exceeds the thermal distribution at the bath temperature for all energies, meaning that excess quasiparticles are created. At 320 mK, the number of quasiparticles only increases a little at higher power, but quasiparticles are taken away from energies $\Delta < E < \Delta + \hbar\omega$.

In Fig. 8.2b we show the corresponding phonon power flow to the heat bath: $dP(\Omega) = 3N_{ion}D(\Omega)\Omega[n(\Omega) - n_{sub}(\Omega, T_{bath})]/\tau_{esc}$. The phonons in the film have a non-equilibrium distribution $n(\Omega)$. Phonons can escape to the substrate, the bath. The phonon distribution in the substrate $n_{sub}(\Omega)$ is assumed to have a Bose-Einstein distribution at the bath temperature T_{bath}. $\tau_{esc} = 0.17$ ns is the phonon escape time, calculated for Al on sapphire using the acoustic mismatch model [26]. N_{ion} is the number of ions per unit volume and $D(\Omega) = 3\Omega^2/\Omega_D^3$ is the phonon density of states. Fig. 8.2b shows strong non-equilibrium behaviour as well, with peaks at multiples of $\hbar\omega$. Phonons at $\Omega < 2\Delta$ arise due to scattering. At energies $\Omega > 2\Delta$ phonons due to both recombination and scattering occur. At 320 mK, we observe phonon transport out of the film, but also into the film ($dP(\Omega) < 0$ at energies $\Omega > 2\Delta$). This is a consequence of the depletion of $f(E)$ for energies $\Delta < E < \Delta + \hbar\omega$ (Fig. 8.2a) [27].

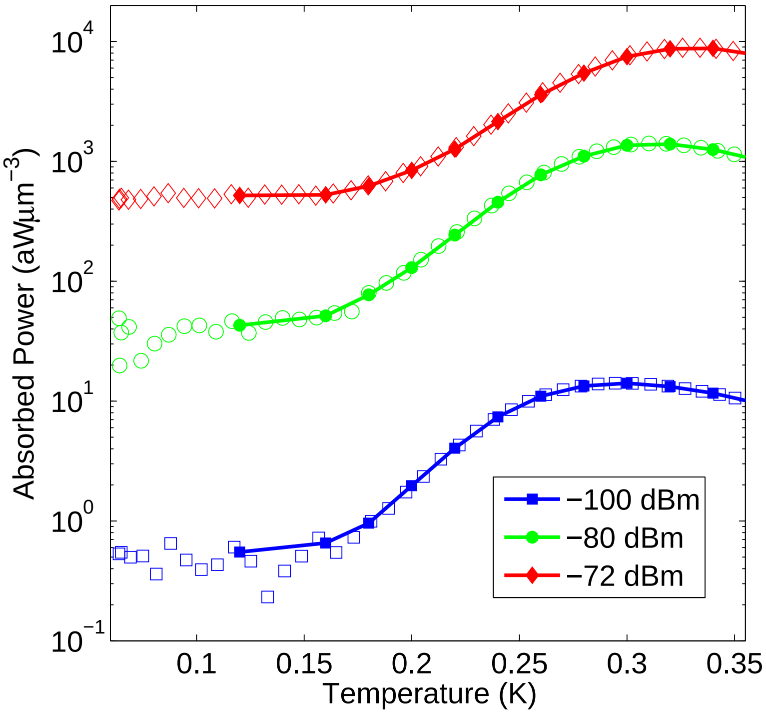

Figure 8.3: The absorbed microwave power per unit volume as a function of temperature for three different microwave readout powers. The open symbols are derived from the measurements. The filled symbols with lines are the values chosen for the simulations to show that we have modeled the same absorbed powers as derived from the measurements.

8.3.4 Effect on the observables

Having determined the quasiparticle distributions for various readout powers, we can calculate the non-equilibrium conductivity. Fig. 8.4a and b show σ_1 and σ_2, calculated using Eqs. 8.3 and 8.4. For comparison, we plot the quasiparticle density and the quasiparticle recombination time, τ_{qp}, in Fig. 8.4c and d. At low temperature, we observe that σ_1 increases and σ_2 decreases with increasing power, together with an increasing number of quasiparticles (analogous to heating), as described in Ref. [12]. At higher temperatures a counterintuitive effect occurs: σ_1 decreases (the microwave losses go down) and σ_2 increases with increasing power, whereas there are still excess quasiparticles being created. This effect cannot be consistently explained with a single effective quasiparticle temperature, but it can be understood from Fig. 8.2a (at 320 mK). For a thermal $f(E)$, the factor $[f(E) - f(E + \hbar\omega)]$ in Eq. 8.3 is larger than for a strongly driven distribution, because of the peaks in the driven distribution with separation $\hbar\omega$. The probability of absorbing a microwave photon is lower for a strongly driven distribution, which decreases σ_1 and therewith the losses. σ_2 is only sensitive

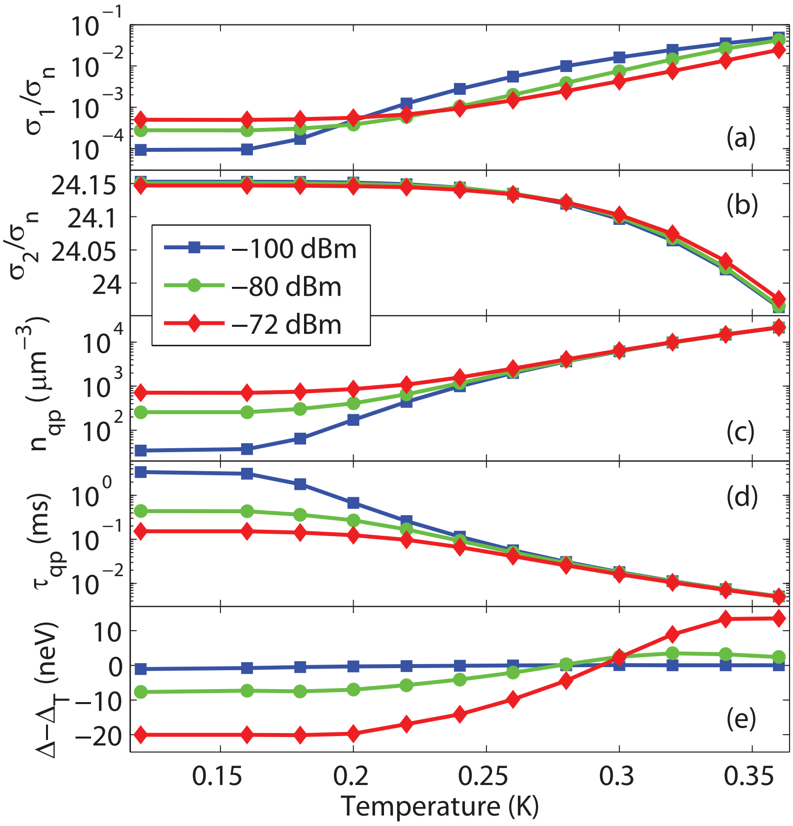

Figure 8.4: (a) The real part of the complex conductivity, σ_1, as a function of temperature, calculated for three microwave readout powers at a frequency of 5.57 GHz. (b) The imaginary part of the conductivity, σ_2, as a function of temperature. (c) The calculated quasiparticle density as a function of temperature. (d) The quasiparticle recombination lifetime as function of temperature. (e) The difference of the energy gap for the driven distributions (Δ) compared to a thermal distribution (Δ_T). The legend applies to all panels.

to quasiparticles at $\Delta < E < \Delta + \hbar\omega$ (Eq. 8.4). Below 250 mK (see Fig. 8.4b), the microwave absorption increases the quasiparticle population at $\Delta < E < \Delta + \hbar\omega$, whereas at higher temperatures the population becomes lower due to redistribution. The energy gap, calculated from Eq. 8.2, is shown in Fig. 8.4e. Clearly, the non-equilibrium $f(E)$ leads to gap suppression below 0.3 K, and gap enhancement above 0.3 K despite the creation of excess quasiparticles. The additional effect of the non-equilibrium Δ on the observables is minor, the structure in $f(E)$ dominates.

8.4 Comparison of simulations and experiments

To connect the calculated σ_1 and σ_2 with the experiment, we calculate Q_i and f_{res} through equations for a microstrip geometry [28] with the same central strip dimensions

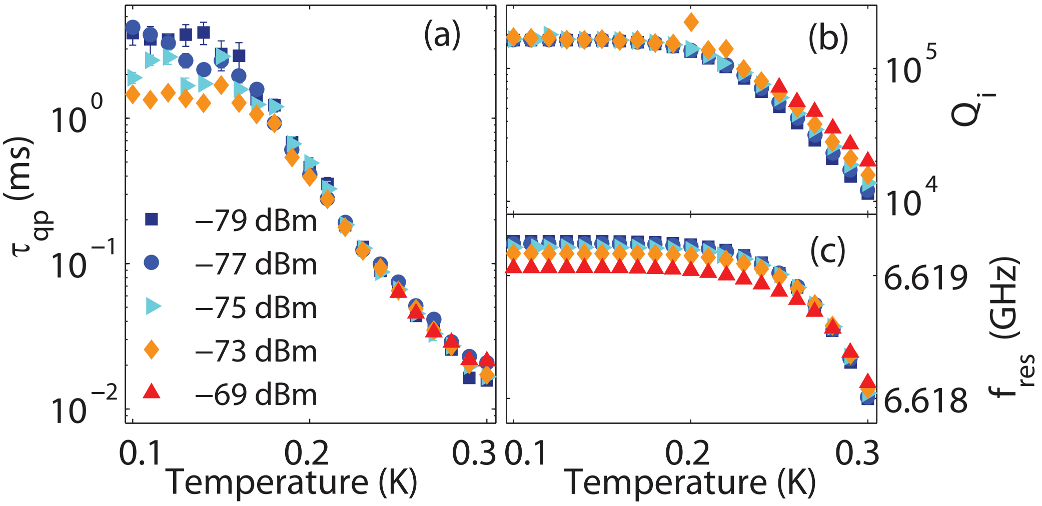

Figure 8.5: (a) The measured quasiparticle recombination time as obtained from a noise measurement for various microwave readout powers measured on sample B. (b) The measured internal quality factor and (c) resonant frequency. The legend applies to all panels.

as the measured resonator[3]. The results are plotted in Figs. 8.1b and c, which shows good agreement with the measurements. In particular, the cross-over temperatures in Q_i and f_{res} are well modelled, as is the temperature dependence of Q_i for both high and low powers. A comparison of Figs. 8.1b and c with Figs. 8.4a and b shows that Q_i is dominated by σ_1 and f_{res} by σ_2, as expected.

The experimental evidence for the different power dependence of τ_{qp} and the conductivity is shown in Fig. 8.5. These results were measured on sample B (see Table 8.1), on which we performed accurate measurements of τ_{qp} as reported on in Refs. [13, 31]. Fig. 8.5a shows τ_{qp} as determined from the cross-power spectral density of quasiparticle fluctuations in the amplitude and the phase of the resonator [13]. Panels b and c show the measured Q_i and f_{res}. The power range for this noise measurement is only 10 dB, due to the amplifier noise limit. We focus on $T > 200$ mK. Q_i increases with increasing power, consistent with Fig. 8.1b, whereas τ_{qp} stays constant, as expected from the simulations in Fig. 8.4d. We thus have a nonlinear conductivity effect due to quasiparticle redistribution, where Q_i increases despite of the creation of excess quasiparticles. This is in contrast with situations in which excess quasiparticles are introduced either on purpose or due to the environment [32–38] where $Q_i \propto 1/n_{qp}$, although also in qubits subtleties can occur due to $f(E)$ [39].

---

[3] These equations allow to calculate the complex propagation constant of the line, including the capacitance, the geometric and kinetic inductance and the losses. Equations for coplanar waveguide geometries usually give separate approximations for the attenuation and the kinetic inductance [29], or only one of the two [30]. The central strip dimensions and the film thickness have been kept the same as for the measured coplanar waveguide geometry. Since we are mainly interested here in the properties of the superconductor, these geometries are comparable.

8.5 Discussion

The qualitative agreement between measurements and calculations as apparent from Fig. 8.1b is quite satisfactory. However, the effect of the microwave power on Q_i and f_{res} is less than calculated. Since the uncertainty in the measured P_{read} is less than 2 dB, there should be a parallel dissipation channel. So far we assumed the same $f(E)$ for the groundplane of the resonator and the central strip. Future work may include the calculation of $f(E)$ in the groundplane, which is difficult due to the additional complexity of quasiparticle outdiffusion. A crude approximation, where the groundplane is an impedance with a thermal $f(E)$, in series with the non-equilibrium central strip [40], indicates indeed a reduced non-equilibrium effect of microwave power on Q_i and f_{res}. The non-equilibrium f(E) could be measured by combining the resonator experiment with tunnel probes [5].

In closing we emphasize that for the non-equilibrium $f(E)$ to occur (Fig. 8.2a), quasiparticle-phonon scattering has to be slow compared to I_{qp} and to ω, which is therefore more likely in materials with a low T_c, such as Al [41]. In addition, redistribution of quasiparticles at low temperatures leads to $n_{qp} \propto \sqrt{P_{abs}}$ [12], which implies that even in the few microwave photon regime this mechanism leads to excess quasiparticles.

We would like to thank Y.J.Y. Lankwarden for fabricating the devices. T.M.K. thanks J. Zmuidzinas and A. Vayonakis for discussions on this topic.

References

[1] S. K. Yip and J. A. Sauls, *Nonlinear Meissner effect in CuO superconductors*, Phys. Rev. Lett. **69**, 2264 (1992).

[2] C. C. Chin, D. E. Oates, G. Dresselhaus, and M. S. Dresselhaus, *Nonlinear electrodynamics of superconducting NbN and Nb thin films at microwave frequencies*, Phys. Rev. B **45**, 4788 (1992).

[3] B. H. Eom, P. K. Day, H. G. LeDuc, and J. Zmuidzinas, *A wideband, low-noise superconducting amplifier with high dynamic range*, Nature Phys. **8**, 623 (2012).

[4] J.-J. Chang and D. J. Scalapino, *Kinetic-equation approach to nonequilibrium superconductivity*, Phys. Rev. B **15**, 2651 (1977).

[5] J. Wolter and R. E. Horstman, *Determination of the quasiparticle energy distribution in superconducting tunneljunctions under microwave irradiation*, Phys. Lett. **86A**, 185 (1981).

[6] G. M. Eliashberg, *Film superconductivity stimulated by a high-frequency field*, JETP Lett. **11**, 114 (1970).

Symbol	Interpretation	Sample A	Sample B	Remarks
t	film thickness	60 nm	40 nm	
T_c	critical temperature	1.17 K	1.11 K	measured
Δ	energy gap	177 μeV	168 μeV	$1.76k_BT_c$
ρ_N	normal state resistivity	0.9 $\mu\Omega$cm	0.8 $\mu\Omega$cm	measured
RRR	residual resistance ratio	4.5	5.2	measured
Q_c	coupling quality factor	20100	54285	measured
C	coupling capacitance	7.5 fF	3.7 fF	from Q_c
w	central strip width of CPW	3 μm	3 μm	
s	gap width of CPW	2 μm	2 μm	
l	length of resonator	9.84 mm	8.33 mm	
V	central strip volume	1770 μm^3	1000 μm^3	$V = wtl$
f_0	measured resonant frequency	5.28 GHz	6.62 GHz	
τ_0	electron-phonon time	440 ns	440 ns	[41]
$\tau_{0,ph}$	phonon time	0.26 ns	0.26 ns	[12]
τ_{esc}	phonon escape time	0.17 ns	0.11 ns	[26]
τ_{pb}	pair breaking time	0.28 ns	0.28 ns	[41]

Table 8.1: Parameters of the films and resonators for both samples.

Symbol	Interpretation	Value
t	film thickness	60 nm
Q_c	coupling quality factor	20100
C	coupling capacitance	7.5 fF
w	width of central strip of resonator	3 μm
s	thickness of the dielectric	1 μm
l	length of resonator	9.84 mm
V	central strip volume	1770 μm^3
f_0	modeled resonant frequency	5.57 GHz

Table 8.2: Parameters of the modelled microstrip geometry

[7] B. I. Ivlev, S. G. Lisitsyn, and G. M. Eliashberg, *Nonequilibrium excitations in superconductors in high-frequency fields*, J. Low Temp. Phys. **10**, 449 (1973).

[8] T. M. Klapwijk and J. E. Mooij, *Microwave-enhanced superconductivity in aluminium films*, Physica B+C **81**, 132 (1976).

[9] T. M. Klapwijk, J. N. van den Bergh, and J. E. Mooij, *Radiation-stimulated superconductivity*, J. Low Temp. Phys. **26**, 385 (1977).

[10] R. E. Horstman and J. Wolter, *Gap enhancement in narrow superconducting tunneljunctions induced by homogeneous microwave currents*, Phys. Lett. **82A**, 43

(1981).

[11] S. Sridhar and J. E. Mercereau, *Effects of quasiparticle redistribution on the surface impedance of superconductors*, Phys. Lett. A **75**, 392 (1980).

[12] D. J. Goldie and S. Withington, *Non-equilibrium superconductivity in quantum-sensing superconducting resonators*, Supercond. Sci. Technol. **26**, 015004 (2013).

[13] P. J. de Visser, J. J. A. Baselmans, S. J. C. Yates, P. Diener, A. Endo, and T. M. Klapwijk, *Microwave-induced excess quasiparticles in superconducting resonators measured through correlated conductivity fluctuations*, Appl. Phys. Lett. **100**, 162601 (2012).

[14] P. K. Day, H. G. LeDuc, B. A. Mazin, A. Vayonakis, and J. Zmuidzinas, *A broadband superconducting detector suitable for use in large arrays*, Nature **425**, 817 (2003).

[15] J. Zmuidzinas, *Superconducting Microresonators: Physics and Applications*, Ann. Rev. Condens. Matter Phys. **3**, 169 (2012).

[16] F. Chiodi, M. Aprili, and B. Reulet, *Evidence for Two Time Scales in Long SNS Junctions*, Phys. Rev. Lett. **103**, 177002 (2009).

[17] P. Virtanen, T. T. Heikkilä, F. S. Bergeret, and J. C. Cuevas, *Theory of Microwave-Assisted Supercurrent in Diffusive SNS Junctions*, Phys. Rev. Lett. **104**, 247003 (2010).

[18] M. Beck, I. Rousseau, M. Klammer, P. Leiderer, M. Mittendorff, S. Winnerl, M. Helm, G. N. Gol'tsman, and J. Demsar, *Transient Increase of the Energy Gap of Superconducting NbN Thin Films Excited by Resonant Narrow-Band Terahertz Pulses*, Phys. Rev. Lett. **110**, 267003 (2013).

[19] N. Bao, X. Dong, E. Silverstein, and G. Torroba, *Stimulated Superconductivity at Strong Coupling*, J. High Energy Phys. **10**, 123 (2011).

[20] J. Baselmans, S. Yates, P. Diener, and P. de Visser, *Ultra low background cryogenic test facility for far-infrared radiation detectors*, J. Low Temp. Phys. **167**, 360 (2012).

[21] P. J. de Visser, S. Withington, and D. J. Goldie, *Readout-power heating and hysteretic switching between thermal quasiparticle states in kinetic inductance detectors*, J. Appl. Phys. **108**, 114504 (2010).

[22] L. J. Swenson, P. K. Day, B. H. Eom, H. G. Leduc, N. Llombart, C. M. McKenney, O. Noroozian, and J. Zmuidzinas, *Operation of a titanium nitride superconducting microresonator detector in the nonlinear regime*, J. Appl. Phys. **113**, 104501 (2013).

[23] S. B. Nam, *Theory of Electromagnetic Properties of Superconducting and Normal Systems*, Phys. Rev. **156**, 470 (1967).

[24] J. E. Mooij and T. M. Klapwijk, *Nonlinear electrodynamics in microwave-stimulated superconductivity*, Phys. Rev. B **27**, 3054 (1983).

[25] D. C. Mattis and J. Bardeen, *Theory of the anomalous skin effect in normal and superconducting metals*, Phys. Rev. **111**, 412 (1958).

[26] S. B. Kaplan, *Acoustic matching of superconducting films to substrates*, J. Low Temp. Phys. **37**, 343 (1979).

[27] A. M. Gulian and G. F. Zharkov, *Nonequilibrium Kinetics of Electrons and Phonons in Superconductors in Intense UHF Fields*, J. Low Temp. Phys. **48**, 125 (1982).

[28] G. Yassin and S. Withington, *Electromagnetic models for superconducting millimetre-wave and sub-millimetre-wave microstrip transmission lines*, J. Phys. D. Appl. Phys. **28**, 1983 (1995).

[29] J. R. Clem, *Inductances and attenuation constant for a thin-film superconducting coplanar waveguide resonator*, J. Appl. Phys **113**, 013910 (2013).

[30] C. L. Holloway and E. F. Kuester, *A quasi-closed form expression for the conductor loss of CPW lines, with an investigation of edge shape effects*, IEEE Trans. Microwave Theory Tech. **43**, 2695 (1995).

[31] P. J. de Visser, J. J. A. Baselmans, P. Diener, S. J. C. Yates, A. Endo, and T. M. Klapwijk, *Number fluctuations of sparse quasiparticles in a superconductor*, Phys. Rev. Lett. **106**, 167004 (2011).

[32] J. Gao, J. Zmuidzinas, A. Vayonakis, P. Day, B. Mazin, and H. Leduc, *Equivalence of the effects on the complex conductivity of superconductor due to temperature change and external pair breaking*, J. Low Temp. Phys. **151**, 557 (2008).

[33] J. M. Martinis, M. Ansmann, and J. Aumentado, *Energy decay in superconducting Josephson-junction qubits from nonequilibrium quasiparticle excitations*, Phys. Rev. Lett. **103**, 097002 (2009).

[34] G. Catelani, L. I. Glazman, and K. E. Nagaev, *Effect of quasiparticle injection on the ac response of a superconductor*, Phys. Rev. B **82**, 134502 (2010).

[35] A. D. Córcoles, J. M. Chow, J. M. Gambetta, C. Rigetti, J. R. Rozen, G. A. Keefe, M. B. Rothwell, M. B. Ketchen, and M. Steffen, *Protecting superconducting qubits from radiation*, Appl. Phys. Lett. **99**, 181906 (2011).

[36] R. Barends, J. Wenner, M. Lenander, Y. Chen, R. C. Bialczak, J. Kelly, E. Lucero, P. O'Malley, M. Mariantoni, D. Sank, H. Wang, T. C. White, Y. Yin, J. Zhao, A. N. Cleland, J. M. Martinis, and J. J. A. Baselmans, *Minimizing quasiparticle generation from stray infrared light in superconducting quantum circuits*, Appl. Phys. Lett. **99**, 113507 (2011).

[37] M. Lenander, H. Wang, R. C. Bialczak, E. Lucero, M. Mariantoni, M. Neeley, A. D. O'Connell, D. Sank, M. Weides, J. Wenner, T. Yamamoto, Y. Yin, J. Zhao,

A. N. Cleland, and J. M. Martinis, *Measurement of energy decay in superconducting qubits from nonequilibrium quasiparticles*, Phys. Rev. B **84**, 024501 (2011).

[38] D. Rainis and D. Loss, *Majorana qubit decoherence by quasiparticle poisoning*, Phys. Rev. B **85**, 174533 (2012).

[39] J. Wenner, Y. Yin, E. Lucero, R. Barends, Y. Chen, B. Chiaro, J. Kelly, M. Lenander, M. Mariantoni, A. Megrant, C. Neill, P. J. J. O'Malley, D. Sank, A. Vainsencher, H. Wang, T. C. White, A. N. Cleland, and J. M. Martinis, *Excitation of Superconducting Qubits from Hot Nonequilibrium Quasiparticles*, Phys. Rev. Lett. **110**, 150502 (2013).

[40] R. L. Kautz, *Picosecond pulses on superconducting striplines*, J. Appl. Phys. **49**, 308 (1978).

[41] S. B. Kaplan, C. C. Chi, D. N. Langenberg, J. Chang, S. Jafarey, and D. J. Scalapino, *Quasiparticle and phonon lifetimes in superconductors*, Phys. Rev. B **14**, 4854 (1976).

Appendix A

Kinetic equations

The kinetic equations describing electron-phonon interaction by scattering and recombination were given in Ref. [1]. The rate of change in the quasiparticle distribution $f(E)$ and the phonon distribution $n(\Omega)$ is given by

$$\begin{aligned}\frac{df(E)}{dt} = I_{qp}(E) &- \frac{1}{\tau_0(k_BT_c)^3}\int_0^\infty d\Omega\Omega^2 N_s(E+\Omega)\left(1-\frac{\Delta^2}{E(E+\Omega)}\right)\times \\ &(f(E)[1-f(E+\Omega)]n(\Omega) - f(E+\Omega)[1-f(E)][n(\Omega)+1]) \\ &- \frac{1}{\tau_0(k_BT_c)^3}\int_0^{E-\Delta} d\Omega\Omega^2 N_s(E-\Omega)\left(1-\frac{\Delta^2}{E(E-\Omega)}\right)\times \\ &(f(E)[1-f(E-\Omega)][n(\Omega)+1] - [1-f(E)]f(E-\Omega)n(\Omega)) \\ &- \frac{1}{\tau_0(k_BT_c)^3}\int_{E+\Delta}^\infty d\Omega\Omega^2 N_s(\Omega-E)\left(1+\frac{\Delta^2}{E(\Omega-E)}\right)\times \\ &(f(E)f(\Omega-E)[n(\Omega)+1] - [1-f(E)][1-f(\Omega-E)]n(\Omega)),\end{aligned} \tag{A.1}$$

and

$$\begin{aligned}\frac{dn(\Omega)}{dt} = &-\frac{2}{\pi\tau_0^{ph}\Delta(0)}\int_\Delta^\infty dEN_s(E)N_s(E+\Omega)\left(1-\frac{\Delta^2}{E(E+\Omega)}\right)\times \\ &(f(E)[1-f(E+\Omega)]n(\Omega) - [1-f(E)]f(E+\Omega)[n(\Omega)+1]) \\ &-\frac{1}{\pi\tau_0^{ph}\Delta(0)}\int_\Delta^{\Omega-\Delta} dEN_s(E)N_s(\Omega-E)\left(1+\frac{\Delta^2}{E(\Omega-E)}\right)\times \\ &([1-f(E)][1-f(\Omega-E)]n(\Omega) - f(E)f(\Omega-E)[n(\Omega)+1]) \\ &-\frac{n(\Omega)-n_{sub}(\Omega,T_{bath})}{\tau_{esc}}.\end{aligned} \tag{A.2}$$

$I_{qp}(E)$ is the injection term, which can describe various processes. For the case of microwave absorption it is given by Eq. 2.42. τ_0 is the characteristic electron-phonon interaction time, τ_0^{ph} the phonon lifetime in the film (usually the pair breaking time), τ_{esc} the average escape time of a phonon to the bath and $n_{sub}(\Omega)$ the phonon distribution in the substrate.

How these equations are used is discussed in Chapters 2 and 8. The numerical procedure to solve these equations for microwave absorption at low temperatures was developed by Goldie and Withington [2].

References

[1] J.-J. Chang and D. J. Scalapino, *Kinetic-equation approach to nonequilibrium superconductivity*, Phys. Rev. B **15**, 2651 (1977).

[2] D. J. Goldie and S. Withington, *Non-equilibrium superconductivity in quantum-sensing superconducting resonators*, Supercond. Sci. Technol. **26**, 015004 (2013).

Appendix B

Quasiparticle and phonon fluctuations

This appendix provides additional experimental data on the noise spectra of aluminium resonators measured as a function of temperature. In Chapter 6 we have studied the spectra of quasiparticle fluctuations as measured with the cross-power spectral density of the resonator amplitude and phase. In Fig. 6.1 we have shown that two characteristic timescales show up in the noise spectra. The primary roll-off, with a timescale of about 2 ms, is due to the quasiparticle recombination time. The second roll-off, which has a 10 dB lower noise level, has a timescale of roughly 80 μs. Here we show additional experimental data that supports the hypothesis that the second timescale is the signature of phonon-fluctuations in the substrate. We compare fluctuation measurements with the decay-time from a LED-pulse. The saturation time in the pulse-decay time above 200 mK is also around 80 μs, which was attributed in similar experiments to a phonon-bottleneck due to the substrate-holder interface [1, 2]. The role of the phonons in the process of quasiparticle recombination is difficult to measure directly, although a lot of non-equilibrium experiments were conducted to resolve the influence of 2Δ-phonons on quasiparticle recombination [3–8]. Most of these studies aim for a measurement of the equilibrium quasiparticle recombination time, but with a non-equilibrium technique. The here presented measurements of quasiparticle fluctuations provide a high enough sensitivity to study the role of the phonons in the generation-recombination process in equilibrium.

The second section describes an extension to the model of quasiparticle number fluctuations by Wilson and Prober [9]. In their model (described in Section 2.3.3), the dielectric substrate is taken as the phonon-bath, and therefore only fluctuations in the phonon-system of the superconductor are considered. Here we take the sample holder as the phonon-bath and show that the fluctuations in the phonons in the substrate can cause an additional and measurable timescale in the spectrum of quasiparticle fluctuations in the superconductor.

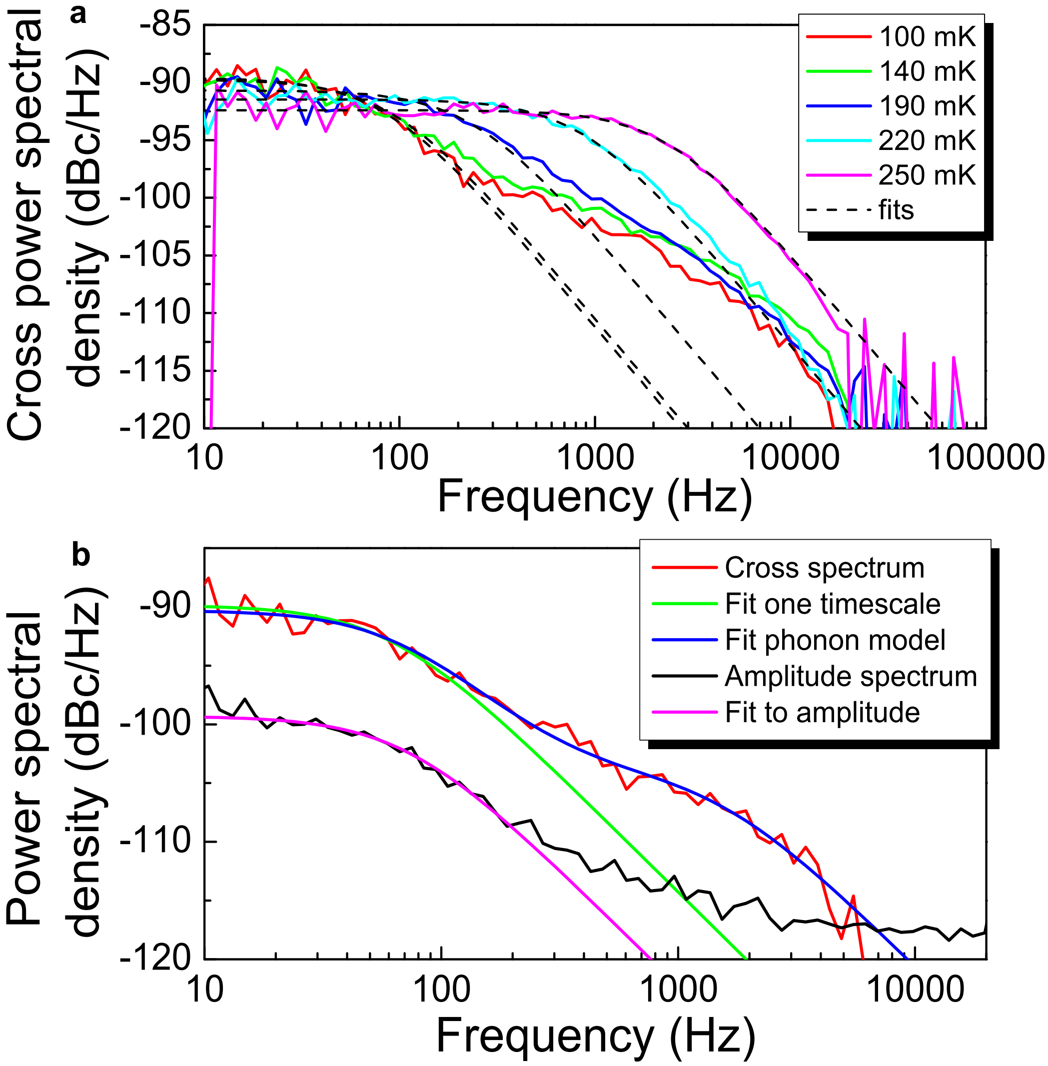

Figure B.1: (a) Cross power spectral density of the resonator amplitude and phase as a function of frequency for different temperatures. The dashed lines are single-timescale Lorentzian fits to the data. (b) Amplitude and cross power spectral density at 120 mK. For the amplitude spectrum, the system noise (mainly amplifier noise) is subtracted. The two single timescale fits are Lorentzian fits. The two-timescale phonon model fit is described in the text.

B.1 Experimental data

The relevant experimental details about the sample, the setup and the measurement are provided in Chapter 6. The measured cross power spectra, at a microwave readout power of -75 dBm, are plotted for different temperatures in Fig. B.1a. Only the negatively correlated part (the negative part of the cross-power spectral density) is shown here. The roll-off frequency increases with increasing temperature and the noise level stays approximately constant as expected (except for the highest temperatures

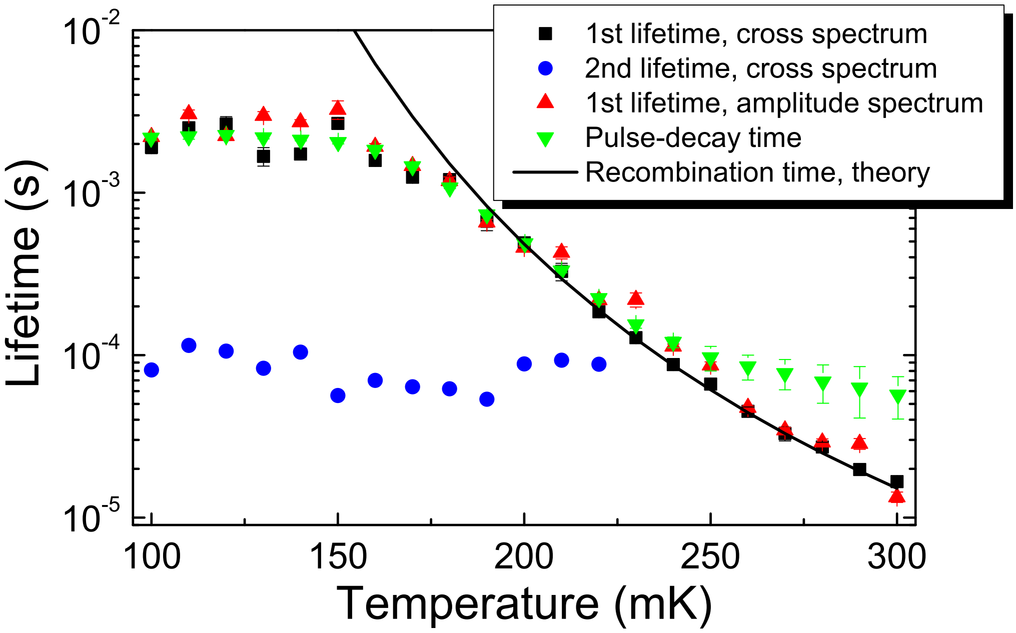

Figure B.2: Various lifetimes as a function of temperature. The black squares represent the quasiparticle recombination lifetime as determined from the cross power spectral densities in Fig. B.1a. The red triangles are the quasiparticle recombination lifetimes from the resonator amplitude spectra. The blue dots represent the second timescale in the cross power spectral density. Additionally we plot the lifetime as determined from the decay time after a short pulse of light.

where the responsivity starts to decrease). The dashed lines in the figure are single timescale Lorentzian fits that show that for the main part (the first 10 dB), the spectra can be fit with a single timescale. The thus extracted lifetimes are plotted as black squares in Fig. B.2 as a function of temperature. They agree with the lifetimes from the amplitude-only spectra, which are plotted as red triangles.

However, as is clearly seen in the spectra in Fig. B.1a at the lowest temperatures, there is a pronounced second roll-off at higher frequency, although with a much lower noise level. We have also shown the amplitude spectrum in Fig. B.1b to show that the first timescale is the same and that there is a small signature of the second roll-off as well. The second timescale in the cross-PSD is plotted as a function of temperature as blue dots in Fig. B.2 and is temperature independent. The second timescale is extracted with a fit to the model presented in Section B.2. The second timescale cannot be due to the resonator ringtime, which is much shorter ($\approx 2\ \mu$s). Above 230 mK the quasiparticle signature dominates the spectrum and the second roll-off is therefore not visible anymore.

Additionally the lifetime obtained using the decay towards equilibrium after a short pulse of light [10] is plotted as green triangles in Fig. B.2. At low temperatures, the pulse-measurement agrees with the quasiparticle lifetime from the noise-measurements,

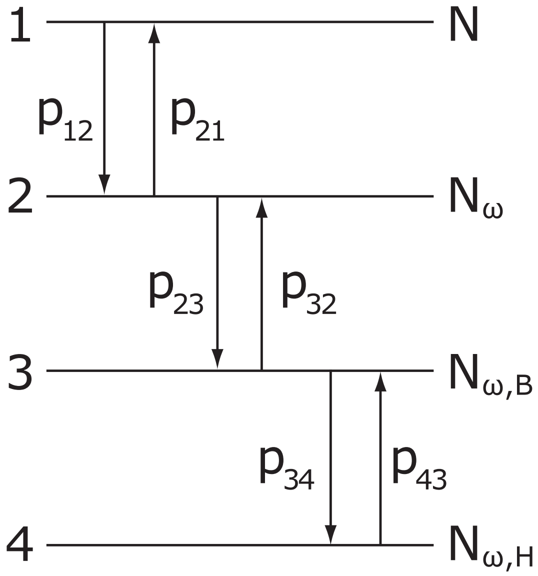

Figure B.3: Schematic of the four level system we consider for our simulation. N is the number of quasiparticles, N_ω the number of phonons in the film, $N_{\omega,B}$ the number of phonons in the substrate and $N_{\omega,H}$ the number of phonons in the sample holder.

but it saturates at higher temperatures. The timescale at which the lifetime from the pulse method saturates (above 230 mK) is strikingly similar to the second lifetime from the noise spectra. To restore equilibrium the pulse energy needs to be transported away, the speed of which is limited by the bottleneck of phonon transport from substrate to sample holder, as was recently shown for different substrates [1]. We therefore interpret the second roll-off in the noise-spectra as equilibrium phonon fluctuations. We show in the next section that the framework of quasiparticle number fluctuations can be extended with the phonons in the substrate, which leads to a good description of the two timescales in the measured quasiparticle fluctuation spectra.

B.2 Quasiparticle and phonon fluctuations - model

The model system that lead to the single timescale quasiparticle spectrum Eq. 2.39 comprises only two systems, the quasiparticles and the phonons, which gives only a single timescale for fluctuations between the systems, the (effective) quasiparticle lifetime. It was shown by Wilson and Prober [9] that a three system model, with quasiparticles, phonons in the superconducting film and phonons in the substrate, could lead to a quasiparticle spectrum with two timescales. The timescale for phonon transfer from film to substrate is the phonon escape time, which can be calculated from the acoustic mismatch model to be 0.1 ns for 40 nm Al on sapphire [11]. The pair breaking time, the time it takes a phonon that enters the film to break a pair is 0.3 ns [12]. From these timescales it is impossible to arrive at a typical timescale of 80 μs as it appears in the

Transition	Symbol	Rate	Probability
Recombination	p_{12}	Γ_R	$\frac{RN^2}{2V}$
Generation / pair breaking	p_{21}	Γ_B	$\Gamma_B N_\omega$
Phonon escape: film to substrate	p_{23}	Γ_{es}	$\Gamma_{es} N_\omega$
Phonon entry: substrate to film	p_{32}	Γ_K	$\Gamma_K N_{\omega,B}$
Phonon escape: substrate to holder	p_{34}	Γ_L	$\Gamma_L N_{\omega,B}$
Phonon entry: holder to substrate	p_{43}	Γ_M	$\Gamma_M N_{\omega,H}$

Table B.1: Interpretation of the transitions in Fig. B.3 and their probability.

measurements. Therefore, and inspired by the saturation in the pulse-decay time, we extend the model by adding a fourth system, the phonons in the sample holder. The connection between the substrate and the sample holder is made by glue and bond-wires which form a phonon bottleneck, giving rise to an apparent timescale of the order of 10-100 μs [1, 2]. With this extension, the framework of Wilson and Prober [9] now allows for calculating the spectrum of the fluctuations in the number of quasiparticles. The model, which is described in the next paragraph, leads to good fits to the measured spectra, as shown in Fig. B.1b. We used these fits to obtain the second timescale as plotted in Fig. B.2.

A schematic of the four systems and the transitions between them is given in Fig. B.3 (which is complementary to Fig. 2.4), the transitions are explained in Table B.1. The probability for each transition from system i to j is labelled p_{ij}. System 1 denotes the quasiparticles which have a number N, which we assume to be the number of quasiparticles in the central strip of the resonator. Systems 2, 3 and 4 are the phonons in the film (N_ω), in the substrate ($N_{\omega,B}$) and in the sample holder ($N_{\omega,H}$) respectively. Note that by considering generation and recombination of quasiparticles as number fluctuations, we only keep track of phonons with energy higher than 2Δ. The model effectively assumes decoupled phonon systems of the film and substrate. It was recently shown experimentally by Pascal et al. [13] that the phonon system of a thin metal film is indeed decoupled from the substrate phonon system, despite of the fact that the phonon wavelength is much longer than the thickness of the metal film.

The following rate equations describe the time evolution of the number occupations in each system.

$$\frac{dN}{dt} = -\frac{RN^2}{V} + 2\Gamma_B N_\omega \tag{B.1}$$

$$\frac{dN_\omega}{dt} = \frac{RN^2}{2V} - \Gamma_B N_\omega - \Gamma_{es} N_\omega + \Gamma_K N_{\omega,B} \tag{B.2}$$

$$\frac{dN_{\omega,B}}{dt} = \Gamma_{es} N_\omega - \Gamma_K N_{\omega,B} - \Gamma_L N_{\omega,B} + \Gamma_M N_{\omega,H} \tag{B.3}$$

$$\frac{dN_{\omega,H}}{dt} = \Gamma_L N_{\omega,B} - \Gamma_M N_{\omega,H} \tag{B.4}$$

Note that recombination involves 2 quasiparticles, which gives rise to the N^2 term. Now we assume that $N_{\omega,H}$ is constant, therefore $\frac{dN_{\omega,H}}{dt} = 0$ and $\Gamma_M N_{\omega,H} = \Gamma_M N^0_{\omega,H} = \Gamma_L N^0_{\omega,B}$. Therefore Eq. B.4 vanishes and we can rewrite Eq. B.3 as:

$$\frac{dN_{\omega,B}}{dt} = \Gamma_{es} N_\omega - \Gamma_K N_{\omega,B} - \Gamma_L (N_{\omega,B} - N^0_{\omega,B}). \tag{B.5}$$

Now these equations are linearized. Inspection of the equations learns that they are almost linear already, except for the term $\frac{RN^2}{V}$, which in linearized form reads $2\Gamma_R \Delta N$, with $\Gamma_R = RN^0/V$. To calculate the spectra, we now follow the approach by Wilson and Prober [9].

We can write the rate equations in matrix form as:

$$\frac{d(\Delta \mathbf{a})}{dt} = -\mathbf{M} \cdot \Delta \mathbf{a}, \tag{B.6}$$

with

$$\mathbf{M} = \begin{pmatrix} 2\Gamma_R & -2\Gamma_B & 0 \\ -\Gamma_R & (\Gamma_B + \Gamma_{es}) & -\Gamma_K \\ 0 & -\Gamma_{es} & (\Gamma_K + \Gamma_L) \end{pmatrix}, \tag{B.7}$$

and $\mathbf{a} = (N, N_\omega, N_{\omega,B})$, $\Delta \mathbf{a} = \mathbf{a} - \mathbf{a}^0$. Now we also have to fill a matrix $\mathbf{B}$ (representing second order Fokker-Planck moments), in which

$$\begin{aligned} B_{ii} &\approx 2\Sigma_{k\neq i} \delta n^2_{ik} p^0_{ik}, \\ B_{ij} &= -\delta n_{ij} \delta n_{ji} (p^0_{ij} + p^0_{ji}), \end{aligned} \tag{B.8}$$

where δn_{ij} is the change of the occupation of the system when a transition happens. The principle of detailed balance ($p^0_{ij} = p^0_{ji}$) is used to evaluate Eq. B.8, which gives for our four systems:

$$\mathbf{B} = \Gamma_R N^0 \begin{pmatrix} 4 & -2 & 0 \\ -2 & (1 + \frac{\Gamma_{es}}{\Gamma_B}) & -\frac{\Gamma_{es}}{\Gamma_B} \\ 0 & -\frac{\Gamma_{es}}{\Gamma_B} & (1 + \frac{\Gamma_L}{\Gamma_K})\frac{\Gamma_{es}}{\Gamma_B} \end{pmatrix}. \tag{B.9}$$

The spectrum of the fluctuations between all those systems is given by

$$\mathbf{G}(\omega) = \frac{2}{\omega^2} \mathrm{Re} \left((\mathbf{1} + \frac{\mathbf{M}}{i\omega})^{-1} \mathbf{B} \right), \tag{B.10}$$

with $\mathbf{1}$ the identity matrix. The spectrum of the fluctuations in the quasiparticle number in a measurement will now be given by G_{11} ($S_N(f)$ in Eq. 6.2). The characteristic timescales of the spectrum are given by the eigenvalues of $\mathbf{M}$, which we call τ_1, τ_2 and τ_3. These timescales are the ones we will observe in the measured spectra. As an example we take a spectrum at 120 mK, which is shown in Fig. B.1b. We fix the rates $\Gamma_{esc} = 9.3 \times 10^9$ s^{-1} and $\Gamma_B = 3.6 \times 10^9$ s^{-1}, which are calculated from Refs. [11, 12]. We than use N^0, Γ_R, Γ_L and Γ_K as fit parameters. In Fig. B.1b we see that we get a good fit. The second lifetime as plotted in Fig. B.2 is the second highest eigenvalue, $\tau_2 = 0.1$ ms. The highest eigenvalue ($\tau_1 = 2.4$ ms) is the effective quasiparticle recombination lifetime and the same as from a single-timescale Lorentzian fit (provided that the levels of the primary and secondary roll-off are far apart). The third eigenvalue is of the order 10^{-11} s and will not be visible in the measurement.

The longest of τ_1, τ_2 and τ_3 will be the apparent lifetime in the non-equilibrium experiment with the light-pulse, which from Fig. B.2 is τ_1 from 100-230 mK and τ_2 for higher temperatures. We note that although mathematically a three-system model would suffice to describe two timescales in the spectrum, the physical interpretation requires the fourth system. In Chapter 5 we discussed the quasiparticle recombination time and number of quasiparticles and compared them to theory. The other timescales that are obtained from the fit, Γ_L and Γ_K, are in our experiment properties of a not very well-defined interface. We therefore leave the analysis to the apparent timescales in the pulse- and noise experiments.

B.3 Discussion

There are a few other mechanisms which could cause a second timescale in the spectrum. We can estimate the fluctuations due to electron-phonon scattering. Based on the observed timescale (80 μs) and a heat capacity of 2.3×10^{-14} J/K [14] we estimate a heat conductance $G = 10^{-10}$ W/K/s, which would give temperature fluctuations with spectral density $S_T = 4kT^2/G$. That leads to a correlated spectrum level of $S_{\theta,A} = -139$ dBc/Hz at 150 mK and $S_{\theta,A} = -121$ dBc/Hz at 180 mK. These values are much lower and show stronger temperature dependence than observed. A treatment of fluctuations based on more general thermodynamic variables could incorporate quasiparticle-phonon scattering into the problem directly, directions to which are given in Wilson [15]. Quasiparticle diffusion is another possible mechanism. However, the typical diffusion length with a diffusion constant of 150 cm^2/s and a time of 80 μs is $l = \sqrt{D\tau} \approx 1$ mm, which is not a typical length scale in our system. We cannot completely exclude quasiparticle trapping which may lead to similar noise characteristics [9], although there are no material interfaces or similar obvious trap locations in our single metal layer system.

Our measurements show that we have a very sensitive method at hand to measure equilibrium fluctuations in a superconductor. This could lead to studies of quasiparticle and phonon equilibrium dynamics in better defined systems, such as resonators on membranes, where the phonon-bottleneck can be engineered. A phonon-bottleneck can be introduced to limit the effective quasiparticle recombination rate. The framework presented here could be used to study the equilibrium (or steady state) fluctuations in such a system. A good understanding of quasiparticle and phonon dynamics is also crucial for improving photon detectors operating at different temperatures and photon-loading conditions, as well as for phonon-mediated detectors [2, 16, 17].

References

[1] N. Vercruyssen, R. Barends, T. M. Klapwijk, J. T. Muhonen, M. Meschke, and J. P. Pekola, *Substrate-dependent quasiparticle recombination time in superconducting resonators*, Appl. Phys. Lett. **99**, 062509 (2011).

[2] D. C. Moore, S. R. Golwala, B. Bumble, B. Cornell, P. K. Day, H. G. LeDuc, and J. Zmuidzinas, *Position and energy-resolved particle detection using phonon-mediated microwave kinetic inductance detectors*, Appl. Phys. Lett. **100**, 232601 (2012).

[3] W. Eisenmenger and A. H. Dayem, *Quantum generation and detection of incoherent phonons in superconductors*, Phys. Rev. Lett. **18**, 125 (1967).

[4] H. Kinder, *Spectroscopy with phonons on* Al_2O_3*:*V^{3+} *using the phonon Bremsstrahlung of a superconducting tunnel junction*, Phys. Rev. Lett. **28**, 1564 (1972).

[5] L. N. Smith and J. M. Mochel, *Phonon and quasiparticle dynamics in superconducting aluminum tunnel junctions*, Phys. Rev. Lett. **35**, 1597 (1975).

[6] W. Eisenmenger, L. Lassmann, H. J. Trumpp, and R. Krauss, *Quasiparticle recombination and 2*Δ*-phonon-trapping in superconducting tunneling junctions*, Appl. Phys. **11**, 307 (1976).

[7] V. Narayanamurti, R. C. Dynes, P. Hu, H. Smith, and W. F. Brinkman, *Direct measurement of quasiparticle-lifetime broadening in a strong-coupled superconductor*, Phys. Rev. B **18**, 6041 (1978).

[8] N. Perrin, *Quasiparticle and phonon nonlinear dynamics in a superconducting film*, Phys. Lett. A **90**, 67 (1982).

[9] C. M. Wilson and D. E. Prober, *Quasiparticle number fluctuations in superconductors*, Phys. Rev. B **69**, 094524 (2004).

[10] R. Barends, J. J. A. Baselmans, S. J. C. Yates, J. R. Gao, J. N. Hovenier, and T. M. Klapwijk, *Quasiparticle relaxation in optically excited high-Q superconducting resonators*, Phys. Rev. Lett. **100**, 257002 (2008).

[11] S. B. Kaplan, *Acoustic matching of superconducting films to substrates*, J. Low Temp. Phys. **37**, 343 (1979).

[12] S. B. Kaplan, C. C. Chi, D. N. Langenberg, J. Chang, S. Jafarey, and D. J. Scalapino, *Quasiparticle and phonon lifetimes in superconductors*, Phys. Rev. B **14**, 4854 (1976).

[13] L. M. A. Pascal, A. Fay, C. B. Winkelmann, and H. Courtois, *Existence of an independent phonon bath in a quantum device*, Phys. Rev. B **88**, 100502(R) (2013).

[14] N. Phillips, *Heat capacity of Aluminum between 0.1 K and 4 K*, Phys. Rev. **114**, 676 (1959).

[15] C. M. Wilson, *Optical/UV Single Photon Spectrometers using Superconducting Tunnel Junctions*, PhD thesis, Yale University, 2002.

[16] L. J. Swenson, A. Cruciani, A. Benoit, M. Roesch, C. S. Yung, A. Bideaud, and A. Monfardini, *High-speed phonon imaging using frequency-multiplexed kinetic inductance detectors*, Appl. Phys. Lett. **96**, 263511 (2010).

[17] O. Quaranta, T. W. Cecil, L. Gades, B. Mazin, and A. Miceli, *X-ray photon detection using superconducting resonators in thermal quasi-equilibrium*, Supercond. Sci. Technol. **26**, 105021 (2013).

Appendix C

Supplementary information to Chapter 7

This appendix contains the supplementary information submitted with Chapter 7 as far as it was not already presented in Chapter 3.

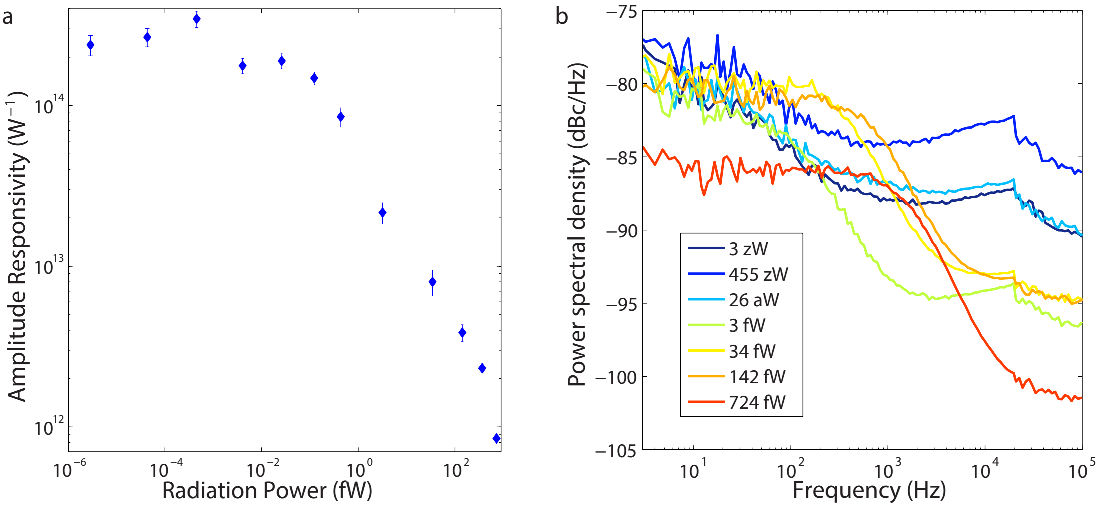

Figure C.1: The measured responsivity and noise spectra which constitute the NEP in Fig. 7.4. **a**, The responsivity of the resonator amplitude to radiation power dA/dP_{rad} as a function of radiation power. The error bars are 1 s.d. **b**, The amplitude noise spectra as a function of frequency for a selection of the radiation powers. (a) and (b) are the ingredients of the NEP as shown in Fig. 4 of the main paper. It is important to note that each of the presented measurements are for the P_{read} that gives the minimum NEP for that radiation power. That P_{read} is listed for each radiation power in Section C.4.

C.1 Phase noise

In Fig. 7.2c we have shown that one can choose to measure the response of the superconductor in either the phase or the amplitude direction with respect to the resonance circle. Fig. C.2a shows both the amplitude and phase spectra at a bath temperature

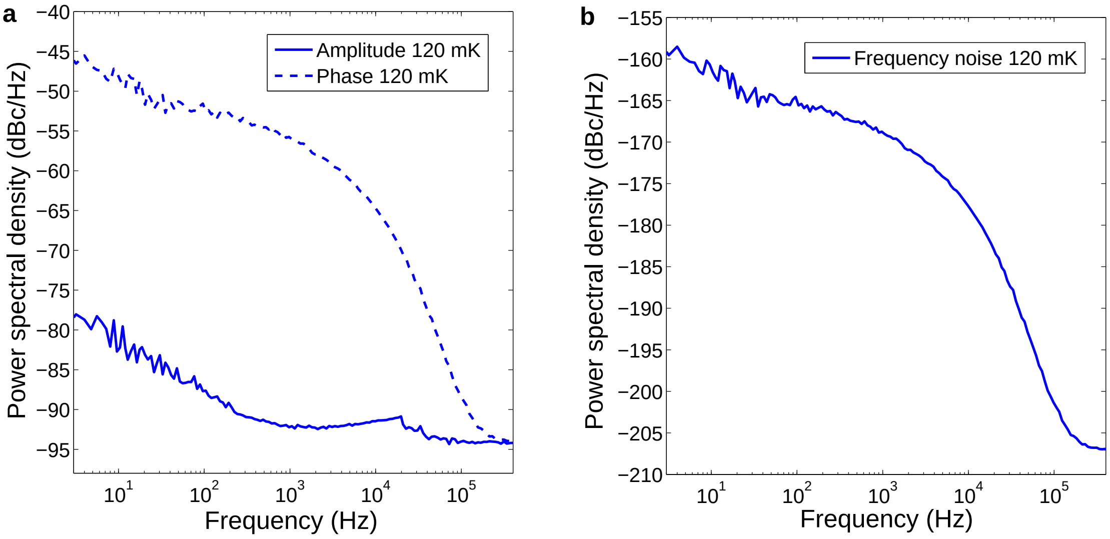

Figure C.2: Phase and frequency noise of the resonator. a, The power spectral density of the resonator amplitude and phase as a function of frequency at a bath temperature of 120 mK at a microwave readout power of -90 dBm. **b**, The frequency noise spectrum: $S_f = \frac{S_\theta}{(4Q)^2}$ at 120 mK and -90 dBm, with Q = 111711.

of 120 mK and a microwave power of -90 dBm. It is evident that the phase noise is 30 dB higher, due to two level system (TLS) noise [1], which makes it impossible for this device to measure quasiparticle fluctuations in phase. Therefore we have only used the amplitude response to study quasiparticle fluctuations. To compare with previous research, we plot in Fig. C.2b the frequency noise spectrum at 120 mK. The frequency noise at 1 kHz is -169 dBc/Hz, which is about 8 dB higher than reported before [2] for Al on sapphire, most likely due to the two layer fabrication process for this device. It is known that frequency noise decreases for higher temperatures [3]. Therefore we have chosen to not operate at the lowest possible temperature, but at a bath temperature of 120 mK. A temperature of 120 mK is still low enough not to dominate the number of quasiparticles.

C.2 Contributions to the amplitude noise spectrum

From Fig. 7.3a, it is evident that there are more contributions to the noise spectra than only the quasiparticle roll-off. In that figure, we already took into account the amplifier noise level, which will give a flat, white, noise spectrum. Fig. C.3a shows as an example the measured amplitude power spectral density at the lowest radiation power and a microwave readout power of -92 dBm. Four contributions to the noise spectrum can be distinguished. Firstly, the amplifier noise, which gives a flat spectrum, the level of which can be determined through the noise level at frequencies of 200-300 kHz (-92.6

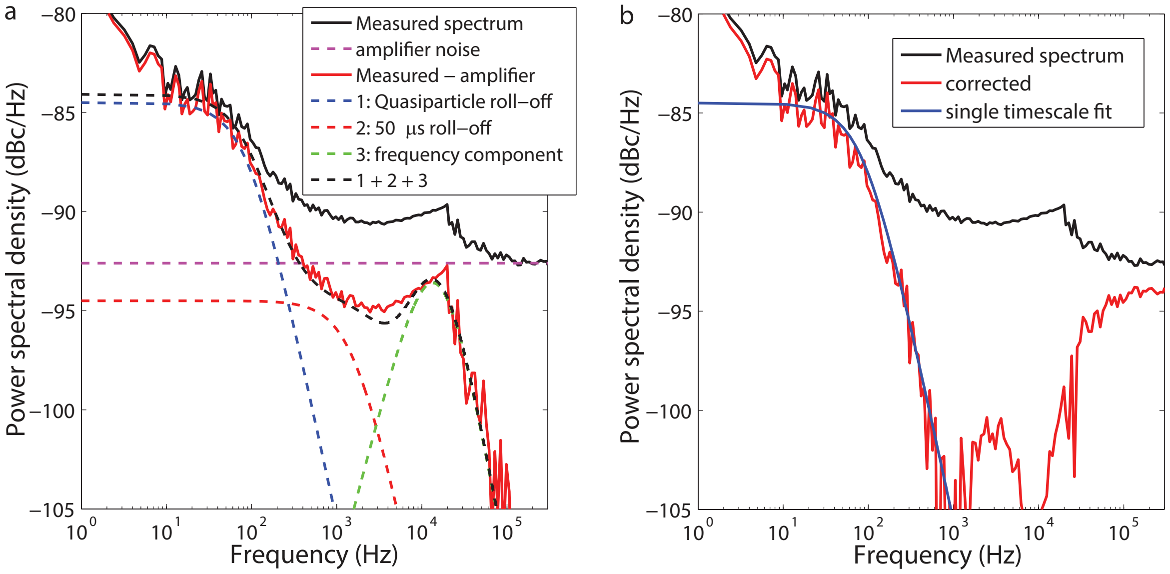

Figure C.3: Corrections to the noise spectrum to extract the quasiparticle recombination time. a, Different contributions to the noise spectra. The measured amplitude power spectra density at a temperature 120 mK and a microwave readout power of -92 dBm is shown as a solid black line. The amplifier noise is a white noise contribution and is determined at frequencies above 300 kHz. The measured spectrum with the amplifier noise subtracted is shown as the red line. The other dashed lines show the other contributions: the roll-off due to quasiparticle fluctuations, a second roll-off with a timescale of 50 μs and a 10 dB lower noise level, and a symmetric bump around the resonator response frequency due to mixing of frequency noise in the amplitude direction. **b**, The same measured spectrum as in **a**, together with a spectrum that is corrected by subtracting the level at 3 kHz. The correction is done to be able to only fit the quasiparticle roll-off, the result of which is shown as well.

dBc/Hz in this case). The amplifier noise level is subtracted, to more clearly show the other three contributions. The second, and dominant, contribution is the roll-off due to quasiparticle fluctuations, with a level of -84.5 dBc/Hz and a characteristic time of 1.8 ms. This power spectral density has the form

$$S(f) = \frac{y}{1+(2\pi f\tau)^2}, \tag{C.1}$$

with y the level and τ the timescale. The third contribution is a second roll-off of the same form, with a timescale of about 50 μs and a level which is 10 dB lower than the quasiparticle roll-off. This contribution is small and not so easily distinguishable here, but was observed more clearly in a similar resonator [4] (see Fig. 6.1). We tentatively attribute this contribution to phonon-fluctuations (see Appendix app:phonontijd). The fourth contribution is a bump around the resonator response time frequency (27 kHz). It can be shown [5] that this phenomenon is consistent with mixing of frequency noise into the amplitude direction, due to a difference in the probe frequency and the resonant frequency of the resonator during the noise measurement. It can be modelled with the equation

$$S(f) = y_\mathrm{b}|\zeta(f) + \zeta^*(-f)|/4, \tag{C.2}$$

with y_b a scaling factor and where the star denotes the complex conjugate.

$$\zeta(f) = \frac{1 + j\delta f_\mathrm{g}/f_\mathrm{ring}}{1 + j(\delta f_\mathrm{g} + f)/f_\mathrm{ring}}, \tag{C.3}$$

with f the modulation frequency, $f_\mathrm{ring} = f_0/\pi Q$ the resonator ring frequency around which the bump will appear (27 kHz) and δf_g the detuning of the generator frequency from the resonant frequency f_0. This detuning can occur in practice due to strong frequency noise or due to drift in either the generator frequency or the resonant frequency during the noise measurement.

Since we are only interested in modulation frequencies well within the quasiparticle recombination time bandwidth (<100 Hz in this case), the other noise contributions do not play a role in determining the sensitivity (NEP) of the detector. However, these contributions limit the extraction of the quasiparticle recombination time and, because they contribute mostly at higher frequencies, give a bias towards shorter lifetimes if one fits the spectra with a single-lifetime spectrum. To get a better estimate of the actual quasiparticle recombination time, we subtract from the measured noise spectrum a level which we take from noise frequencies around 1-3 kHz. The thus corrected spectrum is fitted with a single timescale Lorentzian roll-off as shown in Fig. C.3b. We perform this correction because fitting all noise contributions together would require too many fit parameters. We emphasise that we only do this correction to extract a more realistic recombination time. The NEP is calculated with the measured, uncorrected, noise spectra.

Below about 5 Hz in the measured amplitude spectra, there is a 1/f contribution to the noise as well. This could be caused by system noise of the measurement setup. It was recently shown [6] that in the amplitude direction there is also noise due to dielectric two-level-systems. Given the rather high phase noise in the present device, as discussed before, it could therefore be that the high two-level-system noise has a measurable contribution in amplitude as well.

C.3 Derivation of the optical responsivity vs microwave power

Here we derive how the optical responsivity of the resonator amplitude, dA/dP_rad, changes as a function of microwave readout power. We limit ourselves to the regime where the number of quasiparticles is dominated by readout power dissipation. The number of quasiparticles due to the readout power, $N_\mathrm{qp}^\mathrm{read}$, is related to the quasiparticle recombination time and the absorbed readout power in the quasiparticle system P_abs, through $\eta_{\mathrm{read}} P_{\mathrm{abs}} = N_{\mathrm{qp}}^{\mathrm{read}} \Delta/\tau_{\mathrm{qp}}$. η_{read} is the efficiency with which the absorbed microwave power creates quasiparticles. We will assume here that $P_{\mathrm{abs}} \propto P_{\mathrm{read}}$ and that η_{read} is independent of P_{read}, with P_{read} the power on the readout line (we will come back to these assumptions later). Since we only derive proportionalities, we will use P_{read} in the equations. N_{qp} and τ_{qp} are related by [7]

$$N_{\mathrm{qp}} = \frac{\tau_0}{\tau_{\mathrm{qp}}} \frac{N_0 (k_{\mathrm{B}} T_{\mathrm{c}})^3 V}{2\Delta^2} = \frac{K}{\tau_{\mathrm{qp}}}, \tag{C.4}$$

which also holds for excess quasiparticles at low temperature [8, 9]. K is one constant to replace all the other constants in this equation. In steady state $N_{\mathrm{qp}}^{\mathrm{read}}$ is related to P_{read} as

$$N_{\mathrm{qp}}^{\mathrm{read}} = \sqrt{\frac{\eta_{\mathrm{read}} P_{\mathrm{read}} K}{\Delta}}. \tag{C.5}$$

We assume here that the number of quasiparticles created by the radiation $N_{\mathrm{qp}}^{\mathrm{rad}}$ is small (linear response regime) in which case $N_{\mathrm{qp}}^{\mathrm{read}}$ determines τ_{qp}, ie $N_{\mathrm{qp}}^{\mathrm{read}} \gg N_{\mathrm{qp}}^{\mathrm{rad}}$. That also means τ_{qp} is expected to scale with the readout power as $\tau_{\mathrm{qp}} \propto P_{\mathrm{read}}^{-1/2}$. The number of quasiparticles that is created by the optical signal is given by

$$N_{\mathrm{qp}}^{\mathrm{rad}} = \frac{\eta_{\mathrm{opt}} \eta_{\mathrm{pb}} P_{\mathrm{rad}} \Delta}{\tau_{\mathrm{qp}}} = \frac{\eta_{\mathrm{opt}} \eta_{\mathrm{pb}} P_{\mathrm{rad}} K}{\Delta N_{\mathrm{qp}}^{\mathrm{read}}}, \tag{C.6}$$

with η_{opt} the optical efficiency and η_{pb} the pair breaking efficiency. The total number of quasiparticles is thus given by

$$N_{\mathrm{qp}} = N_{\mathrm{qp}}^{\mathrm{read}} + N_{\mathrm{qp}}^{\mathrm{rad}} = \frac{\eta_{\mathrm{opt}} \eta_{\mathrm{pb}} P_{\mathrm{rad}} K}{\Delta \sqrt{\frac{\eta_{\mathrm{read}} P_{\mathrm{read}}}{K\Delta}}} + \sqrt{\frac{\eta_{\mathrm{read}} P_{\mathrm{read}}}{K\Delta}}. \tag{C.7}$$

We can now derive $dN_{\mathrm{qp}}/dP_{\mathrm{rad}}$:

$$dN_{\mathrm{qp}}/dP_{\mathrm{rad}} = \frac{\eta_{\mathrm{opt}} \eta_{\mathrm{pb}} K}{\Delta \sqrt{\frac{\eta_{\mathrm{read}} P_{\mathrm{read}}}{K\Delta}}} \propto P_{\mathrm{read}}^{-1/2}. \tag{C.8}$$

The resonator amplitude responsivity is now given by $dA/dP_{\mathrm{rad}} = dA/dN_{\mathrm{qp}} \cdot dN_{\mathrm{qp}}/dP_{\mathrm{rad}}$ and dA/dN_{qp} is given by

$$\frac{dA}{dN_{\mathrm{qp}}} = \frac{\alpha \beta Q}{V} \frac{d\sigma_1}{|\sigma| dn_{\mathrm{qp}}}, \tag{C.9}$$

where α is the kinetic inductance fraction V the volume and $\beta = 1 + \frac{2d/\lambda}{\sinh(2d/\lambda)} \approx 2$, with d the film thickness and λ the magnetic penetration depth. The quality factor Q was measured to be constant as function of readout power, as shown in Fig. C.4 and also

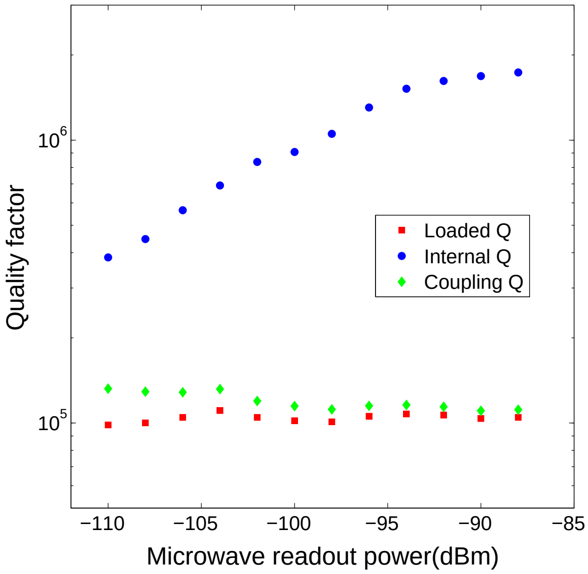

Figure C.4: Measured quality factors. The quality factors as determined from the microwave transmission S_{21} as a function of microwave readout power at the lowest radiation power (the same radiation power as for Fig. 7.5).

$|\sigma|$ is constant. $d\sigma_1/dn_{\mathrm{qp}}$ is a slow function of effective temperature and will change only little over the measured range [8]. Therefore we expect $dA/dP_{\mathrm{rad}} \propto P_{\mathrm{read}}^{-1/2}$.

In this derivation we assumed that the absorbed microwave power in the quasiparticle system $P_{\mathrm{abs}} \propto P_{\mathrm{read}}$. In general this depends on the details of the microwave circuit, and P_{abs} and P_{read} are related by [10]

$$P_{\mathrm{abs}} = \frac{P_{\mathrm{read}}}{2}\frac{4Q^2}{Q_{\mathrm{i}}Q_{\mathrm{c}}}\frac{Q_{\mathrm{i}}}{Q_{\mathrm{i,qp}}}, \tag{C.10}$$

where Q_{i} and Q_{c} are the internal and coupling quality factors, which are both easily measurable. $Q_{\mathrm{i,qp}}$ is the quasiparticle quality factor, which is not known for this device, since Q_{i} is not limited by quasiparticle dissipation. One would expect $Q_{\mathrm{i,qp}}$ to increase for lower P_{read} [9], which would make the readout power dependence of the lifetime and the responsivity stronger. However, in general $Q_{\mathrm{i,qp}}$ cannot be directly derived from N_{qp} [9], it depends on the shape of the driven quasiparticle distribution. We have therefore assumed for simplicity that $Q_{\mathrm{i,qp}}$ is constant as a function of P_{read}. We also assumed that η_{read} is independent of P_{read}. For the same reasons this is a crude assumption. The problem of the readout power dependence of the responsivity requires a future study in which the model of Ref. [9] is extended with a pair breaking term.

The efficiency η_{read} can be calculated by assigning an effective temperature to the measured quasiparticle recombination time. The effective temperature is used to estimate Q_i. The approach is explained in Ref. [4]. Using this, somewhat crude, approximation we estimate that $\eta_{\mathrm{read}} \approx 2 \times 10^{-3}$ at -98 dBm and $\eta_{\mathrm{read}} \approx 6 \times 10^{-4}$ at -92 dBm, which is reasonably close to the value reported in [4] (3×10^{-4}). It is shown by Goldie and Withington [9] that an effective temperature cannot accurately describe both $Q_{\mathrm{i,qp}}$ and τ_{qp}, but we cannot measure $Q_{\mathrm{i,qp}}$ directly in this experiment.

C.4 Readout power dependence for high radiation powers

In Chapter 7 (Fig. 7.5) we have discussed the influence of the readout power on the optical response for the lowest radiation power, thus in the regime where the readout power dissipation dominates the number of quasiparticles. However, also in the regime where the optical signal dominates the number of quasiparticles the optical response is readout power dependent, as is shown in Fig. C.5a for the highest measured radiation power (724 fW). Since the level of the noise spectrum depends on the responsivity (Eq. 7.2), it does not surprise that the level of the photon noise roll-off also varies with the readout power, as shown in Fig. C.5b. Additionally in Fig. C.5b the amplifier noise level (the flat part at high frequencies) changes with readout power as expected. To see up to how far the detector sensitivity changes, we plot $\sqrt{S_A} \cdot (dA/dP_{\mathrm{rad}})^{-1}$ (ie the NEP without the lifetime roll-off factor) in Fig. C.5c, which corrects for the responsivity of the detector and only consist of the photon noise and amplifier noise. We observe that the NEP within the photon-noise roll-off is indeed similar now for all readout powers. In Fig. C.5d we plot the NEP at the reference frequency of 20 Hz, together with an estimate of the amplifier contribution (taken at $f > 300$ kHz). If we subtract the amplifier contribution we see that the leftover photon noise contribution is approximately readout power independent. We conclude that as long as the quasiparticle fluctuations are dominated by photon noise, the readout power dependence of the responsivity does not influence the detector sensitivity (NEP). In practice that means that one can use the highest possible readout power when the detector is photon noise limited to suppress the amplifier noise. Why the responsivity is readout power dependent is a complex problem that requires simulation of the influence of both radiation power and readout power absorption, a start of which has recently been made for the readout power dissipation only [9].

Regarding the readout power, we make a few last remarks:

- The maximum readout power before bifurcation is -88 dBm at the lowest radiation powers and increases to -78 dBm at the highest power of 724 fW.

- In Figs. 7.4 and 7.1c we took the readout power at which the NEP is the lowest. These readout powers are (from low to high radiation power): -94 dBm, -96 dBm, -98 dBm, -92 dBm, -94 dBm, -96 dBm, -96 dBm, -88 dBm, -88 dBm, -86 dBm, -86 dBm, -78 dBm.

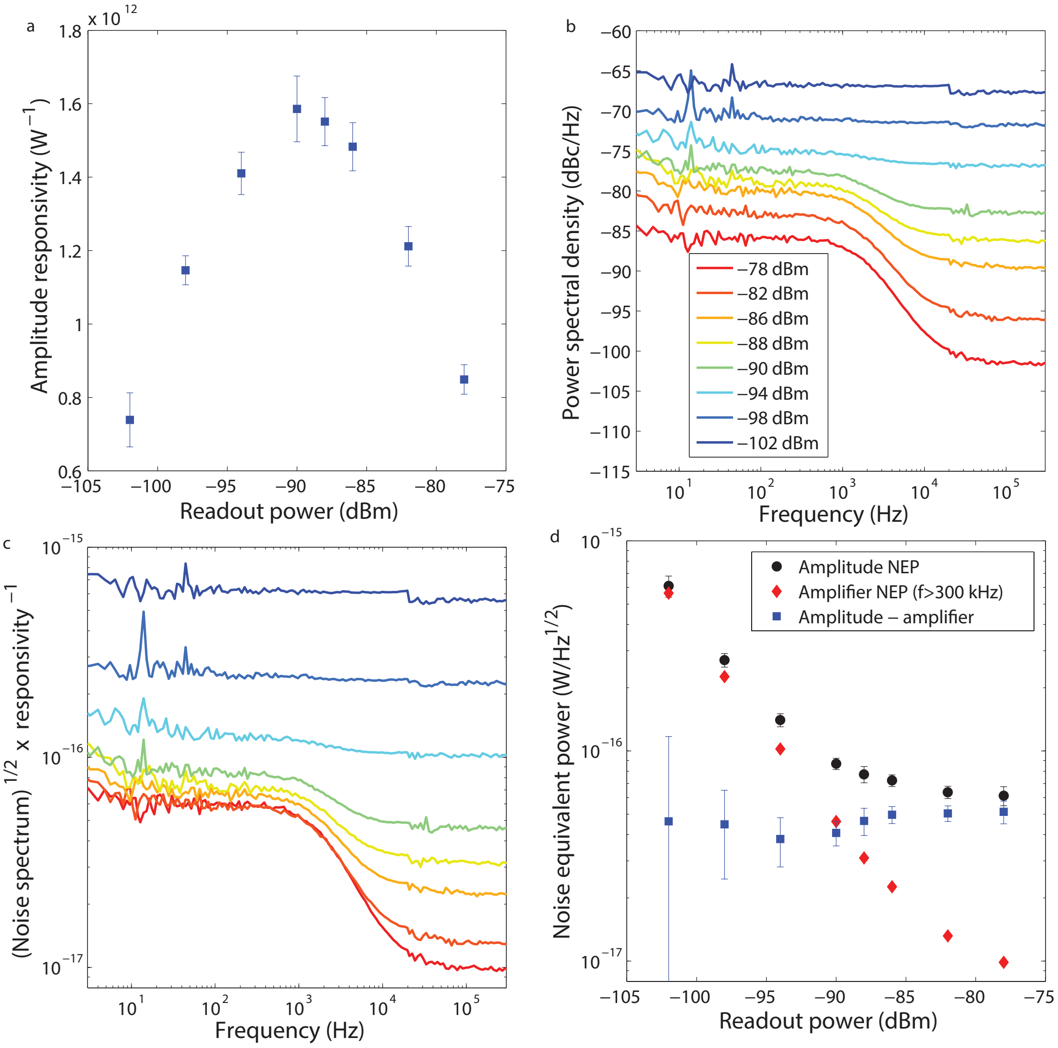

Figure C.5: Microwave readout power dependence of the response at high radiation power. a, The responsivity of the amplitude to radiation power dA/dP_{rad} as a function of microwave readout power for the highest measured radiation power of 724 fW. The error bars denote statistical uncertainties from the fitting procedure (1 s.d.). **b**, The amplitude noise spectra as a function of frequency for various microwave readout powers as indicated in the legend. **c**, The optical NEP, except for the quasiparticle recombination time factor (ie $\sqrt{S_A} \cdot (dA/dP_{\mathrm{rad}})^{-1}$), as a function of frequency for the same readout powers as in **c**. **d**, The optical NEP as a function of microwave readout power taken at the reference frequency of 20 Hz (black dots). The red diamonds show the amplifier contribution to the NEP as measured from the NEP spectra at frequencies above 300 kHz. The black squares are the NEP at 20 Hz minus the NEP above 300 kHz, thus the optical NEP with the amplifier contribution subtracted. The latter is a measure of the NEP due to photon noise only, and is therefore expected to be constant as a function of readout power. The error bars are the combined statistical uncertainty (1 s.d.).

- The increase in noise level upon crossing from generation-recombination noise to photon noise in Fig. a7.3 is only clear for a constant readout power as is shown in that figure. When different readout powers are used for different radiation powers, the changing responsivity changes the picture. We therefore did not quantitatively analyse this problem, because it requires a complex model as discussed before. The quasiparticle recombination time from the roll-off frequency is not influenced by the responsivity and therefore a more direct measure of the behaviour of the quasiparticle system.

References

[1] J. Gao, J. Zmuidzinas, B. A. Mazin, H. G. LeDuc, and P. K. Day, *Noise properties of superconducting coplanar waveguide microwave resonators*, Appl. Phys. Lett. **90**, 102507 (2007).

[2] R. Barends, H. L. Hortensius, T. Zijlstra, J. J. A. Baselmans, S. J. C. Yates, J. R. Gao, and T. M. Klapwijk, *Noise in NbTiN, Al and Ta superconducting resonators on silicon and sapphire substrates*, IEEE Trans. on Appl. Supercond. **19**, 936 (2009).

[3] R. Barends, H. L. Hortensius, T. Zijlstra, J. J. A. Baselmans, S. J. C. Yates, J. R. Gao, and T. M. Klapwijk, *Contribution of dielectrics to frequency and noise of NbTiN superconducting resonators*, Appl. Phys. Lett. **92**, 223502 (2008).

[4] P. J. de Visser, J. J. A. Baselmans, S. J. C. Yates, P. Diener, A. Endo, and T. M. Klapwijk, *Microwave-induced excess quasiparticles in superconducting resonators measured through correlated conductivity fluctuations*, Appl. Phys. Lett. **100**, 162601 (2012).

[5] J. Zmuidzinas, J. Gao, P. K. Day, and H. G. LeDuc, unpublished.

[6] C. Neill, A. Megrant, R. Barends, Y. Chen, B. Chiaro, J. Kelly, J. Y. Mutus, P. J. J. O'Malley, D. Sank, J. Wenner, T. C. White, Y. Yin, A. N. Cleland, and J. M. Martinis, *Fluctuations from edge defects in superconducting resonators*, Appl. Phys. Lett. **103**, 072601 (2013).

[7] S. B. Kaplan, C. C. Chi, D. N. Langenberg, J. Chang, S. Jafarey, and D. J. Scalapino, *Quasiparticle and phonon lifetimes in superconductors*, Phys. Rev. B **14**, 4854 (1976).

[8] J. Gao, J. Zmuidzinas, A. Vayonakis, P. Day, B. Mazin, and H. Leduc, *Equivalence of the effects on the complex conductivity of superconductor due to temperature change and external pair breaking*, J. Low Temp. Phys. **151**, 557 (2008).

[9] D. J. Goldie and S. Withington, *Non-equilibrium superconductivity in quantum-sensing superconducting resonators*, Supercond. Sci. Technol. **26**, 015004 (2013).

[10] J. Zmuidzinas, *Superconducting Microresonators: Physics and Applications*, Ann. Rev. Condens. Matter Phys. **3**, 169 (2012).

Summary

Quasiparticle dynamics in aluminium superconducting microwave resonators

In a superconductor which is cooled well below its critical temperature, most of the electrons that contribute to electrical conduction are paired in so called Cooper pairs. The lower the temperature the more electrons are paired and the less quasiparticles (unpaired electrons) are left. In a state without quasiparticle excitations, the superconductor is sensitive to the tiniest distortion. Photons with an energy larger than the binding energy can break Cooper pairs and cause quasiparticle excitations. The low binding energy in superconductors makes them suitable for the detection of far-infrared and submillimetre radiation. Aluminium for instance has a gap energy of 0.18 meV, which enables pair-breaking detection of radiation with frequencies of 90 GHz and higher. A pair-breaking detector essentially counts the quasiparticle excitations due to radiation absorption. The average recombination time of the quasiparticles, which is inversely proportional to the number of quasiparticles, determines how long an excitation lasts and should therefore be long. In aluminium, the electron-phonon interaction is slow, which makes it an excellent material for such a detector.

The fundamental noise source associated with such a detector is due to fluctuations in the number of quasiparticles. When other noise source are reduced to the level that quasiparticle fluctuations become the limiting factor, the sensitivity can only be increased by reducing the amount of excess quasiparticle excitations and/or by increasing their recombination lifetime. Excess quasiparticles are a common problem for superconducting devices. For example, the coherence time of superconducting qubits depends on the number of quasiparticles. There is thus a common desire to explicitly measure the number of quasiparticles and their recombination lifetime, and to reveal the mechanisms that introduce excess quasiparticles.

Kinetic inductance detectors are superconducting microwave resonators that sense a change in the complex conductivity of the superconductor upon a change in the number of quasiparticles. Superconducting resonators show high quality factors, which results in potentially very sensitive detectors. On top of that, the resonators can be designed to have slightly different lengths, which gives a natural way for frequency multiplexing. Therefore thousands of detector pixels can be read out with just a pair of coaxial cables.

Resonator detectors are therefore the ideal candidate for the large imaging arrays that are required to make the next big step in submillimetre and far-infrared astronomy. For space-based, background limited imaging, these detectors have to be very sensitive, with a noise equivalent power (NEP) of 1-4$\times10^{-19}$ W/Hz$^{1/2}$. On top of that, a power-integrating detector is ideally limited by photon-noise due to the radiation source itself. For a pair-breaking detector, the fluctuations in the photon stream cause fluctuations in the number of broken pairs and thus in the number of quasiparticle excitations.

In microwave resonator detectors the complex conductivity of the superconductor plays a role both in the microwave response (photons with energy much smaller than the gap energy) and in the absorption of pair-breaking radiation. When a *pair-breaking* signal is applied, the real part of the complex conductivity describes how quickly such a signal is absorbed in the superconductor. At low temperatures the *microwave* response of the superconductor has a real and a complex part. The real part is due to absorption of microwave photons by quasiparticles (dissipation). At low temperatures the number of quasiparticles and the dissipation are small, which enables microwave resonators with high quality factors. The imaginary part of the response is due to the inertia of the charge carriers, which causes a kinetic inductance in an alternating electromagnetic field. The complex conductivity is determined by the resistivity of the material, the density of states, and the distribution of quasiparticles over energy.

To test detectors for space-based imaging, space-based conditions need to be mimicked in the test setup (Chapter 3). In practice two requirements have to be fulfilled. Firstly, any stray light has to be eliminated, because our detectors are very sensitive to small signals. The main source of stray light in our cryogenic test setup is thermal radiation from the 3 K stage. To achieve a stray-light tight environment, the sample box is surrounded by another closed box at the same temperature, a so called box-in-box setup. We verify that the setup is stray light tight, with a stray-light level lower than 60 aW. This upper bound is limited by the intrinsic sensitivity of the detectors. Secondly, a well-defined pair-breaking signal has to be applied. As a radiation source we use a cryogenic blackbody, with optical filters that define a passband of 0.1 THz around 1.54 THz. The system allows to vary the radiation power in the 1.54 THz band from 3 zW to 1 pW.

We present measurements of quasiparticle number fluctuations in aluminium microwave resonators as a function of temperature (not illuminated with pair-breaking radiation). The resonators are halfwave coplanar waveguide resonators with an isolated central line. Quasiparticle fluctuations cause fluctuations in the complex conductivity of the superconductor, which shows up in the microwave response of the resonator (Chapter 5). The roll-off in the spectrum of the fluctuations is a measure of the quasiparticle recombination time. The number of quasiparticles can be obtained from the level of the noise spectra. At temperatures of 160 mK and higher the recombination time agrees well with theory, but it saturates below 160 mK, which is consistently explained by a saturation in the number of quasiparticles. By studying the cross power spectral density of the dissipative (amplitude) and reactive part (phase) of the microwave response, we reveal correlated quasiparticle fluctuations, which are the signature of correlated fluctuations in the quasiparticles and the condensate of the superconductor (Chapter 6). Because other noise sources are uncorrelated, quasiparticle fluctuations can be studied with a sensitivity close to the vacuum noise. Using this method, we observe that the saturation level in the number of quasiparticles and their recombination time is microwave power dependent. This observation rules out stray light in our setup as the origin of excess quasiparticles and presents a challenge for microresonator detectors: to reduce the microwave readout power whilst still being generation-recombination noise limited. The measured dark, generation-recombination noise limited NEP is 2×10^{-19} W/Hz$^{1/2}$, using the amplitude response of the resonator.

In a second experiment, pair-breaking radiation is coupled into an aluminium microwave resonator (Chapter 7). Radiation at 1.54 THz is coupled into the coplanar waveguide through a lens and an antenna. The experiment allows to characterise the response of the superconductor as a function of radiation power, temperature and microwave readout power. At radiation powers of 0.1 fW to 0.7 pW, we observe photon-noise limited detection with an optical efficiency of 48%, which is verified through a measurement of the spectra of quasiparticle fluctuations. Below 0.1 fW, the fluctuations are dominated by generation-recombination noise due to excess quasiparticles, which is verified by measuring the noise spectra also as a function of temperature. We observe a readout power dependent optical responsivity and quasiparticle recombination time, which indicates that the responsivity and sensitivity are now limited by microwave dissipation. In the saturation regime the optical NEP is 3.8×10^{-19} W/Hz$^{1/2}$, close to the expected value based on dark experiments, and within the specifications for space-based imaging.

In both the dark experiments and the experiment with pair-breaking radiation, the detector sensitivity is limited by excess quasiparticles due to absorption of microwave readout power. After elucidating the fundamental noise limits of superconducting microwave resonators, the next question is how microwave power creates excess quasiparticles and how that affects the resonator response. To answer the last part of the question, we present a model in which the absorption of microwave readout power is treated as heating (Chapter 4). The quasiparticle system is heated by microwave power absorption and cooled through electron-phonon interaction. We solve the heat balance between those two processes to obtain an effective quasiparticle temperature. We show that the effective temperature peaks at the resonant frequency, where the readout power absorption is highest. Due to the frequency-dependent effective temperature the resonance curves get strongly distorted. At high power levels, multiple solutions to the heat balance occur, which gives rise to hysteretic switching between different thermal states.

Microwave absorption inherently changes the energy of the quasiparticles. Therefore, if the field is strong enough, it leads to a non-equilibrium distribution of the quasiparticles. The absorbed microwave energy is released by electron-phonon interaction. We study the effect of microwave absorption on the quasiparticle distribution of the superconductor and on its electrodynamic response, both experimentally and with numerical simulations (Chapter 8). The non-equilibrium quasiparticle distribution functions lead to a non-equilibrium response of the complex conductivity, which is probed by the quality factor and resonant frequency of an aluminium microwave resonator. At low temperatures microwave absorption induces excess quasiparticles, consistent with a decreasing quality factor with increasing power. Qualitatively this behaviour is analogous to heating. At higher temperatures (above 200 mK), the opposite behaviour is observed. Both the quality factor and resonant frequency increase with increasing microwave power, which cannot be explained with an effective temperature, but which is explained by a non-equilibrium quasiparticle distribution due to microwave absorption. Redistribution of quasiparticles explains the observations of the quality factor, resonant frequency and quasiparticle recombination time in both temperature regimes. Although microwave photons cannot break Cooper pairs directly, the redistribution of the quasiparticles upon microwave absorption eventually creates the excess quasiparticles which currently limit the sensitivity of our detectors.

Pieter de Visser
Delft, January 2014

Samenvatting

De dynamica van quasideeltjes in aluminium supergeleidende microgolf resonatoren

In een supergeleider die tot ver beneden zijn kritische temperatuur is afgekoeld zijn de meeste elektronen die bijdragen aan de elektrische geleiding gepaard. Zij vormen zogenaamde Cooper paren. Des te lager de temperatuur des te meer elektronen gepaard zijn en des te minder quasideeltjes (ongepaarde elektronen) overblijven. In een toestand zonder quasideeltjes is de supergeleider gevoelig voor de kleinste verstoring. Fotonen met een energie die groter is dan de bindingsenergie kunnen Cooper paren verbreken en quasideeltjes creëeren. De lage bindingsenergie van supergeleiders maakt deze materialen bijzonder geschikt om ver-infrarood- en submillimeterstraling te detecteren. Aluminium heeft bijvoorbeeld een bindingsenergie van 0.18 meV, wat detectie van straling met frequenties van 90 GHz en hoger mogelijk maakt. In een detector waarin paren worden gebroken, wordt in essentie het aantal quasideeltjes geteld dat door het absorberen van straling wordt veroorzaakt. De gemiddelde recombinatietijd van de quasideeltjes, die omgekeerd evenredig is met het aantal quasideeltjes, bepaalt hoe lang een excitatie duurt en is daarom bij voorkeur lang. Omdat de elektron-fonon interactie in aluminium langzaam is, is dit een uitstekend materiaal voor deze detectors.

De fundamentele bron van ruis voor deze dectector wordt veroorzaakt door fluctuaties in het aantal quasideeltjes. Wanneer andere bronnen van ruis gereduceerd worden tot een niveau waarbij de fluctuaties van de quasideeltjes domineren, kan de gevoeligheid van de detector alleen nog verbeterd worden door het aantal quasideeltjes te reduceren en/of hun recombinatietijd te verlengen. Voor supergeleidende apparaten is een overmaat aan quasideeltjes een gemeenschappelijk probleem. De coherentietijd van supergeleidende qubits is bijvoorbeeld afhankelijk van het aantal quasideeltjes. Vanuit deze verschillende invalshoeken is er de gemeenschappelijke wens het aantal quasideeltjes en hun levensduur te meten en de mechanismen die een overmaat aan quasideeltjes veroorzaken aan het licht te brengen.

Kinetische inductie detectors bestaan uit supergeleidende microgolf resonatoren waarin een verandering in de complexe geleiding van de supergeleider optreedt wanneer het aantal quasideeltjes verandert. Supergeleidende resonatoren hebben een hoge kwaliteitsfactor, wat in potentie tot zeer gevoelige detectoren leidt. Daarbovenop kan aan iedere resonator een andere lengte worden gegeven, wat op een natuurlijke manier frequentie-multiplexen mogelijk maakt. Hierdoor kunnen duizenden detector pixels worden uitgelezen met slechts één paar coax kabels. Resonator-detectors zijn daarom ideaal voor het bouwen van multipixel camera's die nodig zijn om een nieuwe stap te maken in submillimeter- en ver-infrarood astronomie. Voor een ruimtecamera die gelimiteerd is door de achtergrondstraling moeten deze detectoren bijzonder gevoelig zijn, met een noise equivalent power (NEP) van 1-4$\times 10^{-19}$ W/Hz$^{1/2}$. Daarnaast wordt een detector die het signaal integreert idealiter gelimiteerd door fotonruis, wat veroorzaakt wordt door de bron van straling. In een paarbrekende detector resulteert deze fotonruis in fluctuaties in het aantal gecreëerde quasideeltjes.

In detectors gebaseerd op microgolf resonatoren speelt de complexe geleiding van de supergeleider een rol in zowel de microgolf response (fotonen die geen Cooper paren kunnen breken) als in de absorptie van straling die paren breekt. Wanneer een *paarbrekend signaal* wordt aangelegd beschrijft het reële deel van de complexe geleiding hoe snel dat signaal geabsorbeerd wordt in de supergeleider. De *microgolf* response van de supergeleider heeft op lage temperatuur een reëel en een complex deel. Het reële wordt veroorzaakt door absorptie van microgolf fotonen door de quasideeltjes (dissipatie). Op lage temperatuur zijn het aantal quasideeltjes en de dissipatie klein, wat microgolf resonatoren met hoge kwaliteitsfactoren mogelijk maakt. Het imaginaire deel van de response wordt veroorzaakt door de inertie van de ladingsdragers. Deze inertie veroorzaakt een kinetische inductie in een elektromagnetisch veld. De complexe geleiding wordt bepaald door de resistiviteit van een materiaal, de toestandsdichtheid en de verdeling van quasideeltjes over energie.

Om detectors voor ruimteonderzoek te kunnen testen, moeten de condities voor die detectors nagebootst worden in de testopstelling (Hoofdstuk 3). In de praktijk moet daarom aan twee voorwaarden voldaan worden. Ten eerste moet alle strooilicht geëlimineerd worden, omdat de detectoren gevoelig zijn voor hele kleine signalen. De belangrijkste bron van strooilicht in onze opstelling is thermische straling van het 3 Kelvin-deel van de opstelling. Om de detector af te schermen van strooilicht, wordt de samplehouder omgeven door een andere afgesloten houder op dezelfde temperatuur, een dubbel afgeschermde opstelling. We tonen aan dat de opstelling lichtdicht is, met een strooilichtvermogen van minder dan 60 aW. Deze bovengrens wordt gelimiteerd door de intrinsieke gevoeligheid van de detectoren. Vervolgens moet er een goed gedefinieerd, paarbrekend signaal aangeboden worden. Als bron van straling gebruiken we een cryogene zwarte straler, gevolgd door optische filters die een banddoorlaatfilter definiëren met een bandbreedte van 0.1 THz rondom 1.54 THz. Hierdoor is het mogelijk om het vermogen van de straling te variëren van 3 zW tot 1 pW.

We presenteren metingen van fluctuaties in het aantal quasideeltjes in aluminium supergeleidende microgolf resonatoren als functie van temperatuur (hier wordt nog geen paarbrekende straling gebruikt). De resonatoren zijn coplanaire golfgeleiders die een halve golflengte lang zijn, waarbij de centrale lijn geïsoleerd is. Fluctuaties in het aantal quasideeltjes veroorzaken fluctuaties in de complexe geleiding van de supergeleider, die zichtbaar wordt in de microgolfrespons van de resonator (Hoofdstuk 5). De afsnijfrequentie die in het frequentiespectrum van deze fluctuaties zichtbaar wordt, is de recombinatietijd van de quasideeltjes. Het aantal quasideeltjes kan bepaald worden uit het ruisniveau. Voor temperaturen boven de 160 mK gedraagt de recombinatietijd zich zoals theoretisch voorspeld, maar onder de 160 mK treedt verzadiging op. Deze verzadiging is consistent met een verzadiging van het aantal quasideeltjes. Door het bestuderen van de spectrale vermogensdichtheid van de kruiscorrelatie tussen het dissipatieve (amplitude) en het reactieve deel (fase) van de microgolf respons, brengen we gecorreleerde fluctuaties aan het licht die wijzen op gecorreleerde fluctuaties van de quasideeltjes en het condensaat van de supergeleider (Hoofdstuk 6). Omdat andere bronnen van ruis ongecorreleerd zijn, kunnen de fluctuaties in het aantal quasideeltjes bestudeerd worden met een gevoeligheid die in de buurt komt van de vacuüm ruis. Met deze methode observeren we dat het saturatieniveau in het aantal quasideeltjes afhangt van het microgolfvermogen. Deze waarneming sluit uit dat de overmaat aan quasideeltjes veroorzaakt wordt door strooilicht in onze opstelling, maar zorgt tegelijkertijd voor een uitdaging voor deze detectoren: het reduceren van het microgolfvermogen, terwijl de ruis gelimiteerd blijft door generatie-recombinatieruis. De gemeten, donkere, generatie-recombinatie gelimiteerde NEP is hier 2×10^{-19} W/Hz$^{1/2}$, waarbij gebruik is gemaakt van de respons in de amplitude.

In een tweede experiment koppelen we paarbrekende straling in in een aluminium microgolf resonator (Hoofdstuk 7). Straling met een frequentie van 1.54 THz wordt ingekoppeld door middel van een lens en een antenne. In het experiment karakteriseren we de respons van de supergeleider op paarbrekende straling, op het microgolfsignaal en op een verandering in temperatuur. Bij stralingsvermogens tussen de 0.1 fW en 0.7 pW observeren we door fotonruis gelimiteerde detectie met een optische efficiëntie van 48%, wat we verifieren door middel van een meting van de spectra van de fluctuaties in het aantal quasideeltjes. Beneden de 0.1 fW worden de fluctuaties gedomineerd door de generatie-recombinatieruis die veroorzaakt wordt door quasideeltjes die in overmaat aanwezig zijn. Dit verifiëren we door de ruisspectra te meten als functie van temperatuur. De optische response en de recombinatietijd van de quasideeltjes zijn afhankelijk van het microgolfvermogen, wat erop wijst dat de respons en de gevoeligheid van de detector gelimiteerd worden door dissipatie van het microgolfsignaal. De laagste optische NEP is 3.8×10^{-19} W/Hz$^{1/2}$, dichtbij de voorspelling op basis van de 'donkere' metingen en binnen de specificaties voor fotometrie in de ruimte.

Zowel in de donkere experimenten als in het experiment met paarbrekende straling wordt de gevoeligheid van de detector gelimiteerd door een overmaat aan quasideeltjes, die veroorzaakt wordt door het microgolf uitleessignaal. Na het ophelderen van de fundamentele ruislimieten is de vervolgvraag hoe het microgolfvermogen tot een overmaat aan quasideeltjes leidt en hoe de respons van de resonator hierdoor beïnvloed wordt. Om het laatste deel van de vraag te beantwoorden, presenteren we een model waarin de absorptie van microgolfvermogen behandeld wordt als opwarming (Hoofdstuk 4). Het quasideeltjessysteem van de supergeleider wordt opgewarmd door het absorberen van microgolfvermogen en wordt afgekoeld door elektron-fonon interactie. We berekenen de effectieve temperatuur van de quasideeltjes door de warmtebalans tussen deze twee processen op te lossen. De effectieve temperatuur is maximaal bij de resonantiefrequentie, waar de microgolfabsorptie het hoogst is. Door de frequentie-afhankelijke effectieve temperatuur worden de resonantiecurves sterk verstoord. Bij een hoog microgolfvermogen ontstaan meerdere oplossingen voor de warmtebalans, wat resulteert in het hysteretisch springen tussen de verschillende temperatuursoplossingen.

Het veranderen van de energie van de quasideeltjes is inherent aan de absorptie van microgolf fotonen. Als het microgolfveld sterk genoeg is, resulteert dat daarom in een niet-evenwichtsverdeling van de quasideeltjes. Het geabsorbeerde microgolfvermogen wordt afgevoerd door elektron-fonon interactie. We bestuderen het effect van microgolfabsorptie op de verdeling van de quasideeltjes in de supergeleider door middel van experimenten en numerieke simulaties (Hoofdstuk 8). De niet-evenwichtsverdeling van de quasideeltjes leidt tot een niet-evenwichts respons van de complexe geleiding, wat zich vertaalt in een veranderende kwaliteitsfactor en resonantiefrequentie van een aluminium microgolfresonator. Op lage temperaturen veroorzaakt microgolfabsorptie een overmaat aan quasideeltjes, waardoor de kwaliteitsfactor afneemt met toenemend microgolfvermogen. Dit gedrag is kwalitatief analoog aan opwarming. Op hogere temperaturen (boven de 200 mK) observeren we het tegenovergestelde gedrag. Zowel de kwaliteitsfactor als de resonantiefrequentie nemen toe met toenemend microgolfvermogen, wat niet verklaard kan worden door opwarming, maar wat zich laat verklaren door middel van een niet-evenwichtsverdeling van de quasideeltjes door microgolfabsorptie. De herverdeling van quasideeltjes verklaart het gedrag van de kwaliteitsfactor, de resonantiefrequentie en de recombinatietijd van de quasideeltjes over het hele temperatuursbereik. Ondanks dat microgolffotonen Cooper paren niet direct kunnen breken, kan de herverdeling van quasideeltjes door microgolfabsorptie uiteindelijk leiden tot de overmaat aan quasideeltjes die nu de gevoeligheid van onze detectoren limiteert.

Pieter de Visser
Delft, januari 2014

Curriculum Vitae

Pieter Jan de Visser

06–08–1985	Born in Vlissingen, The Netherlands
1997–2003	Grammar school Calvijn College, Middelburg / Goes
2003–2009	M. Sc. Applied Physics at Delft University of Technology Minor in Astronomy and Instrumentation at Leiden University Master Thesis: *Analysis and manipulation of the beams of quantum cascade lasers with different waveguide designs* Supervisor: Dr. J. R. Gao
2009	Research internship at Cambridge University, UK Supervisors: Prof. dr. S. Withington and Dr. D. J. Goldie
2009–2013	Ph. D. Research SRON (Netherlands Institute for Space Research) and Delft University of Technology Thesis: *Quasiparticle dynamics in aluminium superconducting microwave resonators* Supervisors: Prof. dr. ir. T. M. Klapwijk (promotor) and Dr. ir. J. J. A. Baselmans (copromotor)

List of publications

1. *Fluctuations in the electron system of a superconductor exposed to a photon flux*
   P. J. de Visser, J. J. A. Baselmans, J. Bueno, N. Llombart and T. M. Klapwijk
   Nature Communications, **5**, 3130 (2014)

2. *Evidence of a nonequilibrium distribution of quasiparticles in the microwave response of a superconducting aluminium resonator*
   P. J. de Visser, D. J. Goldie, P. Diener, S. Withington, J. J. A. Baselmans and T. M. Klapwijk
   Physical Review Letters, **112**, 047004 (2014)

3. *Microwave properties of superconducting atomic layer deposited TiN films*
   P. C. J. J. Coumou, M. R. Zuiddam, E. F. C. Driessen, P. J. de Visser, J. J. A. Baselmans and T. M. Klapwijk
   IEEE Transactions on Applied Superconductivity, **23**, 7500404 (2013)

4. *Strongly Disordered TiN and NbTiN s-Wave Superconductors Probed by Microwave Electrodynamics*
   E. F. C. Driessen, P. C. J. J. Coumou, R. R. Tromp, P. J. de Visser and T. M. Klapwijk
   Physical Review Letters **109**, 107003 (2012)

5. *Microwave-induced excess quasiparticles in superconducting resonators measured through correlated conductivity fluctuations*
   P. J. de Visser, J. J. A. Baselmans, S. J. C. Yates, P. Diener, A. Endo and T. M. Klapwijk
   Applied Physics Letters **100**, 162601 (2012)

6. *Quasideeltjes tellen door ruis te meten*
   Pieter de Visser
   Nederlands Tijdschrift voor Natuurkunde, Jaargang 78, Nummer 9, p344-347 (2012)

7. *Development of DESHIMA: A Redshift Machine Based on a Superconducting On-Chip Filterbank*
   A. Endo, J. J. A. Baselmans, P. P. van der Werf, B. Knoors, S. M. H. Javadzadeh,

S. J. C. Yates, D. J. Thoen, L. Ferrari, A. M. Baryshev, Y. J. Y. Lankwarden, P. J. de Visser, R. M. J. Janssen and T. M. Klapwijk
Proc. SPIE **8452**, 84520X-84520X-15 (2012)

8. *Generation-recombination noise: the fundamental sensitivity limit for Kinetic Inductance Detectors*
   P. J. de Visser, J. J. A. Baselmans, P. Diener, S. J. C. Yates, A. Endo and T. M. Klapwijk
   Journal of Low Temperature Physics **167**, 335-340 (2012)

9. *Integrated Filterbank for DESHIMA: A Submillimeter Imaging Spectrograph Based on Superconducting Resonators*
   A. Endo, P. van der Werf, R. M. J. Janssen, P. J. de Visser, T. M. Klapwijk, J. J. A. Baselmans, L. Ferrari, A. M. Baryshev and S. J. C. Yates
   Journal of Low Temperature Physics **167**, 341-346 (2012)

10. *Ultra low background cryogenic test facility for far-infrared radiation detectors*
    Jochem Baselmans, Stephen Yates, Pascale Diener and Pieter de Visser
    Journal of Low Temperature Physics **167**, 360-366 (2012)

11. *Power Handling and Responsivity of Submicron Wide Superconducting Coplanar Waveguide Resonators*
    R. M. J. Janssen, A. Endo, J. J. A. Baselmans, P. J. de Visser, R. Barends and T. M. Klapwijk
    Journal of Low Temperature Physics **167**, 354-359 (2012)

12. *Number fluctuations of sparse quasiparticles in a superconductor*
    P. J. de Visser, J. J. A. Baselmans, P. Diener, S. J. C. Yates, A. Endo and T. M. Klapwijk
    Physical Review Letters **106**, 167004 (2011)

13. *Readout-power heating and hysteretic switching between thermal quasiparticle states in Kinetic Inductance Detectors*
    P. J. de Visser, S. Withington and D. J. Goldie
    Journal of Applied Physics **108**, 114504 (2010)

14. *Reduced frequency noise in superconducting resonators*
    R. Barends, N. Vercruyssen, A. Endo, P. J. de Visser, T. Zijlstra, T. M. Klapwijk, and J. J. A. Baselmans
    Applied Physics Letters **97**, 033507 (2010)

15. *Minimal resonator loss for circuit quantum electrodynamics*
    R. Barends, N. Vercruyssen, A. Endo, P. J. de Visser, T. Zijlstra, T. M. Klapwijk,

P. Diener, S. J. C. Yates, and J. J. A. Baselmans
Applied Physics Letters **97**, 023508 (2010)

16. *Hysteretic thermal switching due to readout power heating in kinetic inductance detectors*
Pieter de Visser, Stafford Withington and David Goldie
Proceedings of the 21st International Symposium on Space Terahertz Technology, Oxford, p96-100 (2010)

17. *3.5 THz surface emitting distributed feedback QCL operated at 70 K as local oscillator*
Y. Ren, P. J. de Visser, J. N. Hovenier, W.Zhang, P. Khosropanah, J. R. Gao, T. M. Klapwijk, S. C. Shi, T-Y. Kao, S. Kumar, Q. Hu, and J. L. Reno
Proceedings of the 21st International Symposium on Space Terahertz Technology, Oxford, p468-471 (2010)

Acknowledgements

Pursuing a PhD is often considered to be a lonely job. However, after four years of research the list of people with whom I had the chance to cooperate and interact is rather long. To a large extent, that is because my position was jointly at SRON and in the Cosmonanoscience group in Delft, which naturally involved many people, and which turned out to be a very fruitful cooperation. Here I would like to express my gratitude to those who supported me personally and professionally.

Teun and Jochem, it was a privilege to have both of you as supervisors. Your approaches to advise people and to organise research nicely complement and strengthen each other. I learned a lot from both of you. Thank you for the opportunity to be a member of the groups in Delft and Utrecht, which provided a vivid and fertile soil for this research. I have also enjoyed the many opportunities you gave me to visit conferences. Teun, I appreciate your critical attitude towards research, the attention to shape ones mental framework, and the desire to dig deeper into the physics. Especially the ability to shape the research around the skills, wishes and personal boundary conditions of a person is admirable. Discussing about other ‘aspects’ of life is always a pleasure. Jochem, you were able to transfer your seemingly endless energy and enthusiasm. Often when I came back from Utrecht, I was full of new ideas and energy to attack problems. You combine an eye for details with a broad view, which are both essential to bring the KID work where it is now. On top of that it was very helpful that you like lab work, measurements and designs so much.

Just before the start of my PhD, I went to Cambridge. Stafford and David, you teached me a lot about resonators and how to numerically model their response. In addition, I improved in speaking and writing proper English. Fortunately, we could continue our fruitful cooperation later on, which resulted recently in another joint paper. Stafford, we should definitely go for a curry again! It was a pleasure to share an office with Chris and Karwan and to play soccer, pingpong and badminton together.

In Delft I have met many interesting people in the Cosmonanoscience/Physics of Nanoelectronics/NF group. I was lucky that Rami extended his stay in our group for a while. Thank you for teaching me everything about the setup and about microwave resonators, and for the nice cooperation. Thanks to my roommates Nathan, Reinier and Jing for providing a stimulating environment. Nathan, you were always attentively taking care of the temperature, desk-aged vitamins and the beer and bike supply of

our room. Thanks as well for the numerous insightful discussions on physics. You have a special talent for organizing social events, which I enjoyed every time. Reinier, thanks for the last ten years we have been studying and working together. It is good to see your continuous dedication for both astronomy and physics. We will all remember the physical and mental struggle we went through to beat those massive Sinterklaas cakes. Rik, we will remember all those epic pingpong matches as well as discussions about sports, life and everything. The photos of boiling nitrogen were very nice, which therefore formed the basis of the cover of this thesis. Eduard and Pieter-Jan, we have had many interesting discussions, much about everything, and some about the interesting topic of disordered superconductivity on which we cooperated. Akira, thanks for all those stimulating discussions on quasiparticles, detectors, KIDs, kids and for bringing the problem of correctly typesetting subscripts to my attention. I hope that you will be able to finish Deshima and to use it for some fascinating astronomy. Gao, thanks for your guidance in combining SRON and TU Delft, as well as discussions on detectors, space research and more. Thanks to Tony and David for fabricating devices and keeping the cleanroom in shape. Yuan, you are now a superdoctor! Also thanks to Alessandro, David, Alibey, Mihai, Morris, and other former group members. Maria, Irma, Dorine and Monique, thanks for your assistance and for balancing the teatable discussions. There were many master students around during this period: Cristina, Tom, Bastian, Rutger, Nuri, Marco, Peng, Remco, Robbert-Jan, Amar, Werner, thank you for keeping our group young and vivid. Thanks as well to all the bachelor-, and other students who joined us for projects. Several visitors were around to enrich our group, of whom I name here Marc, Karl, Kate, Mohammed, Masato, Maryna and Jaime.

I would like to thank the students on whom I could test my supervision skills. Chris, thanks for your help in numerical simulations and all the best with your PhD. Olav, I hope you still enjoy listening to correlated noise. I enjoyed working with Lucinda and Guoji on various aspects of disordered superconductors. Mark, Jaap and Pascal, thanks for contributing to the modelling of the microwave response and I hope we could still finish this project.

At SRON, I learned a lot from Stephen about measurements and data analysis. Also thanks for building the setup together with Jochem. I enjoyed working together with Pascale, and the vivid discussions you were always involved in. Thanks to Jan Joost for all the cleanroom work, which resulted in the samples that made this thesis possible. Juan, you joined the team later on, and I enjoyed cooperating with you. Thanks for showing us around LA, with as highlights the Korean spa and the molecular dinner. Henk, thanks for the opportunity to be part of SR&T and for taking care of the division and the people. Jennifer, thanks for taking care of so many practical issues. With many other SRON colleagues we had nice conference visits and dinners, coffee breakes and interesting discussions: Lorenza, Andrey B., Darren, Andrey K., Pourya, Richard, Jan, Roland, Marcel B., Marcel R., Luciano, Manuela, Martijn, Gert, Hiroki, Piet, Mark, Damian and all the other colleagues and fellow PhD-students who also made the science days and science forums enjoyable. Thanks to the PhD evaluation committee, Floris, Marcel, Martijn and Jean, for keeping an eye on our progress.

I would like to thank Leo DiCarlo, Diego, Raymond and Konrad for the nice cooperation in an effort to use the paramp for our noise measurements. Leo and Diego, thanks for the many interesting discussions on superconducting circuits, measurements and quasiparticles. Also the journal club was very pleasant and useful, for which I would like to thank all the members. Thanks to Sander, Miriam and Marcin for forming the core of the solid state team, which enriched my teaching experience greatly. Nuria and Andrea were the neighbour experts on lenses, antennas, efficiencies and wave propagation. I enjoyed our fruitful cooperation and discussions. I also want to thank all colleagues who form the KID or microresonator community, who made all conferences and workshops both socially and scientifically pleasant.

Belangrijker nog was de steun van vrienden, huisgenoten en familie, van wie ik in het bijzonder papa, mama en Neline wil bedanken. Maria, bedankt voor je liefde, zorg en steun, zelfs als ik om onduidelijke redenen weer 's avonds of 's nachts dacht te moeten werken. Debora, dank dat je je vader al zo goed begreep dat je pas ter wereld wilde komen toen het concept af was. Above all I want to thank God from whom I have received everything I have accomplished. To Him be the glory.

Pieter de Visser
Delft, januari 2014

Casimir PhD Series 2014-3
ISBN: 978-90-8593-178-2